VT-Forschungsbericht 2015-01

Development of Numerical Methods for the Calculation of Thermo-Acoustic Interactions in Gas Turbine Combustion Chambers

Dipl.-Ing. Gilles Reichling

Deutsches Zentrum für Luft- und Raumfahrt
Institut für Verbrennungstechnik
Stuttgart

DLR Deutsches Zentrum für Luft- und Raumfahrt

Herausgeber

Deutsches Zentrum
für Luft- und Raumfahrt

Institut für
Verbrennungstechnik

Pfaffenwaldring 38-40
70569 Stuttgart

Telefon
Telefax

(0 7 11) 68 62 - 3 08
(0 7 11) 68 62 - 5 78

D93, Stuttgart

Development of Numerical Methods for the Calculation of Thermo-Acoustic Interactions in Gas Turbine Combustion Chambers

A thesis accepted by the Faculty of Aerospace Engineering and Geodesy of the Universität Stuttgart in partial fulfillment of the requirements for the degree of Doctor of Engineering Sciences (Dr.-Ing.)

by

Dipl.-Ing. Gilles Reichling

born in Luxembourg

main referee:	Prof. Dr.-Ing. Manfred Aigner
co-referee:	Prof. Dr. rer. nat. Claus-Dieter Munz
Date of defence	October 31, 2014

Institute of Combustion Technology for Aerospace Engineering
University of Stuttgart

2015

To my parents & Franziska

Foreword

The present work was conducted during my employment as a research assistant at the Institute of Combustion Technology of the German Center (DLR) in Stuttgart, Germany.

First of all, I would like to thank my head of institute and my main referee Prof. Dr.-Ing. Manfred Aigner for giving me the trust and possibility to perform this work. I would also like to thank Prof. Dr. rer. nat. Claus-Dieter Munz for his interest in this work and his takeover as co-referee.

A very special and heartfelt thanks goes to the head of Computer Simulation department and my mentor Dr.-Ing. habil. Berthold Noll. His technical and morale support, his guidance, the numerous constructive discussions and the academic freedom granted by him have significantly contributed to the success of this work. I would also like to thank Dr.-Ing. Massimiliano Di Domenico for providing technical support during my first year at DLR. His commitment went far beyond what is expected.

I thank my colleagues at the institute for the very good atmosphere. In particular, I would like to thank the THETA group and Microturbines department for the excellent collaboration.

A very warm thanks goes to my two sisters Conny and Kristin and to my brother Yves. They have always supported and encouraged me to achieve my personal goals. My parents Raymonde and Nicolas are entitled to a special thanks. You have enabled me the education without which the beginning of this work would not have occurred. The most special and heartfelt thanks goes to my wife Franziska. You stood by my side at all times, believed in me and gave me the indispensable courage, support and love to accomplish this work.

Steinfort, November 2014 Gilles Reichling

Contents

List of Figures

List of Tables

Nomenclature

Latin Symbols

A	cross section area
A, B	coefficients
C	constant, [−]
C_s	Smagorinsky constant, [−]
C_w	constant coefficient, [−]
CD	cross-diffusion term
E	Hilbert space
E_a	activation energy, [J / (kg)]
F	blending function
G	Gibbs free energy, [J]
H	enthalpy, [J]
H^1	Sobolev space
K	relaxation coefficient, [1/s]
K_c	equilibrium constant, [−]
L	integral length scale
L_{mix}	mixing limit of the EDM model
L^2	Inner product space
M	molar mass, [kg/mol]
P	generic pressure variable [Pa]
$P_k, \tilde{P}_k$	limited production of the turbulent kinetic energy in the k-ω-SST turbulence model
$P_k, \tilde{P}_k$	limited production of the turbulent kinetic energy in the k-ω-SST turbulence model
R	specific gas constant, [J / (kg · K)]
R	reflection coefficient, [−]

RES	residual
S	entropy, [J/K]
$S_{\text{m\&c}}$	mixing and combustion source term, [kg / (m · s^3)]
T	temperature, [K]
V	volume, [m^3]
Y	mass fraction, [−]
a, d	coefficients
a_1	constant, [−]
b, b^*	right hand side term of the Poisson and Helmholtz equations
c	speed of sound, [m/s]
c_p	specific heat at constant pressure, [J / (kg · K)]
c_v	specific heat at constant volume, [J / (kg · K)]
d	degree of the polynomial ϕ_{ls}
d, d^*	left hand side term of the Helmholtz equation
e	error variable
f	frequency, [Hz]
h	specific enthalpy, [J/kg]
h_f^0	standard enthalpy of formation, [J/kg]
h_t	total specific enthalpy, [J/kg]
i,j,m,n	index variables
k	turbulent kinetic energy, [m^2/s^2]
k	angular wavenumber, [1/m]
k_b, k_f	Arrhenius reaction velocity of the backward and forward reaction
l	length scale, [m]
p	static pressure, [Pa]
$\overline{p}$	mean static pressure, [Pa]
r_k	ratio of the resolved to the overall turbulent kinetic energy, [−]
r_ν	ratio of the turbulent to the laminar viscosity, [−]
rr	reaction rate, [1/s]
s	specific entropy, [J / (kg · K)]
t	time, [s]

u	convective velocity, [m/s]
x	cartesian coordinate, [m]
y	wall distance, [m]
y^+	dimensionless wall distance, [−]
y^{+^*}	modified dimensionless wall distance, [−]

Greek Symbols

Γ	piecewise smooth boundary surface of Ω
Δ	consistency term
Λ	wavelength, $[m]$
Ω	three-dimensional computational domain
Θ	term
α, β	arguments, [−]
$\alpha, \alpha_1, \alpha_2$	model constants, [−]
α_{lim}	limitation factor, [−]
α_{pr}	projection weighting factor, [−]
α_{sd}	degree of stabilization, [−]
β	coefficient, [−]
$\beta_1, \beta_2, \beta^*$	model constants, [−]
$\beta_k, \beta_{\omega 2}$	model constants, [−]
γ	ratio of specific heats, [−]
γ_2	model constant, [−]
ε	dissipation rate of the turbulent kinetic energy, $[\text{m}^2/\text{s}^3]$
ϵ	truncation error, threshold value
ϕ	arbitrary scalar function
ϕ', ϕ''	quantity ϕ of educt $'$, respective product $''$
η	Kolmogorov length scale, [m]
κ	thermal conductivity, $[\text{W} \,/\, (\text{m} \cdot \text{K})]$
$\tilde{\kappa}$	von Kármán constant, [−]
λ	eigenvalue
μ	dynamic viscosity, $[\text{kg} \,/\, (\text{m} \cdot \text{s})]$

ν	kinematic viscosity, [m^2/s]
ν', ν''	stoichiometric coefficients, [$-$]
ω	turbulent dissipation frequency, [1/s]
ψ	turbulence variable, [m^2/s]
ρ	density, [kg/m^3]
$\sigma_{k_1}, \sigma_{\omega_1}$	model constants, [$-$]
$\sigma_{k_2}, \sigma_{\omega_2}$	model constants, [$-$]
σ_ψ	model constant, [$-$]
τ	time scale, [s]
χ	penalty factor, [$-$]
ξ	coefficient
ζ_2	constant, [$-$]

Special Symbols

$\mathcal{A}$	characteristic wave amplitude
$\mathcal{D}$	diffusion coefficient, [m^2/s]
$\mathcal{L}$	characteristic wave amplitude variation
$\mathcal{R}$	gas constant, [$J\,/\,(mol \cdot K)$]
$\mathcal{S}$	invariant measure equal to $\sqrt{2}$ times the Frobenius norm of the strain rate tensor $\underline{\underline{S}}$, [1/s]
$\mathcal{U}$	magnitude of the velocity Laplacian $\Delta_L \underline{u}$, [1/s]
$[j]$	concentration of species j, [g/mol]
$\dot{m}$	mass flux, [kg/s]
$\dot{V}$	volume flux, [m^3/s]
dp	total derivative of the pressure, [Pa]
δp	pressure difference, [Pa]
ρc	acoustic impedance, [$kg\,/\,(m^2 \cdot s)$]
$\tilde{f}, \tilde{g}$	solutions of the one-dimensional wave equation
$\tilde{u}, \tilde{p}$	solutions of the Stokes problem
δt	time recording window, [s]
Δt	time step size, [s]

$f(\Delta t)$	function of the time step size Δt, [s]

Vectors

$\underline{I}$	identity vector
$\underline{P}$	vector between two grid points
$\underline{S}_Y$	species mass source term, $[\mathrm{kg} / (\mathrm{m}^3 \cdot \mathrm{s})]$
$\underline{Y}$	species mass fraction vector, $[-]$
$\underline{b}$	basis vector
$\underline{b}$	right hand side term
$\underline{f}$	specific body force, $[\mathrm{m/s}^2]$
$\underline{n}$	outwards-pointing vector of Γ
$\underline{q}$	heat flux vector, $[\mathrm{W/m}^3]$
$\underline{\mathrm{res}}$	residual vector
$\underline{t}$	span vector of Γ
$\underline{u}$	velocity vector, [m/s]
$\underline{v}, \underline{w}$	vectors containing different variables
$\underline{Y}$	species mass fraction vector, $[-]$
$\underline{\Phi}, \underline{\Psi}$	arbitrary vector fields
$\underline{\phi}$	vector composed of the elements of ϕ at the respective grid nodes
$\underline{\omega}$	vorticity, [1/s]

Tensors

$\underline{\underline{A}}, \underline{\underline{B}}$	coefficient matrices
$\underline{\underline{D}}$	diffusion tensor, $[\mathrm{kg} / (\mathrm{m} \cdot \mathrm{s})]$
$\underline{\underline{I}}$	identity matrix
$\underline{\underline{S}}$	strain rate tensor, [1/s]
$\underline{\underline{j}}$	diffusion flux tensor, $[\mathrm{kg} / (\mathrm{m}^2 \cdot \mathrm{s})]$
$\underline{\underline{\tau}}$	stress tensor, $[\mathrm{kg} / (\mathrm{m} \cdot \mathrm{s}^2)]$

Non-Dimensional Numbers

CFL	Courant-Friedrich-Lewy number
PPW	points per wavelength
Kn	Knudsen number
Le	Lewis number
Ma	Mach number
Pr	Prandtl number
Re	Reynolds number
Sc	Schmidt number

Mathematical Operators and Symbols

$\cdot$	scalar product
$\times$	vector product
$\otimes$	dyadic product
:	Frobenius inner product
$\|\cdot\|_2$	Euclidean norm
$\|\cdot\|_F$	Frobenius norm
$\|\cdot\|_p$	L^p-norm
ℓ^p	p-norm of a sequence of functions
δ	correction (difference)
Δ	difference
Δ_L	Laplacian
$\frac{\partial}{\partial x}$	partial spatial derivative
$\frac{\partial}{\partial t}$	partial temporal derivative
$\frac{D}{Dt}$	material derivative
∇	gradient
$\nabla\cdot$	divergence
$\nabla\times$	rotation
diag	diagonal matrix
i	imaginary unit
tr	trace

$\mathcal{O}$	Landau symbol
$\mathbb{R}$	set of all real numbers
$\mathbb{R}_+$	set of all positive real numbers including zero

Subscripts

$\parallel$	parallel
0	standard
N	number
T	temperature
ac	acoustic
an	analytical
c	chemical
char	characteristic
dc	divergence constraint
disp	dispersion
diss	dissipation
f	faces
fp	first point
frefl	fully reflective boundary condition
ii	inner iteration
in	inlet
ir	irrotational
l	laminar
log	logarithmic
ls	least square
max	maximum
mod	modeled
n	normal
num	numerical
p	points
pnrefl	partially non-reflective boundary condition

r	reaction
ref	reference
sol	solenoidal (divergence free)
s	species
t	turbulent
ts	time steps
vis	viscous
vK	von Kármán

Superscripts

$'$	fluctuating quantity
0	initial
T	transpose
a	arbitrary positive exponent
avg	time-averaged
b	boundary
cor	corrected
i	inner
n	old time step
$n+1$	new time step
rms	root-mean-squared
$*$	interim time step

Abbreviations

General Notations

AIAA	American Institute of Aeronautics and Astronautics
ASCII	American Standard Code for Information Interchange
CAA	Computational Aero Acoustics
CFD	Computational Fluid Dynamics
IRZ	Inner Recirculation Zone
NASA	National Aeronautics and Space Administration
NetCDF	Network Common Data Form
ORZ	Outer Recirculation Zone
PPW	Points Per Wavelength
PVC	Precessing Vortex Core
THETA	Turbulent Heat Release Extension of the TAU code

Numerical Methods

DES	Detached Eddy Simulation
DNS	Direct Numerical Simulation
LES	Large Eddy Simulation
LODI	Local One-Dimensional Inviscid
NSCBC	Navier-Stokes Characteristic Boundary Conditions
SAS	Scale Adaptive Simulation
SST	Shear Stress Transport
(U)RANS	(Unsteady) Reynolds Averaged Navier-Stokes Equations

Iterative Methods for the Numerical Solution of Linear Equations

GMRES	Generalized Minimal Residual
PBCGS	Preconditioned Bi-Conjugate Gradient Stabilized

Strategies for the Solution of the Navier-Stokes Equations

CPM	Compressible Projection Method
EIF	Expansion about Incompressible Flow
ICE	Implicit Continuous-Fluid Eulerian
IPM	Incompressible Projection Method
MAC	Marker And Cell
MPV	Multiple Pressure Variables
PISO	Pressure Implicit with Split Operator
SIMPLE	Semi-Implicit Method for Pressure Linked Equations
SIMPLEC	SIMPLE Consistent
SIMPLER	SIMPLE Revised

Combustion Models

EDM	Eddy Dissipation Model
FRC	Finite Rate Chemistry

Discretization Schemes

CDS	Central Discretization Scheme
LUDS	Linear Upwind Discretization Scheme
QUDS	Quadratic Upwind Discretization Scheme
TVD	Total Variation Diminishing
UDS	Upwind Discretization Scheme
WENO	Weighted Essentially Non-Oscillatory
CN	Crank Nicolson
EUE	Euler Explicit
EUI	Euler Implicit
TPB	Three Points Backward

Measurement Techniques

CARS	Coherent Anti-Stokes Raman Spectroscopy
PIV	Particle Image Velocimetry

Abstract

This work aims to enable the calculation of thermo-acoustic interactions in gas turbine combustor systems through the development of a numerical scheme capable of computing time-dependent compressible reactive flows up to the subsonic limit $\mathrm{Ma} \rightarrow 1$. Aside from this, the Mach number may become very small in regions with high temperatures and low velocities. Besides the occurrence of high Mach numbers within the flow field, the created numerical scheme thus also needs to cope with flows in the incompressible limit. The application of the developed numerical method onto gas turbine combustors creates the possibility of capturing thermo-acoustic interaction mechanisms in application-related combustor systems. This aspect fulfills the need to gather more information on thermo-acoustic interaction phenomena and the detailed physical mechanisms that influence their rise towards thermo-acoustic instabilities.

For this purpose, a novel projection-based numerical method able to compute compressible reactive flows referred to as the CPM (Compressible Projection Method) method has been developed within this work. It is based on a generic form of the Helmholtz decomposition derived within the frame of this work, leading to a fractional step scheme which solves a predictor and a corrector step. The Poisson equation solved for the pressure within the IPM (Incompressible Projection Method) solution strategy is extended to a Helmholtz equation for the computation of compressible flows. Thus, the CPM method can be seen as an extension of the IPM method towards the regime of compressible flows. Applying the predictor and corrector steps to the conservation equations of the enthalpy and species including Dalton's law, mixing and combustion phenomena can be included into the computation process, thus enabling the calculation of reactive flows. Since no iterations of the solution process need to be performed, the CPM method describes a highly efficient numerical scheme for the numerical computation of compressible reactive flows.

The accurate prediction of compressible unsteady flows using computational methods requires an appropriate modeling of the processes at the domain boundaries. In order to satisfy this need, accurate boundary conditions have been adopted based on a characteristic analysis of the governing flow equations. The characteristic boundary condictions have been implemented and verified by means of an analytical approach providing the response of generated

acoustic waves at the in- and outflow boundaries of a one-dimensional rectangular duct.

The ability of the created numerical scheme to compute flows in the incompressible limit has been demonstrated by means of an analytical analysis and a numerical test case. The CPM algorithm has successfully been verified and validated against a one-dimensional acoustic test case. In conjunction with an acoustic CFL number of unity, a spatial resolution of 60 points per wavelength decreases the amount of numerical dissipation and dispersion to an acceptable value of 1 %.

The computation of the homentropic flow in a two-dimensional convergent nozzle has been addressed to. Numerical calculations increasing the highest occurring Mach number up to 0.92 have been conducted and validated by means of analytically derived data and numerical results issued from previous works. The successful validation by means of this test case demonstates the ability of the CPM method of accurately computing flows with a maximum occurring Mach number of 0.92. Together with the results obtained from the analysis in the incompressible limit, the CPM scheme hence shows the ability to compute flows close to the zero Mach number limit $\mathrm{Ma} \rightarrow 0$, as well as flows with a Mach number reaching the subsonic limit $\mathrm{Ma} \rightarrow 1$.

As an application-related and validation test case, the three-dimensional turbulent transient flow in a double-swirled gas turbine combustor has been calculated by means of URANS and SAS methods. Contrary to the SAS computations, the URANS calculations are not able to resolve the unsteadiness of the combustor flow. As a result of this, the high spatial resolution achieved though the LES mode of the SAS computations is of essential importance for the resolution of the unsteady phenomena of the flow field. Regarding the numerical results of the three-dimensional flow, the SAS-based compressible computations reveal a good agreement to the experimental data. The CPM method additionally provides the possibility to resolve acoustic phenomena, which can be detected in contour plots of the solution or in a spectral analysis of the pressure time signal. The computation of this test case demonstrates the ability of the CPM approach of calculating the highly unsteady and turbulent flow field in a double-swirled gas turbine combustor where Mach numbers approaching the incompressible limit $\mathrm{Ma} \rightarrow 0$, as well as Mach numbers of the order of 0.25 occur. Moreover, it could be shown for this test case that the CPM solution strategy is roughly 50 times faster than a comparable unsteady SIMPLE based solution scheme. This demonstrates the computational efficiency of the CPM method.

Kurzfassung

Das Auftreten von thermo-akustischer Instabilitäten in Gasturbinen-Brennkammern kann zu mechanischen Schäden der Brennkammer und im schlimmsten Fall zu einer Zerstörung des Brennersystems führen [22, 99, 120, 195]. Ziel dieser Arbeit ist die Ermöglichung der rechnerischen Erfassung thermo-akustischer Interaktionen in Gasturbinen-Brennkammern durch die Entwicklung eines kompressiblen Lösungsverfahrens. Neben Strömungsgebieten nahe der Schallgrenze $\mathrm{Ma} \rightarrow 1$ können innerhalb der Brennkammer Regionen sehr kleiner Machzahlen $\mathrm{Ma} \ll 1$ auftreten. Das zu entwickelnde numerische Verfahren muss daher in der Lage sein, den Machzahlbereich $0 < \mathrm{Ma} < 1$ abzudecken. Die Anwendung des entwickelten numerischen Verfahrens auf Gasturbinen-Brennkammern schafft zudem die Möglichkeit, thermo-akustische Interaktionsmechanismen in anwendungsbezogenen Brennkammersystemen zu erfassen. Dieser Aspekt führt zum Ziel, einen genaueren Überblick über die Entstehung thermo-akustischer Wechselwirkungen und deren konstruktiven Interferenz bis hin zur Ausbildung thermo-akustischer Instabilitäten zu erlangen.

Für diesen Zweck wurde im Rahmen dieser Arbeit eine kompressible projektionsbasierte Methode - die sogenannte CPM (Compressible Projection Method) Methode - entwickelt. Das CPM Verfahren basiert auf einer in dieser Arbeit entwickelten allgemeinen Formulierung der Helmholtz Aufspaltung, mit welcher sich ein Lösungsverfahren in einen Prädiktor und einen Korrektor Schritt aufgespalten lässt. Die bei Vorliegen einer inkompressiblen Strömung zu lösende Poisson Gleichung erweitert sich für eine kompressible Strömung zur Helmholtz Gleichung. Aus diesem Grund kann die CPM Methode auch als Erweiterung der inkompressiblen Projektionsmethode angesehen werden. Der Anschluss des Prädiktor und der Korrektor Schritte an die Erhaltungsgleichungen für Enthalpie und Speziesmassenbrüche einschließlich des Dalton'schen Gesetzes ermöglicht die Berechnung von Mischungs- und Verbrennungsprozessen. Da keine Iterationen der Lösungsschritte durchgeführt werden müssen, beschreibt die CPM Verfahren ein hoch effizientes numerisches Verfahren zur Berechnung kompressibler Strömungen.

Die genaue Vorhersage von thermo-fluiddynamischen und akustischen Vorgängen anhand numerischer Methoden erfordert eine geeignete Modellierung der Prozesse an den Rändern des Strömungsfeldes. Um dieser Anforderung gerecht zu werden, wurden akkurate Randbedin-

gungen anhand einer charakteristischen Analyse der innerhalb der CPM Methode zu lösenden Gleichungen herangezogen. Die charakteristischen Gleichungen wurden in den Strömungs- und Verbrennungslöser THETA implementiert und durch eine analytische Analyse des reflektierenden Verhaltens von akustischen Wellen an den Ein- und Auslassgrenzen eines eindimensionalen rechteckigen Kanals verifiziert.

Die Fähigkeit des entwickelten numerischen Lösungsverfahrens zur Berechnung von Strömungen an der inkompressiblen Grenze wurde mittels einer analytischen Analyse des inkompressiblen Grenzfalls und eines numerischen Testfalls nachgewiesen. Des Weiteren wurde die Genauigkeit des CPM Verfahrens hinsichtlich der Ausbreitung von Schallwellen anhand eines eindimensionalen Akustik Testfalls ermittelt. Bei einer räumlichen Auflösung von 60 Punkten pro Wellenlänge konnte in Verbindung mit einer akustischen CFL Zahl von Eins die numerischen Dissipation und Dispersion bis auf 1 % reduziert werden.

Im Anschluss daran wurde die homentrope Strömung in einer zweidimensionalen konvergenten Düse berechnet. Dabei wurde die höchste im Feld auftretende Machzahl bis auf einen Wert von 0.92 erhöht. Die Resultate der numerischen Berechnungen wurden dann anhand von analytisch hergeleiteten Daten und numerischen Ergebnissen aus früheren Arbeiten validiert. Beide Datensätze zeigen eine sehr gute Übereinstimmung. Durch die erfolgreiche Durchführung dieses Testfalls wurde die Fähigkeit der CPM Methode zur Berechnung von Strömungsgebieten nahe der subsonischen Grenze nachgewiesen.

Als anwendungsbezogenen Testfall wurde die dreidimensionale instationäre turbulente Strömung in einer doppelt verdrallten Gasturbinen-Modellbrennkammer mittels URANS und SAS Methoden berechnet. Im Gegensatz zu den SAS-basieten Berechnungen sind die URANS Simulationen nicht in der Lage, die Instationarität der Strömung zu erfassen. Dies hat zur Folge, dass die durch den LES-Modus der SAS Rechnungen erreichte hohe räumliche Auflösung einen wesentlichen Beitrag zur Auflösung der turbulenten Skalen leistet. Die Ergebnisse der SAS-basierten kompressiblen Berechnungen zeigen eine gute Übereinstimmung mit den experimentellen Daten. Die CPM-Methode bietet zusätzlich die Möglichkeit, akustische Phänomene aufzulösen, die in Konturdarstellungen oder mit Hilfe einer Spektralanalyse des Druckzeitsignal detektiert werden können. Die Berechnung dieses angewandten Testfalls zeigt die Fähigkeit des CPM Ansatzes zur Berechnung des stark instationären und turbulenten Strömungsfeldes in einer verdrallten Gasturbinen-Modellbrennkammer, in welcher Machzahlen nahe des inkompressiblen Grenzwerts sowie Machzahlen in der Größenordnung von 0.25 auftreten. Darüber hinaus konnte für diesen Testfall gezeigt werden, dass das CPM Verfahren rund 50-mal schneller ist als ein vergleichbarer instationärer SIMPLE-basierter Lösungsalgorithmus.

1. Introduction

A lean-burning flame is characterized by an air-to-fuel ratio much greater than the air-to-fuel ratio obtained when mixing air and fuel together as a stoichiometric mixture. In combustion, the highest NO_x amount is produced when the flame temperature reaches its maximum [99, 251]. This happens when air is burned near stoichiometric conditions with an air-to-fuel ratio slightly greater than unity, i.e. under a small surplus of air [99]. Thus, an increase of the air-to-fuel ratio beyond stoichiometry leads to a reduction of the emitted amount of nitrogen oxide and dioxide. The transfer of the operating conditions in modern gas turbine combustor systems towards lean mixtures however leads to an increase of the sensitivity against thermo-acoustic[1] interactions [22, 23, 99, 79, 80, 120, 128, 129, 130, 131, 146, 179, 186, 195, 233, 234].

Processes within combustion dynamics are of high complexity. Aside from hydro- and thermodynamic phenomena, the acoustics of the flow field require a high degree of modeling. Local variations of the velocity and temperature may create perturbations within the flow field which then generate so-called vortex and entropy modes. These modes move with the convective velocity of the flow field. An acceleration or deceleration of these vortex and entropy modes introduces combustion noise into the operating system, which is referred to as *indirect combustion noise* [126, 143, 159]. In addition to the occurrence of indirect combustion noise, small fluctuations within the mixture composition or the heat release of the flame may excite the density field which then cause oscillations within the pressure and temperature. Through this mechanism, acoustic oscillations are introduced into the compressible flow field. These acoustic fluctuations propagate with the speed of sound and generate sonic noise, which is referred to as *direct combustion noise* [33, 38, 126].

An additional challenge lies within the ability of computational methods to predict the amplitude and frequency of hydrodynamic and thermo-acoustic phenomena occurring within technical combustors. As a matter of fact, the frequency of such phenomena in gas turbine combustors is well depicted by modern computational methods [131, 117, 118, 201, 243]. However, computational methods available up to now are only able to predict the pressure amplitudes of arising phenomena with an accuracy of several orders of magnitude

[1] The term *thermo-acoustics* describes the interaction mechanisms between fluid dynamic and acoustic phenomena.

[131, 117, 118, 201, 243]. If occurring acoustic oscillations are fed back onto the hydro- and thermodynamics of the flow field, acoustic and fluid dynamic[2] phenomena may interact with each other such that thermo-acoustic instabilities arise. In case of constructive interference, these instabilities can accumulate and eventually lead to structural damages of the combustion chamber walls and thus of the overall combustor system. Consequently, attention has to be paid to the occurrence and rise of such operating instabilities. Research efforts in the field of thermo-acoustic interactions have significantly been improved within the last decade in order to achieve a deeper understanding of the arising phenomena [79, 91, 130, 135, 136, 202]. However, there are still various unanswered questions concerning the detailed physical mechanisms that influence the occurrence of thermo-acoustic instabilities. Thus, research on thermo-acoustic interaction phenomena needs to be further strengthened.

1.1. Aims of this Work

This work aims to enable the calculation of thermo-acoustic interactions in gas turbine combustor systems through the development of a numerical scheme capable of computing time-dependent compressible reactive flows without breaking down in the incompressible limit. Within gas turbine combustion systems, the Mach number may become small in regions with high temperatures and small velocities. Moreover, regions with increasing flow speed, e.g. due to a reduction of the cross section, may lead to an augmentation of the Mach number up to unity. The Mach number may hence increase up to the point where compressible effects can no longer be neglected. As a result of this, a solution algorithm needs to be developed which is capable of calculating regions with $\mathrm{Ma} \ll 1$, as well as domains with $\mathrm{Ma} \rightarrow 1$.

In addition to this, acoustic phenomena are meant to be accounted for and visualized by the developed compressible solver. The numerical solution algorithm being developed requires adequate acoustic boundary conditions in order to enable the setup of partially non-reflective in- and outlet boundary conditions in addition to the prescription of fully reflective boundary constraints. For this purpose, partially non-reflective boundary conditions are adopted to work in conjunction with the created compressible scheme. Following this, the compressible method along with the partially non-reflective boundary conditions are incorporated into the framework of the DLR in-house combustion CFD Code THETA [36, 37] (Turbulent Heat Release Extension of the TAU code). In a last step, the developed compressible solver is verified and validated by means of analytical as well as numerical test cases. The verification and validation process of the created numerical methods is conducted by means of defined academic as well as application-related test cases. In doing so, well-defined one- and two-dimensional

[2] Besides the incompressible flow field, the term *fluid dynamics* includes the variation of the temperature field and mixture composition. This field of interest is sometimes referred to as *thermo-fluid dynamics*.

test cases are addressed to. The application-related validation of the compressible solution strategy is conducted using a computational model of a three dimensional model combustor. The implemented partially non-reflective boundary conditions are verified with the aid of a one-dimensional acoustic and validated by means of a two-dimensional test case.

In addition to the ability of calculating flows with very small Mach numbers, the present work creates the fundamental frame which enables the numerical computation of compressible flows up to the subsonic limit $\mathrm{Ma} \rightarrow 1$. Aside from this, the application of the developed numerical methods to gas turbine combustors creates the possibility of capturing thermo-acoustic interaction mechanisms in application-related combustor systems. This aspect fulfills the need to gather more information on thermo-acoustic interaction phenomena and the detailed physical mechanisms that influence the rise of thermo-acoustic instabilities.

1.2. Literature Study

The numerical solution of compressible flows enables the prediction of acoustic phenomena. For this purpose, different strategies can be adopted. They can be categorized into direct and hybrid methods [30, 162, 207], see figure 1.2.1.

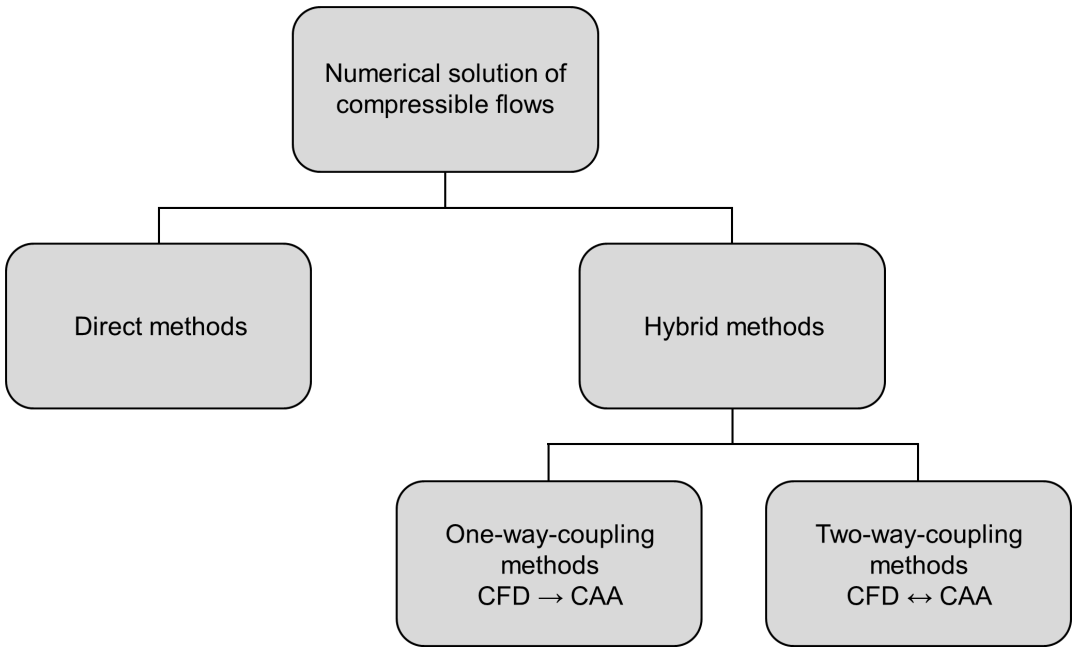

Figure 1.2.1.: Possible strategies for the numerical solution of compressible flows

By means of direct methods, the compressible Navier-Stokes equations are solved with the aid of LES (Large Eddy Simulations) or DNS (Direct Numerical Simulation) computations without any assumptions or additional modeling regarding the acoustics. Over the last years, several authors published applications of direct methods to the numerical computation of

acoustic phenomena [9, 29, 61, 62, 138, 139, 142, 157, 196, 211]. Direct methods generally adopt a *density-based* scheme to solve the governing equations, meaning that the set of equations is solved fully coupled using an iterative solution method. The density is chosen as leading variable and is determined by the continuity equation. The pressure is then evaluated from the density, generally by means of an equation of state as dependent variable. Direct methods possess the inconvenience of being time consuming and have not yet been verified by means of application-related test cases [30]. The second approach to predict sound waves is the hybrid method, which incorporates one-way-coupling (CFD $\rightarrow$ CAA) as well as two-way-coupling (CFD $\leftrightarrow$ CAA) techniques, see figure 1.2.1 and reference [162].

One-way-coupling methods perform a separation of the incompressible flow field from the computation of the acoustics, i.e. a separation of the hydrodynamic and acoustic scales. The one-way-coupling between fluid dynamic and acoustic phenomena can be performed via CFD source terms, which are added to the right hand side of the acoustic system of equations. An example herefore is the coupling of an incompressible Navier-Stokes solver with a relation derived from an acoustic analogy, which has originally been derived by Lighthill [132, 133]. Based on Lighthill's acoustic analogy, Ffowcs Williams and Hawkings [55] developed a more generic direct method for noise predictions. In addition to using acoustic analogies, a one-way CFD-CAA coupling can be conducted in conjunction with the linearized Euler equations - as performed by Bogey et al. [16] and Ewert et al. [51] - or with an acoustic wave equation, as applied by Flemming et al. [57]. In 1992, Hardin and Pope [84, 85] developed the EIF (Expansion about Incompressible Flow) method, which constitutes a one-way CFD-CAA coupling technique for the numerical analysis and prediction of non-linear aerodynamic noise generation. Under the assumption of a low Mach number flow, they perform a splitting of the unsteady compressible Navier-Stokes equations wherein the unsteady incompressible and viscous flow field is computed in a first step before calculating the transient inviscid acoustic field in a second step. The incompressible solution hence does not contain any acoustics. Within the decomposition process, the acoustic field is assumed to be homentropic. According to Batchelor [10] and Rienstra et al. [204], effects due to dissipative forces and heat conduction are generally slow on acoustic phenomena so that only little generality is lost by assuming the sonic flow to be homentropic. Defining ϕ as an arbitrary scalar field, the full non-linear inviscid and adiabatic acoustic field is obtained by first introducing the decomposition $\phi = \phi_0 + \phi'$ for the pressure and velocity components, respective $\phi = \phi_0 + \phi_1 + \phi'$ for the density field and subsequently subtracting the incompressible set of equations from the compressible one [84, 85]. The subscripts 0 and 1 denote the incompressible state and hydrodynamic fluctuation of the variable ϕ, whereas the superscript $'$ characterizes the acoustic part of ϕ. This splitting approach is based on the

hypothesis that for sufficiently small Mach numbers, a homentropic acoustic field acts as a first order correction to the incompressible set of equations, as postulated by Klainerman and Majda [112] in 1981.

The key idea of two-way fluid dynamic acoustic coupling methods is the application of a decomposition technique to the governing equations of a compressible flow. This can be done by splitting the compressible Navier-Stokes equations by means of operator decomposition techniques [93, 94, 108, 161] or vector field splitting methods [6, 52, 63, 64, 170, 185, 265, 266]. Aside from these two approaches, pressure decomposition methods [28, 35, 59, 79, 112, 164, 166, 167, 177, 184, 200, 206, 207, 208, 209] have become very popular in order to design a two-way CFD-CAA coupling method. Pressure decomposition methods are generally constructed around a *pressure-based* solver. A pressure-based solver chooses the pressure over the density as leading variable. The pressure is gained from the so-called *pressure correction equation*, which is derived from the momentum equations including either the mass or energy conservation equation. The density is obtained from the pressure field through the use of an equation of state. Pressure-based methods are generally semi-implicit schemes, applying matrix-free linear solvers for the solution of the set of equations. Matrix-free linear solvers do not invert the coefficient matrix of the set of equations, but determine a residuum for each equation which is then iteratively reduced to a certain threshold, see references [147, 216] for details. Pressure decomposition methods generally perform a splitting of the pressure P into N parts $p^{(i)}$, $i = \{0, 1, \ldots, N-1\}$, each of which is multiplied with a coefficient a_i: $P = \sum_{i=0}^{N-1} a_i \, p^{(i)}$.

Hydrodynamic phenomena, such as vortical structures, carry a lot of energy within a small space. Opposed to this, acoustic wave generally move over great distances with small energy portions. As a result of this, the length scale of acoustic processes is usually far greater than the one of hydrodynamic structures. Moreover, acoustic time scales are generally orders of magnitude smaller than hydrodynamic times scales [59, 130, 208]. Cases may however occur where thermal energy is converted into acoustic energy and vice versa, such as within the exhibit of thermo-acoustic instabilities in gas turbine combustion chambers. For these type of cases, the acoustic and hydrodynamic time and length scales reach the same order of magnitude [130]. One-way CFD-CAA coupling techniques assume a non-interaction of the hydrodynamic and acoustic time and length scales. Moreover, they do not feed acoustic effects back into the fluid dynamics of the flow field. The impact of the sonic terms on the flow field is thus not taken into account so that this kind of methods is not of interest to the solution strategies developed within the present work. Direct methods do not include any additional modeling concerning the interactions between fluid dynamic and acoustic phenomena so that they enable the numerical calculation of thermo-acoustic interactions. Aside

from direct methods, two-way CFD-CAA coupling methods also enable the study of the thermo-acoustic interaction mechanisms, since they include the modeling of both fluid dynamic and acoustic mechanisms. Direct methods solve the full set of compressible equations implicitly using density-based solvers, whereas two-way CFD-CAA coupling techniques take advantage over the decomposition methods applied, so that they are in general computationally more efficient than direct methods. Moreover, direct methods have not yet been applied to complex geometries. In addition to this, the application of direct methods to low Mach number flows still remains challenging [30, 79, 100]. These are key issues, since besides the extension of the computational solver towards the compressible regime, the enabling of the numerical simulation of thermo-acoustic phenomena in gas turbine combustion chambers is one major aim of the present work. Hence, the development of a hybrid two-way CFD-CAA coupling method in order to enable the calculation of compressible reactive flows is the more favorable alternative. This implies an extension of an incompressible pressure-based solver to the compressible flow regime.

An additional issue, being covering the entire compressible subsonic flow regime ($\mathrm{Ma} \in \,]\,0;1\,[\,$), needs to be addressed to. Herefore, two main approaches can be chosen [54, 66, 206]: The first approach consists of extending a compressible (density-based) algorithm towards the incompressible limit. Direct methods are usually derived based on density-based solution strategies. The governing equations are coupled fully implicitly and solved using an iterative solution method, such as splitting methods [147]. Density-based solvers however become computationally inefficient as the Mach number approaches the incompressible limit. This is based on the fact that, as the Mach number reaches the zero-limit, the speed of sound diverges to infinity. If for instance, pressure fluctuations of compressible or thermodynamic nature arise at small but non-zero Mach numbers, they instantaneously vanish since the propagation speed of pressure variations equals the speed of sound. This can also be demonstrated by means of the momentum equations: Transforming the momentum equations into a dimensionless form, it can be shown that the pressure gradient term ∇p scales with the coefficient $1/\mathrm{Ma}^2$ [13, 59, 65, 114, 163, 164, 177, 208, 244]. Based on an asymptotic analysis of the compressible Euler equations in the incompressible limit conducted by Ebin [43, 44], Klainerman and Majda [112, 113] and Schochet [226], Klein and Munz [114, 115, 116, 163] applied an asymptotic expansion to the dimensionless pressure, by which the pressure field is separated into a thermodynamic $p^{(0)}$, an acoustic $p^{(1)}$ and a hydrodynamic $p^{(2)}$ part: $P = \sum_{i=0}^{2} \mathrm{Ma}^i\, p^{(i)} = p^{(0)} + \mathrm{Ma}\, p^{(1)} + \mathrm{Ma}^2 p^{(2)}$. According to this definition, the thermodynamic, acoustic and hydrodynamic pressure parts scale with Ma^0, Ma^1 and Ma^2, respectively. Introducing the pressure decomposition into the pressure gradient term of the momentum equations, one easily sees that the thermodynamic and acoustic pressure pertur-

bations evanesce as the zero Mach number limit is approached. Arising thermodynamic and acoustic pressure variations are thus instantaneously wiped out. As a result of this, only occurring hydrodynamic pressure perturbations have an impact on the velocity and thus the flow field at small Mach numbers. As the Mach number reaches the zero-limit, the speed of sound grows to infinity relative to a finite convective velocity. Considering furthermore an inviscid flow, two eigenvalues of the governing flow equations diverge from one another to $-\infty$ and $+\infty$, respectively [83, 90, 164, 205, 268]. This causes the system of equations to become very stiff. As a consequence of this and the application of a fully implicit coupling of the governing equations, density-based solvers suffer from noticeable deficiencies in computational efficiency and accuracy as the Mach number approaches the zero limit. With so-called All-Mach-Number-Preconditioning techniques [66], this disadvantage can be partially overcome [66], but not fully cured [30, 79, 244]. As an alternative to extending density-based methods towards the zero Mach number limit, incompressible (pressure-based) solvers can be extended to the compressible regime. Calculating low Mach number flows, pressure-based solution strategies are in general semi-implicit schemes and computationally more efficient than density-based algorithms [79, 244]. With the aim to compute weakly compressible flows, Harlow and Amsden [87] introduced the concept of extending a pressure-based numerical scheme to the compressible regime in 1968. The application cases of this work are related to the numerical calculation of the flow in combustor systems, where regions with small to moderate Mach numbers occur. A compressible extension of an incompressible pressure-based scheme hence seems more favorable to develop when dealing with such kind of flows.

Within the literature, several solution schemes belonging to the class of two-way CFD-CAA coupling techniques can be found by which the calculation of compressible flows is enabled. In 1965, Harlow and Welch proposed the MAC (Marker And Cell) [86, 254] algorithm to solve time-dependent viscous incompressible flows. In 1968, Harlow and Amsden [87] developed the so-called ICE (Implicit Continuous-Fluid Eulerian) solution method as a compressible extension of the MAC solution scheme. Issa [93, 94] proposed the so-called PISO (Pressure Implicit with Split Operator) algorithm in 1985 to solve the time-dependent Navier-Stokes equations. The PISO approach belongs to the family of fractional steps methods. It is of non-iterative nature and extends the concept of factorization to the coupling between the pressure and velocity fields. Besides providing a numerical scheme for the solution of the incompressible Navier-Stokes equations, Issa gave a solution approach for the calculation of compressible flows. In the following, the two-staged compressible scheme is briefly described. This formulation of the PISO algorithm is formally of second order accuracy in time. The two-staged formulation of the PISO algorithm first solves the discretized momentum equations in order to obtain an intermediate velocity field. This constitutes the predictor step

of the PISO scheme. A first correction step is then carried out, wherein the intermediate solution of the velocity field is used in order to calculate the pressure field from the pressure correction equation. The pressure correction equation is obtained by introducing the continuity equation into the momentum equations. By formulating the pressure correction equation for the velocity field and inserting the newly obtained pressure field, a first correction of the velocity is performed. After this, the energy equation is solved implicitly in order to determine the state of energy. The pressure correction equation is solved for the second time using the previously determined corrected velocity field. By inserting the corrected pressure values into the momentum equations, the velocity field is corrected for the second time. The density is eventually obtained through the introduction of a thermodynamic equation of state.

Apart from suggesting a coupled pressure temperature correction scheme [166], Nerinckx et al. formulated a fully segregated pressure correction method [167] as well as a fully coupled algorithm [167] in order to solve the unsteady compressible Navier-Stokes equations. On the one hand, the fully coupled approach takes advantage over the fact that no stringent CFL limitation is prescribed. On the other hand, the computational efficiency of one time step is worsened due to the full coupling of the discretized equations. Considering incompressible flows, Kim and Moin [108] give the following reflection: the role of the pressure within the momentum equations can be interpreted as a projection operator, which projects an arbitrary vector field onto a divergence-free vector field. Based on this key thought, Kim and Moin developed a fractional step method in order to solve the unsteady incompressible Navier-Stokes equations with the additional constraint of considering constant density flows. Pierce [187] extended Kim and Moin's approach enabling the numerical solution of time-dependent variable density flows. Moureau, Bérat and Pitsch [161] extended the thoughts of Kim and Moin [108] and Pierce [187] to the application of compressible non-reactive flows and created a segregated semi-implicit approach. Following a characteristic splitting of the compressible viscous Navier-Stokes equations, Moureau, Bérat and Pitsch decompose the governing flow equations into a convective and an acoustic set of equations. Lourier [135, 136] extended the numerical approach noted by Moureau et al. [161] onto the application of reactive flows.

Aside from the numerical methods noted above, two approaches extending an incompressible solver to the compressible regime have become very popular during the last couple of decades: Those are on the one side SIMPLE-based and on the other side projection-based methods. The SIMPLE (Semi-Implicit Method for Pressure Linked Equations) algorithm has originally been developed by Patankar [181, 182] for incompressible steady flows. The SIMPLE scheme is a segregated approach which first solves the momentum equations with known pressure values in a linearized form. The interim velocity field does not directly fulfill

continuity, thus leading to a remaining mass source. With the input of this mass source, a pressure correction equation is solved in a second step. The now corrected values do satisfy the continuity equation, but not the momentum balances. As a result of this, further iterations enclosing the first and second steps need to be performed in order to conserve the mass and momentum [172]. PATANKAR [183] enhanced the SIMPLE-based algorithm in a next step, calling it the SIMPLER (SIMPLE Revised) algorithm. Compared to the original SIMPLE approach, the SIMPLER solution strategy can reach convergence in fewer iteration steps and converges with higher certainty [183]. Over the years to follow, derivatives of the SIMPLE algorithm have been developed, including the SIMPLEST [229], SIMPLEC [246] and SIMPLEX [247] schemes. KARKI and PATANKAR [184] presented a calculation procedure for steady-state viscous flows at all Mach numbers based on the compressible form of the SIMPLER algorithm. DEMIRDŽIĆ, LILEK and PERIĆ [35] applied a pressure density linkage similar to the work of KARKI and PATANKAR [184] in order to compute steady-state compressible flows. Based on the SIMPLE solution method, MOUKALLED and DARWISH [160] used a normalized variable and space formulation methodology to bound the convective fluxes and a high-resolution scheme for calculating interface density values in order to enhance shock-capturing. MUNZ et al. [164, 178, 209] constructed a compressible solution strategy for the Navier-Stokes equations by inserting the MPV (Multiple Pressure Variables) approach proposed by KLEIN and MUNZ [65, 114, 115, 116, 163] into PATANKAR's [181, 182] SIMPLE algorithm. GUNASEKARAN [79] developed a pressure-based scheme for calculating unsteady compressible flows based on the steady-state compressible formulations of KARKI and PATANKAR [184] and DEMIRDŽIĆ, LILEK and PERIĆ [35].

Projection-based methods rely on the pioneering work of CHORIN [24, 25] and TEMAM [239], cf. section 3.1. Under the assumption of considering a constant density flow on a simply connected domain ($\rho = \text{const.}$), they derive a fractional-step scheme based on the Helmholtz decomposition $\underline{\Psi} \equiv \underline{\Psi}_{\text{sol}} + \underline{\Psi}_{\text{ir}}$ [78, 89], which is also known as the Helmholtz-Hodge decomposition. According to this split-up, an arbitrary vector field $\underline{\Psi}$ is decomposed into a solenoidal (divergence-free) $\underline{\Psi}_{\text{sol}}$ and an irrotational part $\underline{\Psi}_{\text{ir}}$. With $\underline{\Psi}_{\text{ir}}$ being an irrotational vector field on a simply connected domain, there is a scalar function $\phi = \phi(\underline{x}, t)$ such that $\underline{\Psi}_{\text{ir}} = \nabla\phi$ holds for any t [26, 110]. Furthermore, the rotation of $\underline{\Psi}_{\text{ir}}$ vanishes, i.e. the condition $\nabla \times \underline{\Psi}_{\text{ir}} = \nabla \times (\nabla\phi) = 0$ is satisfied at all times. A solenoidal vector field $\underline{\Psi}_{\text{sol}}$ is characterized by a zero value of its divergence: $\nabla \cdot \underline{\Psi}_{\text{sol}} = 0$ [26, 110]. Firstly, the linearized momentum equations are solved without the pressure gradient term - as in the original derivation of CHORIN and TEMAM - or - as later on proposed by GODA [68] - with the pressure gradient of the old time step. Thus, an interim velocity field is obtained. By means of the Helmholtz split-up, a pressure correction equation can be derived which projects the

interim velocity field onto the final solution of the velocity by taking into account a divergence constraint. The Helmholtz decomposition thus splits the solution algorithm into a predictor and a corrector step. After solving the corrector step, the mass and momentum equations are fulfilled which results in a non-iterative solution method. This leads to computationally very efficient algorithms for unsteady flows compared to other solution strategies which are of iterative nature, e.g. SIMPLE-based algorithms. The projection method has originally been designed as a solution strategy for the unsteady computation of incompressible constant density flows. Later on, several extensions of the incompressible projection method towards compressible flows have been achieved. Pember [185] enhanced the incompressible projection method to the low Mach number regime by applying a decomposition to the pressure field into a temporally and spatially constant part and a dynamic part, coupled with a constraint on the flow divergence. Based on the work of Klein and Munz [114, 115, 116, 163], Munz and Roller [206, 208] extended the projection method to the compressible regime by first performing a split-up of the Navier-Stokes equations into a convective-diffusive and a sonic system of equations which are then solved separately. In a second step, they applied the MPV (Multiple Pressure Variables) approach proposed by Klein and Munz [65, 114, 115, 116, 163] to the governing equations. The MPV method makes use of an asymptotic analysis originally introduced for one time and space scale by Ebin [43, 44], Klainerman and Majda [112, 113] and Schochet [226] and enhanced to single time and multiple space scales by Klein and Munz [114, 115, 116, 163]. Babik, Gallouët, Gastaldo, Herbin and Latché developed projection-based schemes for solving an unsteady compressible flow field under the assumption of an isentropic [52], a barotropic [63] and an isothermal case [64], as well as for computing generic unsteady reactive low Mach number flows [6]. Moreover, Xiao [265, 266] created a projection-based fractional-step scheme with a convective-acoustic splitting technique. Ni and Komori [170] derived a pressure correction equation based on a three and four step projection scheme. Rauwoens et al. [200] applied a discrete compatibility-constraint to the Navier-Stokes equations in addition to a correction equation for the pressure.

Acoustic phenomena are of transient nature. The resolution of acoustic phenomena generally requires small time step sizes [59, 208, 256]. Under these circumstances, projection-based methods are computationally more efficient than SIMPLE-based schemes due to their non-iterative nature [203]. Within the frame of previous works, an extension of Chorin and Temam's projection method for constant density flows ($\rho = \text{const.}$) to incompressible variable density flows [$\rho = \rho(R,T) \neq \rho(p)$] has been achieved [36]. Choosing between PISO-based and projection-like methods, a projection-based approach was chosen in order to extend an incompressible solver onto the compressible regime including combustion [$\rho = \rho(p,R,T)$].

As a consequence of this, a novel projection-based method extending the incompressible projection method to the combustible compressible regime is developed within this work.

1.3. Numerical Framework - The THETA Code

The present work is performed using the DLR in-house combustion CFD code THETA [36, 37] (Turbulent Heat Release Extension of the TAU code). THETA is based on a three dimensional finite volume discretization method and includes a dual grid approach, thus allowing the calculation of flows on structured, unstructured and hybrid grids. The partial differential equations are solved on a collocated grid, which means that the values of the velocity, pressure and scalar variables are calculated at the same spatial locations. THETA creates a secondary (dual) grid based on the nodes of the primary grid. The dual grid builds control volumes around the vertices of the primary grid. The variables are stored in the center of the cells, i.e. at the nodes of the primary grid. The dual grid thus uses a cell-centered arrangement [106] of the control volumes. Additionally, an automatic grid adaptation module is available. Based on a domain decomposition approach, parallel computations of the flow field can be performed.

Initially conceived for incompressible reactive steady and unsteady flows, THETA is built around a pressure-based core solver [122]. The SIMPLE approach is available and can be used for the numerical computation of steady incompressible flows with variable density. For the numerical computation of unsteady and incompressible fluid and combustion dynamics, the incompressible projection method is implemented. The system of partial differential equations is transformed into algebraic systems of equations via a finite volume method. The latter ones are then solved by matrix-free linear solvers, such as the PBCGS (Preconditioned Bi-Conjugate Gradient Stabilized) method [245], the GMRES (Generalized Minimal RESidual) scheme [215], the Multigrid method [81] and the Jacobi solution algorithm [147]. Whereas the PBCGS, GMRES and Multigrid methods belong to the family of iterative Krylov subspace methods, the Jacobi solution scheme represents a splitting technique, see [147, 148] for details.

The discrete values resulting from the algebraic system of equations are stored at the grid nodes. In addition to the nodal values, fluxes at the cell faces of the control volumes need to be determined. For instance, the mass flux appearing as part of the convective terms at the left hand side of the momentum and scalar equations is treated as a surface flux. The flux values are assumed to be constant along the control volume interfaces and are computed based on an arithmetic average of the adjoined nodal values. This methodology is also referred to as the *midpoint rule* [54]. For a more detailed insight into the treatment of the nodal points and fluxes resulting from the application of a finite volume method, the reader is referred to

the references [54, 172, 182].

In order to compute the convective terms of the momentum and scalar equations, four different spatial discretization schemes for the finite volume formulation of the equations are available in the present THETA code: the upwind difference scheme (UDS) which is of first-order accuracy [54], the central difference scheme (CDS), the linear upwind difference scheme (LUDS) and quadratic upwind difference scheme (QUDS). The CDS and LUDS schemes are of second-order accuracy in space [54]. The spatial accuracy of the QUDS scheme is formally of third order accuracy. The midpoint rule is used to determine the mass flux at the control volume interfaces, which is of second-order accuracy. Thus, the formal spatial accuracy of the discretized convective terms when using the QUDS scheme is formally decreased to an order of $\mathcal{O}(2) < \mathcal{O} < \mathcal{O}(3)$. The diffusive terms are discretized by means of the second-order CDS scheme. Moreover, different temporal discretization schemes are incorporated in THETA: the first-order accurate explicit and implicit Euler schemes (EUE and EUI), as well as the second-order accurate three points backward (TPB) and the Crank-Nicolson (CN) schemes.

Moreover, THETA includes a stiff chemistry solver in conjunction with several combustion models thus capable of calculating both global and detailed chemistry. Further modeling of the convective heat and species transport, diffusion of multispecies flows, turbulence-chemistry interactions, pollutant formation, multiphase flows, ignition behavior, gas volume and solid surface heat radiation can be added to the numerical simulation. Additionally, various RANS, hybrid RANS-LES and pure LES turbulence models have been implemented into the THETA code. The solution strategy implemented in THETA has originally been conceived for constant and variable density incompressible flows. By means of the extension of Moureau's numerical approach [161] onto the application of reactive flows, THETA is currently being extended to the compressible flow regime [135, 136]. As an alternative approach, a new projection-based numerical method is developed in this work.

1.4. Structure of this Work

The structure of the present work is presented in the following: Chapter 2 deals with the fundamentals and governing equations for fluid dynamic and acoustic phenomena thus providing a theoretical background to the physical mechanisms of essential importance within the present work.

The numerical methods applied in this work are described within chapter 3. After noting the governing equations for a compressible reactive flow are noted within section 3.1, the basic idea and derivation of projection-based methods is presented in section 3.2. The projection schemes for incompressible flows with constant density and variable density are shown within sections 3.3 and 3.4, respectively. Based on these schemes, a novel projection-based method

for compressible reactive flows is presented in section 3.4. The derivation of the compressible scheme is described within subsection 3.4.1. Subsection 3.4.3 gives a summary of the equations to be solved, thus providing the algorithm of the compressible solution strategy. The calculation of the pressure Laplacian and occurrence of numerical instabilities is considered within section 3.5. Subsection 3.5.1 is concerned with the computation of the pressure Laplacian, which has to be dealt with when solving the pressure correction equation. Notes on numerical instabilities which may arise during the calculations are provided in subsection 3.5.2. Section 3.6 is devoted to the discussion of the temporal and spatial order of accuracy of projection-based methods.

Chapter 4 is concerned with the description of accurate boundary conditions. Aside from giving a theoretical background to the modeling of such constraints, section 4.1 provides a feasible methodology as a result of a literarture study. The application of accurate boundary constraints requires the treatment of the pressure Laplacian at the boundaries. This is dealt with in section 4.2. Sections 4.3 and 4.4 are concerned with the definition of wave amplitude variations and local one-dimensional inviscid relations needed to derive accurate acoustic boundary conditions.

The verification and validation process of the created numerical scheme is presented within chapter 5. After noting the terminology in section 5.1, the incompressible limit of the compressible solution strategy is addressed to in section 5.2 by means of an analytical analysis and a numerical test case. Following this, several numerical test cases have been selected in order to verify and validate the numerical methods developed within this work. In a first step, the compressible scheme is validated by means of a one-dimensional acoustic test case described within subsection 5.3.1. In addition to this, subsection 5.3.2 reviews the implementation of the acoustic boundary conditions by verifying the acoustic response within a one-dimensional channel. A two-dimensional test case validating the implemented acoustic boundary conditions and the ability of the compressible scheme to compute flows reaching the subsonic limit of $\mathrm{Ma} \rightarrow 1$ is presented in subsection 5.3.3. The numerical prediction of the three-dimensional unsteady turbulent flow in a swirled gas turbine model combustor is addressed to within subsection 5.3.4.

Chapter 6 closes this work by giving a summary and final conclusions.

2. Fundamentals of Fluid Dynamics and Acoustics

2.1. Preliminary Considerations

An incompressible flow is characterized by the following properties [59, 66, 191, 208]:

1. The density is a function of a mean thermodynamic background pressure $\overline{p}$, but not a function of the fluid-dynamic pressure (hydrodynamic and acoustic pressure parts).

2. The effect of pressure material derivative $Dp/Dt = \partial p/\partial t + \underline{u} \cdot \nabla p$ on the energy is neglectable.

3. The influence of the dissipation term $\underline{\underline{\tau}} : \nabla \underline{u}$ on the energy is neglectable.

Dealing with reactive flows, the enthalpy proves to be the most favorable choice as a variable representing the energy of the flow. Thus, the enthalpy is from now on used as variable describing the energy of the flow field. Reaching the incompressible limit, the speed of sound becomes infinite which leaves the Mach number to be zero for a small but finite convective flow speed.

Computing incompressible flows, the relation between the density and the fluid-dynamic pressure vanishes. As a consequence of this, the pressure can be seen as thermodynamically constant so that the density can be computed using a mean pressure $\overline{p}$ [191].

Aside from this, acoustic phenomena are neglectable a low Mach number flow, so that the pressure material derivative within occurring on the left hand side of the enthalpy equation is only influenced by the hydrodynamic pressure variations and can thus be approximated with $Dp/Dt \approx D\overline{p}/Dt$ [191]. In industrial gas turbine combustors with moderate Mach numbers, the ratio of the pressure drop to the mean pressure is of the order of $(2 \div 5)$ % [99, 249]. The hydrodynamic pressure is thus one to two magnitudes smaller than the mean pressure. As a consequence of this, the hydrodynamic pressure fluctuations can be set to zero $D\overline{p}/Dt \approx 0$. Computing low Mach number flows ($\mathrm{Ma} \rightarrow 0$), the effect of occurring pressure fluctuations on the enthalpy is thus neglectable. As the pressure within the calculation of the density

is fixed, it is henceforth denoted as reference pressure p_{ref}. Based on a dimension analysis of the momentum equations, arising thermodynamic and acoustic pressure variations are instantaneously wiped out of the pressure gradient term ∇p, as they scale with the coefficients Ma^{-2}, respective Ma^{-1} [59, 208]. Following these simplifications, it has to be borne in mind that as the Mach number approaches the zero-limit, the hydrodynamic pressure fluctuations figuring as part of the pressure gradient term ∇p within the momentum equations is still able to alter the velocity flow field. It it thus not allowed to drop the pressure gradient term from the momentum equations.

In addition to this, the influence of the dissipation term $\underline{\underline{\tau}} : \nabla \underline{u}$ on the enthalpy is neglectable. This postulate is elaborated in the following. The scaling coefficient of the dissipation term in the enthalpy equation derived from a dimension analysis amounts to Ma^2/Re [59, 208]. For most combustor applications the Reynolds number becomes high due to the small value of the kinematic viscosity of the gas mixture, which is of the order of $\mathcal{O}\left(10^{-5} \div 10^{-4}\right)$ m^2/s. The Reynolds number may even be increased further on in regions where the flow accelerates. In combination with small Mach numbers, the influence of dissipation on the enthalpy can thus be neglected when computing incompressible flows.

Compressibility can be expressed through the value of the Mach number, which is equal to the ratio of the convective velocity to the speed of sound [90, 204, 219]:

$$\text{Ma} \equiv \frac{\|\underline{u}\|_2}{c} \tag{2.1.1}$$

with the homentropic speed of sound [90, 204, 219]

$$c \equiv \sqrt{\left.\frac{\partial p}{\partial \rho}\right|_s} = \sqrt{\gamma \frac{p_{\text{ref}} + p}{\rho}}\,. \tag{2.1.2}$$

Note that in the calculation formula for the homentropic speed of sound (2.1.2), the pressure p characterizes the relative fluctuating pressure which is obtained by subtracting the reference pressure p_{ref} from the absolute pressure. From this point on, the relative pressure p is chosen to describe the behavior of the pressure. The coefficient γ

$$\gamma \equiv \frac{c_p}{c_v} = \frac{c_p}{c_p - R} = \frac{1}{1 - \frac{R}{c_p}} \tag{2.1.3}$$

describes the ratio of the specific heat at constant pressure c_p to the specific heat at constant volume c_v and is often referred to as the heat capacity ratio. Equation (2.1.3) makes use of $R = c_p - c_v$, by which the gas constant R can be formulated as the difference between the specific heat capacity at constant pressure and the specific heat capacity at constant volume.

The definition of the speed of sound according to equation (2.1.2) assumes homentropic conditions and can be derived by making use of the equation of state for an ideal gas, the first (conservation of energy) and second (irreversibility of natural processes) law of thermodynamics, see [204] for details. It is important to bear in mind that the restriction to homentropic conditions is only applied to acoustic flow processes and does not hold on to the fluid dynamics of the flow field. As a result of this, fluid-dynamic phenomena are affected by occurring non-homentropic effects, such as dissipative forces and diffusive fluxes. A homentropic flow can be understood as a flow field, wherein the entropy s does not vary in time and space, i.e. wherein the following condition holds [123, 256]:

$$\frac{\partial s}{\partial t} = 0 \quad \text{and} \quad \nabla s = \underline{0}\,. \tag{2.1.4}$$

A homentropic flow can be characterized as an inviscid adiabatic flow neglecting the influence of heat conduction. In addition to this, heat sources and sinks as well as species diffusion and chemical reactions do not occur within the flow field. A homentropic flow is distinguished from an isentropic flow by a homogeneous distribution of the entropy, i.e. a constant entropy level for all isentropes. An isentropic flow is consequently characterized by a varying entropy level from isentrope to isentrope. Aside from assuming homentropic conditions, the speed of sound may also be defined under isothermal conditions [11, 140, 268]:

$$c \equiv \sqrt{\left.\frac{\partial p}{\partial \rho}\right|_T} = \sqrt{\frac{p_{\mathrm{ref}} + p}{\rho}} = \sqrt{RT}\,. \tag{2.1.5}$$

Newton [168] assumed in 1687 that fluids are rarefied and compressed isothermally, cf. references [11, 194]. However, there was a disagreement between the observed and calculated speed of sound, so that his assumption proved to be wrong. The reason for his misinterpretation is due to the fact that Newton did not account for the second law of thermodynamics, which was only formalized in 1850 by Clausius [27]. Knowing that the heat capacity ratio γ of air at 273 K amounts to 1.4, Laplace [124] postulated in 1816 that rarefactions and compressions in fluids are of homentropic nature. He enforced his assertion by comparing theoretical and experimental results, which ended in a good agreement. For further details concerning this background, the reader is referred to the given literature [11]. Effects due to dissipative forces and heat conduction are generally slow on acoustic phenomena so that only little generality is lost by assuming the sonic flow to be homentropic, see Batchelor [10] and Rienstra et al. [204] and section 1.2. Knowing this, it can be said that choosing to define the speed of sound by assuming homentropic conditions (2.1.2) over isothermal conditions (2.1.5) is the more correct choice for the mathematical representation of the movement

velocity of sound waves.

2.2. Governing Equations for a Compressible Reactive Flow

For a compressible reactive flow, the conservation equations read [66]:

$$\frac{\partial \rho}{\partial t} + \nabla \cdot (\rho \underline{u}) = 0\,, \tag{2.2.1}$$

$$\frac{\partial (\rho \underline{u})}{\partial t} + \nabla \cdot [(\rho \underline{u}) \otimes \underline{u}] + \nabla p = \nabla \cdot \underline{\underline{\tau}} + \rho \underline{f}\,, \tag{2.2.2}$$

$$\frac{\partial (\rho h)}{\partial t} + \nabla \cdot (\rho \underline{u} h) - \frac{\partial p}{\partial t} - \underline{u} \cdot \nabla p = -\nabla \cdot \underline{q} + \underline{\underline{\tau}} : \nabla \underline{u} + \rho \underline{u} \cdot \underline{f}\,, \tag{2.2.3}$$

$$\frac{\partial (\rho \underline{Y})}{\partial t} + \nabla \cdot [(\rho \underline{u}) \otimes \underline{Y}] = -\nabla \cdot \underline{\underline{j}} + \underline{S}_Y\,. \tag{2.2.4}$$

The governing equations for a compressible reactive flow consist of the transport equations for mass (2.2.1), momentum (2.2.2), energy (2.2.3) and species mass fractions (2.2.4). As the equations noted above are applied to a three-dimensional computational domain, the momentum equations are of the dimension dim = 3. The dimension of the species mass fractions amounts to the number of species N_s. The equations given within this work are written using the so-called tensor notation [109, 110, 188], see appendix A for details.

Within the system of equations (2.2.1)-(2.2.4), the variable t characterizes the time. ρ, $\underline{u}$, p and h denote the density, the velocity vector, the pressure and the enthalpy, respectively. The vector containing the species mass fractions is described by the variable $\underline{Y}$ and is of the dimension N_S. In this work, the fluid is modeled as a chemically reactive ideal gas mixture of N_s components. In addition to this, it is assumed that the specific heat capacities at constant pressure and volume do only vary with the temperature T and mixture composition Y_i, $i \in \{1, 2, \ldots, N_s\}$, which is an eligible assumption for gas mixtures involved in mixing and combustion processes [66]. The equation of state relates the density to the pressure, the specific gas constant and the temperature and is applied according to the following equation:

$$\rho = \frac{p_{\text{ref}} + p}{RT} \quad \text{with} \quad R \equiv \mathcal{R} \sum_{i=1}^{N_s} \frac{Y_i}{M_i}\,. \tag{2.2.5}$$

Note that the pressure p characterizes the relative pressure which is obtained by subtracting the reference pressure p_{ref} from the absolute pressure. Within the equation of state, R denotes the specific gas constant of the gas mixture applied, whereas the symbol $\mathcal{R}$ described the universal gas constant. Y_i and M_i are the mass fraction and the molar mass of the species i, respectively.

The variable $\underline{\underline{\tau}}$ characterizes the stress tensor, which is defined by the following formula

[59, 206]:

$$\underline{\underline{\tau}} \equiv 2\mu \left[\underline{\underline{S}} - \frac{1}{3} (\nabla \cdot \underline{u}) \underline{\underline{I}} \right] \quad \text{with} \quad \underline{\underline{S}} \equiv \frac{1}{2} \left[\nabla \underline{u} + (\nabla \underline{u})^T \right] . \tag{2.2.6}$$

$\underline{\underline{S}}$ denotes the strain rate tensor. $\underline{\underline{S}}$ and $\underline{\underline{\tau}}$ constitute tensors of the dimension 3×3. The variable μ describes the dynamic viscosity and is obtained from a weighted mean of the pure species viscosity values [36]. The enthalpy h of a chemically reactive ideal gas mixture of N_s components equals the sum of the enthalpies of the species i multiplied with their respective mass fractions Y_i:

$$h = \sum_{i=1}^{N_s} Y_i h_i \, . \tag{2.2.7}$$

The enthalpy of the species i is defined by the following equation:

$$h_i \equiv h_{f_i}^0 + \int_{T_0}^{T} c_{p_i} \left(\tilde{T} \right) d\tilde{T} \, . \tag{2.2.8}$$

Following the definition (2.2.8), the enthalpy of the species i is often referred to as the sensible chemical enthalpy [66, 190]. Inserting definition (2.2.8) into equation (2.2.7) gives the following formula for the determination of the enthalpy h:

$$h \equiv \sum_{i=1}^{N_s} Y_i \left[h_{f_i}^0 + \int_{T_0}^{T} c_{p_i} \left(\tilde{T} \right) d\tilde{T} \right] . \tag{2.2.9}$$

The temperature is denoted by the quantity T. The variable c_{p_i} describes the specific heat at constant pressure for the species i and constitutes a polynomial - and thus a non-linear - function of the temperature. The variable $h_{f_i}^0$ characterizes the standard enthalpy of formation of the species i. The superscript ^{0} denotes the state at standard conditions, which is defined as the state at $T_0 \equiv 298.15\,\mathrm{K}$ and $p_0 \equiv 101325\,\mathrm{Pa}$ [69, 102, 236].

The vector $\underline{f}$ appearing on the right hand side of the momentum (2.2.2) and enthalpy equation (2.2.3) summarizes occurring specific body forces, such as forces due to gravity. This work is concerned with the numerical simulation of duct flows and flows in gas turbine combustor systems. Since the flows within these test cases only cover small heights and gravity is the only arising body force, the influence of gravity and thus of specific body forces can be neglected against convection and pressure gradient effects.

The species source term $\underline{S}_Y$ takes into account chemical production due to occurring reactions and vanishes in the case of non-reactive flows. $\underline{\underline{j}}$ and $\underline{q}$ denote the diffusion and heat fluxes. Their determination is dealt with in the following sections.

2.2.1. Calculation of the Diffusion Flux

The diffusion of a multi-species flow is modeled within this work based on FICK's law [56]. The diffusion flux tensor $\underline{\underline{j}}$ is thus approximated by a gradient-like form:

$$\underline{\underline{j}} \equiv -\underline{\underline{D}} \cdot \nabla \underline{Y} \,. \tag{2.2.10}$$

According to equation (2.2.10), the diffusion flux tensor is described as the product of the diffusion tensor and the gradient of the vector containing the species mass fractions. The diffusion tensor has the dimension $N_s \times N_s$. Considering a three-dimensional flow, the gradient of the species mass fraction vector possesses the dimension $N_s \times 3$. Thus, the diffusion flux tensor is characterized by a $N_s \times 3$ matrix. It is important to note at this point that by describing the diffusion flux tensor through FICK's law [56], the LUDWIG-SORET effect [137, 227] - also known as *thermophoresis, thermodiffusion* and *Soret* effect - as well as the influences of pressure and body force terms are neglected [130].

Depending on whether the flow is characterized as being laminar or turbulent, the diffusion tensor $\underline{\underline{D}}$ is approximated differently. It is therefore useful to decompose $\underline{\underline{D}}$ into a laminar part $\underline{D}_l$ and a turbulent part D_t:

$$\underline{\underline{D}} \equiv \left[\mathrm{diag}\left(\underline{D}_l\right) + D_t \cdot \underline{\underline{I}} \right] \,. \tag{2.2.11}$$

The operator $\mathrm{diag}\left(\underline{D}_l\right)$ projects the laminar diffusion vector $\underline{D}_l$ onto a diagonal matrix of the dimension $N_s \times N_s$. Note that the laminar part of the diffusion tensor $\underline{D}_l$ contains N_s laminar diffusion coefficients for each species equation and thus represents a vector of the dimension N_s in the species mass fraction equations (2.2.4).

The calculation of the laminar and turbulent parts depends on whether the flow is characterized as being laminar or turbulent. If the flow is laminar, the turbulent viscosity μ_t is set to zero. As a consequence of this, the turbulent diffusion coefficient vanishes. The computation of the laminar diffusion coefficient $\underline{D}_l$ can be performed via two ways. The simplest approach is to assume a constant Schmidt number for all species i. In this case, the laminar diffusion coefficient $\underline{D}_l$ is calculated through the ratio of the laminar viscosity μ_l to the laminar Schmidt number Sc_l, yielding the following formula:

$$\forall i \in \{1, \ldots, N_s\} \,, \quad D_{l_i} = D_l \equiv \frac{\mu_l}{\mathrm{Sc}_l} \,. \tag{2.2.12}$$

In equation (2.2.12), the laminar Schmidt number is set to a constant value of 0.7. Since the right hand side of equation (2.2.12) does not involve any variables dependent on the species

i and for laminar flows D_t equals zero, all species i are characterized by an identical diffusion coefficient D_l:

$$\underline{\underline{D}} \equiv D_l \cdot \underline{\underline{I}}. \tag{2.2.13}$$

The second approach to determine the laminar diffusion coefficient is more complicated but also more accurate. In this case, the laminar diffusion coefficients D_{l_i} are expressed through the following definition:

$$\forall i \in \{1, \ldots, N_s\}, \quad D_{l_i} \equiv \rho \mathcal{D}_i \,. \tag{2.2.14}$$

The diffusion coefficient of the species i figuring as part of the gas mixture is denoted by $\mathcal{D}_i$ and is calculated based on the binary diffusion coefficients $\mathcal{D}_{ij}$ of a given gas mixture according to the following relation [36]:

$$\forall i \in \{1, \ldots, N_s\}, \quad \mathcal{D}_i \equiv \frac{1 - Y_i}{\sum_{\substack{j=1 \\ j \neq i}}^{N_s} \frac{M}{M_j} \frac{y_j}{\mathcal{D}_{ij}}} \cdot \frac{p_0}{p_{\text{ref}}} \,. \tag{2.2.15}$$

The binary diffusion coefficients $\mathcal{D}_{ij}$ have the unit $[\text{m}^2/\text{s}]$ and are calculated based on mean molecular parameters. For a more detailed insight into the determination of the binary diffusion coefficients, see [36].

Let us introduce the following dimensionless numbers [36]:

- Prandtl number: $\text{Pr} \equiv \frac{\mu c_p}{\kappa}$,
- Schmidt number: $\text{Sc} \equiv \frac{\mu}{D}$,
- Lewis number: $\text{Le} \equiv \frac{\text{Sc}}{\text{Pr}} = \frac{\kappa}{D c_p}$,

where μ, κ, D and c_p denote the dynamic viscosity, thermal conductivity, specific heat capacity at constant pressure and diffusion coefficient.

Compared to laminar flows, the laminar part of the diffusion tensor has a much smaller impact on the diffusion processes in case of computing turbulent flows [36]. Hence, a simplified approximation assuming a Lewis number of unity for all species i

$$\forall i \in \{1, \ldots, N_s\}, \quad \text{Le}_i \equiv \frac{\kappa}{c_p D_{l_i}} = 1 \tag{2.2.16}$$

suffices in order to calculate the laminar part of the diffusion tensor $\underline{\underline{D}}_l$. Following equation (2.2.16), the laminar diffusion coefficient of the species i can be determined by the ratio of the thermal conductivity κ to the specific heat at constant pressure c_p:

$$\forall i \in \{1, \ldots, N_s\}, D_{l_i} = D_l = \frac{\kappa}{c_p} \,. \tag{2.2.17}$$

κ and c_p are the thermal conductivity, respective the specific heat at constant pressure of the gas mixture. As a result of this, all species i possess a common laminar diffusion coefficient D_l. If the Prandtl number does not vary within the turbulent flow considered, the computation of the laminar diffusion coefficient can be further simplified. With the definition of the laminar Prandtl number

$$\mathrm{Pr}_l \equiv \frac{\mu_l c_p}{\kappa} \tag{2.2.18}$$

and a Lewis number of all species i equal to one, the laminar diffusion coefficient D_{l_i} can be reformulated to obtain the following result:

$$\forall i \in \{1, \ldots, N_s\}\,, D_{l_i} = D_l \equiv \frac{\mu_l}{\mathrm{Pr}_l} = \frac{\mu_l}{\mathrm{Sc}_l}\,. \tag{2.2.19}$$

Within the frame of this work, the laminar Prandtl Pr_l is set to a value of 0.7. With $\mathrm{Le}_i = 1$, $\forall i \in \{1, \ldots, N_s\}$, the laminar Schmidt number $\mathrm{Sc}_l = \mathrm{Le}_i \mathrm{Pr}_l$

$$\forall i \in \{1, \ldots, N_s\}\,, \mathrm{Sc}_l = \underbrace{\mathrm{Le}_i}_{=1 \forall i}\, \mathrm{Pr}_l = 0.7 \tag{2.2.20}$$

equals 0.7. Under the assumption of neglecting the temperature dependence of the non-dimensional Prandtl, Schmidt and Lewis numbers, this result implies that species and energy transport possess proportional time scales, independently of the temperature level and species considered [36].

The thermal conductivity κ is calculated analogously to the dynamic viscosity μ based on a weighted mean of the pure species conductivities. The latter ones are obtained from the pure species viscosities. For a more detailed insight into the calculation of the thermal conductivity, the reader is referred to [36].

The turbulent diffusion coefficient D_t is obtained from the ratio of the turbulent dynamic viscosity to the turbulent Schmidt number:

$$D_t \equiv \frac{\mu_t}{\mathrm{Sc}_t}\,. \tag{2.2.21}$$

The value of the turbulent Schmidt number Sc_t is set to 0.7 within this work.

By summarizing equations (2.2.19) and (2.2.21), one sees that all species i possess the same laminar and turbulent diffusion coefficients. the diffusion tensor $\underline{\underline{D}}$ is thus obtained through the following equation:

$$\underline{\underline{D}} \equiv (D_l + D_t) \cdot \underline{\underline{I}}\,. \tag{2.2.22}$$

The matrix $\underline{\underline{I}}$ denotes the identity matrix.

2.2.2. Calculation of the Heat Flux

Apart from soot diffusion and heat radiation due to soot formation and oxidation, the two most influential effects concerning the description of the heat flux are heat conduction based on FOURIER's law [60] and diffusion conduction. Diffusion conduction characterizes the energy flux due to occurring mass concentration gradients and is often referred to as the so-called *Dufour effect* [263]. Taking into account heat and diffusion conduction, the heat flux vector $\underline{q}$ is expressed through the following equation:

$$\underline{q} \equiv -\kappa \nabla T + \sum_{i=1}^{N_s} h_i j_{ij} \underline{I}\,, \tag{2.2.23}$$

where the vector $\underline{I}$ describes the identity vector. The variable j_{ij} is the element ij of the diffusion flux tensor $\underline{\underline{j}}$ derived within the previous section. Since this work does not feature any testcases with soot formation and oxidation (and the thereby arising influence and importance of heat radiation), the effect of soot diffusion and heat radiation on the enthalpy are not treated. We are now interested in reformulating the right hand side of equation (2.2.23) such that the temperature T is replaced by the enthalpy h. Following the definition of an ideal gas, the total derivative of the enthalpy is obtained from the following formula:

$$dh = \underbrace{\left.\frac{\partial h}{\partial T}\right|_{\underline{Y}}}_{\equiv c_p} dT + \sum_{i=1}^{N_s} \underbrace{\left.\frac{\partial h}{\partial Y_i}\right|_{T,Y_{j,j\neq i}}}_{\equiv h_i} dY_i = c_p dT + \sum_{i=1}^{N_s} h_i dY_i\,. \tag{2.2.24}$$

Recasting the above equation for the differential change of the temperature yields:

$$dT = \frac{1}{c_p}\left(dh - \sum_{i=1}^{N_s} h_i dY_i\right) \Rightarrow \nabla T = \frac{1}{c_p}\left(\nabla h - \sum_{i=1}^{N_s} h_i \nabla Y_i\right)\,. \tag{2.2.25}$$

Inserting formula (2.2.25) into equation (2.2.23) leads to the following equation determining the heat flux vector:

$$\underline{q} = -\frac{\kappa}{c_p}\nabla h + \frac{\kappa}{c_p}\sum_{i=1}^{N_s} h_i \nabla \underline{Y} + \sum_{i=1}^{N_s} h_i j_{ij} \underline{I}\,. \tag{2.2.26}$$

The temperature does not appear anymore within the calculation of the heat flux vector $\underline{q}$. Equation (2.2.26) is from now on considered the basic formula determining the heat flux vector.

For turbulent flows, the laminar part of the diffusion tensor $\underline{\underline{D}}$ has a much smaller impact on the diffusion processes than in case of computing laminar flows [36]. As a consequence

of this, differential species diffusion can be neglected so that all species i possess the same diffusion coefficient D, see equation (2.2.19). In this case, a simplified gradient-like approach based on FICK's law [56] can be applied to model the diffusion flux tensor [36]:

$$j_{ij} = -D\frac{\partial Y_i}{\partial x_j}\,. \tag{2.2.27}$$

Introducing the definitions of the Prandtl number $\mathrm{Pr} \equiv \mu c_p/\kappa$ and Schmidt number $\mathrm{Sc} \equiv \mu/D$ along with the simplified approach (2.2.27), equation (2.2.26) can be reformulated giving the following equation [66]:

$$\underline{q} = -\frac{\mu}{\mathrm{Pr}}\nabla h + \left(\frac{\mu}{\mathrm{Pr}} - \frac{\mu}{\mathrm{Sc}}\right)\sum_{i=1}^{N_s} h_i \nabla \underline{Y}\,. \tag{2.2.28}$$

As differential species diffusion is neglected, the Lewis number $\mathrm{Le} \equiv \mathrm{Sc}/\mathrm{Pr}$ equals one for all species i. As a result, we can write $\mathrm{Pr} = \mathrm{Sc}$ and the second term within equation (2.2.28) vanishes. The heat flux vector may then be calculated by means of the following simplified equation [66]:

$$\underline{q} = -\frac{\mu}{\mathrm{Pr}}\nabla h\,. \tag{2.2.29}$$

2.3. Turbulence Modeling

The laminar viscosity constitutes the characteristic quantity for friction processes figuring as part of the momentum transfer. Analogously here to, the momentum transfer caused by turbulent vortices can be modeled with the aid of the turbulent viscosity, as postulated by BOUSSINESQ [17] in 1877. The turbulent viscosity can be obtained through the formulation and solution of a system of transport equations for the turbulent quantities. Several turbulent models have been developed since the postulation made by Boussinesq. One way to categorize turbulence models consists of assorting them based on the number of differential equations solved. Due to their vast regime of application, the development of two-equation-models for the turbulent closure of the RANS (Reynolds-Averaged Navier-Stokes) and URANS (Unsteady RANS) equations has quite advanced in the last couple of decades. It is typical for two-equation-turbulence-models to solve transport equations for the turbulent kinetic energy $k \equiv 1/2\,\overline{\underline{u}' \cdot \underline{u}'}$ and the turbulent dissipation rate $\varepsilon \equiv \nu\,\overline{\nabla \underline{u}'^T : \nabla \underline{u}'}$ or turbulent dissipation frequency $\omega \equiv \varepsilon/k$, depending on the turbulent model applied [96, 98, 125, 149, 150, 261, 151, 152, 153, 155]. The k-ω-SST and k-ω-SST-SAS turbulence models are applied in this work. They provide the formulas which determine the turbulent viscosity ν_t in turbulent flows and are described in the following.

2.3.1. The k-ω-SST turbulence model

The k-ω-SST (Shear Stress Transport) turbulence model has originally been proposed by Menter [149] in 1994. Within the DLR THETA code, the later version of Menter [150] developed in 2003 is implemented. The key idea of the k-ω-SST turbulence model is to blend automatically between the k-ω turbulence model of Wilcox [261] near the domain walls and the standard k-ε turbulence model of Jones and Launder [98, 125] in the mean flow field. Additionally, the k-ω-SST turbulence model includes a modification of the traditional k-ω model formulation in the vicinity of the domain walls concerning the turbulent viscosity. The aim of this modification is to satisfy the assumption that the shear stress in a boundary layer is proportional to the turbulent kinetic energy [149]. A more detailed theoretical background to the k-ω-SST turbulence model is given within the references [96, 149, 150].

The following two transport equations for the turbulent kinetic energy k and turbulent dissipation frequency ω are solved within the k-ω-SST turbulence model [149, 150]:

$$\frac{\partial(\rho k)}{\partial t} + \nabla \cdot (\rho \underline{u} k) - \nabla \cdot \left[(\mu + \sigma_k \mu_t) \nabla k \right] = \tilde{P}_k - \beta^* \rho k \omega \,, \tag{2.3.1}$$

$$\frac{\partial(\rho \omega)}{\partial t} + \nabla \cdot (\rho \underline{u} \omega) - \nabla \cdot \left[(\mu + \sigma_\omega \mu_t) \nabla \omega \right] = \frac{\alpha}{\nu_t} \tilde{P}_k - \beta \rho \omega^2 + 2 (1 - F_1) \rho \sigma_{\omega_2} \frac{1}{\omega} (\nabla k \cdot \nabla \omega) \,. \tag{2.3.2}$$

The blending function F_1 is defined by the following formula:

$$F_1 = \tanh \left\{ \left[\min \left(\max \left(\frac{\sqrt{k}}{\beta^* \omega y}, \frac{500\nu}{y^2 \omega} \right), \frac{4 \rho \sigma_{\omega 2} k}{\mathrm{CD}_{k\omega} y^2} \right) \right]^4 \right\} \tag{2.3.3}$$

with the use of the cross-diffusion term $\mathrm{CD}_{k\omega}$:

$$\mathrm{CD}_{k\omega} = \max \left(2 \rho \sigma_{\omega_2} \frac{1}{\omega} (\nabla k \cdot \nabla \omega) \,, 10^{-10} \right) \,. \tag{2.3.4}$$

The variable y denotes the wall distance. F_1 equals zero far away from the surface (k-ε model) and switches over to one inside the boundary layer (k-ω model). The turbulent kinematic viscosity ν_t is defined by the following equation:

$$\nu_t = \frac{a_1 k}{\max (a_1 \omega, F_2 \cdot \mathcal{S})} \,, \tag{2.3.5}$$

where $\mathcal{S}$ is an invariant measure of the strain rate tensor $\underline{\underline{S}}$ equal to $\sqrt{2}$ times the Frobenius

norm of $\underline{\underline{S}}$, see equation (A.0.18) in appendix A for details. F_2 is a second blending function, defined by the following relation:

$$F_2 = \tanh\left\{\left[\max\left(\frac{2\sqrt{k}}{\beta^*\omega y}, \frac{500\nu}{y^2\omega}\right)\right]^2\right\} . \tag{2.3.6}$$

A production limiter is used in the k-ω-SST model to prevent the build-up of turbulence in stagnation regions:

$$P_k = \mu_t \nabla\underline{u} \cdot \left[\nabla\underline{u} + (\nabla\underline{u})^T\right] \;\Rightarrow\; \tilde{P}_k = \min\left(P_k, 10 \cdot \beta^*\rho k\omega\right) . \tag{2.3.7}$$

Let $\underline{v}$ be a vector containing the variables α, β and σ. The components of $\underline{v}$ are then given by the following blending function:

$$\underline{v} = F_1\underline{v}_1 - (1 - F_1)\,\underline{v}_2 \quad \text{with} \quad \underline{v} \equiv \left[\alpha \;\; \beta \;\; \sigma\right]^T . \tag{2.3.8}$$

The constants for the k-ω-SST turbulence model are listed in the following:

$$\begin{aligned} &\alpha_1 = 0.\overline{5},\ \beta_1 = 0.075,\ \beta^* = 0.09,\ \sigma_{k_1} = 0.85,\ \sigma_{\omega_1} = 0.5, \\ &\alpha_2 = 0.44,\ \beta_2 = 0.828,\ \sigma_{k_2} = 1,\ \sigma_{\omega_2} = 0.856,\ a_1 = 0.31 . \end{aligned} \tag{2.3.9}$$

Within the inner flow field, the dissipation frequency ω possesses rather small values. Opposed to this, the values of ω rise dramatically as the walls of the computational domain are approached. Consequently, the use of the k-ω-SST turbulence model requires a proper resolution of the boundary layer. In order to achieve an adequate boundary layer resolution, conditions concerning the meshing of the computational domain need to be applied to the near-wall region. A resolution of the boundary layer region of $y^+ \approx 1$ is therefore recommended when the k-ω-SST turbulence model is used. According to [262], the dimensionless wall distance y^+ is defined by the following relation:

$$y^+ \equiv \frac{u_\tau}{\nu} \cdot y \quad \text{with} \quad u_\tau = \sqrt{\frac{\tau_w}{\rho}} \quad \text{and} \quad \tau_w = \rho\nu\frac{\partial u_\parallel}{\partial x_n} . \tag{2.3.10}$$

In the above equation, u_τ is the shear velocity, whereas τ_w and ν denote the wall shear stress and the kinematic viscosity, respectively. $u_\parallel$ and x_n stand for the velocity component parallel and the coordinate normal to the wall, respectively. y describes the wall distance. As a consequence of this, the first point should be at a distance of $y^+ \approx 1$. The boundary layer of the flow in the near-wall area should be resolved using at least eight to ten grid points

[49]. A dimensionless wall distance higher than unity can lead to a boundary layer which will not be correctly calculated within the numerical simulation carried out later on. In this case, the overall solution might be erroneous. In addition to this, convergence problems may occur. However, for the numerical computation of complex industrial flows the requested grid resolution near the walls is in general too high, since this would lead to a large amount of computational time. The strict application of wall functions enables the use of coarser grid regions, but has the inconvenience of limiting the model accuracy. As a remedy to this issue, the automatic near-wall treatment [50] is applied. The key idea of the automatic near-wall treatment is that it shifts gradually between a viscous sublayer formulation and the use of wall functions based on the grid density within the near-wall region. This automatic near-wall treatment is well-suited for the ω-equation, as the ω-equation provides analytical solutions for both the sublayer and the logarithmic zone. A blending function depending on y^+ can therefore be defined, which can be used to derive a formulation that describes the behavior of ω in the linear and logarithmic near-wall region [50, 96]:

$$\omega\left(y^+\right) = \sqrt{\omega_{\text{vis}}^2\left(y^+\right) + \omega_{\text{log}}^2\left(y^+\right)} \tag{2.3.11}$$

with

$$\omega_{\text{vis}}\left(y^+\right) = \frac{6\nu}{0.075y^2} \quad \text{and} \quad \omega_{\text{log}}\left(y^+\right) = \frac{u_\tau}{0.3\tilde{\kappa}y}\,, \tag{2.3.12}$$

where u_τ stands for the friction velocity, defined as

$$u_\tau = \sqrt[4]{u_{\tau_{\text{vis}}}^4\left(y^+\right) + u_{\tau_{\text{log}}}^4\left(y^+\right)} \tag{2.3.13}$$

with

$$u_{\tau_{\text{vis}}} = \frac{u_{\text{fp}}}{y^+}\ , \quad u_{\tau_{\text{vis}}} = \frac{u_{\text{fp}}}{\frac{1}{\tilde{\kappa}}\ln\left(y^+\right) + C_w} \tag{2.3.14}$$

The variable u_{fp} denotes the absolute velocity at the first near-wall point. $\tilde{\kappa}$ and C_w describe the von Kármán constant and a constant coefficient, respectively. Within the literature, varying values are found for $\tilde{\kappa}$ and C_w. The most widespread values are 0.41 ± 0.2 and 5.5 ± 0.3 for $\tilde{\kappa}$ and C_w [39, 40, 96, 262]. Within this work, the standard values of 0.41 and 5.5 are used for $\tilde{\kappa}$ and C_w. The automatic near-wall treatment is incorporated in the THETA combustion CFD code and is used for the test case in this section.

2.3.2. The k-ω-SST-SAS turbulence model

The k-ω-SST-SAS (Scale Adaptive Simulation) turbulence model was developed by Egorov and Menter [45, 150, 151, 152, 153, 155] as a hybrid URANS/LES model based on Rotta's [210] k-kL turbulence model. The variable k describes the turbulent kinetic energy, whereas

L denotes an integral length scale. The k-ω-SST-SAS turbulence model enables the partial resolution of the turbulent spectrum by transitioning from the URANS mode into an LES-like mode within certain flow regions. Unlike other hybrid URANS/LES methods - such as the DES (Detached Eddy Simulation) turbulence model [228], where the blending between the URANS and the LES-like mode is governed by the grid cell size - the blending of the k-ω-SST-SAS turbulence model operates as a function of the flow field, which itself is limited by the grid cell size. The k-ω-SST-SAS turbulence model typically operates in the LES-like mode in flow regions possessing a certain unsteadiness, i.e. regions where large separation zones or vortex interactions occur [96, 153, 155]. The k-ω-SST-SAS model adjusts the turbulent length scale dynamically to the length scale of the resolved structures [96]. This is realized by introducing the von Kármán length scale l_{vK} as a measure for the amount of resolved structures. l_{vK} is calculated based on the ratio of the first to the second velocity derivatives [96, 134, 153]:

$$l_{\mathrm{vK}} \equiv \tilde{\kappa} \cdot \frac{\mathcal{S}}{\mathcal{U}}\,, \tag{2.3.15}$$

with the numerator

$$\mathcal{S} \equiv \sqrt{2}\,\|\underline{\underline{S}}\|_F = \sqrt{\frac{1}{2}\sum_{i=1}^{3}\sum_{j=1}^{3}\left(\frac{\partial u_i}{\partial x_j}+\frac{\partial u_j}{\partial x_i}\right)^2} \tag{2.3.16}$$

and denominator

$$\mathcal{U} \equiv \|\Delta_{\mathrm{L}}\underline{u}\|_2 = \sqrt{\sum_{i=1}^{3}\left(\sum_{j=1}^{3}\frac{\partial^2 u_i}{\partial x_j^2}\right)^2}\,. \tag{2.3.17}$$

$\mathcal{S}$ and $\mathcal{U}$ are an invariant measure equal to $\sqrt{2}$ times the Frobenius norm of the strain rate tensor $\underline{\underline{S}} \equiv \frac{1}{2}\left[\nabla\underline{u} + (\nabla\underline{u})^T\right]$ and the magnitude of the velocity Laplacian $\Delta_{\mathrm{L}}\underline{u}$, respectively. $\nabla\underline{u}$ describes the velocity gradient tensor. $\tilde{\kappa}$ denotes the von Kármán constant. Thus, the modeling of a dynamically adjusted length scale enables the k-ω-SST-SAS turbulence model to operate in the URANS mode within attached layers, e.g. in the vicinity of the boundary walls. The LES mode is turned on in case a detachment of the flow structures occurs. The k-ω-SST-SAS turbulence model given by Egorov and Menter [45, 153, 155] is formulated in the k-$\sqrt{k}\,L$ form. Defining $\psi \equiv \sqrt{k}\,L$, the transport equations to be solved read [45, 153, 155]

$$\frac{\partial(\rho k)}{\partial t} + \nabla\cdot(\rho\underline{u}k) - \nabla\cdot\left[(\mu+\sigma_k\mu_t)\,\nabla k\right] = P_k - \rho c_\mu^{\frac{3}{4}}\frac{k^2}{\omega} + \nabla\cdot\left(\frac{\mu_t}{\sigma_k}\nabla k\right)\,, \tag{2.3.18}$$

$$\frac{\partial(\rho\psi)}{\partial t} + \nabla\cdot(\rho\underline{u}\psi) - \nabla\cdot\left[(\mu+\sigma_\psi\mu_t)\,\nabla\psi\right] = \frac{\psi}{k}P_k\left(\zeta_1 - \zeta_2\,\tilde{\kappa}\frac{l}{\tilde{l}_{\mathrm{vK}}}\right) - \zeta_3\,\rho\,k + \nabla\cdot\left(\frac{\mu_t}{\sigma_\psi}\nabla\psi\right)\,. \tag{2.3.19}$$

By setting ψ to the turbulent dissipation frequency ω, equation (2.3.19) can be transformed into an ω-type equation, similar to the one of the k-ω-SST turbulence model (2.3.2). Equation (2.3.19) then differs from the original ω equation (2.3.2) by an additional production term $Q_{\text{SST-SAS}}$ appearing on the right hand side [45, 153, 155]:

$$Q_{\text{SST-SAS}} \equiv \rho \cdot \max\left[\zeta_2\,\tilde{\kappa}\,S^2\frac{l_t}{\tilde{l}_{\text{vK}}} - \frac{2\,C}{\sigma_\psi}k \cdot \max\left(\frac{\Delta_L\omega}{\omega^2}, \frac{\Delta_L k}{k^2}\right), 0\right] . \tag{2.3.20}$$

$\zeta_2 = 3.51$, $\tilde{\kappa} = 0.41$, $C = 2$ and $\sigma_\omega = 0.\overline{6}$ denote the model constants. The variable $\tilde{l}_{\text{vK}}$ used within the above equations constitutes a bounded value of the von Kármán length scale l_{vK} defined by equation (2.3.15) and is obtained from the following comparison:

$$\tilde{l}_{\text{vK}} = \max\left(l_{\text{vK}}, C_s\sqrt{\frac{\zeta_2\,\tilde{\kappa}}{\frac{\beta_{\omega 2}}{\beta_k} - \gamma_2}}\Delta_{\text{grid}}\right) . \tag{2.3.21}$$

Δ_{grid} denotes the characteristic length of a grid cell. It is computed as cube root of the grid cell volume V:

$$\Delta_{\text{grid}} = \sqrt[3]{V} . \tag{2.3.22}$$

Within equation (2.3.21), $\beta_{\omega 2}$, β_k and γ_2 are the modeling constants equal to the following values [96]:

$$\beta_{\omega 2} = 0.0828,\ \beta_k = 0.09,\ \gamma_2 = \frac{\beta_{\omega 2}}{\beta_k} - \frac{\sigma_{\omega 2}\,\tilde{\kappa}^2}{\sqrt{\beta_k}} = 0.44 , \tag{2.3.23}$$

where $\sigma_{\omega 2} = 0.856$ is a model constant taken from the k-ω-SST turbulence model. C_s stands for the Smagorinsky constant which represents the rate of decay of the homogeneous isotropic turbulence. It has to be calibrated based on the numerical models used in order to avoid both the accumulation and excessive dissipation of energy at the smallest scales [96, 152]. As a result of previous works [36, 96], C_s is set to the reference value of 0.145. The limiting function expressed through equation (2.3.21) has the purpose of controlling the damping strength of the finest resolved turbulent fluctuations. The structure of equation (2.3.21) is derived by means of an equilibrium analysis (balance between production and dissipation of turbulent kinetic energy) of the turbulent viscosity [45]. The turbulent viscosity ν_t is obtained analogously to the k-ω-SST model from equation (2.3.5).

The influence of the production term $Q_{\text{SST-SAS}}$ rises as the ratio of the turbulent length scale $l_t \equiv k^{1/2}/\,\omega$ to the von Kármán length scale $\tilde{l}_{\text{vK}}$ increases, cf. equation (2.3.20). An unsteady velocity field is characterized by a small von Kármán length scale $\tilde{l}_{\text{vK}}$, whereas a velocity field with a small amount of unsteadiness is described by a much larger value of $\tilde{l}_{\text{vK}}$, see [45, 96, 152, 155, 154] for details. In case the computational grid is fine enough to resolve

the small scale flow structures, $Q_{\text{SST-SAS}}$ increases the production of the turbulent dissipation frequency in unsteady regions, such as in the wake of strongly swirled flows. Equation (2.3.5) unveils an inverse proportionality of the turbulent viscosity to the turbulent dissipation frequency ω. An increase of ω thus leads to a reduction of the turbulent kinematic viscosity ν_t. As a result of this, the damping of the turbulent kinematic viscosity on the resolved fluctuations is decreased. The momentum equations then operate in a "scale-resolving" mode [95, 96, 155].

The k-ω-SST-SAS turbulence model approaches the formulation of the k-ω-SST model in the vicinity of the boundary wall [96, 155]. The near wall region should thus be resolved fine enough by applying a dimensionless wall distance of the order of unity. The boundary layer should be resolved with at least eight to ten grid points [49].

2.4. Combustion Modeling

The combined Eddy Dissipation/Finite Rate Chemistry (EDM/FRC) model is applied in order to model the combustion phenomena within the reactive test cases. The EDM/FRC approach constitutes a combination of the EDM (Eddy Dissipation Model) and FRC (Finite Rate Chemistry) models. The EDM approach has originally been proposed by Magnussen [141] as an extension of the eddy break-up model originally developed by Spalding [230, 231]. The EDM combustion model is based on the assumption that the chemical reactions are fast compared to the transport processes of the flow. The reaction rate of the occurring chemical reactions is assumed to be inversely proportional to a turbulent mixing time τ_t defined as the ratio of the turbulent kinetic energy k to the turbulent dissipation rate ε [141]:

$$\tau_t \equiv \frac{k}{\varepsilon} = \omega^{-1} \,. \tag{2.4.1}$$

As $\omega \equiv \varepsilon/k$, the turbulent mixing time τ_t is equal to the inverse of ω. The EDM combustion model assumes chemical equilibrium infinitely fast chemistry, so that its application is limited to cases where chemistry is governed by mixing processes [99].

The implementation of the EDM model within the THETA code incorporates the enhancement of the fast chemistry limit suggested by Gran and Magnussen [70]. The reaction rate rr of one reaction r is thus obtained through the application of the following equation [70, 99]:

$$\text{rr}_{\text{EDM}_r} = A\,\rho \min\left(\frac{1}{\tau_t}, L_{\text{mix}}\right)\left[\min\left(\min_{i,\nu'_{i_r}\neq 0}\frac{Y'_i}{\nu'_{i_r}M'_i}, B\frac{\sum_{i=1}^{N_s} Y''_i}{\sum_{i=1}^{N_s}\nu''_{i_r}M''_i}\right)\right] . \tag{2.4.2}$$

where $A = 4$ and $B = 0.5$ stand for the empirically determined reactant and product limiter,

respectively. ν denotes the stoichiometric coefficient, whereas the notation ϕ' and ϕ'' describes the quantity $\phi = \{M, Y, \nu\}$ of the educt $'$, respective the product $''$.

In the near-wall region of turbulent no-slip boundary walls, ω may increase significantly. In this case, the reaction rate increases to very high values. This causes the EDM combustion model to produce unphysical behavior in the near-wall region, such as ignition at boundaries or flame movement along the wall. In order to prevent such unphysical results, the inverse of the turbulent mixing time $1/\tau_t = \omega$ is limited by an upper boundary L_{mix}, see equation (2.4.2). L_{mix} is referred to as the mixing rate limit of the EDM combustion model. For methane/air mixtures, $L_{\text{mix}} = 2\,500$ 1/s constitutes a reasonable value. The EDM combustion model does however not account for non-equilibrium effects, which may produce erroneous results in case chemical kinetics limit the reaction rate.

Contrary to the EDM combustion model, the FRC approach is based on the key idea that mixing processes of gas mixtures are much faster than kinetically controlled mechanisms. In addition to this, the FRC combustion model is able to account for non-equilibrium effects [99]. In a mixture consisting of N_r elementary chemical reactions, the reaction rate rr of one reaction r is obtained on the following equation [66, 99]:

$$\text{rr}_{\text{FRC}_r} = k_{f_r} \prod_{j=1}^{N_s} [j]^{\ \nu'_{jr}} - k_{b_r} \prod_{j=1}^{N_s} [j]^{\ \nu''_{jr}} \ . \tag{2.4.3}$$

Within the above equation, $[j]$ characterizes the concentration of the species j. The variables k_f and k_b denote the forward and backward reaction velocities of the reaction r, respectively. They can be computed using the Arrhenius function

$$k_i = A_i T^{\beta_i} \exp\left(-\frac{E_{a_i}}{\mathcal{R}T}\right) \quad \text{for} \ \ i = \{f, b\} \ , \tag{2.4.4}$$

where the A denotes the so-called pre-exponential factor, β the exponent of the temperature T, E_a the activation energy of the respective chemical reaction and $\mathcal{R}$ the universal gas constant. The Arrhenius parameters for the determination of the backward reaction velocities are often unknown for standard reaction mechanisms. Therefore, the backward reaction velocities are evaluated using the theory of chemical equilibrium. The equilibrium constant K_c is defined through the following equation [15, 66]:

$$K_c \equiv \frac{k_f}{k_b} = \left(\frac{p}{\mathcal{R}T}\right)^{\Delta\nu} \exp\left(\frac{\Delta G^0}{\mathcal{R}T}\right) \quad \text{with} \ \ \Delta\nu = \nu'' - \nu' \, . \tag{2.4.5}$$

The difference within the Gibbs free energy at standard conditions ΔG^0 is determined by the

following formula:

$$\Delta G^0 \equiv \sum_{i=1}^{N_s} \left(\nu_i'' - \nu_i'\right) \left[H_i^0\left(T\right) - TS_i^0\left(T\right)\right] \ . \tag{2.4.6}$$

H_i^0 and S_i^0 describe the enthalpy and entropy of the species i at standard conditions. The computation of the backward reaction velocities during runtime is computationally expensive. As a remedy to this, they are determined within a preprocessing step preceding the numerical simulation [15].

In this work, the combined EDM/FRC model is used in order to model the combustion phenomena occurring within the flow field of the swirled model combustor. The reaction rates of the EDM and FRC methods are computed a priori independently from each other. The combined EDM/FRC combustion model then takes the minimum value of both reaction rates in order to determine the reaction rate source term of the species conservation equations (2.2.4) [99, 218]:

$$\forall i \in \left\{1, \ldots, N_s - 1\right\}, \, S_{Y_i} = M_i \sum_{r=1}^{N_r} \left(\nu_{i_r}'' - \nu_{i_r}'\right) \cdot \min\left(\mathrm{rr}_{\mathrm{EDM}_r}, \mathrm{rr}_{\mathrm{FRC}_r}\right) \ . \tag{2.4.7}$$

Following this approach, the chemical production rate is either limited by the chemical kinetics of the reaction rates or the turbulent mixing time. However, the application of the combined EDM/FRC model is only reasonable when global irreversible reactions of the type

$$\forall i \in \left\{1, \ldots, N_s\right\}, \, \forall j \in \left\{1, \ldots, N_r\right\}, \, \sum_{i=1}^{N_s} \nu_{i_j}' A_i \rightarrow \sum_{i=1}^{N_s} \nu_{i_j}'' A_i \tag{2.4.8}$$

are considered. The hypothesis behind the EDM combustion model makes the use of elementary reactions meaningless. For this specific reason, the combined EDM/FRC model should not be used with more than four global irreversible reactions. Aside from this, it should be mentioned at this point that the FRC combustion model is based on laminar chemistry theory and does hence not account for turbulence-chemistry interaction phenomena [99]. The EDM combustion model is capable of displaying turbulence chemistry interactions in the case the hypothesis of infinitely fast chemistry proves to be true for the combustion problem considered.

3. Numerical Methods

3.1. Projection-Based Schemes - Basic Idea and Derivation

The momentum equations (2.2.2) couple the velocity vector to the pressure field. The velocity-pressure coupling becomes a key issue when reaching the incompressible limit. This is due to the fact that the pressure gradient term in the momentum equations scales with $1/\mathrm{Ma}^2$ as the momentum equations are transformed into their dimensionless form [13, 59, 65, 114, 163, 164, 177, 208, 244]. As the Mach number approaches the zero-limit, the pressure-density coupling evanesces. The thermodynamic and acoustic pressure parts then vanish, which reduces the pressure gradient term to the hydrodynamic pressure part [59, 208]. This may lead to numerical difficulties when solving the governing equations through the application of a density-based solution scheme, see section 1.2. A decoupling of the velocity and pressure fields can be achieved by applying a decomposition to the velocity field into an interim and a final solution leading to a fractional step method. This is the basic idea of projection-based schemes. The projection method has originally been introduced by Chorin [24, 25] and Temam [239] in the late 1960's for constant density flows. They perform a Helmholtz decomposition by which an arbitrary vector field $\underline{\Psi}$ is split up into a solenoidal and an irrotational part [78, 89]. In this work, a more generic form of Helmholtz's decomposition is developed: On a simply connected domain, an arbitrary vector field $\underline{\Psi}$ can be decomposed into a vector field with a so-called divergence-constraint $\underline{\Psi}_{\mathrm{dc}}$ and an irrotational vector field $\underline{\Psi}_{\mathrm{ir}}$:

$$\underline{\Psi} \equiv \underline{\Psi}_{\mathrm{dc}} + \underline{\Psi}_{\mathrm{ir}} \,. \tag{3.1.1}$$

Defining $\underline{\Psi}_{\mathrm{ir}}$ as an irrotational vector field on a simply connected domain, there is a scalar function $\phi = \phi\left(\underline{x}, t\right)$ such that $\underline{\Psi}_{\mathrm{ir}} = \nabla\phi$ and $\nabla \times \underline{\Psi}_{\mathrm{ir}} = \nabla \times (\nabla\phi) = 0$ holds for any t [26, 110]. Taking the divergence of equation (3.1.1) thus leads to the following equation:

$$\nabla \cdot \underline{\Psi} = \nabla \cdot \underline{\Psi}_{\mathrm{dc}} + \nabla \cdot \underline{\Psi}_{\mathrm{ir}} = \nabla \cdot \underline{\Psi}_{\mathrm{dc}} + \nabla \cdot (\nabla\phi) \,. \tag{3.1.2}$$

Equation (3.1.2) is solved for the scalar field ϕ leading to the derivation of the so-called correction equation:

$$\Delta_{\mathrm{L}}\phi \equiv \nabla \cdot (\nabla\phi) = \nabla \cdot \underline{\Psi} - \nabla \cdot \underline{\Psi}_{\mathrm{dc}} \,. \tag{3.1.3}$$

In the original derivation of the projection method for constant density flows, the vector field $\underline{\Psi}$ is set to an interim velocity vector, denoted by $\underline{u}^*$. $\underline{\Psi}_{\mathrm{dc}}$ is determined based on the final solution of the velocity. The scalar variable ϕ is set to the pressure, multiplied with a constant value. Thus, equation (3.1.3) is often referred to as *pressure correction equation*. In this context, equation (3.1.3) is henceforth called the *generic pressure correction equation*.

The interim velocity vector is obtained from a predictor step by solving the momentum equations and first ignoring the pressure gradient term. This formulation of the predictor step leads to the so-called non-incremental projection scheme. Incremental projection schemes add the pressure gradient term obtained from the last time step as an explicitly treated term to the momentum equations. In this case, ϕ is set to the pressure difference $\delta p^{n+1} \equiv p^{n+1} - p^n$, multiplied with a constant coefficient. The incremental projection method for constant density flows has been introduced by Goda [68] in 1979. The non-incremental and incremental methods both realize a decoupling of the velocity and pressure variables as part of the predictor step.

Following this approach, the Helmholtz decomposition projects the predicted velocity field onto the final solution of the velocity by taking into account the divergence constraint. By means of equation (3.1.3), the divergence constraint is included into the solution scheme. After performing the corrector step, the conservation equations are fulfilled. This is due to the fact that no additional approximation is applied to the governing equations. As a consequence of this, no further iterations need to be computed. This non-iterative property together with the decoupling of the velocity and pressure fields leads to computationally very efficient solution strategies for solving the time-dependent Navier-Stokes equations.

3.2. Incompressible Projection Method for Constant Density Flows

In case of an incompressible constant density flow, $\underline{\Psi}$ is set to the interim velocity field $\underline{u}^*$ and ϕ is set to the pressure difference $\delta p^{n+1} \equiv p^{n+1} - p^n$ multiplied with the constant coefficient $a \equiv (\alpha_{\mathrm{pr}}\rho)^{-1} f(\Delta t)$. Using the pressure difference instead of the absolute or relative pressure, small pressure differences can be resolved more accurately. The coefficient a includes a so-called projection weighting factor α_{pr}, which is introduced due to stability and accuracy reasons. The interim velocity vector is obtained from the predictor step by solving the momentum equations (2.2.2). The projection methods presented within this work refer to the

incremental formulation of projection-based schemes, as proposed by GODA [68]. Moreover, the derivation of the projection methods is performed by making use of the semi-discretized form of the equations in order to facilitate the understanding of the numerical schemes and to provide a description independent of the discretization scheme applied.

The predictor step of the incompressible projection method for constant density flows consists of solving the linearized momentum equations for an intermediate velocity:

$$\rho \left.\frac{\partial \underline{u}}{\partial t}\right|_{*} + \rho \nabla \cdot (\underline{u}^{n} \otimes \underline{u}^{*}) + \nabla p^{n} = \nabla \cdot \underline{\underline{\tau}}^{*} \quad \text{with } \nabla \cdot \underline{\underline{\tau}}^{*} \equiv \mu \left[\Delta_{\mathrm{L}} \underline{u}^{*} + \frac{1}{3} \nabla \left(\nabla \cdot \underline{u}^{n} \right) \right] . \quad (3.2.1)$$

To enable the solution of the equations by means of a linear solver, the convective term $\rho \nabla \cdot (\underline{u}^{n} \otimes \underline{u}^{*})$ has been linearized. There exit different ways to treat the diffusion term of the conservation equations: The first one consists of applying a fully implicit discretization. A second approach constitutes of discretizing the diffusive term fully explicitly. The fully implicit approach strengthens the stability of the solution process, but generally requires more computational time than the fully explicit methodology to compute one time step. As a third possibility, a hybrid approach wherein one part of the diffusive term is treated explicitly and the other part is discretized implicitly, can be adopted. This methodology refers to the so-called *deferred-correction approach* [54, 107, 165]. In terms of stability and computational efficiency - especially when dealing with moderately or even highly skewed grids cells - the deferred-correction approach constitutes the best way to discretize the diffusive terms [54]. This methodology has thus been incorporated into THETA. However, for simplicity reasons, the diffusion terms appearing within the equations are written in the fully implicit form.

A constant density flow demands the velocity divergence to be zero, thus leading to the divergence constraint for a constant density flow:

$$\nabla \cdot \underline{u}^{n+1} = 0 \Rightarrow \nabla \cdot \underline{\Psi}_{\mathrm{dc}} = 0 \, . \quad (3.2.2)$$

Knowing this, the dissipation tensor $\underline{\underline{\tau}}^{*}$ is reduced to $\mu \Delta_{\mathrm{L}} \underline{u}^{*}$, thus giving a shorter form of the momentum equations equation (3.2.1). Based on the generic correction equation (3.1.3), the pressure correction equation for constant density flows can be formulated:

$$\Delta_{\mathrm{L}} \delta p^{n+1} = \frac{\alpha_{\mathrm{pr}} \rho}{f\left(\Delta t\right)} \nabla \cdot \underline{u}^{*} \, . \quad (3.2.3)$$

Equation (3.2.3) has the form of Poisson's equation

$$\Delta_{\mathrm{L}} \delta p = b \quad (3.2.4)$$

and is solved for the pressure difference δp^{n+1}. δp^{n+1} acts as a correction of the pressure field and is also often referred to as *pressure correction*. In a final step of the solution strategy, the velocity vector can be corrected using the previously computed pressure difference:

$$\underline{u}^{n+1} = \underline{u}^{*} - \frac{f\,(\Delta t)}{\alpha_{\mathrm{pr}}\rho}\nabla\delta p^{n+1}\,. \tag{3.2.5}$$

f denotes a function dependent on the time step size Δt and of the discretization scheme used for the discretization of the velocity time derivative. This discretization scheme has to be consistent to the one used in the momentum equations (3.2.1) to compute the interim velocity vector. For instance, if a first-order accurate implicit or explicit Euler scheme is used for the temporal discretization of the equations (3.2.1), the function f equals the time step size Δt. If the second-order accurate three points backward scheme is used instead, f amounts to $2/3\,\Delta t$. By setting α_{pr} to 1, using the absolute pressure as opposed to the pressure difference and removing the pressure gradient term of the old time step in the momentum equations (3.2.1), the original non-incremental projection method of Chorin and Temam is obtained. Due to the spatial and temporal constancy of the density, the temperature cannot vary in space and time. As a consequence of this, the energy conservation equation becomes redundant and is thus not needed within the solution strategy for constant density flows.

A SIMPLE-type solution algorithm solves a predictor step for the velocity field and derives a pressure correction equation. Solving the momentum equations as predictor step results in a remaining mass source, so that the computed interim velocity field does not conserve mass. As a subsequent step, a correction equation is solved for the pressure. Using the corrected pressure, a correction of the velocity is performed [181, 182]. The corrected velocity field satisfies mass conservation, but not the momentum balance equations. An iterative solution of the pressure correction equation is hence necessary in order to reach the fulfillment of the mass and momentum conservation equations. Opposed here to, projection-type methods solve a predictor step, by which the predicted velocity field is projected onto a final velocity under the enforcement of a divergence constraint. By accounting for the divergence constraint - which constitutes in the case of a constant density flow a zero value of the velocity divergence - the latter approach does satisfy the momentum balance right away and does hence not require an iterative treatment of the pressure correction equation. In the following, a summary of the steps performed within the incompressible constant density projection method is given:

1. Describing the predictor step, the momentum equations for a variable density flow at the interim time step $*$ are solved for an interim solution of the velocity field:

$$\rho\,\frac{\partial \underline{u}}{\partial t}\bigg|_{*} + \rho\,\nabla\cdot(\underline{u}^{n}\otimes\underline{u}^{*}) + \nabla p^{n} = \nabla\cdot\underline{\underline{\tau}}^{*} \quad \text{with } \nabla\cdot\underline{\underline{\tau}}^{*} \equiv \mu\Delta_{\mathrm{L}}\underline{u}^{*}\,.$$

2. A Poisson-type equation is next solved for the pressure correction $\delta p^{n+1} = p^{n+1} - p^n$:

$$\Delta_{\mathrm{L}} \delta p^{n+1} = \frac{\alpha_{\mathrm{pr}} \rho}{f\left(\Delta t\right)} \nabla \cdot \underline{u}^* \,.$$

3. This leads to the correction of the pressure field:

$$p^{n+1} = p^n + \delta p^{n+1} \,.$$

4. By means of the calculated pressure correction δp^{n+1}, the correction of the velocity field is performed in a final step:

$$\underline{u}^{n+1} = \underline{u}^* - \frac{f\left(\Delta t\right)}{\alpha_{\mathrm{pr}} \rho} \nabla \delta p^{n+1} \,.$$

Thus, the pressure correction equation provides a pressure correction δp^{n+1}, by which the predicted velocity $\underline{u}^*$ field is projected onto a divergence-free velocity field. This final solution of the velocity ensures the fulfillment of the momentum equations.

3.3. Incompressible Projection Method for Variable Density Flows

In addition to the properties mentioned in section 2.1, an incompressible variable density flow is characterized by a density which can vary with the temperature and mixture changes, but not with pressure variations, i.e. $\rho = \rho\left(R, T\right) \neq \rho\left(p\right)$. Since the flow is incompressible, the density is independent of any pressure variations. Regarding the numerical solution of incompressible flows, choosing the pressure over the density as leading variable is the more favorable choice. This results in pressure-based numerical schemes. Instead of calculating the density from the continuity equation, an equation of state is applied.

Within this work, the fluid is modeled as a chemically reactive ideal gas mixture of N_s components. Its equation of state, relating the density ρ to the pressure p, the specific gas constant R and the temperature T is given through equation (2.2.5). Taking into account that for incompressible flows the density does not depend on the pressure variations, the equation of state reduces to the following form:

$$\rho = \frac{p_{\mathrm{ref}}}{RT} \quad \text{with } R \equiv \mathcal{R} \sum_{i=1}^{N_s} \frac{Y_i}{M_i} \,. \tag{3.3.1}$$

Projection-based solution strategies for solving the equations for an incompressible variable

density flow have been proposed by GUERMOND et al. [76, 77] and by BELL and MARKUS [12]. GUERMOND et al. interpret the pressure correction equation as a penalty method, by which a parameter χ is introduced as a penalty factor. Additionally, an equation based on the conservation of mass to model the variations of the density is solved. BELL and MARKUS [12] add a convection equation of the density to the incompressible projection method to calculate the transport of the density field. Aside from these approaches, it is possible to derive a solution strategy for solving the system of equations of an incompressible variable density flow based on the Helmholtz decomposition explained in subsection 3.1. This approach is derived in the following and can be understood as an extension of von CHORIN and TEMAM's original incompressible projection method for constant density to variable density flows.

The vector field $\underline{\Psi}$ is set to the interim solution of the momentum $(\rho\underline{u})^*$. ϕ is defined as the product of the pressure correction δp^{n+1} and a constant coefficient $a \equiv \alpha_{\mathrm{pr}}^{-1} f\,(\Delta t)$.

The predictor step can be formulated analogously to the one derived for an incompressible constant density flow. However, the density changes from a constant value to a function dependent on the temperature and gas mixture. The linearized momentum equations for a variable density flow at the interim time step $*$ thus read:

$$\left.\frac{\partial\,(\rho\underline{u})}{\partial t}\right|_{*} + \nabla\cdot\left[(\rho\underline{u})^n\otimes\underline{u}^*\right] + \nabla p^n = \nabla\cdot\underline{\underline{\tau}}^* \quad \text{with } \nabla\cdot\underline{\underline{\tau}}^* \equiv \mu\left[\Delta_{\mathrm{L}}\underline{u}^* + \frac{1}{3}\nabla\left(\nabla\cdot\underline{u}^n\right)\right]. \tag{3.3.2}$$

The velocity divergence included in the calculation of the dissipation term at the right hand side of equation (3.3.2) is approximated by assuming a zero divergence of the mass flux:

$$\nabla\cdot(\rho\underline{u})^n \approx 0 \Rightarrow \nabla\cdot\underline{u}^n = -\frac{1}{\rho^n}\,\underline{u}^n\cdot\nabla\rho^n\,. \tag{3.3.3}$$

In a next step, the density is updated based on the equation of state:

$$\rho^{n+1} = \frac{p_{\mathrm{ref}}}{(RT)^n}\,. \tag{3.3.4}$$

Recasting the continuity equation (2.2.1) for the divergence of the momentum yields:

$$\nabla\cdot(\rho\underline{u})^{n+1} = -\left.\frac{\partial\rho}{\partial t}\right|_{n+1}. \tag{3.3.5}$$

Since $\underline{\Psi}_{\mathrm{dc}}$ is set to the divergence of the momentum, equation (3.3.5) leads to the definition of the divergence constraint for incompressible variable density flows:

$$\nabla\cdot(\rho\underline{u})^{n+1} = -\left.\frac{\partial\rho}{\partial t}\right|_{n+1} \Rightarrow \nabla\cdot\underline{\Psi}_{\mathrm{dc}} = -\left.\frac{\partial\rho}{\partial t}\right|_{n+1}. \tag{3.3.6}$$

The pressure correction equation for an incompressible variable density flow is obtained by introducing $\phi \equiv \alpha_{\mathrm{pr}}^{-1} f\left(\Delta t\right) \delta p^{n+1}$, $\underline{\Psi} \equiv \left(\rho \underline{u}\right)^{*} = \rho^{n} \underline{u}^{*}$ and the divergence constraint (3.3.6) into the generic correction equation (3.1.3):

$$\Delta_{\mathrm{L}} \delta p^{n+1} = \frac{\alpha_{\mathrm{pr}}}{f\left(\Delta t\right)} \left[\nabla \cdot \left(\rho^{n} \underline{u}^{*}\right) + \left. \frac{\partial \rho}{\partial t} \right|_{n+1} \right] . \tag{3.3.7}$$

Since for incompressible flows the density is not a function of the pressure, the right hand side of equation (3.3.7) is independent of the pressure and can be seen as an explicit source term. Equation (3.3.7) has thus the form of Poisson's equation (3.2.4). Using the equation of state (3.3.4) and applying the first-order accurate Euler time discretization scheme, the time derivative of the density can be written as a difference between two fractions:

$$\left. \frac{\partial \rho}{\partial t} \right|_{n+1} = p_{\mathrm{ref}} \left. \frac{\partial \left(\frac{1}{RT}\right)}{\partial t} \right|_{n+1} \approx \frac{p_{\mathrm{ref}}}{\Delta t} \left[\left. \frac{1}{\left(RT\right)} \right|_{n} - \left. \frac{1}{\left(RT\right)} \right|_{n-1} \right] . \tag{3.3.8}$$

Knowing the pressure correction δp^{n+1}, the velocity field can eventually be corrected:

$$\underline{u}^{n+1} = \underline{u}^{*} - \frac{f\left(\Delta t\right)}{\alpha_{\mathrm{pr}} \rho^{n}} \nabla \delta p^{n+1} . \tag{3.3.9}$$

In order for temperature changes or changes within the mixture composition to be considered, the enthalpy equation is solved. Hereby, the properties for an incompressible flow mentioned in section 2.1 are accounted for. This results in the following equation:

$$\left. \frac{\partial \left(\rho h\right)}{\partial t} \right|_{n+1} + \nabla \cdot \left[\left(\rho \underline{u}\right)^{n+1} h^{n+1} \right] = -\nabla \cdot \underline{q}^{n+1} . \tag{3.3.10}$$

Modeling the transport and mixing of species, $N_s - 1$ species transport equations

$$\left. \frac{\partial \left(\rho \underline{Y}\right)}{\partial t} \right|_{n+1} + \nabla \cdot \left[\left(\rho \underline{u}\right)^{n+1} \otimes \underline{Y}^{n+1} \right] = -\nabla \cdot \underline{\underline{j}}^{n+1} + \underline{S}_{Y}^{n+1} \tag{3.3.11}$$

are solved. By using Dalton's law

$$\sum_{i=1}^{N_s} Y_i^{n+1} = 1 \Rightarrow Y_{N_s}^{n+1} = 1 - \sum_{i=1}^{N_s - 1} Y_i^{n+1} \tag{3.3.12}$$

the mass fraction of the last species can be computed. Combustion phenomena can thus be added to the projection solution algorithm. A summary of the steps performed within the incompressible projection methods for variable density flows is given in the following:

1. In a first step, the velocity divergence is obtained from a zero divergence of the mass flux:
$$\nabla \cdot \underline{u}^n = -\frac{1}{\rho^n}\,\underline{u}^n \cdot \nabla \rho^n$$
and the momentum equations are solved for the predicted velocity field $\underline{u}^*$:
$$\left.\frac{\partial\left(\rho\underline{u}\right)}{\partial t}\right|_* + \nabla \cdot \left[\left(\rho\underline{u}\right)^n \otimes \underline{u}^*\right] + \nabla p^n = \nabla \cdot \underline{\underline{\tau}}^n \quad \text{with} \quad \nabla \cdot \underline{\underline{\tau}}^n \equiv \mu\left[\Delta_L \underline{u}^n + \frac{1}{3}\nabla\left(\nabla \cdot \underline{u}^n\right)\right].$$

2. In a next step, the density is updated based on the equation of state:
$$\rho^{n+1} = \frac{p_{\text{ref}}}{\left(RT\right)^n}.$$

3. The pressure correction equation can now be formulated and solved for $\delta p^{n+1} = p^{n+1} - p^n$:
$$\Delta_{\text{L}}\delta p^{n+1} = \frac{\alpha_{\text{pr}}}{f\left(\Delta t\right)}\left\{\nabla \cdot \left(\rho^n \underline{u}^*\right) + \frac{p_{\text{ref}}}{\Delta t}\left[\left.\frac{1}{\left(RT\right)}\right|_n - \left.\frac{1}{\left(RT\right)}\right|_{n-1}\right]\right\}.$$

4. After the pressure correction δp^{n+1} is obtained, the pressure p^{n+1} is determined:
$$p^{n+1} = p^n + \delta p^{n+1}.$$

5. By using the newly obtained pressure correction, the velocity field can eventually be corrected:
$$\underline{u}^{n+1} = \underline{u}^* - \frac{f\left(\Delta t\right)}{\alpha_{\text{pr}}\rho^n}\nabla \delta p^{n+1}.$$

6. Modeling the transport and mixing of species, the enthalpy equation and $N_s - 1$ species transport equations are solved additionally:
$$\begin{aligned}
\left.\frac{\partial\left(\rho h\right)}{\partial t}\right|_{n+1} + \nabla \cdot \left[\left(\rho\underline{u}\right)^{n+1} h^{n+1}\right] &= -\nabla \cdot \underline{q}^{n+1}, \\
\left.\frac{\partial\left(\rho\underline{Y}\right)}{\partial t}\right|_{n+1} + \nabla \cdot \left[\left(\rho\underline{u}\right)^{n+1} \otimes \underline{Y}^{n+1}\right] &= -\nabla \cdot \underline{\underline{j}}^{n+1} + \underline{S}_Y^{n+1}.
\end{aligned}$$

7. The mass fraction of the last species is considered as dependent variable and is obtained from Dalton's law:
$$\sum_{i=1}^{N_s} Y_i^{n+1} = 1 \Rightarrow Y_{N_s}^{n+1} = 1 - \sum_{i=1}^{N_s-1} Y_i^{n+1}.$$

3.4. Compressible Projection Method

3.4.1. Derivation of the Compressible Projection Method

The non-iterative property of projection-based schemes allows them to be computationally very efficient when performing unsteady computations of the flow field. Since the incompressible projection method for variable density flows does not consider any compressibility effects, the density can only vary with temperature and mixture changes. In order to enable the computation of compressible flows and thus of thermo-acoustic interactions, the following changes to the incompressible projection scheme need to be done:

- Introduce the temporal and spatial variations of the pressure and the dissipation term into the enthalpy equation (3.3.10).
- Define a relation between the density and the pressure.
- Alter the solution algorithm in order to design a *consistent* solver.

The first two points describe the implementation of additional terms into the enthalpy equation and the connection between the density and pressure, respectively. The third point deals with a more complicated issue. In order to design a *consistent* solver, the following three conditions have to be fulfilled:

- The number of equations to be solved has to be equal to the number of unknowns.
- By deriving the equations, it has to be assured that no redundant equation is used.
- The equations have to be solved such that that mass, momentum, energy and species mass fractions are conserved.

Hereby, the fulfillment of the mass, momentum, energy and species mass fractions balances is of essential importance. For instance, occurring mass sources or sinks within one or several grid cells of the computational grid consitute a non-physical behavior of the flow field and lead to a erroneous numerical solution.

By accounting for the conditions described above, an entirely new solver for compressible flow phenomena is derived, verified and validated by means of several well-defined test cases within the frame of the present work. The solution strategy of the compressible projection method is derived following: Firstly, the predictor step is defined. This is done by deriving an equation for the calculation of the intermediate velocity field. The divergence constraint for compressible reactive flows is defined next in order to derive a pressure correction equation. According to section 3.1 and the properties of compressible flows, The vector field $\underline{\Psi}$ is set to

an intermediate momentum field $(\rho\underline{u})^* = \rho^n\underline{u}^*$. The scalar variable ϕ is chosen to be equal to the product of the pressure correction δp^{n+1} with a constant multiplier $a \equiv \alpha_{\mathrm{pr}}^{-1} f\,(\Delta t)$.

The pressure equation (energy equation in primitive variables formulated for the pressure) will constitute the basis for the incorporation of the divergence constraint into the compressible solution algorithm. The derivation of the divergence constraint - which has been related to the velocity divergence in the paragraph above - from the pressure equation (3.4.1) has been found to work more stable than deducing $\underline{\Psi}_{\mathrm{dc}}$ from the continuity equation (2.2.1), as is it done for the incompressible projection method for variable density flows (cf. section 3.3). This relation will be elucidated in more detail within section 3.4.2. The pressure equation reads:

$$\frac{\partial p}{\partial t} + \underline{u}\cdot\nabla p + \gamma p \nabla\cdot\underline{u} = (\gamma-1)\left(S_{\mathrm{m\&c}} - \nabla\cdot\underline{q} + \underline{\underline{\tau}} : \nabla\underline{u}\right) \tag{3.4.1}$$

with the mixing and combustion source term

$$S_{\mathrm{m\&c}} \equiv \sum_{i=1}^{N_s}\left(\frac{\gamma}{\gamma-1}\frac{p_{\mathrm{ref}}+p}{\rho Y_i} - h_i\right)\left(S_{Y_i} - \nabla\cdot\underline{j}_i\right). \tag{3.4.2}$$

The pressure equation (3.4.1) can be derived based on the enthalpy conservation equation (2.2.3), see appendix B.1. $S_{\mathrm{m\&c}}$ accounts for the influence of mixing processes and combustion on the pressure. Within most combustion test cases, the flow is characterized as being turbulent. As a consequence of this, the following simplification is performed: For turbulent flows, differential species diffusion can be neglected so that the heat flux vector $\underline{q}$ and the diffusion flux tensor $\underline{\underline{j}}$ can be reduced to the following expressions, see sections 2.2.1 and 2.2.2:

$$\underline{q} = -\frac{\mu}{\mathrm{Pr}}\nabla h \quad \text{and} \quad \underline{j}_i = -\left(\frac{\mu_l}{\mathrm{Sc}_l} + \frac{\mu_t}{\mathrm{Sc}_t}\right)\nabla Y_i\,. \tag{3.4.3}$$

The dissipation term $\underline{\underline{\tau}} : \nabla\underline{u}$ is given by the following equation:

$$\begin{aligned}
\underline{\underline{\tau}} : \nabla\underline{u} &= \mu\left[\nabla\underline{u} + (\nabla\underline{u})^T - \frac{2}{3}(\nabla\cdot\underline{u})\,\underline{\underline{I}}\right] : \nabla\underline{u} \\
&= \mu\left[\frac{4}{3}(\nabla\cdot\underline{u})^2 + \frac{4}{3}\left(\frac{\partial u_1}{\partial x_1}\frac{\partial u_2}{\partial x_2} + \frac{\partial u_1}{\partial x_1}\frac{\partial u_3}{\partial x_3} + \frac{\partial u_2}{\partial x_2}\frac{\partial u_3}{\partial x_3}\right)\right. \\
&\quad \left. + \left(\frac{\partial u_1}{\partial x_2}\frac{\partial u_2}{\partial x_1}\right)^2 + \left(\frac{\partial u_1}{\partial x_3}\frac{\partial u_3}{\partial x_1}\right)^2 + \left(\frac{\partial u_2}{\partial x_3}\frac{\partial u_3}{\partial x_2}\right)^2\right].
\end{aligned} \tag{3.4.4}$$

By recasting equation (3.4.1), a constraint for the divergence of the velocity field

$$\nabla\cdot\underline{u} = \frac{1}{\gamma\,(p_{\mathrm{ref}}+p)}\left[(\gamma-1)\left(S_{\mathrm{m\&c}} - \nabla\cdot\underline{q} + \underline{\underline{\tau}} : \nabla\underline{u}\right) - \frac{\partial p}{\partial t} - \underline{u}\cdot\nabla p\right] \tag{3.4.5}$$

can be formulated. The interim velocity field being part of the predictor step is calculated using a linearized form of the momentum equations:

$$\left.\frac{\partial\left(\rho\underline{u}\right)}{\partial t}\right|_{*} + \nabla\cdot\left[\left(\rho\underline{u}\right)^{n}\otimes\underline{u}^{*}\right] + \nabla p^{n} = \nabla\cdot\underline{\underline{\tau}}^{*} \quad \text{with } \nabla\cdot\underline{\underline{\tau}}^{*} \equiv \mu\left[\Delta_{\mathrm{L}}\underline{u}^{*} + \frac{1}{3}\nabla\left(\nabla\cdot\underline{u}^{n}\right)\right] . \quad (3.4.6)$$

Compared to the incompressible projection method for variable density flows, the form of the momentum equations remains unchanged. The velocity divergence on the right hand side of equation (3.4.6) is however calculated differently. It is obtained by formulating the previously derived velocity divergence constraint (3.4.5) at the time step n:

$$\nabla\cdot\underline{u}^{n} = \frac{1}{\gamma^{n}\left(p_{\mathrm{ref}}+p^{n}\right)}\left[\left(\gamma^{n}-1\right)\left(S^{n}_{\mathrm{m\&c}} - \nabla\cdot\underline{q}^{n} + \underline{\underline{\tau}}^{n} : \nabla\underline{u}^{n}\right) - \left.\frac{\partial p}{\partial t}\right|_{n} - \underline{u}^{n}\cdot\nabla p^{n}\right] . \quad (3.4.7)$$

The pressure derivative with respect to time appearing on the right hand side of the above equation is discretized using the second-order accurate three points backward scheme. Recasting equation (3.4.1) for the velocity divergence at the new time step $n+1$, treating the time derivative of the pressure implicitly, introducing the interim velocity field and setting the remaining variables to the known solutions form the old time step results in the following equation:

$$\nabla\cdot\underline{u}^{n+1} = \frac{1}{\gamma^{n}\left(p_{\mathrm{ref}}+p^{n}\right)}\left[\left(\gamma^{n}-1\right)\left(S^{n}_{\mathrm{m\&c}} - \nabla\cdot\underline{q}^{n} + \underline{\underline{\tau}}^{*} : \nabla\underline{u}^{*}\right) - \left.\frac{\partial p}{\partial t}\right|_{n+1} - \underline{u}^{*}\cdot\nabla p^{n}\right] . \quad (3.4.8)$$

Since the vector field $\underline{\Psi}$ is defined as $\left(\rho\underline{u}\right)^{*} = \rho^{n}\underline{u}^{*}$, the divergence constraint $\nabla\cdot\underline{\Psi}_{\mathrm{dc}}$ equals $\nabla\cdot\left(\rho\underline{u}\right)^{n+1}$. Applying the product rule to $\nabla\cdot\left(\rho\underline{u}\right)^{n+1}$ yields the following decomposition:

$$\nabla\cdot\left(\rho\underline{u}\right)^{n+1} = \rho^{n+1}\nabla\cdot\underline{u}^{n+1} + \underline{u}^{n+1}\cdot\nabla\rho^{n+1} . \quad (3.4.9)$$

As the density at the new time step $n+1$ is not yet known, the known density field of the old time step ρ^{n} is used instead for the computation of the divergence constraint. Aside from the density, the convective part of above equation is also replaced by the known values of the intermediate and old time steps. This results in the following equation for the divergence constraint $\nabla\cdot\underline{\Psi}_{\mathrm{dc}}$:

$$\nabla\cdot\underline{\Psi}_{\mathrm{dc}} = \rho^{n}\nabla\cdot\underline{u}^{n+1} + \underline{u}^{*}\cdot\nabla\rho^{n} . \quad (3.4.10)$$

Inserting equation (3.4.8) into the formula (3.4.10) yields:

$$\nabla\cdot\underline{\Psi}_{\mathrm{dc}} = \frac{\rho^{n}}{\gamma^{n}\left(p_{\mathrm{ref}}+p^{n}\right)}\left[\left(\gamma^{n}-1\right)\left(S^{n}_{\mathrm{m\&c}} - \nabla\cdot\underline{q}^{n} + \underline{\underline{\tau}}^{*} : \nabla\underline{u}^{*}\right) - \left.\frac{\partial p}{\partial t}\right|_{n+1} - \underline{u}^{*}\cdot\nabla p^{n}\right] . \quad (3.4.11)$$

Equation (3.4.11) describes the divergence constraint of the compressible projection method. Note that the convective transport of the density $\underline{u}^* \cdot \nabla \rho^n$ inserted by equation (3.4.9) into the divergence constraint (3.4.11) is already covered by the convective transport of the pressure $\underline{u}^* \cdot \nabla p^n$. This is demonstrated in the following:

The convection of the pressure on the right hand side of the divergence constraint (3.4.11) originates from the energy conservation equation. In case of the compressible projection method, it is introduced into the pressure correction equation (3.4.16). For compressible flows, the pressure is a function of the density, so that, by looking at the total derivative of the pressure for a multi-component flow composed of N_s species

$$\frac{\partial p}{\partial t} = \left.\frac{\partial p}{\partial \rho}\right|_{T,Y_i} \frac{\partial \rho}{\partial t} + \left.\frac{\partial p}{\partial T}\right|_{\rho,Y_i} \frac{\partial T}{\partial t} + \sum_{i=1}^{N_s} \left.\frac{\partial p}{\partial Y_i}\right|_{\rho,T,Y_{j,j\neq i}} \frac{\partial Y_i}{\partial t}\,, \tag{3.4.12}$$

the derivative of the density is introduced through the first term on the right hand side. This dependency leads to the result in which the convective transport of the density is already included in the convective transport of the pressure. This is proven by recasting the divergence constraint (3.4.5) so that it is directly linked to the material derivative of the density:

$$\nabla \cdot \underline{u} = -\frac{1}{\rho}\left(\frac{\partial \rho}{\partial t} + \underline{u} \cdot \nabla \rho\right)\,. \tag{3.4.13}$$

Appendix B.2 provides the detailed deduction of equation (3.4.13) from equation (3.4.5). The introduction of $\underline{u} \cdot \nabla \rho$ through equation (3.4.10) into the divergence constraint (3.4.11) would thus lead to the dissatisfaction of mass conservation. As a result of this, the convective transport of the density does not need to be inserted separately.

Inserting $\underline{\Psi} \equiv (\rho \underline{u})^* = \rho^n \underline{u}^*$, $\phi \equiv \alpha_{\mathrm{pr}}^{-1} f\left(\Delta t\right) \delta p^{n+1}$ and equation (3.4.11) into the generic correction equation (3.1.3) leads to the following equation:

$$\begin{aligned}\Delta_L \delta p^{n+1} - \frac{\alpha_{\mathrm{pr}}}{f\left(\Delta t\right)} \left(c^n\right)^{-2} \left.\frac{\partial p}{\partial t}\right|_{n+1} = \frac{\alpha_{\mathrm{pr}}}{f\left(\Delta t\right)} \Big[&\nabla \cdot \left(\rho^n \underline{u}^*\right) + \left(c^n\right)^{-2} \underline{u}^* \cdot \nabla p^n \\ &- \left(\gamma^n - 1\right)\left(S_{\mathrm{m\&c}} - \nabla \cdot \underline{q}^n + \underline{\underline{\tau}}^* : \nabla \underline{u}^*\right)\Big]\end{aligned} \tag{3.4.14}$$

with the inverse of the squared speed of sound

$$\left(c^n\right)^{-2} = \frac{\rho^n}{\gamma^n \left(p_{\mathrm{ref}} + p^n\right)}\,. \tag{3.4.15}$$

The time derivative term of the pressure is approximated with an Euler backward time discretization scheme, leading to the pressure correction equation for compressible reactive

flows:

$$\Delta_L \delta p^{n+1} - \frac{\alpha_{\mathrm{pr}}}{f\left(\Delta t\right)\Delta t}\left(c^n\right)^{-2}\delta p^{n+1} = \frac{\alpha_{\mathrm{pr}}}{f\left(\Delta t\right)}\left[\nabla\cdot\left(\rho^n\underline{u}^*\right) + \left(c^n\right)^{-2}\underline{u}^*\cdot\nabla p^n \right. \\ \left. - \left(\gamma^n - 1\right)\left(S_{\mathrm{m\&c}} - \nabla\cdot\underline{q}^n + \underline{\underline{\tau}}^* : \nabla\underline{u}^*\right)\right] . \tag{3.4.16}$$

It is important to emphasize at this point that the pressure correction equation for compressible flows (3.4.16) has the form of the Helmholtz equation:

$$\Delta_{\mathrm{L}}\delta p + d\cdot\delta p = b\,. \tag{3.4.17}$$

Compared to Poisson's equation, an additional term $d\cdot\delta p$ is introduced into the left hand side. Figuring as part of the corrector step, the velocity field can now be corrected based on the calculated pressure correction δp^{n+1}:

$$\underline{u}^{n+1} = \frac{\rho^n}{\rho^{n+1}}\underline{u}^* - \frac{f\left(\Delta t\right)}{\alpha_{\mathrm{pr}}\rho^{n+1}}\nabla\delta p^{n+1}\,. \tag{3.4.18}$$

The density from the new time step ρ^{n+1} is not yet known. As a remedy to this issue, ρ^{n+1} can be replaced by the known density from the last time step ρ^n. Applying this approximation to the momentum time derivative

$$\left.\frac{\partial\left(\rho\underline{u}\right)}{\partial t}\right|_{n+1} f\left(\Delta t\right) \approx \frac{\rho^{n+1}\underline{u}^{n+1} - \rho^n\underline{u}^*}{f\left(\Delta t\right)} f\left(\Delta t\right) \begin{aligned} &= \rho^{n+1}\underline{u}^{n+1} - \rho^n\underline{u}^* \\ &\approx \rho^n\underline{u}^{n+1} - \rho^n\underline{u}^* \\ &= \rho^n\left(\underline{u}^{n+1} - \underline{u}^*\right) \end{aligned} \tag{3.4.19}$$

has proven not to have any significant influence on the solution of the velocity field. Moreover, approximation (3.4.19) leads to an improvement of the stability of the compressible projection method. As a consequence of this, equation (3.4.18) is rewritten to give the velocity correction equation:

$$\underline{u}^{n+1} = \underline{u}^* - \frac{f\left(\Delta t\right)}{\alpha_{\mathrm{pr}}\rho^n}\nabla\delta p^{n+1}\,. \tag{3.4.20}$$

The pressure values of the new time step $n+1$ are updated by the aid of equation (3.4.21):

$$p^{n+1} = p^n + \delta p^{n+1}\,. \tag{3.4.21}$$

The density field needs to be updated next. Opposed to incompressible flows, occurring pressure fluctuations due to compressible flow phenomena affect the density field. This

influence is accounted for by performing a splitting of the static pressure P into a constant part p_{ref} and a fluctuating part p and by relating P to the density via the equation of state:

$$\rho^{n+1} = \frac{P^{n+1}}{(RT)^n} \quad \text{with} \quad P^{n+1} = p_{\text{ref}} + p^{n+1} \,. \tag{3.4.22}$$

The velocity divergence $\nabla \cdot \underline{u}$ is formulated and solved at the new time step $n+1$:

$$\begin{aligned} \nabla \cdot \underline{u}^{n+1} = \frac{1}{\gamma^n \left(p_{\text{ref}} + p^{n+1}\right)} \Bigg[& \left(\gamma^n - 1\right) \left(S_{\text{m\&c}} - \nabla \cdot \underline{q} + \underline{\underline{\tau}}^{n+1} : \nabla \underline{u}^{n+1} \right) \\ & - \left. \frac{\partial p}{\partial t} \right|_{n+1} - \underline{u}^{n+1} \cdot \nabla p^{n+1} \Bigg] \,. \end{aligned} \tag{3.4.23}$$

In order to remain consistent with the discretization scheme applied to formula (3.4.7), the pressure time derivative $\partial p / \partial t|_{n+1}$ is discretized using the second-order accurate three points backward scheme (TPB). All spatial gradients occurring within the equations are discretized using the central difference scheme (CDS), which is of second order accuracy.

The numerical computation of a compressible flow requires the energy equation to be included in the solution process. As multi-component flows with mixing or mixing and combustion constitute one major target application case on a long-term basis of this work, the conservation equation for the sensible chemical enthalpy h is chosen:

$$\left. \frac{\partial \left(\rho h\right)}{\partial t} \right|_{n+1} + \nabla \cdot \left[\left(\rho \underline{u}\right)^{n+1} h^{n+1} \right] - \left. \frac{\partial p}{\partial t} \right|_{n+1} - \underline{u}^{n+1} \cdot \nabla p^{n+1} = -\nabla \cdot \underline{q}^{n+1} + \underline{\underline{\tau}}^{n+1} : \nabla \underline{u}^{n+1} \,. \tag{3.4.24}$$

The assessment of multi-component flows requires the solution of $N_s - 1$ conservation equations for the species mass fractions

$$\left. \frac{\partial \left(\rho \underline{Y}\right)}{\partial t} \right|_{n+1} + \nabla \cdot \left[\left(\rho \underline{u}\right)^{n+1} \otimes \underline{Y}^{n+1} \right] = -\nabla \cdot \underline{\underline{j}}^{n+1} + \underline{S}_Y^{n+1} \tag{3.4.25}$$

in addition to the energy equation. The mass fraction of the last species is computed as dependent variable by using Dalton's law:

$$\sum_{i=1}^{N_s} Y_i^{n+1} = 1 \Rightarrow Y_{N_s}^{n+1} = 1 - \sum_{i=1}^{N_s - 1} Y_i^{n+1} \,. \tag{3.4.26}$$

Knowing the enthalpy and species mass fractions, the temperature field T is then obtained from solving

$$h = \sum_{i=1}^{N_s} Y_i \left[h_{f_i}^0 + \int_{T_0}^{T} c_{p_i} \left(\tilde{T} \right) d\tilde{T} \right] \tag{3.4.27}$$

iteratively, since the specific heat at constant pressure is a non-linear function of T.

As opposed to the conservation equation formulated for the chemical enthalpy or the temperature evolution equation, the conservation equation for the sensible chemical enthalpy (3.4.24) does not require the direct knowledge of the standard formation enthalpies $h^0_{f_i}$, $i \in \{1, 2, \ldots, N_s\}$, cf. references [190, 193]. This is due to the fact that the standard formation enthalpy of the transported species are already included in the definition of the sensible chemical enthalpy, see equation (3.4.24). The choice if solving for the sensible chemical enthalpy h constitutes a significant advantage, since by using the NASA polynomials [19, 20, 144], the temperature can directly be computed from the sensible chemical enthalpy (3.4.27). If turbulent flows are addressed to, additional transport equations are added to the compressible projection method which are then solved for the turbulent quantities ψ.

Generally speaking, pressure decomposition methods conduct a split-up of the pressure field P into N parts $p^{(i)}$, $i = \{0, 1, \ldots, N-1\}$:

$$P = \sum_{i=0}^{N-1} a_i \, p^{(i)} \, . \tag{3.4.28}$$

The pressure parts $p^{(i)}$ are each for themselves weighted with a coefficient a_i. The split-up of the pressure P expressed by equation (3.4.28) can hence be seen as a linear combination of the pressure parts $p^{(i)}$. For a more detailed insight into pressure decomposition techniques, the reader is referred to the introduction of this thesis. Performing a splitting of the pressure into a constant part p_{ref} and a fluctuating part p

$$P = p_{\text{ref}} + p \, , \tag{3.4.29}$$

the compressible projection solution strategy belongs to the family of pressure decomposition methods which are part of two-way CFD-CAA coupling methods. Since the reference pressure p_{ref} remains constant at all time, the fluctuating pressure part p is responsible for coupling thermodynamic to acoustic phenomena.

The velocity divergence (3.4.5) used in the derivation of the pressure correction equation (3.4.16) can be casted into the mass conservation equation formulated for $\nabla \cdot \underline{u}$, see appendix B.2 for details. So by satisfying the pressure correction equation, conservation of mass is fulfilled. The projection of the predicted velocity vector onto the final velocity field by accounting for the divergence constraint guarantees the satisfaction of the momentum equations. By fulfilling mass conservation prior to solving the conservation equation of $\rho\phi$, $\phi = \{h, Y_1, Y_2, \ldots, Y_{N_s-1}, \psi\}$, the scalar field $\rho\phi$ is also conserved. By solving the governing equations in this form and order, the compressible projection method describes a *conser-*

vative[1] scheme. This leads to a computationally very efficient algorithm, since no further iterations need to be computed. In the following, the numerical scheme of the compressible projection method - which shall be from now on be referred to as CPM (Compressible Projection Method) - is summarized in the form of the following algorithm.

3.4.2. Additional Notes on the Compressible Projection Method

Aside from including the divergence constraint deduced from the pressure equation (3.4.1), the continuity equation can also be used to derive a divergence constraint for the compressible projection method. The latter approach directly leads to equation (3.4.13) in order to determine the divergence constraint required for the derivation of the pressure correction equation. Inserting equation (3.4.13) into the generic pressure correction equation leads to the following formula determining the pressure correction δp^{n+1}:

$$\Delta_{\mathrm{L}}\delta p^{n+1} = \frac{\alpha_{\mathrm{pr}}}{f\left(\Delta t\right)}\left[\nabla\cdot\left(\rho^{n}\underline{u}^{*}\right) + \left.\frac{\partial\rho}{\partial t}\right|_{n+1}\right]. \tag{3.4.30}$$

At first glance, equation (3.4.30) resembles the pressure correction equation from the incompressible projection method for variable density flows, cf. equation (3.3.7). For a compressible flow, the density is not only a function of the pressure level p_{ref}, gas constant R and temperature T, but also of the pressure variation p. By making use of the equation of state, the density of a compressible chemically reactive ideal gas mixture can be expressed through the following formula:

$$\rho = \rho\left(p, R, T\right) = \frac{p_{\mathrm{ref}} + p}{RT}. \tag{3.4.31}$$

The property $\rho = \rho\left(p, R, T\right)$ alters the characterization of the pressure correction equation significantly, as it changes from a Possion- to a Helmholtz-type equation. The direct implementation of the correction equation (3.4.30) into the compressible projection method has proven to be unstable even for simple test cases and is thus not suitable to be incorporated into the compressible solution algorithm. Opposed here to, the incorporation of the divergence constraint deduced from the pressure equation (3.4.1) has been found to work stably. It has to be kept in mind that the pressure equation in this context here stands for the primitive form of the energy balance equation formulated for the pressure and is therefore not to be confused with the pressure correction equation.

Instead of calculating the divergence of the velocity appearing within the computation of the stress tensor $\underline{\underline{\tau}}$ at the right hand side of the momentum conservation equations (3.4.6) and within the calculation of the dissipation term $\underline{\underline{\tau}} : \nabla\underline{u}$ at the right hand side of the enthalpy

[1] The term *conservative* refers to the property of a numerical scheme of assuring the conservation of all quantities $\rho\phi$ required to fully describe the physical problem considered, cf. references [6, 265, 266].

balance equation (3.4.24) by means of the divergence constraint (3.4.7), the determination of $\nabla \cdot \underline{u}^m$, $m = \{n, n+1\}$ through the sum of the velocity component gradients

$$\nabla \cdot \underline{u}^m = \sum_{i=1}^{3} \left. \frac{\partial u_i}{\partial x_i} \right|_m \quad \text{for} \quad m = \{n, n+1\} \tag{3.4.32}$$

seems at first glance to be the more intuitive choice. However, the determination of the divergence constraint from the energy balance equation creates a more conservative scheme and its application onto the calculation of the stress tensor and dissipation term ensures the consistency of $\nabla \cdot \underline{u}^m$, $m = \{n, n+1\}$ to the integration of the divergence constraint in the derivation of the pressure correction equation (3.4.16). In addition to this, it is important to note that the velocity divergence (3.4.5) derived from the pressure equation (3.4.1) is consistent to the calculation of $\nabla \cdot \underline{u}$ from the continuity equation, as it is done in the incompressible projection method for variable density flows, see appendix B.1 and equation (3.3.3). The implementation of equation (3.4.5) thus ensures the fulfillment of mass conservation.

3.4.3. Algorithm of the Compressible Projection Method

The solution strategy of the CPM method developed within the present work reads:

1. In a first step, the divergence constraint $\nabla \cdot \underline{u}^n$

$$\nabla \cdot \underline{u}^n = \frac{1}{\gamma^n \left(p_{\text{ref}} + p^n\right)} \left[\left(\gamma^n - 1\right) \left(S^n_{\text{m\&c}} - \nabla \cdot \underline{q}^n + \underline{\underline{\tau}}^n : \nabla \underline{u}^n \right) - \left. \frac{\partial p}{\partial t} \right|_n - \underline{u}^n \cdot \nabla p^n \right]$$

   and the interim solution of the velocity field $\underline{u}^*$

$$\left. \frac{\partial \left(\rho \underline{u}\right)}{\partial t} \right|_* + \nabla \cdot \left[\left(\rho \underline{u}\right)^n \otimes \underline{u}^* \right] + \nabla p^n = \nabla \cdot \underline{\underline{\tau}}^*$$

   are computed. The interim solution step denoted by the subscript $*$ beneath the momentum time derivative can be understood as solution of the predictor step and characterizes the difference operator between the old time step n and interim step $*$, refer to section 3.1 and equation (3.1.3) for a more detailed description.

2. The pressure correction equation is then solved for the pressure correction:

$$\Delta_L \delta p^{n+1} - \frac{\alpha_{\text{pr}}}{f\left(\Delta t\right) \Delta t} \left(c^n\right)^{-2} \delta p^{n+1} = \frac{\alpha_{\text{pr}}}{f\left(\Delta t\right)} \left[\nabla \cdot \left(\rho^n \underline{u}^*\right) + \left(c^n\right)^{-2} \underline{u}^* \cdot \nabla p^n \right.$$
$$\left. - \left(\gamma^n - 1\right) \left(S_{\text{m\&c}} - \nabla \cdot \underline{q}^n + \underline{\underline{\tau}}^* : \nabla \underline{u}^* \right) \right] .$$

3. This leads to the correction of the pressure field:

$$p^{n+1} = p^n + \delta p^{n+1} \,.$$

4. The correction of the velocity field is performed in a next step:

$$\underline{u}^{n+1} = \underline{u}^* - \frac{f\left(\Delta t\right)}{\alpha_{\mathrm{pr}} \rho^n} \nabla \delta p^{n+1} \,.$$

5. The density field is updated next by means of the equation of state for an ideal gas mixture:

$$\rho^{n+1} = \frac{p_{\mathrm{ref}} + p^{n+1}}{\left(RT\right)^n} \,.$$

6. The divergence constraint is updated next:

$$\nabla \cdot \underline{u}^{n+1} = \frac{1}{\gamma^n \left(p_{\mathrm{ref}} + p^{n+1}\right)} \left[\left(\gamma^n - 1\right) \left(S_{\mathrm{m\&c}} - \nabla \cdot \underline{q} + \underline{\underline{\tau}}^{n+1} : \nabla \underline{u}^{n+1} \right) - \left. \frac{\partial p}{\partial t} \right|_{n+1} - \underline{u}^{n+1} \cdot \nabla p^{n+1} \right] \,.$$

7. The enthalpy is calculated using the energy conservation equation:

$$\left. \frac{\partial \left(\rho h\right)}{\partial t} \right|_{n+1} + \nabla \cdot \left[\left(\rho \underline{u}\right)^{n+1} h^{n+1} \right] - \left. \frac{\partial p}{\partial t} \right|_{n+1} - \underline{u}^{n+1} \cdot \nabla p^{n+1} = -\nabla \cdot \underline{q}^{n+1} + \underline{\underline{\tau}}^{n+1} : \nabla \underline{u}^{n+1} \,.$$

Modeling the transport, mixing and chemical reactions of species, $N_s - 1$ species transport equations are solved additionally:

$$\left. \frac{\partial \left(\rho \underline{Y}\right)}{\partial t} \right|_{n+1} + \nabla \cdot \left[\left(\rho \underline{u}\right)^{n+1} \otimes \underline{Y}^{n+1} \right] = -\nabla \cdot \underline{\underline{j}}^{n+1} + \underline{S}_Y^{n+1} \,.$$

The mass fraction of the last species is computed as dependent variable from Dalton's law:

$$\sum_{i=1}^{N_s} Y_i^{n+1} = 1 \Rightarrow Y_{N_s}^{n+1} = 1 - \sum_{i=1}^{N_s - 1} Y_i^{n+1} \,.$$

8. The temperature field is eventually obtained from the sensible chemical enthalpy

$$h^{n+1} = \sum_{i=1}^{N_s} Y_i^{n+1} \left[h_{f_i}^0 + \int_{T_0}^{T^{n+1}} c_{p_i}^{n+1} \left(T^{n+1}\right) dT \right] \,.$$

iteratively by means of the Newton-Raphson method [169, 199].

9. In case of addressing turbulent flows, transport equations are added and solved for the turbulent quantities.

The difference operator denoted by the subscript $n+1$ beneath the time derivative of the scalar functions denotes the corrector step and describes the difference between the time steps $n+1$ and n. The first step can be seen as predictor step. The steps 2-6 represent corrector steps. The steps 7-9 form the thermodynamic and turbulent closure of the CPM method.

3.5. Notes on the Treatment of the Pressure Laplacian and Numerical Instabilities

This subsection is concerned with the computation of the pressure Laplacian, which has to be dealt with when solving the pressure correction equation (3.4.16) and instabilities, which may arise during the numerical calculation.

3.5.1. Treatment of the Pressure Laplacian

The Laplacian of the pressure correction δp^{n+1} at the time step $n+1$ is obtained by applying the divergence operator onto the pressure correction gradient:

$$\Delta_L \delta p^{n+1} \equiv \nabla \cdot \left(\nabla \delta p^{n+1} \right) . \tag{3.5.1}$$

Integrating (3.5.1) over the control volume Ω and applying Gauss' theorem [4, 82, 101] yields:

$$\int_\Omega \Delta_L \delta p^{n+1} d\Omega = \int_\Omega \left[\nabla \cdot \left(\nabla \delta p^{n+1} \right) \right] d\Omega = \oint_\Gamma \left(\nabla \delta p^{n+1} \cdot \underline{n}|_\Gamma \right) d\Gamma . \tag{3.5.2}$$

Note that Γ represents the piecewise smooth boundary surface of Ω. The integral formulation (3.5.2) can be approximated by assuming a constant value of the pressure correction gradient along the cell faces j, $j \in \{1, \ldots, N_f\}$:

$$\oint_\Gamma \left(\nabla \delta p^{n+1} \cdot \underline{n}|_\Gamma \right) d\Gamma \approx \sum_{j=1}^{N_f} \nabla \delta p_j^{n+1} \cdot \underline{n}_j = \sum_{j=1}^{N_f^i} \nabla \delta p_j^{n+1} \cdot \underline{n}_j \tag{3.5.3}$$

with

$$N_f = N_f^i + N_f^b , \tag{3.5.4}$$

where N_f, N_f^i and N_f^b denote the number faces, the number of inner and the number of boundary faces of one control volume, respectively. In the case of walls, symmetry and

periodic faces, and fully reflective in- and outflow boundaries, a Neumann boundary condition is imposed which prescribes the constancy of the pressure correction. The pressure correction Laplacian has thus no contribution on the said boundary faces, which is equal to the following equation:

$$\forall j \in \left\{1, \ldots, N_f^b\right\}, \nabla \delta p_j^{n+1} \cdot \underline{n}_j = 0 \Rightarrow \sum_{j=1}^{N_f^b} \nabla \delta p_j^{n+1} \cdot \underline{n}_j = 0\,. \tag{3.5.5}$$

The treatment of the pressure correction Laplacian in case of setting a partially reflective boundary face is dealt with in section 4.2. The product of the pressure correction gradient and the normal face vector has to be computed next. Since THETA uses a cell-centered formulation of the finite volume method, the variables are only stored on the vertices of the primary grid. The values at the cell faces are not known, they have to be approximated using the nodal values. As mentioned before, a constant value of the pressure correction gradient along the cell faces is assumed. Figure 3.5.1(a) gives a two-dimensional graphical overview of the location of the nodal points, cell faces and their respective centers [122]. The nodal values are denoted by the index i, whereas the cell faces are described by the index j.

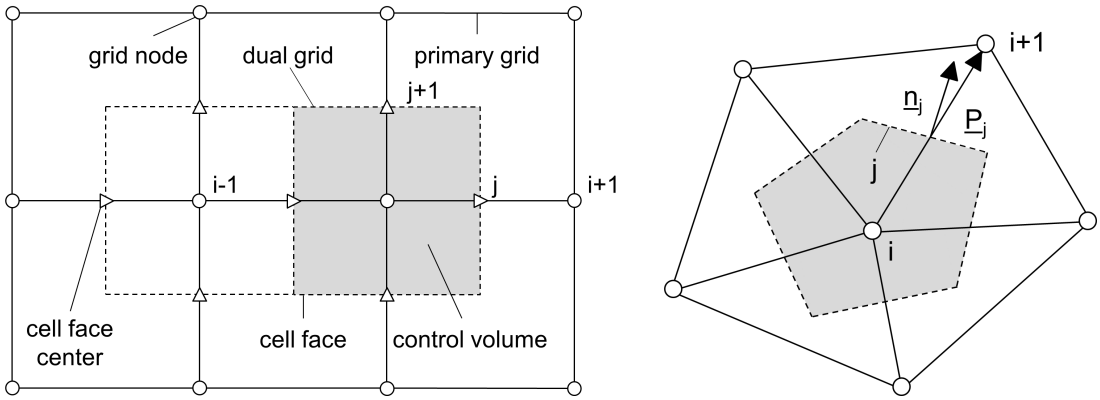

(a) Points, cell faces and their centers on a structured grid (b) Definition of the vectors $\underline{n}_j$ and $\underline{P}_j$

Figure 3.5.1.: Two-dimensional geometrical overview of the dual grid used by THETA (according to [122])

Let $\underline{P}_j$, $j \in \{1, \ldots, N_f\}$ be the vector defined between two grid points, see figure 3.5.1(b). Then, $\underline{P}_j$ can be used to calculate the product of the pressure correction gradient and the normal face vector $\underline{n}_j$ [122]. This is shown in the following. In a first step, the vector $\underline{P}_j$ is decomposed into its normal and tangential parts [122]:

$$\underline{P}_j = \frac{\underline{n}_j \cdot \underline{P}_j}{\|\underline{n}_j\|_2^2} \underline{n}_j + \left(\underline{P}_j - \frac{\underline{n}_j \cdot \underline{P}_j}{\|\underline{n}_j\|_2^2} \underline{n}_j \right) \quad \text{with} \quad \underline{n}_j \cdot \underline{P}_j \neq 0\,. \tag{3.5.6}$$

Taking the scalar product of the pressure correction gradient at the cell interface j and $\underline{P}_j$

leads to [122]:

$$\forall j \in \left\{1, \ldots, N_f^b\right\}, \nabla \delta p_j^{n+1} \cdot \underline{P}_j = \nabla \delta p_j^{n+1} \cdot \frac{\underline{n}_j \cdot \underline{P}_j}{\|\underline{n}_j\|_2^2} \underline{n}_j + \nabla \delta p_j^{n+1} \cdot \left(\underline{P}_j - \frac{\underline{n}_j \cdot \underline{P}_j}{\|\underline{n}_j\|_2^2} \underline{n}_j \right) . \quad (3.5.7)$$

Reformulating and multiplying equation (3.5.7) with the fraction $\|\underline{n}_j\|_2^2 / \left(\underline{n}_j \cdot \underline{P}_j\right)$ results in the following expression [122]:

$$\forall j \in \left\{1, \ldots, N_f^b\right\},$$
$$\nabla \delta p_j^{n+1} \cdot \underline{n}_j = \underbrace{\frac{\|\underline{n}_j\|_2^2}{\underline{n}_j \cdot \underline{P}_j} \nabla \delta p_j^{n+1} \cdot \underline{P}_j}_{1} - \underbrace{\frac{\|\underline{n}_j\|_2^2}{\underline{n}_j \cdot \underline{P}_j} \nabla \delta p_j^{n+1} \cdot \left(\underline{P}_j - \frac{\underline{n}_j \cdot \underline{P}_j}{\|\underline{n}_j\|_2^2} \underline{n}_j \right)}_{2} . \quad (3.5.8)$$

Note that the scalar product $\underline{n}_j \cdot \underline{P}_j$ is not allowed to be zero. Aside from the value zero which is strictly prohibited, $\underline{n}_j \cdot \underline{P}_j$ may adopt small values at grid cells with sharp inner angles. This is due to the fact that as inner cell angles become smaller, the angle between $\underline{n}_j$ and $\underline{P}_j$ is getting larger, which eventually leads to a decrease of the scalar product $\underline{n}_j \cdot \underline{P}_j$. This is sometimes the case when pyramids are employed to connect prism layers at surface boundaries to tetrahedral cells towards the inner field. If the dimensions of one prism element is much greater than the base area of the respective tetrahedron, the pyramid connecting both elements will be compressed. This leads to the occurrence of sharp angles at the inner side of the pyramid base. The generation of "bad" cells within the inner field may also increase the risk leading to small inner angles. The occurrence of such sharp inner angles results in a relatively large value of the coefficient $1 / \left(\underline{n}_j \cdot \underline{P}_j\right)$ and thus to numerical difficulties when solving the pressure correction equation. As a consequence of this, sharp angles within the generation process of the computational mesh should be avoided.

In a next step, the cell face values of the pressure correction gradient have to be evaluated. This is accomplished by making use of the *deferred correction approach* [54, 122]. By applying the deferred correction approach, the pressure correction gradient is discretized accurately in a time-efficient manner, see reference [54] and section 3.2 for details. Following this methodology, the gradient of part 1 is treated implicitly, whereas the gradient of part 2 is computed explicitly. In addition to the higher-order treatment of the explicit part, a second-order approximation of the pressure correction gradient is constructed in order to determine the implicit part. The computation of both parts is presented in the following: The pressure correction gradient of part 1 is calculated by applying a linear extrapolation of the nodal values [122]:

$$\forall i \in \{1, \ldots, N_p\}, \forall j \in \left\{1, \ldots, N_f^i\right\}, \nabla \delta p_j^{n+1} \cdot \underline{P}_j = p_{\underline{P}_{i+1}}^{n+1} - p_{\underline{P}_i}^{n+1} . \quad (3.5.9)$$

Equation (3.5.9) represents a central-differential approximation of the pressure correction gradient and is thus of second-order accuracy. The gradient of part 2 is computed by taking the arithmetic average of the nodal values, thus resulting in a second-order approximation of the cell face values. Applying this to the pressure correction derivative yields [122]:

$$\forall i \in \{1,\ldots,N_p\}\,,\ \forall j \in \left\{1,\ldots,N_f^i\right\},\ \nabla\delta p_j^{n+1} = \frac{1}{2}\left(\nabla\delta p_{\underline{P}_i}^n + \nabla\delta p_{\underline{P}_{i+1}}^n\right). \tag{3.5.10}$$

Introducing (3.5.9) and (3.5.10) into equation (3.5.8) results in the final expression for the pressure correction gradient multiplied with the normal vector at the inner cell faces [122]:

$$\forall i \in \{1,\ldots,N_p\}\,,\ \forall j \in \left\{1,\ldots,N_f^i\right\},$$
$$\nabla\delta p_j^{n+1}\cdot\underline{n}_j = \frac{\|\underline{n}_j\|_2^2}{\underline{n}_j\cdot\underline{P}_j}\left[\left(\delta p_{\underline{P}_{i+1}}^{n+1} - \delta p_{\underline{P}_i}^{n+1}\right) + \frac{1}{2}\left(\nabla\delta p_{\underline{P}_i}^n + \nabla\delta p_{\underline{P}_{i+1}}^n\right)\cdot\left(\underline{n}_j - \frac{\|\underline{n}_j\|_2^2}{\underline{n}_j\cdot\underline{P}_j}\underline{P}_j\right)\right]. \tag{3.5.11}$$

The second term on the right hand side of equation (3.5.11) is of explicit nature and can be seen as a stabilization term in the calculation of the pressure Laplacian. Equation (3.5.11) is completely described by the nodal values of the pressure correction and its gradient from the known time step n, thus describing the computation of the pressure Laplacian for a control volume Ω, which has initially been given by equation (3.5.2). Note that, if $\underline{n}_j$ and $\underline{P}_j$ are linearly dependent, i.e. $\sphericalangle\left(\underline{n}_j,\underline{P}_j\right)=0$, the second term of equation (3.5.11) disappears. This holds e.g. for orthogonal grids. Equation (3.5.11) then reduces to [122]:

$$\begin{aligned}\forall i \in \{1,\ldots,N_p\}\,,\ \forall j \in \left\{1,\ldots,N_f^i\right\},\ \left\{\forall j \in \left[1;N_f^i\right]\,\middle|\,\sphericalangle\left(\underline{n}_j,\underline{P}_j\right)=0\right\},\\ \nabla\delta p_j^{n+1}\cdot\underline{n}_j = \frac{\|\underline{n}_j\|_2}{\|\underline{P}_j\|_2}\left(\delta p_{\underline{P}_{i+1}}^{n+1} - \delta p_{\underline{P}_i}^{n+1}\right).\end{aligned} \tag{3.5.12}$$

The product of the pressure correction gradient and the normal face vector represents the first term of the left hand side of the pressure correction equation (3.4.14). THETA uses a cell-centered formulation of the finite volume method, so that the contribution of the pressure Laplacian is not taken into account at the cell interfaces, but at the cell vertices. The cell face contributions can be taken into account at the vertices by taking the sum of all cell faces surrounding the control volume [122]:

$$\forall i \in \{1,\ldots,N_p\}\,,\ \Delta_L\delta p_i^{n+1} = \sum_{j=1}^{N_f^i}\nabla\delta p_j^{n+1}\cdot\underline{n}_j\,. \tag{3.5.13}$$

3.5.2. Numerical Instabilities

According to the dual grid approach, THETA uses a collocated grid arrangement of the grid points. Let us consider a one-dimensional computational domain discretized using an equidistant grid. Choosing a central differencing scheme for the spatial discretization of the pressure correction derivative leads to the following formula [54, 214]:

$$\left.\frac{\partial \delta p^{n+1}}{\partial x}\right|_i = \frac{\delta p_{i+1}^{n+1} - \delta p_{i-1}^{n+1}}{2\Delta x}\,. \tag{3.5.14}$$

It can be seen that the pressure correction at the location i does not appear on the right hand side of equation (3.5.14), so that one discrete value is always skipped during the computation of the derivative. Let the periodic pressure function δp^{n+1} be the solution of a one-dimensional flow oscillating with a wavelength of $\Lambda = 2\Delta x$, see figure 3.5.2.

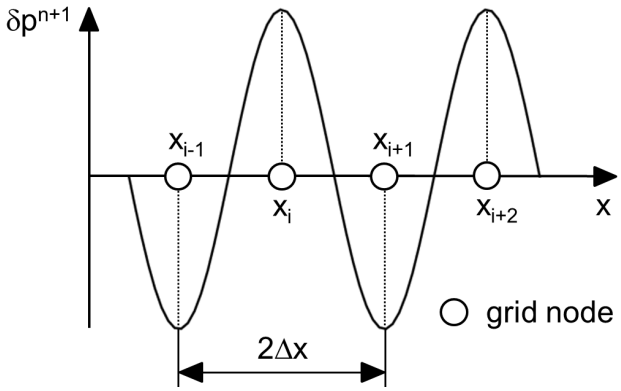

Figure 3.5.2.: One-dimensional periodic function oscillating with $\Lambda = 2\Delta x$

Calculating the derivative of δp^{n+1} by means of equation (3.5.14) results in a zero-gradient field of the pressure correction δp^{n+1}, cf. figure 3.5.2. Conversely, the numerical simulation of a uniform field may result in a periodic field of δp^{n+1}, which is also widely known as checkerboard distribution [54]. These oscillations are of non-physical nature, so that they can lead to a divergence of the simulation in case of accumulation.

The occurrence of such non-physical oscillations can be overcome by applying a transformation to the discretization of the pressure Laplacian on the left hand side of the pressure correction equation (3.4.14). The idea is to discretize the spatial derivative of the pressure with the central difference scheme based on a Δx-discretization, as it is usually done in the case of a staggered grid arrangement of the variables [54, 214]. Since the discretization of the pressure derivative within the pressure correction and momentum equations have to be consistent with each other, a correction needs to be added to the pressure correction equation [54]. This is due to the fact that both terms originate from the same pressure gradient term

of the momentum equations.

The derivative of the pressure correction in the equations (3.5.9) and (3.5.10) is discretized using a Δx step width:

$$\left.\frac{\partial \delta p^{n+1}}{\partial x}\right|_i = \frac{\delta p_{i+\frac{1}{2}}^{n+1} - \delta p_{i-\frac{1}{2}}^{n+1}}{\Delta x}\,. \tag{3.5.15}$$

Equations (3.5.11) and (3.5.11) give the formulas to compute the pressure Laplacian of the pressure correction equation for a control volume Ω. Equation (3.5.11) has been derived using a Δx-discretization and is therefore inconsistent with the discretization of the pressure correction gradient of equation (3.4.20), whose size amounts to $2\Delta x$. In order to ensure the consistency of the discretized gradient terms used within the momentum balance and pressure correction equations, a correction term is added to the right hand side of the pressure correction equation, cf. reference [54]. This correction term is denoted by the variable Δ and is obtained by subtracting of the $2\Delta x$-discretization from the Δx-discretization formula [54]. The derivation of Δ is shown in the following. In doing so, a one-dimensional equidistant grid is assumed for simplicity reasons.

Equation (3.5.12) provides the formulation for the Δx-based discretization of the pressure correction gradient term. Together with equation (3.5.13), one obtains the nodal contribution of the pressure correction Laplacian for the grid node i [54]:

$$\Delta_L \delta p^{n+1}\big|_i = \frac{\delta p_{i+1}^{n+1} - 2\delta p_i^{n+1} + \delta p_{i-1}^{n+1}}{(\Delta x)^2}\,. \tag{3.5.16}$$

Equation (3.5.16) can also be obtained through the application of a Δx-based discretization of formula (3.5.15). Taking the $2\Delta x$-based derivative of equation (3.5.14) yields the following result [54]:

$$\Delta_L \delta p^{n+1}\big|_i = \frac{\delta p_{i+2}^{n+1} - 2\delta p_i^{n+1} + \delta p_{i-2}^{n+1}}{4\,(\Delta x)^2}\,. \tag{3.5.17}$$

Equation (3.5.17) has the same form as equation (3.5.16), except that it is discretized on a grid which is twice as coarse. The $2\Delta x$-based discretizations of the δp^{n+1} derivative at the grid nodes $i+1$, respective $i-1$ read:

$$\left.\frac{\partial \delta p^{n+1}}{\partial x}\right|_{i+1} = \frac{\delta p_{i+2}^{n+1} - \delta p_i^{n+1}}{2\Delta x}\,, \tag{3.5.18}$$

$$\left.\frac{\partial \delta p^{n+1}}{\partial x}\right|_{i-1} = \frac{\delta p_i^{n+1} - \delta p_{i-2}^{n+1}}{2\Delta x}\,. \tag{3.5.19}$$

By applying a decomposition to equation (3.5.17) and using the formulas (3.5.18) and (3.5.19),

equation (3.5.17) can be rewritten into the following form [54]:

$$\begin{aligned}\Delta_L \delta p^{n+1}\big|_i = \frac{\delta p_{i+2}^{n+1} - 2\delta p_i^{n+1} + \delta p_{i-2}^{n+1}}{4\left(\Delta x\right)^2} &= \frac{1}{2\Delta x}\left(\frac{\delta p_{i+2}^{n+1} - \delta p_i^{n+1}}{2\Delta x} - \frac{\delta p_i^{n+1} - \delta p_{i-2}^{n+1}}{2\Delta x}\right) \\ &= \frac{1}{2\Delta x}\left(\left.\frac{\partial \delta p^{n+1}}{\partial x}\right|_{i+1} - \left.\frac{\partial \delta p^{n+1}}{\partial x}\right|_{i-1}\right) . \end{aligned} \tag{3.5.20}$$

By taking the difference of equations (3.5.16) and (3.5.20) yields the correction term Δ at the node i [54]:

$$\Delta_i = \frac{\delta p_{i+1}^{n+1} - 2\delta p_i^{n+1} + \delta p_{i-1}^{n+1}}{\left(\Delta x\right)^2} - \frac{1}{2\Delta x}\left(\left.\frac{\partial \delta p^{n+1}}{\partial x}\right|_{i+1} - \left.\frac{\partial \delta p^{n+1}}{\partial x}\right|_{i-1}\right) . \tag{3.5.21}$$

Recasting equation (3.5.21) to a more generic formula defining the contribution of Δ at the node i, $\forall i \in \{1, \ldots, N_p\}$ within the pressure correction equation (3.4.14) results in the following equation:

$$\begin{aligned} &\forall i \in \{1, \ldots, N_p\} , \\ \Delta_i = \sum_{j=1}^{N_f^i} \frac{\|\underline{n}_j\|_2^2}{\underline{n}_j \cdot \underline{P}_j} &\left[\left(\delta p_{\underline{P}_{i+1}}^{n+1} - \delta p_{\underline{P}_i}^{n+1}\right) - \frac{1}{2}\left(\nabla \delta p_{\underline{P}_{i+1}}^{n+1} + \nabla \delta p_{\underline{P}_i}^{n+1}\right) \cdot \underline{P}_j\right] . \end{aligned} \tag{3.5.22}$$

Since the correction term Δ is added to the right hand side term of the pressure correction equation (3.4.14) and is treated explicitly, the values of the pressure correction appearing within the above equation are those from the known time step n. By additionally introducing the so-called degree of stabilization α_{sd}, Δ is thus obtained from the following equation, cf. reference [122]:

$$\begin{aligned} &\forall i \in \{1, \ldots, N_p\} , \\ \Delta_i = \sum_{j=1}^{N_f^i} \alpha_{\mathrm{sd}} \frac{\|\underline{n}_j\|_2^2}{\underline{n}_j \cdot \underline{P}_j} &\left[\left(\delta p_{\underline{P}_{i+1}}^{n} - \delta p_{\underline{P}_i}^{n}\right) - \frac{1}{2}\left(\nabla \delta p_{\underline{P}_{i+1}}^{n} + \nabla \delta p_{\underline{P}_i}^{n}\right) \cdot \underline{P}_j\right] . \end{aligned} \tag{3.5.23}$$

α_{sd} is set to unity by default [122]. Prior studies revealed that a range of $]\,0; 1\,]$ is reasonable for α_{sd} [122]. The correction term reaches its maximum if numerical oscillations occur and induces in this case a smoothing of the pressure and hence of the flow field [122]. It can be demonstrated that the correction term Δ_i (3.5.23) is proportional to the central difference approximation of the fourth-order pressure correction derivative, see reference [54] for details.

3.6. On the Temporal and Spatial Order of Accuracy of Projection-Based Methods

In this section, the order of accuracy in space and time of both the standard non-incremental and incremental incompressible projection schemes for constant density flows is discussed. First temporal error estimates of projection-based schemes have been conducted by Temam [240] and Shen [222, 223]. Later on, Rannacher [197], Shen [224], E and Liu [42], Guermond [73], Guermond and Minev [74] and Guermond, Minev and Shen [75] have enforced the effort in research concerning error estimates of projection-based methods in time. In a first step, the error introduced by the discretization in time is estimated based on the work of Shen [224] and Guermond, Minev and Shen [75].

Let the computational domain be three-dimensional, $\Delta t > 0$ be a time step size and define $t^i \equiv i \cdot \Delta t > 0$ for $i \in \{0, 1, \ldots, N_{\text{ts}}\}$. Let $\phi^0, \phi^1, \ldots, \phi^{N_{\text{ts}}}$ be a sequence of functions on a Hilbert space E, described by $\phi_{\Delta t}$. Knowing this, the following discrete norms can be defined:

$$\|\phi_{\Delta t}\|_{\ell^2(E)} \equiv \left(\Delta t \sum_{i=0}^{N_{\text{ts}}} \|\phi^i\|_E^2 \right)^{\frac{1}{2}} \quad \text{and} \quad \|\phi_{\Delta t}\|_{\ell^\infty(E)} \equiv \max_{0<i<N_{\text{ts}}} \left(\|\phi^i\|_E \right) . \tag{3.6.1}$$

Moreover, let H^1 be a Sobolev space [1, 2] and L^2 be an inner product space [97, 255], equipped with their respective norms $\|\cdot\|$. The indices ℓ^2 and ℓ^∞ denote the 2- and ∞-norm of a sequence of functions defined on a Hilbert Space [97, 255], respectively. The functions $\tilde{u}$ and $\tilde{p}$ describe solutions of the Stokes problem (Navier-Stokes problem without convective terms). Based on the definitions given above, Guermond, Minev and Shen [75] give the following error estimation for the non-incremental incompressible projection method for constant density flows:

$$\|\underline{\tilde{u}}_{\Delta t} - \underline{u}_{\Delta t}\|_{\ell^\infty\left([L^2(\Omega)]^3\right)} + \|\underline{\tilde{u}}_{\Delta t} - \underline{u}^*_{\Delta t}\|_{\ell^\infty\left([L^2(\Omega)]^3\right)} \lesssim \Delta t \,, \tag{3.6.2}$$

$$\|\tilde{p}_{\Delta t} - p_{\Delta t}\|_{\ell^\infty([L^2(\Omega)])} + \|\underline{\tilde{u}}_{\Delta t} - \underline{u}^*_{\Delta t}\|_{\ell^\infty\left([H^1(\Omega)]^3\right)} \lesssim (\Delta t)^{\frac{1}{2}} \,. \tag{3.6.3}$$

The superscript $*$ denotes the interim solution of a variable obtained from the predictor step of the projection scheme. The variables which do not have any superscript denote the final solution of the projection-based scheme. As the Neumann boundary condition $\nabla p \cdot \underline{n}|_\Gamma = 0$ is applied to the pressure, the standard non-incremental scheme is not fully first-order accurate on the velocity in the H^1-norm and on the pressure in the L^2-norm, see equations 3.6.2 and 3.6.3. Typically, boundary conditions decrease the accuracy of the spatial derivatives near the boundaries. This is based on the fact that grid point values are available on one side

only relative to the boundary [197].

By means of an incremental projection-based scheme, the temporal order is increased compared to the use of the non-incremental algorithm. The incremental projection method proposed by Goda [68] introduces the pressure gradient from the old time step into the left hand side of the momentum equations within the predictor step. As a result of this, a pressure correction δp between the new and old pressure field appears in the corrector step, as opposed to Chorin and Temam's original non-incremental projection scheme. Based on the demonstrations made in the publication of Guermond [75], the temporal error of the incremental projection method for constant density flows can be estimated as follows:

$$\|\tilde{\underline{u}}_{\Delta t} - \underline{u}_{\Delta t}\|_{\ell^2\left([L^2(\Omega)]^3\right)} + \|\tilde{\underline{u}}_{\Delta t} - \underline{u}^*_{\Delta t}\|_{\ell^2\left([L^2(\Omega)]^3\right)} \lesssim (\Delta t)^2 \,, \tag{3.6.4}$$

$$\|\tilde{p}_{\Delta t} - p_{\Delta t}\|_{\ell^\infty([L^2(\Omega)])} + \|\tilde{\underline{u}}_{\Delta t} - \underline{u}^*_{\Delta t}\|_{\ell^\infty\left([H^1(\Omega)]^3\right)} \lesssim \Delta t \,. \tag{3.6.5}$$

The incremental projection scheme reaches second-order accuracy on the velocity in the L^2-norm. However, the Neumann boundary condition $\nabla \delta p \cdot \underline{n}|_\Gamma = 0$ enforced on the pressure correction δp hinders the incremental method to reach second-order accuracy on the velocity in the H^1-norm and on the pressure in the L^2-norm [75]. Thus, the order of accuracy in time of the incremental projection method on the pressure is of the order of $\mathcal{O}(1)$ in the L^2-norm, see equations 3.6.4 and 3.6.5.

Shen [224] analyzed several incremental projection-based algorithms for the approximation of the Navier-Stokes equations by interpreting them as second-order time discretizations. It is important to note though that his analyses were restricted to the consideration of unsteady incompressible flows with constant density. Shen introduced, similar to the introduction of the projection weighting factor α_{pr}, a weighting factor β into the correction equation of the projection scheme, thus calling the system of equations to be solved a perturbed system. The pressure correction equation then reads [224]:

$$\nabla \cdot \underline{u}^* - \beta \frac{\Delta t}{\rho} \Delta_L \delta p^{n+1} = 0 \,. \tag{3.6.6}$$

Introducing $\alpha_{\mathrm{pr}} \equiv 1/\beta$ into equation (3.6.6) yields:

$$\Delta_L \delta p^{n+1} = \alpha_{\mathrm{pr}} \frac{\rho}{\Delta t} \nabla \cdot \underline{u}^* \,. \tag{3.6.7}$$

Setting the time derivative function $f(\Delta t)$ equal to the time step size Δt, equation (3.6.7) is equal to the pressure correction equation for incompressible flows with constant density derived in subsection 3.2. Based on the work of Shen [224], $\beta < 0.25 \Leftrightarrow \alpha_{\mathrm{pr}} > 4$ results in

an unstable solution scheme. The perturbed projection scheme is of second-order accuracy for the velocity and is at least first-order accurate for the pressure in the L^2-norm [224]. Moreover, the imposed Neumann boundary condition on the pressure induces a significant error onto the pressure field, thus limiting the accuracy of the pressure at boundaries [224]. This error is reduced as the time step size Δt is decreased.

Further analysis of the inner field (by ignoring the boundaries of the computational domain) showed that choosing the perturbation factor to $\beta = 0.5$, which equals $\alpha_{\mathrm{pr}} = 2$, second-order accuracy has been achieved for the pressure, whereas the setup $\{\forall \beta \in \,]\,0.25; +\infty\,[\;|\;\beta \neq 0.5\}$ results in a reduction of the inner-field order of accuracy [224]. Increasing the value of β beyond 2 leads to a growth of the amount of numerical dissipation [224]. It is important to say at this point that these conclusions were achieved based on a numerical test case assuming an incompressible flow with constant density, without taking into account the influence of convection and by setting the molecular viscosity to a constant value of $\nu = 1\,\mathrm{m}^2/\mathrm{s}$, which represents a very high value. A viscosity of the order of magnitude of $\nu = 1\,\mathrm{m}^2/\mathrm{s}$ corresponds to the flow behavior of molten polymers at room temperature and pressure, under the assumption of being driven by strain rates far smaller than one 1/s [8]. As a result of this, a dynamic viscosity of $\nu = 1\,\mathrm{m}^2/\mathrm{s}$ represents a highly viscous behavior and thus a very high value compared to the values generally considered when dealt with gases, which are of the order of $\mathcal{O}\left(10^{-6} \div 10^{-5}\right)\,\mathrm{m}^2/\mathrm{s}$.

The influence of the viscosity on the temporal order of accuracy is not dealt within the work of Shen [224]. This issue has been addressed to by Zhang [267], who conducted convergence tests in space and time of the incompressible projection method for constant density flows by setting the kinematic viscosity to the values of $1\,\mathrm{m}^2/\mathrm{s}$ and $10^{-6}\,\mathrm{m}^2/\mathrm{s}$. These tests have been performed based on a two-dimensional computational domain with the knowledge of a known analytical solution. By comparing the numerical to the analytical solution for different grid and time step sizes, errors of the velocity and pressure values were calculated, thus giving an estimate for the spatial and temporal order of accuracy. The TPB discretization scheme has been applied as a temporal discretization method. The discretization of the diffusive parts within the momentum equations is performed using the CDS scheme. Applying the second-order accurate QUDS, LUDS and CDS discretization methods to the convective terms within the momentum equations, Zhang found the incompressible projection method for constant density flows at $\nu = 10^{-6}\,\mathrm{m}^2/\mathrm{s}$ to be second-order accurate in the L^2-norm for the velocity and first-order accurate in the L^2-norm for the pressure in space. Changing the kinematic viscosity to $\nu = 1\,\mathrm{m}^2/\mathrm{s}$ does not alter the spatial accuracy of the velocity field [267]. However, this setting causes the pressure to become 1.5-th order accurate in space [267]. It is important to mention that Zhang used an incompressible flow with constant density for his research

efforts. In addition to this, the convergence tests conducted with a dynamic viscosity of $\nu = 1\,\mathrm{m}^2/\mathrm{s}$ represent a highly viscous behavior rather found when dealt with liquid than gaseous substances or mixtures. In combination of a prescribed inlet velocity magnitude of $\|\underline{u}\|_2 = \pi\,\mathrm{m/s}$ and a chosen cell width of $(1/320 \div 1/40)$ m, the Reynolds number is of the order of $\mathcal{O}\left(10^{-3} \div 10^{-2}\right)$. Furthermore, Zhang used the unperturbed system of equations, which means that the projection weighting factor has been set to a value of 1. The changes in the spatial and temporal order of accuracy of projection-based methods when dealing with compressible flows hence need to be clarified. This is done further below in this work, cf. section 5.3.1.

4. Derivation of Accurate Boundary Conditions

4.1. Literature Study and Approach

The accurate computation of compressible unsteady flows demands a precise modeling of the processes at the boundaries of the computational domain. Oliger and Sundström [175], Dutt [41] and Strikwerda [232] addressed the issue of the necessary and sufficient number of physical boundary conditions to be specified. Modeling a three-dimensional compressible reactive flow consisting of N_s species, the inlet boundary requires $4 + N_s$ variables to be specified. It is common practice to specify the density, the three velocity components, the temperature and the mixture composition in form of N_s species mass fractions at an inlet boundary. These variables constitute independent quantities and are given by means of the so-called *physical boundary conditions* [189]. Physical constraints may directly be prescribed at the respective boundary, which results in a fully reflective behavior of incoming sonic waves.

Compressible transient flow fields generate characteristic waves of convective and acoustic nature. Depending on the case, a reflection or transmission of incoming sonic waves is desired at a specific boundary. If a partially non-reflective behavior at a specific boundary is wanted, a different approach than prescribing the variables, as it is performed when prescribing physical boundary conditions, is required. This approach needs to ensure an accurate resolution and control of incoming and outgoing waves. Consider a gas turbine combustor system. The oxidizer - in general air - enters the combustion chamber, where it mixes with the injected fuel. After ignition of the air/fuel mixture, the burned gas accelerates and moves towards the blades of the turbine. The computational resources available today do not allow the complete modeling and accurate numerical calculation of the combustion chamber including the turbine. It is therefore common use to model the combustion chamber and to set a certain boundary condition at the combustion chamber outlet. Setting for instance a fixed value of pressure at the outlet boundary surface results in a fully reflective behavior of the acoustic waves at this boundary. In reality however, a part of the acoustic waves is transmitted

through the combustion chamber outlet. As a consequence of this, the prescription of a fully reflective boundary condition may lead to the wrong physical behavior of the flow at the combustion chamber outlet. Opposed to this, the setup of a partially reflective boundary condition is the more appropriate choice for this kind of application.

KREISS [121], ENGQUIST and MAJDA [48] and THOMPSON [241] proposed the introduction of Local One-Dimensional Inviscid (LODI) relations for the numerical treatment of the Euler equations in order to determine the behavior of the propagating waves at the boundaries. These LODI relations are derived based on the method of characteristics. Later on, POINSOT and LELE [189] extended the LODI relations onto the numerical computation of the compressible unsteady Navier-Stokes equations. In order to achieve a partially non-reflective behavior of incoming acoustic waves at a boundary, the variables constituting physical boundary constraints are not directly prescribed at the boundary. Instead, a LODI relation is suggested for every physical boundary condition prescribed. This approach is referred to as the NSCBC (Navier-Stokes Characteristic Boundary Conditions) [189] method. Later on, POINSOT and VEYNANTE [190] described the extension of the LODI relations to reactive flows. An extensive description of the mathematical background of characteristic wave analysis has been conducted by KREISS [121] and ENGQUIST and MAJDA [48].

Dependent variables are determined based on the independent quantities and are referred to as *numerical boundary conditions* [189]. Whereas physical boundary conditions are required for a flow field to be physically well-posed, numerical boundary conditions are needed by the numerical method to calculate the remaining dependent variables. Basically, there are two methods for the specification of numerical boundary conditions [189]: The first methodology is to use artificial conditions by applying an extrapolation to the missing variables from the inner field to the boundary. Besides the boundary value of the quantity, the n-th order accurate extrapolation of a quantity at a boundary additionally requires its first n derivatives. However, the value itself as well as its first n derivatives are unknown at the boundary. Moreover, an n-th order accurate extrapolation technique introduces an additional error of the order $\mathcal{O}(n+1)$ into the calculation at the respective boundary due to the truncation error induced. Moreover, an additional point needs to be addressed to: Considering e.g. a linear extrapolation, the second and higher order gradients vanish at the respective boundary surface. These constraints are additional artificial boundary conditions which are added to the numerical scheme, so that the consistency of the artificial conditions with the set of physical conditions is not guaranteed anymore. It is important to note at this point that an approach involving the use of an extrapolation technique is of arbitrary nature and should thus be avoided when considering the incorporation of accurate boundary conditions [158]. The second approach for prescribing numerical constraints along boundaries consists of using

the governing equations themselves in order to derive characteristic wave relations which may then be used to determine the remaining dependent quantities at the domain boundaries. Following this methodology, the set of physical boundary constraints is complemented with the governing equations for a compressible flow to express the numerical boundary conditions. Compared to the use of artificial boundary conditions, the application of characteristic wave relations to define not only numerical, but also physical boundary constraints is the more consistent approach. This methodology was introduced in 1986 by Thompson [241].

The work presented in this paper aims to enable the calculation of a partially non-reflective behavior of incoming acoustic waves at an in- and outflow boundary for a pressure-based solution procedure capable of computing low and high Mach number flows. This is conducted based on the aforementioned NSCBC approach of Poinsot and Lele [189, 190]. The characteristic relations derived within the NSCBC approach depend however on the equations solved within the solution strategy applied. The original derivation of the NSCBC method performed by Poinsot and Lele [189] has been realized based on a density-based solution algorithm. Poinsot and Lele's NSCBC approach has been previously applied a pressure-based SIMPLE algorithm [79, 257], as well as to a segregated semi-implicit solution approach based upon a characteristic splitting of the Navier-Stokes equations [136]. In the present work, the NSCBC approach is applied to the set of equations referring to the pressure-based CPM method presented within section 3.4.

In some cases, spurious waves originating from numerical errors may create unphysical waves, which then perturb the flow field. The concept of a partially non-reflective behavior at in- and outflow boundaries adds the ability to get rid of such unwanted spurious waves. The ability of prescribing partially non-reflective in- and outflow boundaries thus improves the stability of a solution scheme.

4.2. Determination of the Pressure Laplacian at Boundaries

A fixed boundary condition leads to a fully reflective behavior of the incoming waves. The solution of the pressure correction is not needed at locations where the pressure is fixed, since for these locations the pressure correction $\delta p^{n+1} = p^{n+1} - p^n$ always vanishes. An example herefore is an outflow with a given value of the pressure. In this case, the right hand side terms of the pressure correction equation (3.4.16) vanish so that the gradient of the pressure correction equals zero along the boundary cell faces. As a consequence of this, the pressure correction equation does not need to be solved at the boundary faces.

Computing flows with a pressure-based incompressible solver, the absolute value of the pressure is not relevant, as the flow is only determined by pressure differences. Without any modification to the solution strategy, this results in an absolute level of the pressure

field which is not uniquely defined. As a remedy to this important issue, PATANKAR [182] proposed to set the reference value of the pressure to zero in one arbitrary inner control volume point and to solve the pressure for the remaining control volumes by means of the pressure correction equation as values relative to the one at the specified reference point. In the case of setting a fixed pressure boundary condition using a pressure-based compressible solver, a reference point for the pressure is not needed anymore. This is based on the fact that the absolute value of the pressure is related to the density of the flow, thus leading to a uniquely defined solution of the flow field.

In order to compute non-reflective boundary conditions by means of the NSCBC approach, the pressure correction equation needs to be solved at the boundary faces. This implies that the left and right hand side terms of the pressure correction equation need to be formulated at the boundaries and must be included in the calculation. The right hand side terms of the pressure correction equation at the boundaries are computed analogously to the ones at inner points. As the Laplacian of the pressure correction $\Delta_L \delta p$ plays an important role within the computation of the pressure itself, its determination at domain boundaries is presented in this work. A detailed derivation of the computation regarding the pressure correction Laplacian at inner field grid points is given within section 3.5. The result of this derivation is given in the following: For every inner grid point i, the cell face contributions of the pressure correction Laplacian can be taken into account by taking the sum of all contributions at cell faces surrounding the control volume:

$$\forall i \in \{1, \ldots, N_p\}\,,\ \Delta_L \delta p_i^{n+1} = \sum_{j=1}^{N_f^i} \nabla \delta p_j^{n+1} \cdot \underline{n}_j\,, \tag{4.2.1}$$

wherein the term $\nabla \delta p_j^{n+1} \cdot \underline{n}_j$ is computed by means of the following equation:

$$\begin{aligned} &\forall i \in \{1, \ldots, N_p\}\,,\ \forall j \in \left\{1, \ldots, N_f^i\right\},\ \nabla \delta p_j^{n+1} \cdot \underline{n}_j = \\ &\frac{\|\underline{n}_j\|_2^2}{\underline{n}_j \cdot \underline{P}_j} \left[\left(\delta p_{\underline{P}_{i+1}}^{n+1} - \delta p_{\underline{P}_i}^{n+1} \right) + \frac{1}{2} \left(\nabla \delta p_{\underline{P}_i}^{n} + \nabla \delta p_{\underline{P}_{i+1}}^{n} \right) \cdot \left(\underline{n}_j - \frac{\|\underline{n}_j\|_2^2}{\underline{n}_j \cdot \underline{P}_j} \underline{P}_j \right) \right]. \end{aligned} \tag{4.2.2}$$

One important step within the derivation of the pressure correction Laplacian is the application of the so-called deferred-correction approach to determine the gradient of δp, see section 3.5. Within the original formulation of the deferred-correction approach, the vector $\underline{P}$ is split up into a normal and tangential part with respect to the cell face. The inner angle between the vector $\underline{P}$ and the cell face normal $\underline{n}$ is not limited to any range of values. Dealing with highly skewed control volume cells, the inner angle $\sphericalangle\left(\underline{n}_j, \underline{P}_j\right)$ may adopt large values. This difficulty is illustrated within figure 4.2.1 for an approximately uniform (figure 4.2.1(a)) and

a skewed cell (4.2.1(b)). Traoré [242] found that a restriction of the angle spanned by

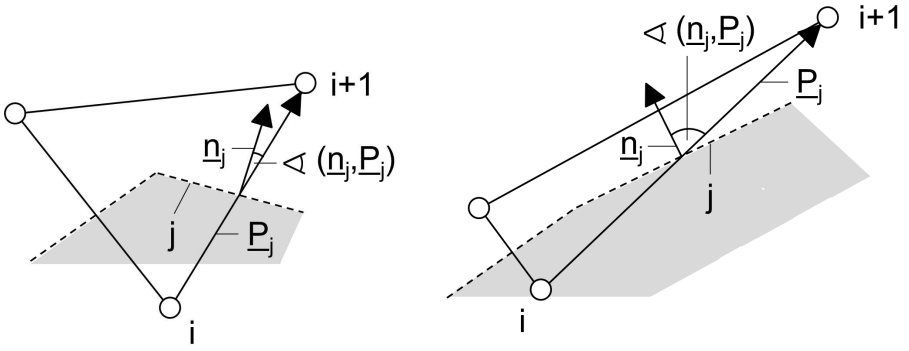

(a) Approximately uniform cell (b) Skewed cell

Figure 4.2.1.: Two-dimensional geometrical illustration of two different cell forms

the cell face normal vector $\underline{n}$ and the vector defined between two grid points $\underline{P}$ to a value of $\pi/3$ improves the stability concerning the computation of the Laplacian term of the pressure correction equation on unstructured grids with highly skewed cells.

As the determination of the pressure correction gradient term shown in equation (3.5.11) includes the reciprocal value of the scalar product of the vectors $\underline{n}$ and $\underline{P}$, the restriction of the angle to a value of $\{\forall j \in 1,\ldots,N_f^i | \sphericalangle\left(\underline{n}_j, \underline{P}_j\right) = \pi/3\}$ results in a restriction factor α_{lim} of

$$\forall j \in 1,\ldots,N_f^i,\ \alpha_{\mathrm{lim}_j} \equiv \frac{1}{\|\underline{n}_j\|_2 \cdot \|\underline{P}_j\|_2 \cdot \cos\left(\frac{\pi}{3}\right)} = \frac{2}{\|\underline{n}_j\|_2 \cdot \|\underline{P}_j\|_2}\,. \tag{4.2.3}$$

This limitation factor is introduced into the calculation of the pressure correction Laplacian at the boundaries within this work, leading to the following equation determining the Laplacian of the pressure correction at the boundary control volumes:

$$\forall i \in \left\{1,\ldots,N_{p_b}\right\},\ \exists!\, j \in \left\{1,\ldots,N_f^b\right\},\ \Delta_L \delta p_i^{n+1} = \nabla \delta p_j^{n+1} \cdot \underline{n}_j \tag{4.2.4}$$

with

$$\begin{aligned} &\forall i \in \left\{1,\ldots,N_{p_b}\right\},\ \exists!\, j \in \left\{1,\ldots,N_f^b\right\}, \\ \nabla \delta p_j^{n+1} \cdot \underline{n}_j = -\min &\left(\frac{\|\underline{n}_j\|_2^2}{\underline{n}_j \cdot \underline{P}_j},\ \alpha_{\mathrm{lim}_j}\right) \left[\delta p_{\underline{P}_i}^{n+1} - \nabla \delta p_{\underline{P}_i}^{n} \cdot \left(\underline{n}_j - \frac{\|\underline{n}_j\|_2^2}{\underline{n}_j \cdot \underline{P}_j}\underline{P}_j\right)\right]. \end{aligned} \tag{4.2.5}$$

In the above equations, N_{p_b} and N_f^b denote the number of grid points and the number of cell faces contained within the boundary surface.

4.3. Wave Amplitude Variations

This section is concerned with the definition of the wave amplitude variations, which are required for the derivation of the characteristic boundary conditions to be derived. The derivation of the wave amplitude variations is performed according to the work conducted by Poinsot and Lele [189]. Before doing so, the eigenvalues of the governing flow equations need to be noted. By assuming a homentropic flow on domain boundaries, the following eigenvalues are obtained [83, 90, 164, 205, 268]:

$$\begin{aligned} \lambda_1 &\equiv \|\underline{u}\|_2 - c\,, \\ \lambda_2 &\equiv \|\underline{u}\|_2\,, \\ \lambda_3 &\equiv \|\underline{u}\|_2 + c\,, \end{aligned}$$

where c denotes the speed of sound:

$$c \equiv \sqrt{\left.\frac{\partial p}{\partial \rho}\right|_s} = \sqrt{\gamma \frac{p_{\mathrm{ref}} + p}{\rho}}\,. \tag{4.3.1}$$

Note that the speed of sound assumes homentropic conditions (constant entropy in time and space, see section 2.1). Let Ω be a three-dimensional computational domain. For simplicity reasons, Ω is defined as a cubic domain on an orthonormal basis consisting of the three vectors $\underline{b}_1 \equiv [1\ 0\ 0]^T$, $\underline{b}_2 \equiv [0\ 1\ 0]^T$ and $\underline{b}_3 \equiv [0\ 0\ 1]^T$ with the respective associate metric coordinates x_1, x_2 and x_3. Without loss of generality, the in- and outflow surfaces are set perpendicular to the first coordinate x_1. This leads to the simplification of the velocity to $\|\underline{u}\|_2 = u_1$. Based on this, a derivation with arbitrarily defined in- and outflow surfaces is straight forward. Additionally, $x_1 = 0$ and $x_1 = l$ are set to the locations where the inflow and outflow boundary are located at, see figure 4.3.1. The convective velocities at the in- and outlet boundary faces are assumed to be strictly positive.

Following the theory of characteristics for a subsonic flow [241], the characteristic wave $\mathcal{L}_1$ is entering the computational domain at the inflow, whereas the characteristic waves $\mathcal{L}_2\,, \mathcal{L}_3\,, \ldots\,, \mathcal{L}_{5+N_s}$ are leaving the domain at $x_1 = 0$. At the outflow, $\mathcal{L}_1$ describes an incoming wave, whereas the characteristic waves $\mathcal{L}_2\,, \mathcal{L}_3\,, \ldots\,, \mathcal{L}_{5+N_s}$ denote outgoing waves.

The characteristic waves $\mathcal{L}_2\,$, $\mathcal{L}_3$, $\mathcal{L}_4$ and $\mathcal{L}_{5+1}, \ldots\,, \mathcal{L}_{5+N_s}$ progagate with the convective velocity $\lambda_2 = u$, whereas the acoustic waves $\mathcal{L}_1$ and $\mathcal{L}_5$ travel with the characteristic speed $\lambda_1 = u - c$ and $\lambda_3 = u + c$, respectively. A physical interpretation of the $\mathcal{L}_i$'s is given by Poinsot and Veynante [190]: Consider the linearized Navier-Stokes equations for a one-dimensional inviscid flow with an upstream propagating sonic wave. The characteristic

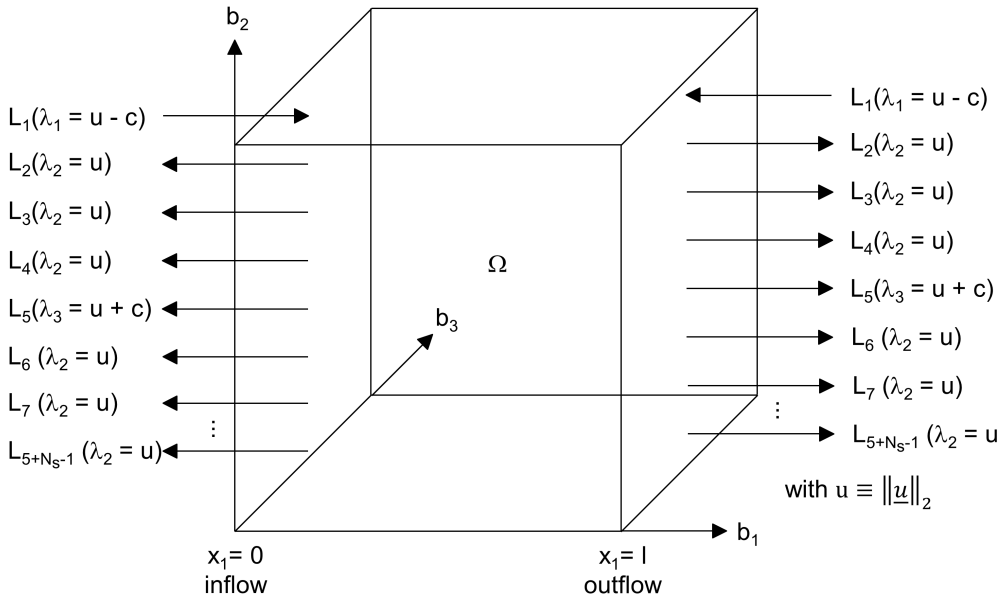

Figure 4.3.1.: Characteristic waves at the in- and outlow of a cubic domain [190]

velocity of this wave amounts to $\lambda_1 = u - c$. In this case, the following hyperbolic equation can be derived which describe the behavior of the propagating wave [190]:

$$\frac{\partial \mathcal{A}_1}{\partial t} + \lambda_1 \frac{\partial \mathcal{A}_1}{\partial x_1} = 0\,. \tag{4.3.2}$$

$\mathcal{A}_1$ denotes the characteristic wave amplitude of the upstream moving wave. Introducing

$$\mathcal{L}_1 \equiv \lambda_1 \frac{\partial \mathcal{A}_1}{\partial x_1} \tag{4.3.3}$$

and reformulating equation (4.3.2) results in [190]:

$$\frac{\partial \mathcal{A}_1}{\partial t} + \mathcal{L}_1 = 0 \Leftrightarrow \mathcal{L}_1 = -\frac{\partial \mathcal{A}_1}{\partial t}\,. \tag{4.3.4}$$

Considering linear acoustics, a physical quantity ϕ can be divided into a mean reference value ϕ_{ref} and an acoustic perturbation ϕ' which is far smaller than the reference value:

$$\phi \equiv \phi_{\text{ref}} + \phi' \quad \text{with} \quad \phi' \ll \phi_{\text{ref}}\,. \tag{4.3.5}$$

Using linear acoustics, an acoustic relation can be derived which fulfills the hyperbolic differential equation (4.3.2) [190]:

$$\mathcal{A}_1 = p' - (\rho c)_{\text{ref}}\, u'\,. \tag{4.3.6}$$

The above relation is conserved along the characteristic line $x_1 + \lambda_1 t = \text{constant}$ [190]. The

product $(\rho c)_{\text{ref}}$ relates the acoustic pressure and velocity perturbations to another and is referred to as the acoustic impedance of the flow. As it can be seen from equation (4.3.4), $\mathcal{L}_1$ may be understood as the negative time variation of the wave amplitude $\mathcal{A}_1$ [190]. $\mathcal{L}_i$, $i = \{1, \ldots, 5 + N_s\}$ is therefore referred to as the amplitude variation of the i-th characteristic wave crossing the boundary surface.

The wave amplitude variations have been originally derived by Kreiss [121], Engquist and Majda [48] and Thompson [241] with the aid of characteristic analysis applied to the Euler equations. Poinsot and Lele [189] extended the formulation of the wave amplitude variations to the Navier-Stokes equations. Poinsot and Veynante [190] added later on the equations for a viscous reactive flow. The wave amplitude variations for a viscous reactive flow are given by the following equations [190]:

$$\mathcal{L}_1 \equiv \lambda_1 \left(\frac{\partial p}{\partial x_1} - \rho c \frac{\partial u_1}{\partial x_1} \right) , \tag{4.3.7}$$

$$\mathcal{L}_2 \equiv \lambda_2 \left(c^2 \frac{\partial \rho}{\partial x_1} - \frac{\partial p}{\partial x_1} \right) , \tag{4.3.8}$$

$$\mathcal{L}_3 \equiv \lambda_2 \frac{\partial u_2}{\partial x_1} , \tag{4.3.9}$$

$$\mathcal{L}_4 \equiv \lambda_2 \frac{\partial u_3}{\partial x_1} , \tag{4.3.10}$$

$$\mathcal{L}_5 \equiv \lambda_3 \left(\frac{\partial p}{\partial x_1} + \rho c \frac{\partial u_1}{\partial x_1} \right) , \tag{4.3.11}$$

$$\mathcal{L}_6 \equiv \lambda_2 \frac{\partial Y_1}{\partial x_1} , \tag{4.3.12}$$

$$\mathcal{L}_7 \equiv \lambda_2 \frac{\partial Y_2}{\partial x_1} , \tag{4.3.13}$$

$$\vdots$$

$$\mathcal{L}_{5+N_s-1} \equiv \lambda_2 \frac{\partial Y_{N_s-1}}{\partial x_1} . \tag{4.3.14}$$

The wave amplitude variation belonging to the mass fraction of the last species Y_{N_s} does not have to be computed, as the boundary value of Y_{N_s} is already determined by all other boundary mass fractions through the use of Dalton's law. So far, an approach which enables the two- or three-dimensional solution of the wave amplitude variations given above does not exist. However, by assuming a one-dimensional inviscid flow at the boundary surface, it is possible to solve the $\mathcal{L}_i$'s, $i = \{1, \ldots, 5 + N_s\}$. Following this assumption, the so-called Local One-Dimensional Inviscid (LODI) relations can be introduced and derived for the specific solution strategy considered [190]. This is performed in the following for the CPM method.

4.4. Local One-Dimensional Inviscid Relations

The introduction of the wave amplitude variations $\mathcal{L}_i$, $i = \{1, \ldots, 5 + N_s\}$ into the reactive Navier-Stokes equations at the boundaries is the key idea of the NSCBC approach, whereby the wave amplitudes crossing the boundaries have to be determined each for themselves.

The LODI (Local One-Dimensional Inviscid) relations are derived next for the CPM solution method. The formulation of these is limited within this work to the application of subsonic flows. An extension to trans- and supersonic flows can be performed analogously, taking into account the theory of characteristics. It should be mentioned at this point that the application of the LODI relations onto the boundary surfaces is restricted to one-dimensional considerations, which means that the boundary surfaces have to be planar and located perpendicular to the flow crossing the boundary plane.

In a first step, the linear equations to be solved - being equations (3.4.7)-(3.4.16), (3.4.20) and (3.4.23)-(3.4.33) - are formulated in one dimension. Moreover, the terms modeling heat conduction, friction and the influence of chemical reactions are set to zero. The application of this approach onto the divergence constraint results in the following equation:

$$\frac{\partial u_1^n}{\partial x_1} = -\frac{1}{\gamma^n \left(p_{\mathrm{ref}} + p^n\right)} \left(\left.\frac{\partial p}{\partial t}\right|_n + u_1^n \frac{\partial p^n}{\partial x_1} \right) . \tag{4.4.1}$$

The interim formulation of the momentum equations then read:

$$\left.\frac{\partial \left(\rho u_1\right)}{\partial t}\right|_* + \frac{\partial \left[\left(\rho u_1\right)^n u_1^*\right]}{\partial x_1} + \frac{\partial p^n}{\partial x_1} = 0 , \tag{4.4.2}$$

$$\left.\frac{\partial \left(\rho u_2\right)}{\partial t}\right|_* + \frac{\partial \left[\left(\rho u_1\right)^n u_2^*\right]}{\partial x_1} = 0 , \tag{4.4.3}$$

$$\left.\frac{\partial \left(\rho u_3\right)}{\partial t}\right|_* + \frac{\partial \left[\left(\rho u_1\right)^n u_3^*\right]}{\partial x_1} = 0 . \tag{4.4.4}$$

The pressure correction equation reduces to the following equation:

$$\frac{\partial^2 \delta p^{n+1}}{\partial x_1^2} - \frac{\alpha_{\mathrm{pr}}}{f\left(\Delta t\right) \Delta t} \frac{\rho^n}{\gamma^n \left(p_{\mathrm{ref}} + p^n\right)} \delta p^{n+1} = \frac{\alpha_{\mathrm{pr}}}{f\left(\Delta t\right)} \left[\frac{\partial \left(\rho^n \underline{u}^*\right)}{\partial x_1} + u_1^* \left(c^n\right)^{-2} \frac{\partial p^n}{\partial x_1} \right] . \tag{4.4.5}$$

The correction of the velocity field and divergence constraint yield:

$$u_1^{**} = u_1^* - \frac{f\left(\Delta t\right)}{\alpha_{\mathrm{pr}} \rho^n} \frac{\partial \delta p^{n+1}}{\partial x_1} , \tag{4.4.6}$$

$$\frac{\partial u_1^{n+1}}{\partial x_1} = -\frac{1}{\gamma^n \left(p_{\mathrm{ref}} + p^{n+1}\right)} \left(\left.\frac{\partial p}{\partial t}\right|_{n+1} + u_1^{n+1} \frac{\partial p^{n+1}}{\partial x_1} \right) . \tag{4.4.7}$$

The one-dimensional form of the enthalpy and species mass equations without the influence of heat conduction, dissipation and chemical production read:

$$\left.\frac{\partial\left(\rho h\right)}{\partial t}\right|_{n+1} + \frac{\partial[\left(\rho u_1\right)^{n+1} h^{n+1}]}{\partial x_1} - \left.\frac{\partial p}{\partial t}\right|_{n+1} - u_1^{n+1}\frac{\partial p^{n+1}}{\partial x_1} = 0\,, \tag{4.4.8}$$

$$\forall i \in \{1,\ldots,N_s\}\,,\ \left.\frac{\partial\left(\rho Y_i\right)}{\partial t}\right|_{n+1} + \frac{\partial[\left(\rho u_1\right)^{n+1} Y_i^{n+1}]}{\partial x_1} = 0\,. \tag{4.4.9}$$

In a next step, the terms within the partial differential equations to be solved at the boundaries consisting of spatial derivatives are converted into algebraic terms by means of the finite volume discretization method. For this to happen, the computational domain is split up into a finite number of control volumes. The partial differential equations are then solved on each control volume. This requires the equations to be integrated over the respective control volume. THETA uses a cell-centered arrangement [106] of the dual grid. The control volumes are placed around the vertices of the primary grid. As a result, the grid points are located at the center of the control volume cells. The variables are consequently stored in the points located at the center of the dual grid cells, see figure 4.4.2. Within the equations to be solved, first and second derivatives of variables appear. These derivatives introduce additional unknowns into the system of equations. By means of Gauss' theorem [4, 82, 101] - which is also known as Ostrogradsky's theorem and theorem of Gauss-Ostrogradsky -, terms including the i-th derivative of a variable can be transformed into terms consisting of the $(i-1)$-th. This reduces the number of unknowns in the system of equations to be solved and thus decreases the computational effort. The theorem of Gauss is described in the following.

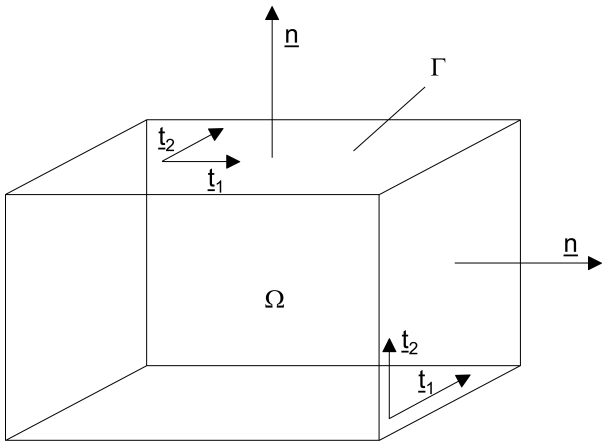

Figure 4.4.1.: Sketch of the compact computational domain Ω and its piecewise smooth boundary surface Γ

Let Ω be a compact and simply connected computational domain and Γ its boundary

surface, which is defined as being plane and piecewise smooth[1]. Moreover, let $\underline{\Psi}$ be a continuously differentiable vector field. GAUSS' theorem relates the flux of $\underline{\Psi}$ through Γ to the divergence of the vector field inside Ω by the following relation:

$$\int_{\Omega} \nabla \cdot \underline{\Psi} d\Omega = \oint_{\Gamma} (\underline{\Psi} \cdot \underline{n}|_{\Gamma}) \, d\Gamma \,. \tag{4.4.10}$$

$\underline{n}$ denotes the outwards-pointing vector of the piecewise smooth boundary surface Γ, see figure 4.4.1. The normal vector of a plane surface can be determined based on the vector product of the vectors $\underline{t}_1$ and $\underline{t}_2$ spanning the surface Γ.

$$\underline{n} \equiv \underline{t}_1 \times \underline{t}_2 \,. \tag{4.4.11}$$

The Euclidean norm of the vector $\underline{n}$ corresponds to the area of the parallelogram spanned by the vectors $\underline{t}_1$ and $\underline{t}_2$ and thus to the area of the surface Γ:

$$\|\underline{n}\|_2 \equiv \|\underline{t}_1\|_2 \cdot \|\underline{t}_2\|_2 \cdot \sin\left[\sphericalangle\left(\underline{t}_1, \underline{t}_2\right)\right] \,. \tag{4.4.12}$$

The application of GAUSS' theorem introduces fluxes at cell interfaces, which are not initially known. However, they can be constructed using nodal values. For instance, the mass flux appearing as part of the convective terms at the left hand side of the momentum and scalar equations is treated as a surface flux and can be put together based on the nodal density and velocity values. The mass flux values are assumed to be constant along the control volume interfaces and are computed based on the arithmetic average of the adjoined nodal values, see section 1.3.

Applying the finite volume discretization and GAUSS' theorem to the generic convective term $\rho\underline{u}\phi$ leads to the following expression:

$$\begin{aligned} \int_{\Omega} \nabla \cdot (\rho\underline{u}\phi) \, d\Omega = \oint_{\Gamma} (\rho\underline{u}\phi \cdot \underline{n}|_{\Gamma}) \, d\Gamma &= \oint_{\Gamma} (\rho\underline{u} \cdot \underline{n}|_{\Gamma} \, \phi) \, d\Gamma \\ &\approx \sum_{j=1}^{N_f} (\underbrace{\rho\underline{u} \cdot \underline{n}}_{\equiv \dot{m}} \phi)_j \\ &= \sum_{j=1}^{N_f^i} \dot{m}_j \phi_j + \sum_{j=1}^{N_f^b} \dot{m}_j \phi_j \,, \end{aligned} \tag{4.4.13}$$

where $N_f^i + N_f^b$ equals N_f. $\dot{m}_j \equiv \rho_j \underline{u}_j \cdot \underline{n}_j$ denotes the mass flux at the cell face j of a control

[1] A smooth surface is defined as being constructed by continuously differentiable curves, i.e. with the restriction that their spatial derivatives do not vanish at any given point.

volume. The values of ϕ at the cell faces are built by taking into account its nodal neighbors. Herefore, different known interpolation techniques can be used, as e.g. the commonly used upwind, linear upwind, quadratic upwind or central differencing schemes, which have been implemented into THETA within the scope of previous works [36, 267].

Let Θ be an arbitrary term. Moreover, Assume a constant value of Θ within the control volume Ω_i. The integration of Θ over Ω_i can then be performed through the following computation:

$$\forall i \in \{1, \ldots, N_p\}\,, \int_{\Omega_i} \Theta d\Omega_i \approx \Theta \int_{\Omega_i} d\Omega_i = \Theta \Delta V_i\,. \tag{4.4.14}$$

ΔV_i denotes the volume of the respective control volume i being integrated over. Based on the descriptions conducted above, the spatial derivatives of the equations (4.4.1)-(4.4.8) are now converted into algebraic terms. This is performed exemplarily for one control volume Ω_i. The derivation regarding the remaining control volumes is performed analogously. Concering the notation of the equations to follow, the subscript i is omitted for simplicity reasons. As the discretization schemes applied to the time derivative of the respective terms is not of primary interest for the derivation of the LODI relations, the time derivatives are given in the following in the undiscretized form. The derivation presented within this work is conducted following the assumption that the boundaries are located perpendicular to the one-dimensional approximation of the flow, see figure 4.3.1. As a consequence of this, only one velocity component is required to construct the mass flux, being u_1. The mass flux at the boundary b used in the following set of equations thus reads:

$$\dot{m}_b = \rho_b \underline{u}_b \cdot \underline{n}_b = \rho_b u_{1_b} \|\underline{n}_b\|_2\,. \tag{4.4.15}$$

Moreover, the variable N_f^i characterizes in the following the number of inner faces belonging to the respective boundary cell. Assuming one control volume is mapped to exactly one in- or outflow boundary face, the number of boundary faces N_f^b equals one. The subscript b denotes consequently the boundary cell face of the respective boundary control volume.

Since all terms of the equation (4.4.1) determining the velocity divergence are discretized using the same volume integration, the numerical computation of the divergence constraint remains unchanged:

$$\left.\frac{\partial u_1^n}{\partial x_1}\right|_b = -\frac{1}{\gamma_b^n \left(p_{\mathrm{ref}} + p_b^n\right)} \left(\left.\frac{\partial p}{\partial t}\right|_{n,b} + u_1^n \left.\frac{\partial p^n}{\partial x_1}\right|_b \right)\,. \tag{4.4.16}$$

The determination of the derivative of the pressure p with respect to x_1 at the boundary b will be described further below. Integrating the momentum equations at the interim step

(4.4.2) over one control volume leads to the following set of equations:

$$\left.\frac{\partial\left(\rho u_1\right)}{\partial t}\right|_{*,b}\Delta V_b+\sum_{j=1}^{N_f^i}\dot{m}_j^n u_{1_j}^*+\dot{m}_b^n u_{1_b}^*+\left.\frac{\partial p^n}{\partial x_1}\right|_b\Delta V_b = 0\,, \tag{4.4.17}$$

$$\left.\frac{\partial\left(\rho u_2\right)}{\partial t}\right|_{*,b}\Delta V_b+\sum_{j=1}^{N_f^i}\dot{m}_j^n u_{2_j}^*+\dot{m}_b^n u_{2_b}^* = 0\,, \tag{4.4.18}$$

$$\left.\frac{\partial\left(\rho u_3\right)}{\partial t}\right|_{*,b}\Delta V_b+\sum_{j=1}^{N_f^i}\dot{m}_j^n u_{3_j}^*+\dot{m}_b^n u_{3_b}^* = 0\,. \tag{4.4.19}$$

V_b describes the volume of the respective boundary cell b regarded. The semi-discretized pressure correction equation can be expressed through the following equation:

$$\begin{aligned}&\sum_{j=1}^{N_f^i}\left.\frac{\partial\delta p^{n+1}}{\partial x_1}\right|_j\cdot\underline{n}_j+\left.\frac{\partial\delta p^{n+1}}{\partial x_1}\right|_b\cdot\underline{n}_b-\frac{\alpha_{\mathrm{pr}}}{f\left(\Delta t\right)}\frac{\Delta V_b}{\Delta t}\frac{\rho_b^n}{\gamma_b^n\left(p_{\mathrm{ref}}+p_b^n\right)}\delta p_b^{n+1}\\ &=\frac{\alpha_{\mathrm{pr}}}{f\left(\Delta t\right)}\left[\sum_{j=1}^{N_f^i}\dot{m}_j^*+\dot{m}_b^*+u_{1_b}^*\left(c^n\right)^{-2}\left.\frac{\partial p^n}{\partial x_1}\right|_b\Delta V_b\right]\,.\end{aligned} \tag{4.4.20}$$

The formula determining the second interim velocity field and the velocity divergence at the time step $n+1$ read:

$$u_{1_b}^{**}=u_{1_b}^*-\frac{f\left(\Delta t\right)}{\alpha_{\mathrm{pr}}\rho^n}\left.\frac{\partial\delta p^{n+1}}{\partial x_1}\right|_b\,, \tag{4.4.21}$$

$$\left.\frac{\partial u_1^{n+1}}{\partial x_1}\right|_b=-\frac{1}{\gamma_b^n\left(p_{\mathrm{ref}}+p_b^{n+1}\right)}\left(\left.\frac{\partial p}{\partial t}\right|_{n+1,b}+u_{1_b}^{n+1}\left.\frac{\partial p^{n+1}}{\partial x_1}\right|_b\right)\,. \tag{4.4.22}$$

Applying the finite volume discretization at the domain boundaries to the semi-discretized enthalpy and species mass equations results in the following set of equations:

$$\begin{aligned}&\left.\frac{\partial\left(\rho h\right)}{\partial t}\right|_{n+1,b}\Delta V_b+\sum_{j=1}^{N_f^i}\dot{m}_j^{n+1}h_j^{n+1}+\dot{m}_b^{n+1}h_b^{n+1}\\ &-\left(\left.\frac{\partial p}{\partial t}\right|_{n+1,b}+u_{1_b}^{n+1}\left.\frac{\partial p^{n+1}}{\partial x_1}\right|_b\right)\Delta V_b=0\,,\end{aligned} \tag{4.4.23}$$

$$\forall i\in\{1,\ldots,N_s\}\,,\ \left.\frac{\partial\left(\rho Y_i\right)}{\partial t}\right|_{n+1,b}\Delta V_b+\sum_{j=1}^{N_f^i}\dot{m}_j^{n+1}Y_{i_j}^{n+1}+\dot{m}_b^{n+1}Y_{i_b}^{n+1}=0\,. \tag{4.4.24}$$

As noted earlier on, the surface boundaries are located perpendicular to the first basis vector

which corresponds to the x_1 coordinate, see figure 4.3.1. In the following, the spatial derivative terms at the boundaries to be determined by the LODI approach are presented:

$$\left.\frac{\partial\left(\rho^n u_1^*\right)}{\partial x_1}\right|_b = \left.\frac{\partial\left(\rho u_1\right)^n}{\partial x_1}\right|_b = \frac{1}{\left(c_b^n\right)^2}\left[\mathcal{L}_{2_b}^n + \frac{1}{2}\left(\mathcal{L}_{5_b}^n + \mathcal{L}_{1_b}^n\right)\right], \tag{4.4.25}$$

$$\left.\frac{\partial\left(\rho u_1\right)^{n+1}}{\partial x_1}\right|_b = \frac{1}{\left(c_b^{n+1}\right)^2}\left[\mathcal{L}_{2_b}^{n+1} + \frac{1}{2}\left(\mathcal{L}_{5_b}^{n+1} + \mathcal{L}_{1_b}^{n+1}\right)\right], \tag{4.4.26}$$

$$\left.\frac{\partial p^n}{\partial x_1}\right|_b = \frac{1}{2}\left(\frac{\mathcal{L}_{5_b}^n}{\lambda_{3_b}^n} - \frac{\mathcal{L}_{1_b}^n}{\lambda_{1_b}^n}\right), \tag{4.4.27}$$

$$\left.\frac{\partial \delta p^{n+1}}{\partial x_1}\right|_b = \frac{1}{2}\left[\left(\frac{\mathcal{L}_{5_b}^*}{\lambda_{3_b}^*} - \frac{\mathcal{L}_{1_b}^*}{\lambda_{1_b}^*}\right) - \left(\frac{\mathcal{L}_{5_b}^n}{\lambda_{3_b}^n} - \frac{\mathcal{L}_{1_b}^n}{\lambda_{1_b}^n}\right)\right], \tag{4.4.28}$$

$$\begin{aligned}\left.\frac{\partial h^{n+1}}{\partial x_1}\right|_b = {} & \frac{1}{2\rho_b^{n+1}}\left[\frac{\gamma_b^n}{\gamma_b^n - 1} - \frac{h_b^n}{\left(c_b^{n+1}\right)^2}\right]\left(\frac{\mathcal{L}_{5_b}^{n+1}}{\lambda_{3_b}^{n+1}} - \frac{\mathcal{L}_{1_b}^{n+1}}{\lambda_{1_b}^{n+1}}\right) \\ & - \frac{h_b^n}{\rho_b^{n+1}}\frac{\mathcal{L}_{1_b}^{n+1}}{\lambda_{2_b}^{n+1}\cdot\left(c_b^{n+1}\right)^2},\end{aligned} \tag{4.4.29}$$

$$\forall i \in \{1,\ldots,N_s-1\},\ \left.\frac{\partial Y_i^{n+1}}{\partial x_1}\right|_b = \frac{\mathcal{L}_{5+i_b}^{n+1}}{\lambda_{2_b}^{n+1}}. \tag{4.4.30}$$

According to Poinsot and Lele [189], the equations relating the terms noted above to the characteristic wave amplitude variations are from now on referred to as the LODI relations. The LODI relations (4.4.25)-(4.4.28) and (4.4.30) are a simple linear combination of the wave amplitude variations (4.3.7)-(4.3.14). The determination of the LODI relation for the spatial derivative of the enthalpy is more complicated. Its derivation is thus presented in the following: Consider a calorically and thermally perfect homogeneous gas mixture composed of N_s pure substances. The definition of a pure substance is in this context limited to the ones characterized by a standard enthalpy of formation equal to zero, e.g. O_2, N_2, H_2, etc. (standard state of a pure substance). The enthalpy change dh is then defined through the following relation:

$$\begin{aligned} dh &= \underbrace{\left.\frac{\partial h}{\partial T}\right|_{p,Y_i}}_{\equiv c_p} dT + \sum_{i=1}^{N_s}\left.\frac{\partial h}{\partial Y_i}\right|_{T,p,Y_{j,j\neq i}}\underbrace{dY_i}_{=0\,\forall i} \\ &= \sum_{i=1}^{N_s} Y_i \int_{T_0}^{T}\left.\frac{\partial c_{p_i}\left(\tilde{T}\right)}{\partial \tilde{T}}\right|_{p,Y_i} d\tilde{T} \quad \text{with} \quad h \equiv \sum_{i=1}^{N_s} Y_i\left[h_{f_i}^0 + \int_{T_0}^{T} c_{p_i}\left(\tilde{T}\right) d\tilde{T}\right] \\ &= \sum_{i=1}^{N_s} Y_i c_{p_i} dT = c_p dT\,. \end{aligned} \tag{4.4.31}$$

Equation (4.4.31) describes the variation of the enthalpy. The second term describing the influence of changes within the mixture composition vanishes as the derivation of the LODI relation for the spatial derivative of the enthalpy is limited to homogeneous gas mixtures. Let us consider a one-dimensional flow in the following. For this type of flow, equation (4.4.31) can be set up and integrated over two separate points 1 and 2 along one streamline:

$$\int_1^2 dh = \int_1^2 c_p dT \Rightarrow h_2 - h_1 = c_p \left(T_2 - T_1\right) . \tag{4.4.32}$$

Based on equation (4.4.31), point 1 has the state $h_1 = c_p T_1$, whereas point 2 possesses the state $h_2 = c_p T_2$. In a more general sense, let us denote

$$h = c_p T \tag{4.4.33}$$

as one arbitrary state of a homogeneous calorically and thermally perfect gas mixture composed of N_s pure substances. Inserting the equation of state (2.2.5) into formula (4.4.33) results in an equation of state describing the relation between the density, pressure and enthalpy:

$$h = c_p T = \frac{c_p}{R} \frac{p_{\mathrm{ref}} + p}{\rho} = \frac{\gamma}{\gamma - 1} \frac{p_{\mathrm{ref}} + p}{\rho} . \tag{4.4.34}$$

Formulating equation (4.4.34) for the pressure at the boundary b yields the following equation:

$$p_b = \frac{\gamma_b - 1}{\gamma_b} \rho_b h_b - p_{\mathrm{ref}} . \tag{4.4.35}$$

The boundary pressure derivative with respect to the coordinate x_1 can be written as a total derivative dependent on the density and enthalpy:

$$\left.\frac{\partial p}{\partial x_1}\right|_b = \rho_b h_b \left.\frac{\partial (\frac{\gamma - 1}{\gamma})}{\partial x_1}\right|_b + \frac{\gamma_b - 1}{\gamma_b} \rho_b \left.\frac{\partial \rho}{\partial x_1}\right|_b + \frac{\gamma_b - 1}{\gamma_b} h_b \left.\frac{\partial h}{\partial x_1}\right|_b . \tag{4.4.36}$$

Considering homogeneous gas mixtures, the spatial changes of the heat capacity ratio are far smaller than the ones regarding the pressure and density and are thus neglected in the following. This results in the following approximation:

$$\begin{aligned} \left.\frac{\partial p}{\partial x_1}\right|_b &\approx \frac{\gamma_b - 1}{\gamma_b} \rho_b \left.\frac{\partial \rho}{\partial x_1}\right|_b + \frac{\gamma_b - 1}{\gamma_b} h_b \left.\frac{\partial h}{\partial x_1}\right|_b \\ \Rightarrow \quad \left.\frac{\partial h}{\partial x_1}\right|_b &\approx \frac{\gamma_b}{\gamma_b - 1} \left(\frac{1}{\rho_b} \left.\frac{\partial p}{\partial x_1}\right|_b - \frac{h_b}{\rho_b} \left.\frac{\partial \rho}{\partial x_1}\right|_b \right) . \end{aligned} \tag{4.4.37}$$

The pressure derivative is already known from the LODI relation (4.4.27). The density

derivative is determined based on formula (4.3.8). Introducing relations (4.3.8) and (4.4.27) into equation (4.4.37) results in the determination of the sought spatial enthalpy derivative:

$$\begin{aligned}\left.\frac{\partial h}{\partial x_1}\right|_b &\approx \frac{\gamma_b}{\gamma_b-1}\left\{\frac{1}{2\rho_b}\left(\frac{\mathcal{L}_{5_b}}{\lambda_{3_b}}-\frac{\mathcal{L}_{1_b}}{\lambda_{1_b}}\right)-\frac{1}{c_b^2}\frac{h_b}{\rho_b}\left[\frac{\mathcal{L}_{2_b}}{\lambda_{2_b}}-\frac{1}{2}\left(\frac{\mathcal{L}_{5_b}}{\lambda_{3_b}}-\frac{\mathcal{L}_{1_b}}{\lambda_{1_b}}\right)\right]\right\} \\ &= \frac{1}{2\rho_b}\left(\frac{\gamma_b}{\gamma_b-1}-\frac{h_b}{c_b^2}\right)\left(\frac{\mathcal{L}_5}{\lambda_3}-\frac{\mathcal{L}_{1_b}}{\lambda_{1_b}}\right)-\frac{h_b}{\rho_b}\frac{\mathcal{L}_{2_b}}{\lambda_{2_b}\cdot c_b^2}\,. \end{aligned} \tag{4.4.38}$$

As can be seen based on the equations to be solved (4.4.16)-(4.4.24), a part of the spatial derivatives within these equations have been converted into their respective algebraic terms. For instance, the convective term within the momentum equations has been transformed into an algebraic term involving the mass flux, see equations (4.4.17)-(4.4.19).

The terms which have been altered by Gauss' theorem can be recomputed based on their known derivatives (4.4.25)-(4.4.29). This can be done by using Gauss' theorem reversely, as proposed by Lourier [136]. By applying a Gauss reconstruction of the algebraic terms based on their derivatives ensures both to be consistent with each other, since they are calculated one from another. The algebraic terms denote the terms obtained through a numerical integration of their respective spatial derivatives.

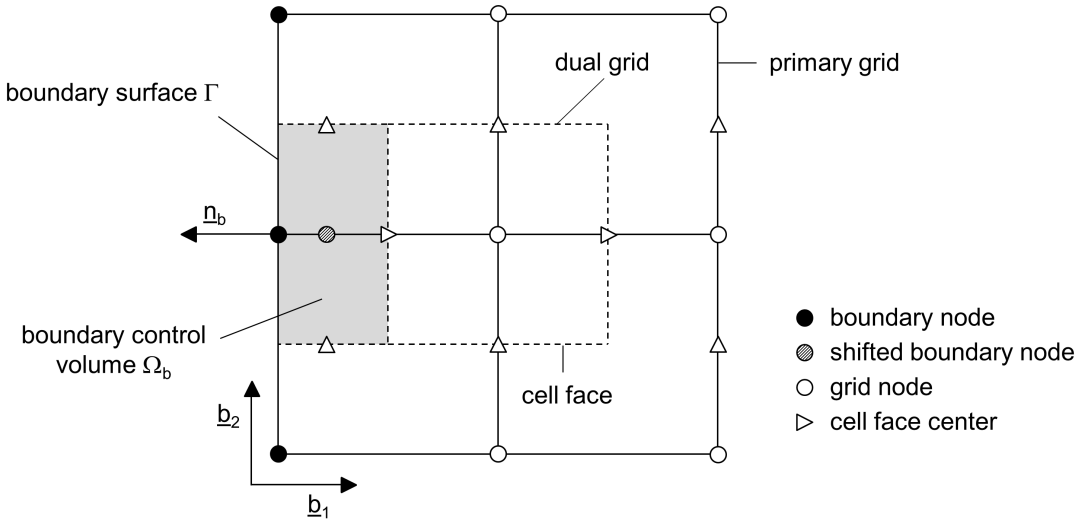

Figure 4.4.2.: Graphical visualization of the rectangular-shaped boundary control volume Ω_b (according to [122])

The Gauss reconstruction is given in the following in detail for the computation of the boundary mass flux $\dot{m}_b$. Let Ω_b be a rectangular-shaped control volume of the boundary. Γ denotes its piecewise smooth boundary surface, see figure 4.4.2.

Integrating the divergence of the momentum $\rho\underline{u}$ together with the outwards-pointing vector of Γ then results in the following approximation:

$$\begin{aligned}
\int_{\Omega_b} \nabla\cdot(\rho\underline{u})\ \underline{n}_b\, d\Omega_b &= \oint_{\Gamma} (\rho\underline{u}\cdot\underline{n})_{\Gamma}\ \underline{n}_b\, d\Gamma \\
&\approx \sum_{j=1}^{N_f} (\rho\underline{u}\cdot\underline{n})_j\ \underline{n}_b \\
&= \sum_{j=1}^{N_f^i} (\rho\underline{u}\cdot\underline{n})_j\ \underline{n}_b + \sum_{j=1}^{N_f^b} (\rho\underline{u}\cdot\underline{n})_j\ \underline{n}_b \\
&= \sum_{j=1}^{N_f^i} (\rho\underline{u}\cdot\underline{n})_j\ \underline{n}_b + (\rho_b\underline{u}_b\cdot\underline{n}_b)\ \underline{n}_b \\
&= \sum_{j=1}^{N_f^i} (\rho\underline{u}\cdot\underline{n})_j\ \underline{n}_b + (\rho_b u_{1_b}\,\underline{b}_1\cdot\underline{n}_b)\ \underline{n}_b \quad \text{as } \underline{n}_b \parallel \underline{b}_1 = \begin{bmatrix}1\\0\\0\end{bmatrix} \\
&= \sum_{j=1}^{N_f^i} (\rho\underline{u}\cdot\underline{n})_j\ \underline{n}_b + \rho_b u_{1_b}\,\|\underline{n}_b\|_2^2\,\underline{b}_1\,. \qquad (4.4.39)
\end{aligned}$$

As the mass flux at the boundary reads $\dot{m}_b = \rho_b u_{1_b}\|\underline{n}_b\|_2$, the approximation (4.4.39) can be reformulated into the following formula:

$$\begin{aligned}
\dot{m}_b\,\underline{b}_1 &\approx \frac{1}{\|\underline{n}_b\|_2}\left[\int_{\Omega_b}\nabla\cdot(\rho\underline{u})\ \underline{n}_b\,\Gamma - \sum_{j=1}^{N_f^i}(\rho\underline{u}\cdot\underline{n})_j\ \underline{n}_b\right] \\
&\approx \frac{1}{\|\underline{n}_b\|_2}\left[\nabla\cdot(\rho\underline{u})_b\ \underline{n}_b\,\Delta V_b - \sum_{j=1}^{N_f^i}(\rho\underline{u}\cdot\underline{n})_j\ \underline{n}_b\right] \\
&= \frac{1}{\|\underline{n}_b\|_2}\left[\nabla\cdot(\rho u_1\underline{b}_1)_b\ \underline{n}_b\,\Delta V_b - \sum_{j=1}^{N_f^i}(\rho\underline{u}\cdot\underline{n})_j\ \underline{n}_b\right] \\
&= \frac{1}{\|\underline{n}_b\|_2}\left[\left.\frac{\partial(\rho u_1)}{\partial x_1}\right|_b \underline{n}_b\,\Delta V_b - \sum_{j=1}^{N_f^i}(\rho\underline{u}\cdot\underline{n})_j\ \underline{n}_b\right]. \qquad (4.4.40)
\end{aligned}$$

The boundary surfaces are assumed to be located perpendicular to the first basis vector $\underline{b}_1$, see figure 4.3.1. Thus, the mass flux at the boundary can finally be calculated through the

following approximation:

$$\begin{aligned} \dot{m}_b &\approx \frac{1}{\|\underline{n}_b\|_2} \left[\left. \frac{\partial (\rho u_1)}{\partial x_1} \right|_b \|\underline{n}_b\|_2 \, \Delta V_b - \sum_{j=1}^{N_f^i} (\rho \underline{u} \cdot \underline{n})_j \, \|\underline{n}_b\|_2 \right] \\ &= \left. \frac{\partial (\rho u_1)}{\partial x_1} \right|_b \Delta V_b - \sum_{j=1}^{N_f^i} (\rho \underline{u} \cdot \underline{n})_j \, . \end{aligned} \tag{4.4.41}$$

Figure 4.4.2 illustrates the graphical visualization of the rectangular-shaped boundary control volume Ω_b according to the reference [122]. The shifted boundary node seen within figure 4.4.2 denotes a copy of the boundary point, which has been displaced by a certain distance perpendicular to the boundary surface. This point is shifted from the boundary surface towards the inner field for the purpose of being able to determine the gradient of the physical quantities at the boundary surface [122]. Following this approach, the shifted boundary point is treated by the linear solver as it were an inner grid point. The derivation of the GAUSS reconstruction for the pressure, pressure derivative, enthalpy and species mass fractions can be performed analogously to the GAUSS reconstruction for the mass flux. The results are given by the following set of equations:

$$\underline{v}_b \approx \left. \frac{\partial \underline{v}}{\partial x_1} \right|_b \Delta V_b - \sum_{j=1}^{N_f^i} (\underline{v} \cdot \underline{n})_j \quad \text{with} \quad \underline{v} \equiv \begin{bmatrix} p \\ \delta p \\ h \\ Y_1 \\ Y_2 \\ \vdots \\ Y_{N_s-1} \end{bmatrix} . \tag{4.4.42}$$

The density at the boundary ρ_b is determined by means of the equation of state, see equation (2.2.5):

$$\rho_b = \frac{p_{\text{ref}} + p_b}{R_b T_b} \, . \tag{4.4.43}$$

For the variables T_b and R_b appearing in formula (4.4.43), known values of the previous time step are used. The velocity vector at the boundary $\underline{u}_b$ is reconstructed using the known mass flux and density boundary values:

$$\underline{u}_b = \frac{\dot{m}_b}{\rho_b} \cdot \frac{\underline{n}_b}{\|\underline{n}_b\|_2^2} \, . \tag{4.4.44}$$

The temperature T_b is finally obtained by solving relation (2.2.9) iteratively at the boundary

by means of the Newton-Raphson method [169, 199].

The NSCBC approach has been implemented into the THETA code to be used in conjunction with the CPM solution strategy. Thus aside from fully reflective boundary constraints, partially non-reflective boundary conditions can be applied to a numerical simulation.

Based on the theory of characteristics [121, 189, 190], outgoing waves are calculated from inner field values and their respective derivatives. However, the incoming waves cannot be computed directly from known values. $\mathcal{L}_1$ describes the variation of the incoming wave at a subsonic outflow by which the pressure is determined. This is due to the introduction of reflected waves by the outside flow back into the domain. A reflected wave is produced in the case the outflow pressure differs from the reference pressure at infinity, given by p_{ref} [190]. Figure 4.4.3 illustrates the induced waves at a partially non-reflective outflow according to the thoughts of Poinsot and Veynante [190].

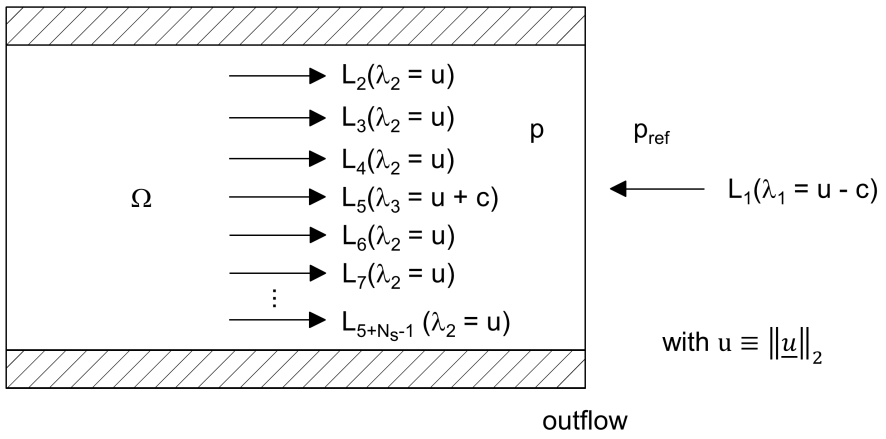

Figure 4.4.3.: Induced waves at a partially non-reflective outflow [190]

A reflected wave at the outlet surface is generated as the outflow pressure tries to converge towards the reference pressure [190]. By setting a perfectly non-reflective boundary condition, this information is not brought back into the domain causing the problem to be ill-posed [103, 212, 213]. A remedy to this difficulty is to specify a partially non-reflective outflow along with the prescription of an incoming wave $\mathcal{L}_1$ at the outlet boundary surface [190]. Poinsot and Veynante [190] give the following formula for the calculation of an incoming wave at the outflow:

$$\mathcal{L}_1 = K \cdot (p_b - p_{\text{ref}}) \ . \tag{4.4.45}$$

K denotes the relaxation coefficient. A K-value of zero forces the amplitude of the reflected waves to be zero, thus being equivalent to a perfectly non-reflective behavior of the boundary.

RUDY and STRIKWERDA [212] suggested the following formula for K:

$$K \equiv \sigma \left(1 - \mathrm{Ma}_{\mathrm{max}}^2\right) \frac{c}{l_{\mathrm{char}}} \,. \tag{4.4.46}$$

σ, $\mathrm{Ma}_{\mathrm{max}}$ and l_{char} describe a constant coefficient, the maximum occurring Mach number within the flow field and a characteristic size of the computational domain, respectively. Small values of σ may lead to drifts of the mean boundary pressure, whereas high σ-values produce significant amount of reflection.

SELLE et al. [221] proposed the following analytical formula which relates the reflection coefficient R to the relaxation coefficient K:

$$R \equiv \frac{1}{\sqrt{1 + \left(\frac{4\pi f}{K}\right)^2}} \,. \tag{4.4.47}$$

Equation (4.4.47) has recently been checked by MÜHLBAUER [162] in comparison with experimental data for a partially non-reflective behavior of the outflow of a three-dimensional application test case. The reflection coefficient R can be understood as the amount of reflection generated by an induced acoustic wave. R can thus be obtained by taking the ratio of the reflected to the incoming wave amplitude. Equation (4.4.47) reveals a dependency of the reflection coefficient on the frequency f of the emitted waves. Large values of σ produce high values of K and thus a reflection coefficient approaching unity. This has to be avoided in the case where a partially non-reflective boundary condition is wanted [190]. SELLE et al. [221] suggested a σ-range of $\sigma \in [0.1; \pi]$ to prevent mean pressure drifts and high R-values. This proposition is in accordance with suggestions provided by RUDY and STRIKWERDA [212], who derived an optimal value of $\sigma = 0.27$ to ensure well posedness of the computational problem. Conducting numerical simulations within this work, a σ-value of 0.27 is applied.

5. Verification and Validation of the Compressible Projection Method

5.1. Terminology

Before addressing the verification and validation of the compressible projection method, it is important to differentiate between the terms *verification* and *validation*. The American Institute of Aeronautics and Astronautics (AIAA) defines the verification and validation processes of numerical methods as follows [3]:

- Verification: *"The process of determining that a model implementation accurately represents the developer's conceptual description of the model and the solution to the model."*
- Validation: *"The process of determining the degree to which a model is an accurate representation of the real world from the perspective of the intended uses of the model."*

Oberkampf [173, 174] has been doing some work on clarifying the verification and validation processes in computational fluid dynamics. He gives the following understandings of code verification and validation [173]:

"Verification provides evidence (substantiation) that the conceptual [...] *model is solved correctly by the discrete mathematics computer code. Verification does not address whether the conceptual model has any relationship to the real world. Validation, on the other hand, provides evidence (substantiation) for how accurately the computational model simulates reality. This perspective implies that the model is solved correctly, or verified."*

According to Oberkampf [173], verification can thus be seen as the first step of the validation process. Validation itself rather addresses the capability of the numerical method to predict the physics under specific conditions of the real world and is hence far more involved than the verification process. For instance, multiple occurring error or inaccuracy sources can - under certain circumstances - cancel out one another and give the appearance of a validated solution.

Verification can be divided into two processes [173]: Code verification and solution verification. Code verification denotes a generic term for errors, which may be produced in the

process of source code programming, but also in numerical algorithms, input and output data files, compilers and operating systems. The process of solution verification deals with errors occurring due to the use of finite-order accurate spatial and temporal discretization schemes, grid discretization, singularities or discontinuities in the solution domain and on the boundaries, insufficient iterative convergence for solving nonlinear equations, truncation errors[1] and computer round-offs [173, 174].

5.2. Analysis in the Incompressible Limit

The compressible projection method has been created based on an incompressible scheme. As a first step of the verification process, the ability of the CPM scheme to compute flows in the incompressible limit ($\mathrm{Ma} \to 0^+$) is demonstrated within this section by means of an analytical analysis of the CPM Method in the incompressible limit and a numerical test case.

5.2.1. Analytical Approach

The compressible projection method is first verified by means of an analytical methodology. The purpose of this verification method is to examine if the equations of the CPM method converge towards the incompressible set of equations of the IPM solution strategy. Approaching the incompressible limit, the effects of pressure changes on the density become negligible. This can be shown by considering the zero Mach number limit of the speed of sound with the assumption of a small, but non-zero convective flow speed:

$$\lim_{\mathrm{Ma}\to 0^+} c = \lim_{\mathrm{Ma}\to 0^+} \frac{\|\underline{u}\|_2}{\mathrm{Ma}} = +\infty\,. \tag{5.2.1}$$

Equation (5.2.1) makes use of the definition of the Mach number (2.1.1). The pressure difference dp can be written as a total derivative dependent on the density ρ and entropy s. This yields:

$$dp = \underbrace{\left.\frac{\partial p}{\partial \rho}\right|_s}_{\equiv c^2} d\rho + \left.\frac{\partial p}{\partial s}\right|_\rho ds = c^2 d\rho + \left.\frac{\partial p}{\partial s}\right|_\rho ds\,. \tag{5.2.2}$$

[1] The truncation error denotes the error originating from the mistake of assuming the solution of the previous time step ϕ^{n-1} to be *exact*, meaning that within an iteratively obtained solution, there is no error conducted at a certain iteration and propagated to the next iteration towards the final solution. In reality, there is however a certain truncation error appearing at each iteration, so that this source of error is equivalent to the error between the actual and exact solution of ϕ^{n-1}. The overall truncation error seen within the solution file represents the total amount of truncation error accumulated over the number of iterations conducted, cf. references [92] and [237].

Based on equation (5.2.2), the square of the speed of sound can be expressed through the following formula:

$$c^2 \equiv \left.\frac{\partial p}{\partial \rho}\right|_s . \tag{5.2.3}$$

The speed of sound is defined by assuming homentropic processes. This assumption holds for acoustic phenomena, since amplitudes generated by acoustic processes are usually small compared to the mean flow values and sonic waves propagate fast compared to the timescales of the hydrodynamic flow field so that in general heat losses and dissipation generated through acoustic mechanisms can be neglected as the flow field is computed [10]. Using equations (5.2.1) and (5.2.3) thus yields:

$$\left.\frac{\partial \rho}{\partial p}\right|_s = \frac{1}{c^2} \xrightarrow[\mathrm{Ma}\to 0^+]{} 0 . \tag{5.2.4}$$

Consequently, the relation between the density and the fluid-dynamic pressure evanesces as the Mach number approaches the zero-limit.

By following the definition of the Reynolds number

$$\mathrm{Re} \equiv \frac{\|\underline{u}\|_2 l}{\nu} \tag{5.2.5}$$

and applying a dimension analysis to the enthalpy conservation equation (3.4.24), it can be shown that dissipation scales with the coefficient $\mathrm{Ma}^2/\mathrm{Re}$ [59, 208]. For this relationship to be valid, a finite but non-zero Reynolds number has to be assumed. As a result, the following condition has to be satisfied:

$$\mathrm{Re} > \epsilon , \tag{5.2.6}$$

with ϵ being a threshold value strictly greater than zero. For gas turbine combustor flows, condition (5.2.6) is assumed to be fulfilled, as Reynolds numbers tend to be quite high for this kind of flow [203, 233]. As a result of this, the following relationship can be assumed:

$$\lim_{\substack{\mathrm{Re}>\epsilon \\ \mathrm{Ma}\to 0^+}} \frac{\mathrm{Ma}^2}{\mathrm{Re}} = 0 . \tag{5.2.7}$$

As a result of consideration (5.2.7), the influence of the dissipation term in the enthalpy equation (3.4.24) can be neglected.

Let us consider a flow in the incompressible limit $\mathrm{Ma}\to 0^+$. For a non-zero finite convective flow velocity $\|\underline{u}\|_2$, the speed of sound thus diverges to infinity. As a result of this, the thermodynamic and acoustic pressure variations are instantaneously wiped out [59, 208]. Considering low Mach number flows in gas turbine combustors, the influence of hydrodynamic pressure fluctuations on the enthalpy can usually be neglected, cf. section 2.1. Computing

flows in the incompressible limit, the effect of occurring pressure fluctuations on the enthalpy equation (3.4.24) can thus be neglected. Taking into account the result (5.2.7), one sees that the enthalpy equation of the incompressible projection method for variable density flows (3.3.10) is restored.

As shown within appendix B.2, the velocity divergence can be recast into a formula involving the material derivative of the density:

$$\nabla \cdot \underline{u} = -\frac{1}{\rho}\left(\frac{\partial \rho}{\partial t} + \underline{u} \cdot \nabla \rho\right) . \tag{5.2.8}$$

This form is well-suited for the analysis in the incompressible limit, since it contains much less terms than the formulation originating from the pressure equation (3.4.5).

Since the density is a function of the temperature and mixture composition only $\rho = \rho\left(T, Y_i\right), i = \{1, 2, \ldots, N_s\} \neq \rho\left(p\right)$ as the Mach number approaches the zero-limit, the velocity divergence in the incompressible limit is described by the following expression:

$$\lim_{\substack{\mathrm{Re}>\epsilon \\ \mathrm{Ma}\to 0^+}} \nabla \cdot \underline{u} = -\frac{1}{\rho}\left(\frac{\partial \rho}{\partial t} + \underline{u} \cdot \nabla \rho\right) \quad \text{with} \quad \rho \neq \rho\left(p\right) . \tag{5.2.9}$$

For compressible flows, the pressure correction equation (3.4.14) adopts the form of the Helmholtz equation (3.4.17). The term b of the Helmholtz equation vanishes at the zero Mach number limit:

$$\lim_{\substack{\mathrm{Re}>\epsilon \\ \mathrm{Ma}\to 0^+}} d = \left[\lim_{\substack{\mathrm{Re}>\epsilon \\ \mathrm{Ma}\to 0^+}} \frac{\alpha_{\mathrm{pr}}}{f\left(\Delta t\right)\Delta t}\frac{\rho^n}{\gamma^n\left(p_{\mathrm{ref}} + p^n\right)}\delta p^{n+1}\right] = 0 . \tag{5.2.10}$$

By using the product rule and equation (5.2.8), the right hand side of the pressure correction equation (3.4.14) can be rewritten to the following formula:

$$\begin{aligned} b &= \frac{\alpha_{\mathrm{pr}}}{f\left(\Delta t\right)}\left[\nabla \cdot \left(\rho^n \underline{u}^*\right) - \nabla \cdot \left(\rho \underline{u}\right)^{n+1}\right] \\ &= \frac{\alpha_{\mathrm{pr}}}{f\left(\Delta t\right)}\left[\nabla \cdot \left(\rho^n \underline{u}^*\right) - \rho^{n+1}\nabla \cdot \underline{u}^{n+1} - \underline{u}^{n+1} \cdot \nabla \rho^{n+1}\right] \\ &= \frac{\alpha_{pr}}{f\left(\Delta t\right)}\left[\nabla \cdot \left(\rho^n \underline{u}^*\right) + \left.\frac{\partial \rho}{\partial t}\right|_{n+1}\right] . \end{aligned} \tag{5.2.11}$$

Approaching the incompressible limit, equation (5.2.11) transitions to

$$\lim_{\substack{\mathrm{Re}\gg 1 \\ \mathrm{Ma}\to 0^+}} b = \frac{\alpha_{pr}}{f\left(\Delta t\right)}\left[\nabla \cdot \left(\rho^n \underline{u}^*\right) + \left.\frac{\partial \rho}{\partial t}\right|_{n+1}\right] \quad \text{with} \quad \rho \neq \rho\left(p\right) . \tag{5.2.12}$$

By introducing the considerations (5.2.10) and (5.2.12) into the pressure correction equation (3.4.17), the Poisson equation of the incompressible projection method for variable density flows (3.3.7) is recovered:

$$\begin{aligned}\Delta_L \delta p^{n+1} &= \frac{\alpha_{pr}}{f\,(\Delta t)}\left[\nabla\cdot(\rho^n \underline{u}^*) + \left.\frac{\partial \rho}{\partial t}\right|_{n+1}\right] \\ &= \frac{\alpha_{pr}}{f\,(\Delta t)}\left\{\nabla\cdot(\rho^n \underline{u}^*) + \frac{p_{\mathrm{ref}}}{\Delta t}\left[\left.\frac{1}{(RT)}\right|_{n} - \left.\frac{1}{(RT)}\right|_{n-1}\right]\right\}. \end{aligned} \tag{5.2.13}$$

In summary, the enthalpy and pressure correction equations of the incompressible projection method for variable density flows described in section 3.3 are restored for the consideration $\mathrm{Ma}\rightarrow 0^+$. This is in accordance with the theoretical background and enables the transition from compressible to incompressible flows.

5.2.2. Numerical Approach

In order to confirm the analytical derivation conducted above, the CPM method is used for a numerical test case in the incompressible limit. Vidovic [248] proposed a test case originally set up by Eidelman et al. [47] to verify a compressible numerical scheme at the limit $\mathrm{Ma}\rightarrow 0$. This test case consists of a steady-state, inviscid, inert duct flow with an arc-shaped bump. The projected length of the duct equals three times its height. The height of the bump amounts to 10 % of the total duct height. For the duct height, a value of $h = 0.05\,\mathrm{m}$ is chosen. The geometry is meshed structurally with a uniform grid node distribution consisting of $[150 \times 50]$ nodes. Figure 5.2.1 depicts the geometry and computational mesh of the duct.

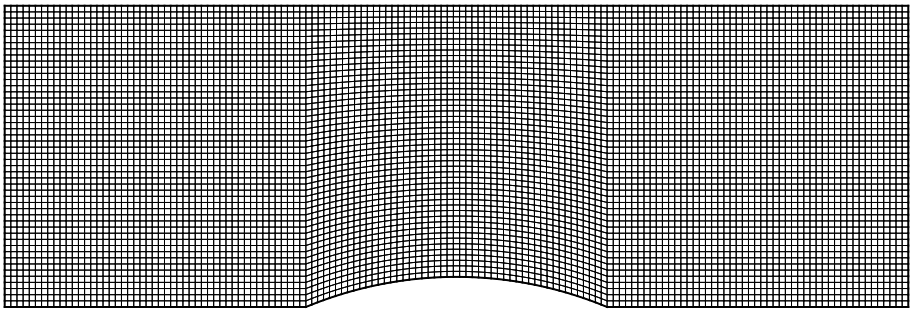

Figure 5.2.1.: Geometry and computational mesh of the duct

Due to its symmetric geometry and steady-state character, the chosen test case is well-suited for the verification of a numerical method capable of computing compressible and incompressible flows. In order to verify the CPM scheme in the incompressible limit, two numerical simulations are carried out: one conducted with the incompressible solver of THETA based on Chorin [24, 25] and Temam's [239] incompressible projection method, extended

for the computation of variable-density flows and the other one using the compressible solver developed within the present work.

The Mach number at the inlet is set to 10^{-4}. This value should be small enough to represent the incompressible limit. The flow is modeled as ideal air consisting of the pure substances N_2 and O_2 with the corresponding mass fractions of 0.768 and 0.232, respectively. Opposed to a homogeneous flow, an inert flow consisting of N_s species allows the mixture composition to change through convection and diffusion (conservation of species mass fractions, see equation (2.2.4)). As the present test case prescribes a constant mass fraction distribution of the substances N_2 and O_2 over the inlet boundary and no further inlets are defined, the mass fraction gradients of the flow should be small enough not to create any inhomogeneity. As a result of this, the flow within the current test case can be considered as being homogeneous. The degree of freedom added by solving the species mass fraction balance equation for O_2 additionally allows the verification of prescribing air as gas mixture at an inlet boundary and thus increases the degree of verification complexity towards real-world applications. At the outlet, a constant pressure boundary condition with $p = 0$ is prescribed. The upper and lower boundaries are set to inviscid walls. At the lateral boundaries, a symmetry condition is applied. The reference values of the density and pressure are set to $1.172\,\mathrm{kg/m^3}$ and $101325\,\mathrm{Pa}$, respectively.

The convective part of the momentum, enthalpy and species equations is discretized using the QUDS scheme (see section 1.3 for details). The CDS discretization formula is applied to the diffusive terms of the governing equations. The temporal discretization is performed using the three points backward (TPB) scheme [54]. As the test case presented within this section is of laminar nature, the turbulent parts within the diffusive terms of the enthalpy and species equations vanish so that only the laminar parts need to be determined. The heat and diffusion fluxes within the enthalpy and species mass fractions equations are thus expressed through the following formulas:

$$\underline{q} = -\frac{\mu_l}{\mathrm{Pr}_l}\nabla h\,, \tag{5.2.14}$$

$$\underline{\underline{j}} = -\frac{\mu_l}{\mathrm{Sc}_l}\nabla \underline{Y}\,. \tag{5.2.15}$$

The laminar Prandtl and Schmidt numbers are set to a value of 0.7. Let us now introduce the definition of the CFL (Courant-Friedrich-Lewy) number [32]:

$$\mathrm{CFL} \equiv \frac{\underline{u}\cdot\underline{P}}{\|\underline{P}\|_2^2}\Delta t\,. \tag{5.2.16}$$

$\underline{P}$ denotes the vector between two grid points. Let us consider a one-dimensional flow which

moves at a finite but non-zero velocity u on a equi-sized grid with a cell size of Δx. Let u_{num} be the numerical velocity defined as the ratio of the grid cell size Δx to the time step size Δt. Then, the CFL number can be seen as ratio of the physical to the numerical velocity:

$$\text{CFL} = \frac{u}{u_{\text{num}}} = u\frac{\Delta t}{\Delta x}\,. \tag{5.2.17}$$

On the other hand, let Δt be the time required by the flow to travel from one discrete cell to the adjacent one. In this case, Δt can be determined based on the CFL number, u and Δx:

$$\text{CFL} = u\frac{\Delta t}{\Delta x} \Leftrightarrow \Delta t = \text{CFL}\frac{\Delta x}{u}\,. \tag{5.2.18}$$

Explicit schemes require a numerical velocity strictly smaller than the physical flow velocity. For this kind of schemes, $\text{CFL} < 1$ constitutes a necessary condition in order for the numerical scheme to converge [218]. Implicit schemes generally allow a CFL number greater than unity [218]. With a CFL number set to one, the amount of dissipation and dispersion in a numerical solution is reduced to a minimum value [202, 208]. Computing the presented test case, the CFL number is thus set to unity. For the sake of simplicity, the one-dimensional formulation of (5.2.16) is applied for the determination of a "global" time step size Δt:

$$\text{CFL} \approx u\frac{\Delta t}{\Delta x} \Rightarrow \Delta t = \text{CFL}\frac{\Delta x}{u_{\text{in}}} \quad \text{with} \quad u = u_{\text{in}} = \text{Ma}\cdot c_{\text{ref}} = \text{Ma}\cdot\sqrt{\left.\frac{\gamma p}{\rho}\right|_{\text{ref}}}\,. \tag{5.2.19}$$

The CFL number is related to the eigenvalues of the prevalent flow [119]. Assuming an incompressible homentropic flow, the convective flow velocity is the only existing eigenvalue [164]. This does not hold anymore for compressible flows. The compressible Euler equations in one dimension possess the following eigenvalues [83, 90, 164, 205, 268]:

$$\begin{aligned}\lambda_1 &\equiv u - c\,,\\ \lambda_2 &\equiv u\,,\\ \lambda_3 &\equiv u + c\,.\end{aligned}$$

It is assumed at this point that the eigenvalues noted above provide the characteristic velocities for the flow field considered in this section. The greatest eigenvalue (by its absolute value) prescribes the strictest condition for the CFL number, thus also for the time step size. By definition, the speed of sound is always positive. In the present test case, the inlet velocity u_{in} is also positive. $\lambda_3 \equiv u + c$ thus represents the greatest eigenvalue and the strictest condition for the CFL number. This result leads to the determination of the acoustic CFL

number $\mathrm{CFL}_{\mathrm{ac}}$:

$$\mathrm{CFL}_{\mathrm{ac}} \equiv \left(\frac{\underline{u} \cdot \underline{P}}{\|\underline{P}\|_2} + c \right) \frac{\Delta t}{\|\underline{P}\|_2} \,. \tag{5.2.20}$$

For a one-dimensional flow field, equation (5.2.20) reduces to:

$$\mathrm{CFL}_{\mathrm{ac}} \equiv (u + c) \, \frac{\Delta t}{\Delta x} \,. \tag{5.2.21}$$

Is the convective CFL number (5.2.16) or the acoustic CFL number (5.2.21) the underlying condition for the determination of the time step size when a compressible method is applied to calculate the flow field accurately in the incompressible limit?

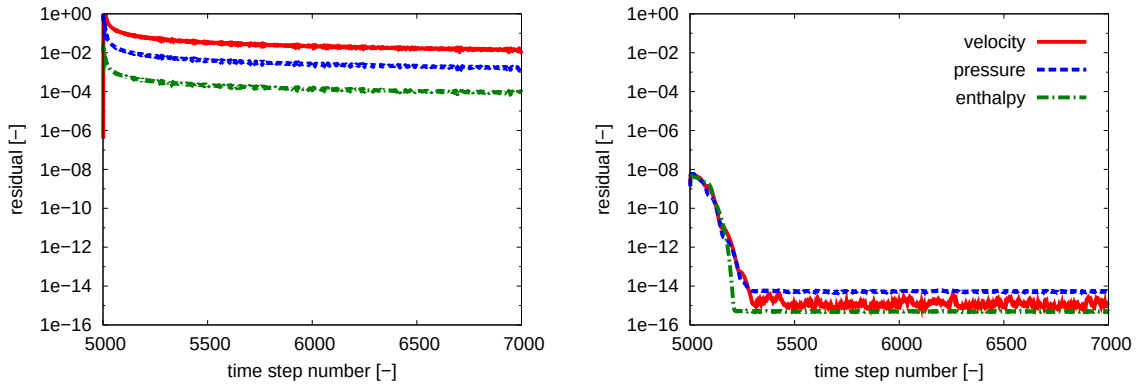

(a) Acoustic CFL condition (b) Convective CFL condition

Figure 5.2.2.: Residuals of the momentum, pressure correction and enthalpy equations dependend on the time step number

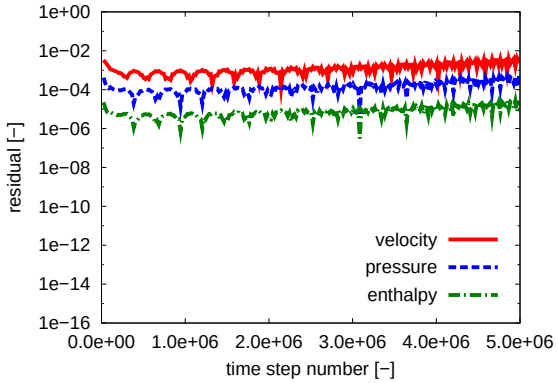

Figure 5.2.3.: Residuals of the momentum, pressure correction and enthalpy equations dependend on the time step number (acoustic CFL condition)

In order to answer this question, two simulations applying the CPM solution strategy calculating the compressible flow within the present test case are carried out: One using the convective CFL condition and the other one with the acoustic CFL condition. The assessment

of the convergence behavior of the numerical simulations conducted requires the description and determination of the residual of the equations solved by the linear solver. These are shown in appendix C. Figures 5.2.2 and 5.2.3 depict the residuals as a function of the time step number of the momentum equations (velocity), the pressure correction (pressure) and the energy (enthalpy) equation for both numerical simulations. Compared to the application of the convective CFL number, applying the acoustic CFL condition to a flow approaching the zero Mach number limit results in a very slow decrease of the residuals, see figure 5.2.2(a).

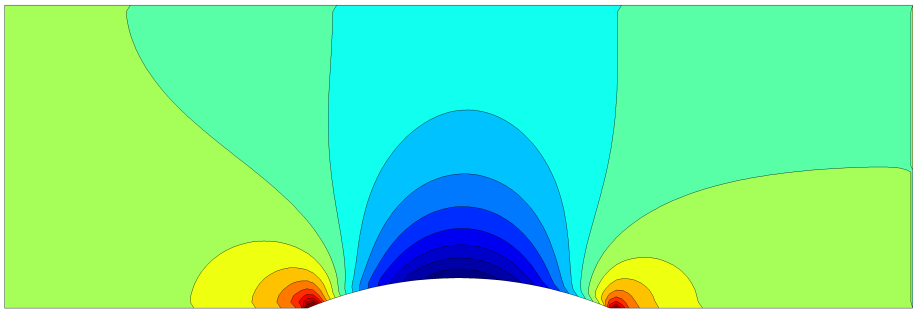

(a) Contour plot of the pressure with isobars (incompressible solution)

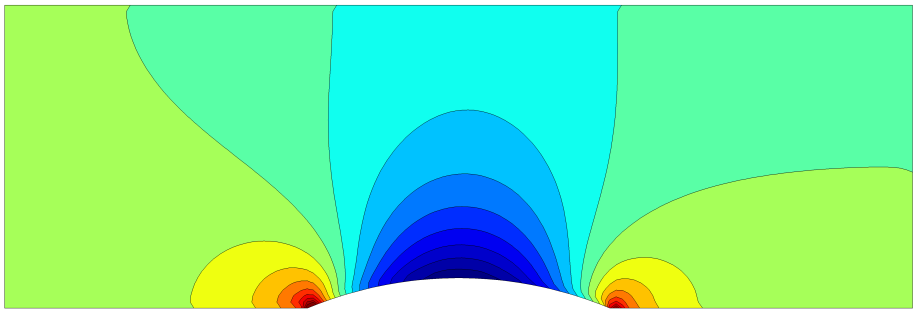

(b) Contour plot of the pressure with isobars (compressible solution)

(c) Pressure p [Pa]

Figure 5.2.4.: Distribution of the pressure field of the incompressible and compressible solution

As the solution of the present test case is of steady-state nature, the unsteadiness of the flow should eventually evanesces thus leading to a “converged“ solution of the computation. However, running the calculation further on under the condition of the acoustic CFL number does not lead to a converged solution. This can be seen in figure 5.2.3. Using the convective CFL number in order to determine the time step size leads to a decrease of the residuals below machine accuracy thus giving a ”fully converged“ solution, see figure 5.2.2(b). The

definition of a fully converged solution is given in this work as follows: The residuals of the equations to be solved decrease below machine accuracy in a fully converged solution, which is defined as 10^{-14} according to MEISTER [148].

It thus appears that for the test case considered at the zero Mach number limit, the convective CFL number is the more appropriate choice over the acoustic CFL number for the determination of Δt. As a result, the convective CFL condition (5.2.16) is applied to the compressible computation of the present test case. It is worth noting though that since the CPM method constitutes a semi-implicit solution scheme, the condition CFL = 1 is not a stringent criterion in the sense of ensuring stability of the numerical simulation performed. It can rather be seen as a reference for the gain of an accurate solution. The Mach number of the present test case amounts to 10^{-4}. It is thus very small and figures as representative value for the incompressible limit. For low[2], moderate or high Mach number flows, the acoustic CFL number is the more appropriate choice over the convective CFL number for the determination of the time step size, as shown in the references [71, 105, 136, 166, 167, 250].

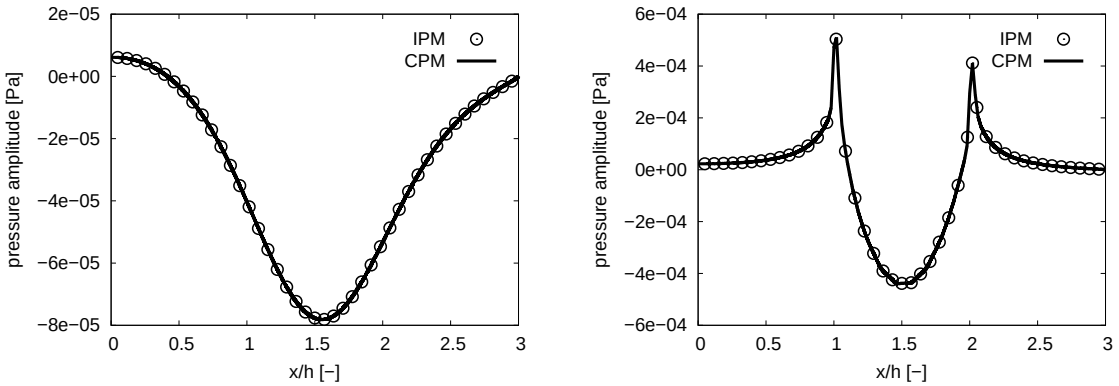

(a) Upper wall (b) Lower wall

Figure 5.2.5.: Pressure amplitude profiles along the lower wall

In order to compare the compressible projection method (CPM) to the incompressible projection method (IPM), the two-dimensional distribution of the pressure field along with the isobars is visualized. Figure 5.2.4 shows the distribution of the pressure field and the isobars regarding the incompressible and compressible solution. From the figures 5.2.4(a) and 5.2.4(b) it can be seen that the pressure pattern of the incompressible and compressible solutions are almost identical.

In addition to the countour plots, the pressure course along the lower and upper walls of the channel is evaluated and compared. For this analysis, the fully converged solutions are

[2] Low means in this context a small, but finite amount. It shall however be differentiated between a low Mach number flow and a flow in the incompressible limit. The latter one is characterized by a Mach number approaching the zero-limit. Opposed here to, a low Mach number flow has a small, but finite Mach number.

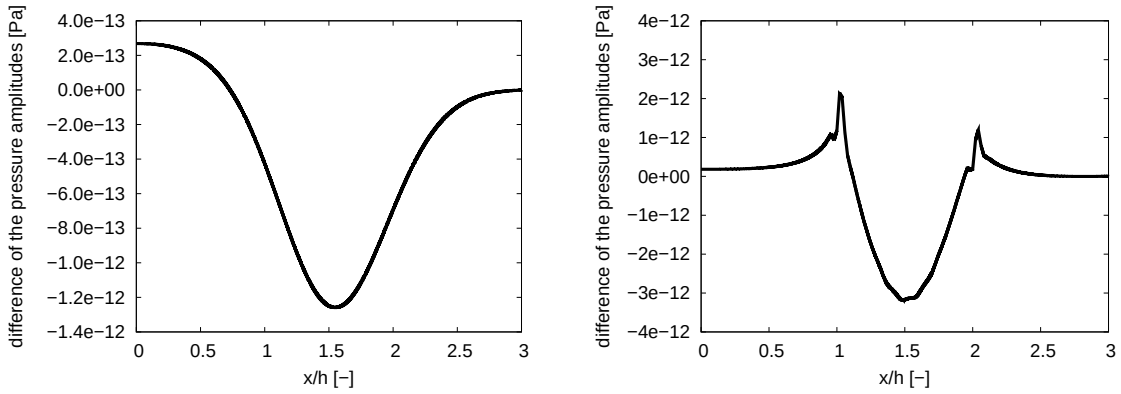

(a) Upper wall (b) Lower wall

Figure 5.2.6.: Difference between the pressure amplitude profiles of the compressible and incompressible solutions

used. The pressure amplitude profiles of both computational methods are presented in figures 5.2.5(a) and 5.2.5(b). It can be told from the figures 5.2.5(a) and 5.2.5(b), that the pressure curves match perfectly at the lower and upper walls of the channel. In order to enhance the visualization concerning the differences between both profiles, the pressure amplitudes of the incompressible calculation are subtracted from the pressure values of the compressible solution resulting in profile differences, shown in figures 5.2.6(a) and 5.2.6(b).

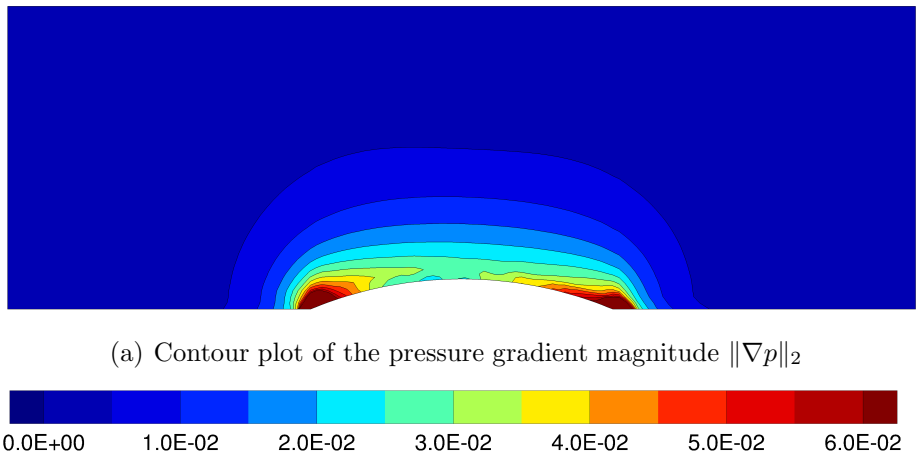

(a) Contour plot of the pressure gradient magnitude $\|\nabla p\|_2$

(b) Pressure gradient magnitude $\|\nabla p\|_2$ [Pa/m]

Figure 5.2.7.: Distribution of the pressure gradient magnitude (compressible solution)

It can be seen from figures 5.2.6(a) and 5.2.6(b) that the maximum discrepancy (based on its absolute value) occurs at the center of the channel for both, the upper and lower boundary of the channel. The peak in the pressure difference $p_{\mathrm{CPM}} - p_{\mathrm{IPM}}$ within the lower boundary pressure course appears at the location of the bump. This peak is assumed to be related to the fact that the highest gradients of the velocity and thus of the pressure occur at the channel

bump, since the bump appears to the flow as obstacle which it has to overcome by changing locally its direction. This assumption proves to be true, as can be seen from the distribution of the pressure gradient magnitude $\|\nabla p\|_2 \equiv \sqrt{\sum_{i=1}^{3} (\partial p/\partial x_i)^2}$ visualized in figure 5.2.7. It has to be said additionally that the pressure is fixed at the outlet boundary, which represents a constraint to the pressure field and thus diminishes the influence of differences between the compressible and incompressible solutions. The prescription of constant velocity and temperature profiles at the inlet additionally introduces a certain constancy into the pressure field, which contributes to a reduction of the differences between the solutions issued from the CPM and IPM solution strategies in the vicinity of the domain inlet, cf. figures 5.2.4(a) and 5.2.4(b). The peak within the course of $p_{\mathrm{CPM}} - p_{\mathrm{IPM}}$ at the upper boundary located at the center of the channel is assumed to be a consequence of the pressure difference peak originating from the lower boundary. Nevertheless, it has to be emphasized at this point that the maximum occurring difference between the pressure profiles along the upper and lower walls of the duct is of the order $\mathcal{O}\left(10^{-12}\right)$ Pa. Considering the pressure level of the order of $\mathcal{O}\left(10^{-4}\right)$ Pa, the differences between the compressible and incompressible solutions are marginal and can thus be neglected. As a result of this, it can be concluded that the CPM method provides a very good representation of the duct flow presented within this section at the zero Mach number limit.

5.3. Numerical Test Cases

5.3.1. One-dimensional Acoustic Test Case

In order to demonstrate the ability of the CPM method to calculate the propagation of acoustic waves in an accurate manner, the presented scheme is validated by means of a one-dimensional acoustic test case. As a verification and validation test case, the one-dimensional acoustic test case proposed by FÖLLER [58] is chosen. This test case has later on been picked up by GUNASEKARAN [79]. Additionally, an analytical solution can be derived to the test case [58], which solution serves as verification data to the outcome of the numerical computations.

The flow within the chosen test case is characterized of being laminar. Consequently, the definition of the laminar diffusion vector within equation (2.2.4) is used. The test case chosen features a one-dimensional flow in a channel built up by an orthonormal computational grid consisting of hexahedral cells. Symmetric boundary conditions are applied to the lateral boundaries, thus neglecting the influence of viscous forces on the flow field. A Dirichlet boundary condition is applied for the pressure at the outlet boundary surface, whereby the pressure is set to zero. The inlet velocity is excited with a sinusoidal profile. This velocity excitation generates plane acoustic waves which then propagate along the channel. In the following, the acoustic excitation profile and analytical solution are derived. For this to be conducted, the generic homogeneous wave equation in one dimension is considered, cf. reference [204]:

$$\frac{\partial^2 u'}{\partial t^2} - c^2 \frac{\partial^2 u'}{\partial x^2} = 0\,. \tag{5.3.1}$$

The solution of this partial differential equation can be split into two functions $\tilde{f}$ and $\tilde{g}$ [204]:

$$u'\,(x,t) = \tilde{f}\,(x - ct) + \tilde{g}\,(x - ct)\ . \tag{5.3.2}$$

Consider the wave traveling from the left to the right side (function $\tilde{f}$) and let the backwards traveling wave (function $\tilde{g}$) be zero. Furthermore, the function $\tilde{f}$ is defined as being of sinusoidal nature, yielding in the following formula:

$$\tilde{f}\,(x - ct) = \tilde{f}\,[k\,(x - ct)] \equiv \tilde{f}' \sin\left[2\pi\left(\frac{x}{\Lambda} - ft\right)\right]\ . \tag{5.3.3}$$

Choosing the function $\tilde{f}$ equal to the convective flow speed results in the following equation for the velocity field:

$$u = u_{\mathrm{ref}} + u' \sin\left[2\pi\left(\frac{x}{\Lambda} - ft\right)\right]\ . \tag{5.3.4}$$

Setting the inlet to the position $x = 0$, the inlet velocity profile can be expressed through the

following equation:

$$u_{\text{in}} = u_{\text{ref}} - u' \sin\left(2\pi f t\right) . \tag{5.3.5}$$

The mean velocity of the flow field equals $u_{\text{ref}} = 0.25\,\text{m/s}$. To prevent the flow from a change of direction, the amplitude of the velocity excitation is set to $u' = 0.2\,\text{m/s}$. The excitation frequency is chosen to be 100 Hz. The reference values of the density, pressure and temperature amount to $1.179\,\text{kg/m}^3$, 101300 Pa and 298.15 K, respectively. Air consisting of nitrogen and oxygen with the respective mass fractions 0.768 and 0.232 is taken as a gas mixture. At this reference state, the speed of sound amounts to 346.2 m/s. The wavelength is determined by dividing the speed of sound through the excitation frequency resulting in a wavelength of $\Lambda_{\text{ref}} = 3.462\,\text{m}$. The enthalpy is computed from the compressible energy equation (2.2.4).

The heat and diffusion fluxes within the enthalpy and species mass fractions equations are modeled using the following formulas:

$$\underline{q} = -\left(\frac{\kappa}{c_p}\nabla h + \frac{\kappa}{c_p}\sum_{i=1}^{N_s} h_i \nabla \underline{Y} + \sum_{i=1}^{N_s} h_i j_{ij} \underline{I}\right) , \tag{5.3.6}$$

$$\underline{\underline{j}} = -\text{diag}\left(\underline{D}_l\right)\nabla Y . \tag{5.3.7}$$

As the flow field of the present test case is laminar, the turbulent parts vanish in the above equations. The laminar part of the diffusion tensor $\underline{D}_l$ is computed by means of the equations (2.2.14) and (2.2.15).

The temporal discretization is performed using the three points backward (TPB) scheme. The convective part of the momentum equations is discretized using the CDS scheme. The convective part of the enthalpy and species mass fractions equations are discretized applying the QUDS scheme. The diffusive terms within the governing equations are discretized using the CDS scheme. THETA uses a three-dimensional formulation of the conservation equations (2.2.1)-(2.2.4). THETA thus needs a three-dimensional mesh, even in the case where the physical problem to be solved requires less than three dimensions. As a results of this, the physically one-dimensional, but computationally three-dimensional channel is meshed in the radial and tangential directions with four nodes, giving three equi-sized cells in each direction. Initializing the flow field with the constant mean velocity u_{ref} and exciting the inlet velocity with the sinusoidal profile given by equation (5.3.5), the dissipation and dispersion errors are evaluated after the generated sonic wave has passed 10 wavelengths. The length of the channel is designed to embed 12 wavelengths of the generated acoustic waves, thus preventing reflections of the acoustic waves at the outlet with the constraint that only 10 wavelengths of the acoustic wave are considered in space and time.

Consider a homogeneous calorically and thermally perfect gas mixture composed of N_s pure substances. The definition of a pure substance is in this context limited to the ones characterized by a standard enthalpy of formation equal to zero, e.g. O_2, N_2, H_2, etc. (standard state of a pure substance). Using the change of the enthalpy (4.4.31) and the equation of state (2.2.5), an equation of state describing the relation between the enthalpy, pressure and density can be derived:

$$h = c_p T = \frac{\gamma}{\gamma - 1} \frac{p_{\text{ref}} + p}{\rho} \,. \tag{5.3.8}$$

For details concerning the derivation of equation (5.3.8), the reader is referred to the equations (4.4.31)-(4.4.34) described within section 4.4.

As the acoustic waves travel along the one-dimensional channel, only small spatial and temporal changes within the temperature of the gas mixture are expected. As a consequence, the influence of temperature variations on the specific heat of capacity can be neglected. This simplification is applied within the derivation of equation (4.4.34). Using

$$p' = (\rho c)_{\text{ref}} u' \,, \tag{5.3.9}$$

$$\rho' = \frac{1}{c_{\text{ref}}^2} p' \,, \tag{5.3.10}$$

$$h' = \frac{\gamma}{\gamma - 1} \left(\frac{p_{\text{ref}} + p'}{\rho_{\text{ref}} + \rho'} - \frac{p_{\text{ref}}}{\rho_{\text{ref}}} \right) \,, \tag{5.3.11}$$

as well as the sinusoidal excitation function of the velocity (5.3.4), the acoustic part of the density, pressure and enthalpy can be calculated analytically based on the following equations:

$$\rho' = \left(\frac{\rho}{c} \right)_{\text{ref}} u' \sin \left[2\pi \left(\frac{x}{\Lambda} - ft \right) \right] \,, \tag{5.3.12}$$

$$p' = (\rho c)_{\text{ref}} u' \sin \left[2\pi \left(\frac{x}{\Lambda} - ft \right) \right] \,, \tag{5.3.13}$$

$$h' = \frac{\gamma}{\gamma - 1} \left[\frac{p_{\text{ref}} + (\rho c)_{\text{ref}} u'}{\rho_{\text{ref}} + \left(\frac{\rho}{c} \right)_{\text{ref}} u'} - \frac{p_{\text{ref}}}{\rho_{\text{ref}}} \right] \sin \left[2\pi \left(\frac{x}{\Lambda} - ft \right) \right] \,. \tag{5.3.14}$$

Concering the one-dimensional acoustic test case, FÖLLER [58] performs compressible LES computations using the flow solver AVBP [220]. Moreover, FÖLLER makes use of the second-order accurate Lax-Wendroff scheme for the spatial discretization and an explicit, second-order accurate, time stepping scheme for the discretization in time. GUNASEKARAN [79] developed a SIMPLE-based numerical scheme capable of calculating compressible flows. Within the latter work, a second-order accurate TVD scheme (Total Variation Diminishing) and a fifth order accurate WENO scheme (Weighted Essentially Non-Oscillatory) is applied to dis-

cretize the system of equations.

In order to predict acoustic phenomena accurately, the time step size has to be selected appropriately. Considering compressible flows with a moderate Mach number, the acoustic CFL number

$$\mathrm{CFL}_{\mathrm{ac}} \equiv (u+c)_{\mathrm{ref}} \frac{\Delta t}{\Delta x}\,. \tag{5.3.15}$$

is the determining quantity, cf. section 5.2.2 and references [71, 105, 136, 166, 167, 250]. Considering one-dimensional acoustics, an acoustic CFL number greater or smaller than one leads to an increase of the amount of numerical dispersion. Additionally, the application of an acoustic CFL number greater than unity produces a higher amount of numerical dissipation. This relationship has been identified by Roller [208] within the verification process of a compressible pressure-based solver and is demonstrated within section 5.3.1.1 for the CPM method. As an acoustic CFL number of unity produces very low dissipation and dispersion errors, a $\mathrm{CFL}_{\mathrm{ac}}$ value of one is used within the present test case.

It should be emphasized at this point that the acoustic CFL number does not directly influence the stability of the numerical simulations in case of using the CPM method. This is based on the fact that the CPM approach is a semi-implicit solution algorithm and is hence not coupled to stringent CFL number restrictions concerning the stability of numerical calculations, as opposed to explicit schemes. Thus, the application of acoustic CFL numbers greater or lower than unity is permitted.

Another important quantity for predicting the propagation of acoustic waves is the number of Points Per Wavelength (PPW) used in the computational domain. This quantity respresents the number of sampling points chosen to resolve one acoustic wavelength and is obtained by dividing the wavelength by the grid cell size, thus resulting in the following expression for a one-dimensional flow:

$$\mathrm{PPW} \equiv \frac{\Lambda_{\mathrm{ref}}}{\Delta x}\,. \tag{5.3.16}$$

In the following, the influence of the projection weighting factor α_{pr} on the amount of numerical dissipation and dispersion is analyzed. This is conducted via convergence tests in space and time, cf. references [63, 267]. Aside from analyzing the influence of the projection weighting factor, these convergence tests allow the separate determination of the numerical error in space and time and are well-suited to see if the numerical scheme converges properly for a simple, yet well-posed flow problem. This methodology thus improves code reliability through solution verification.

The order of accuracy of a numerical solution strategy heavily relies on the discretization schemes used to discretize the spatial and temporal derivatives appearing within the partial

differential equations applied. However, the order of accuracy of the considered numerical method cannot directly be determined from the numerical error contained within the solution. This is based on the fact that numerical errors such as computer round-offs, singularities or discontinuities in the solution domain and on the boundaries, grid discretization errors and errors originating from an insufficient iterative convergence for solving nonlinear equations, superimpose on the errors produced from the spatial and temporal discretization schemes. Convergence tests in space and time present a remedy to this issue, as they provide the accumulated error due to the occurring numerical error sources separately for space and time. In fact, these numerical errors do degrade the formal order of accuracy so that the actual accuracy determined from computed solutions - such as convergence tests - may also be referred to as *observed order of accuracy* [174].

Calculating the propagation of acoustic waves in the one-dimensional channel and comparing the numerical to the analytical solution, the value of the projection weighting factor has a significant influence on the arising amount of numerical dissipation. This finding is illustrated in figure 5.3.1 for a fixed spatial resolution of 80 PPW. The results obtained from the numerical simulations conducted with the THETA code are extracted directly from the result files, which are based on the NetCDF[3] format. The binary result files can be transformed into the ASCII format thus allowing them to be read and processed by means of bash scripting routines. Thus, no further post-processing software is needed which may lead to errors introduced into the results, e.g. due to an interpolation scheme of the discrete numerical solution points.

Setting the acoustic CFL number to a fixed value of one, starting at a projection weighting factor of 0.5 and increasing α_{pr} step by step by the amount of 0.5 up to 2 yields in a stepwise reduction of the amount of numerical dissipation, see figure 5.3.1(a) and 5.3.1(b). Figure 5.3.1(a) compares the numerical solution obtained through the application of $\alpha_{\mathrm{pr}} = 2$ with the analytical solution derived further above, whereas figure 5.3.1(b) depicts the numerical solutions obtained through varying the projection weighting factor. Increasing α_{pr} beyond the value of 2 results in an unstable behavior of the transient simulation, see figure 5.3.1(b). As a result, the discrepancy between the numerical and analytical solution rises again. Thus, adjusting the projection weighting factor to $\alpha_{\mathrm{pr}} = 2$ has been found of being the configuration with the smallest amount of numerical dissipation. For the present test case, the highest possible order of accuracy of the CPM method is thus gained by the set-up of $\alpha_{\mathrm{pr}} = 2$. These results verify the observations made by Shen [224] for incompressible flows with constant density. No noticeable changes in the amount of numerical dispersion have been observed,

[3] *"NetCDF (Network Common Data Form) is a set of software libraries and self-describing, machine-independent data formats that support the creation, access, and sharing of array-oriented scientific data."* Taken from `http://www.unidata.ucar.edu/software/netcdf` on May 7th 2013.

see figure 5.3.1(b).

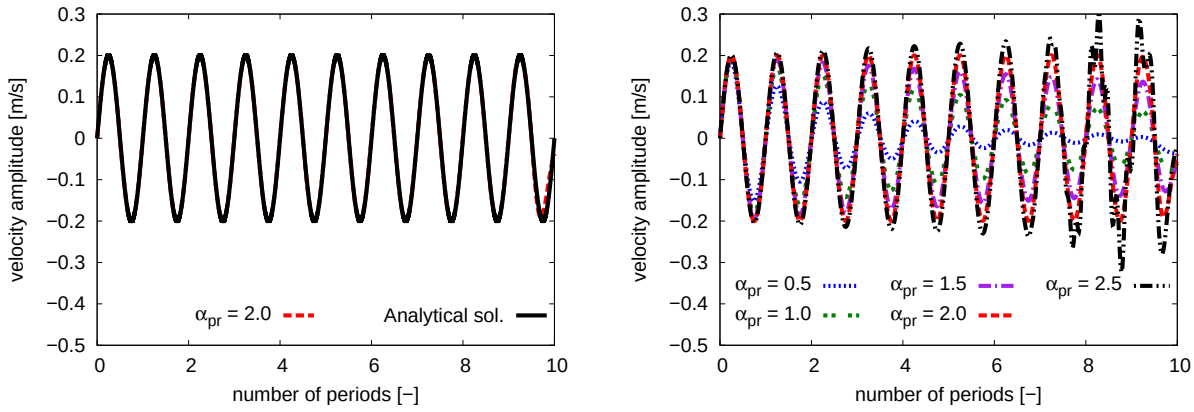

(a) $\alpha_{\mathrm{pr}} = 2$ vs. analytical solution (b) Variation of α_{pr}

Figure 5.3.1.: Wave amplitude plotted for different values of the projection weighting factor α_{pr} for a fixed resolution of 80 PPW

In order to enforce the understanding of the behavior of the temporal and spatial order of accuracy in case of altering the projection weighting factor, the spatial and temporal order of accuracy of the CPM method is evaluated. This is achieved through the determination of the occurring numerical errors of the flow variables in space and time for the one-dimensional acoustic test case dealt with in this section. The errors are evaluated based on the velocity, the pressure and the enthalpy in the L^2-norm. Denote

$$e_\phi \equiv \frac{\sqrt{\sum_{i=1}^{N_p} \left(\phi_i - \phi_{\mathrm{an}_i}\right)^2}}{N_p \cdot \max_{i=1,2,\ldots,N_p} |\phi_{\mathrm{an}_i}|} \tag{5.3.17}$$

the error of the amplitude of an arbitrary variable ϕ relative to the analytical solution in the L^2-norm. Dividing the error in the original L^2-norm by the number of grid nodes and the absolute value of the maximum amplitude issuing from the analytical solution describes a normalization which improves the comparability between the flow variables. The L^2-norm is used as a measurement instrument for the evaluation of the error and describes the more favorable choice over the L^∞-norm, since errors of the pressure in the L^∞-norm may become large in the vicinity of boundaries and therefore do not appropriately represent the error estimations to be determined [224].

Figures 5.3.2 and 5.3.3 show the temporal and spatial errors of the velocity, pressure and enthalpy amplitudes in the L^2-norm for different values of the projection weighting factor. It can be seen that the error is basically reduced for a decreasing time step size and cell width. However, the error course shows an asymptotic behavior towards smaller time step and cell sizes for higher values of the projection weighting factors (for $\alpha_{\mathrm{pr}} \geq 2$ for the convergence

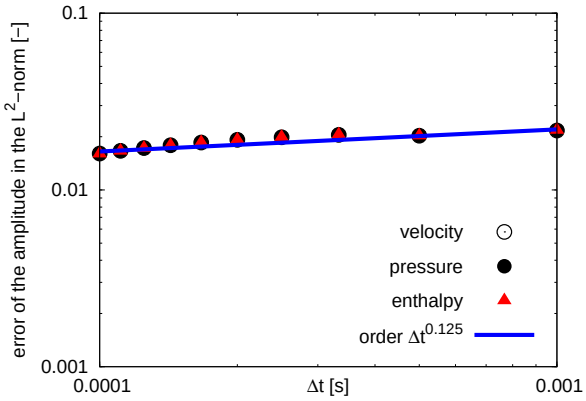

(a) $\alpha_{\mathrm{pr}} = 0.5$

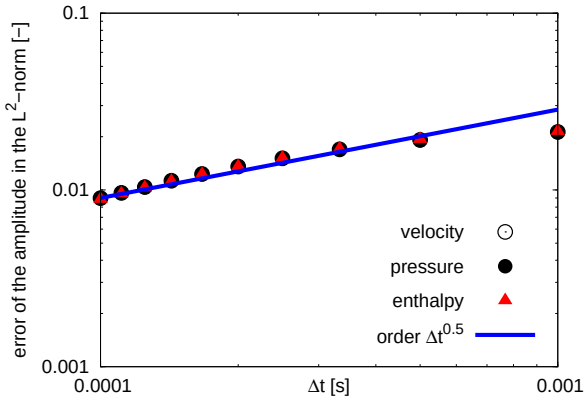

(b) $\alpha_{\mathrm{pr}} = 1$

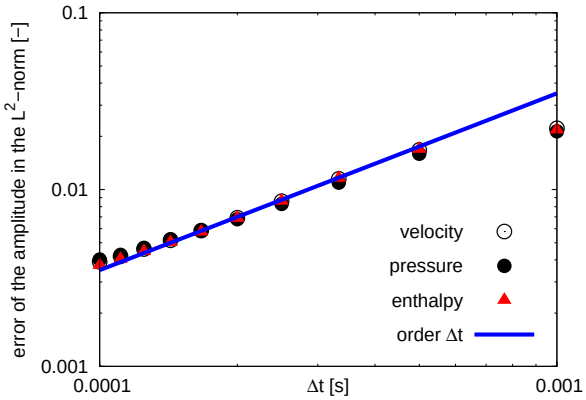

(c) $\alpha_{\mathrm{pr}} = 1.5$

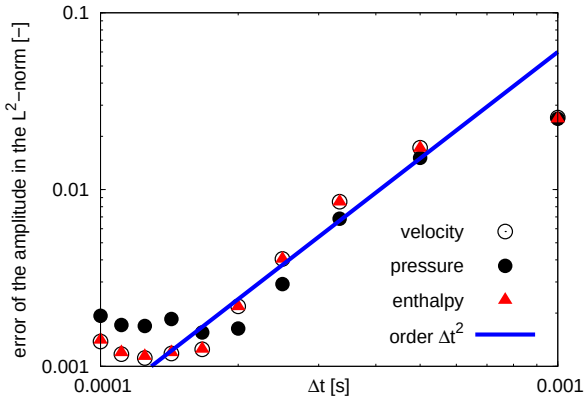

(d) $\alpha_{\mathrm{pr}} = 2$

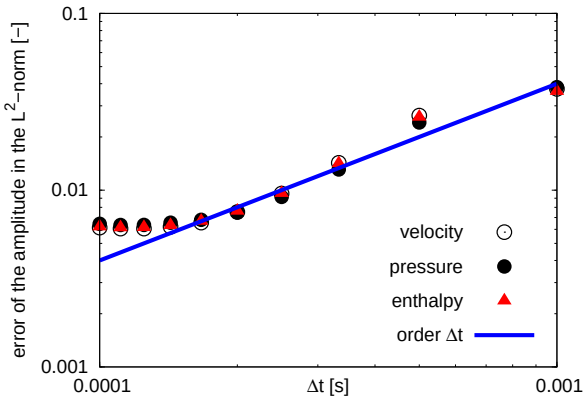

(e) $\alpha_{\mathrm{pr}} = 2.5$

Figure 5.3.2.: Temporal error of the amplitudes of the velocity, pressure and enthalpy in the L^2-norm for different values of the projection weighting factor

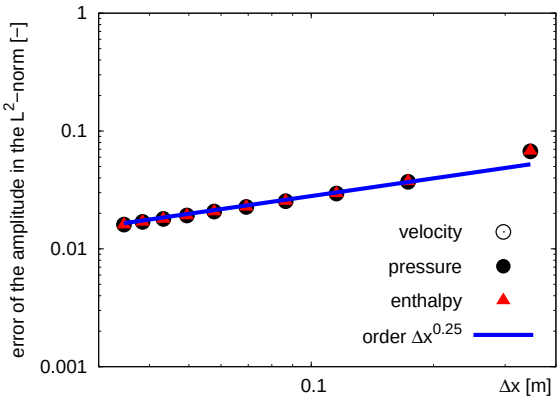

(a) $\alpha_{\mathrm{pr}} = 0.5$

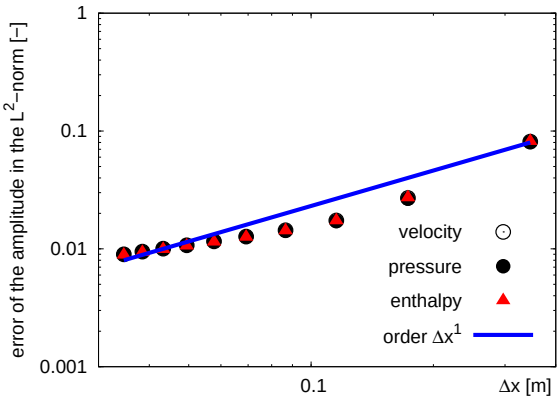

(b) $\alpha_{\mathrm{pr}} = 1$

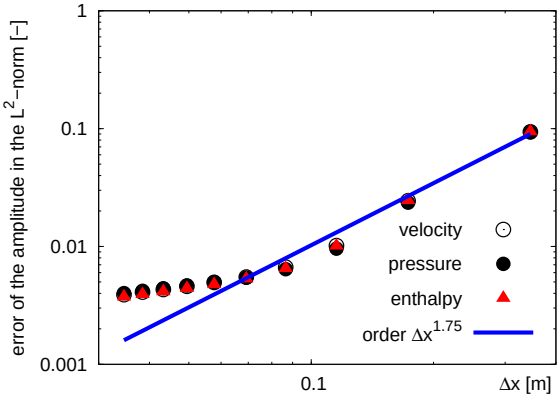

(c) $\alpha_{\mathrm{pr}} = 1.5$

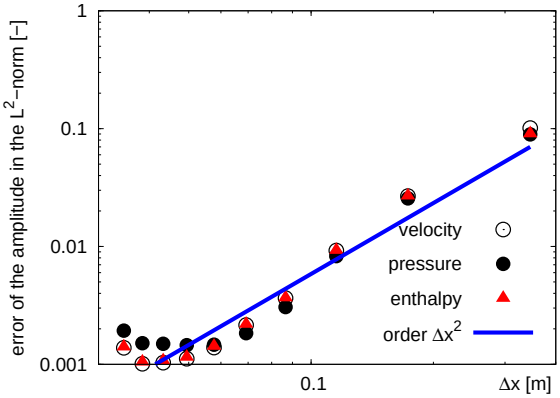

(d) $\alpha_{\mathrm{pr}} = 2$

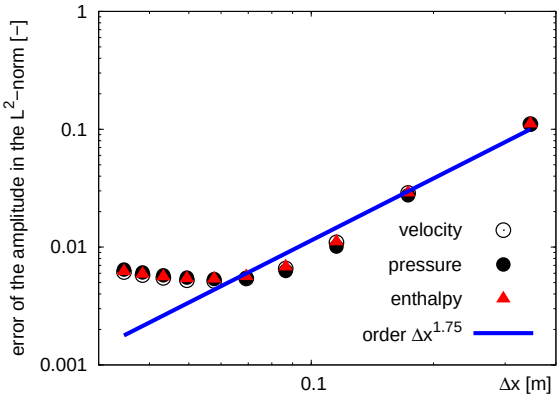

(e) $\alpha_{\mathrm{pr}} = 2.5$

Figure 5.3.3.: Spatial error of the amplitudes of the velocity, pressure and enthalpy in the L^2-norm for different values of the projection weighting factor

tests in time and $\alpha_{\text{pr}} \geq 1.5$) for those in space, which ends in a stagnation-like curve (cf. figures 5.3.2 and 5.3.3). For $\alpha_{\text{pr}} \geq 2$, the solution error even increases slightly with smaller time step, respective cell size, see figures 5.3.2(d)-5.3.2(e) and 5.3.3(d)-5.3.3(e). This means that by reaching some time step or cell size, the further reduction of these quantities without altering the other one does thus not lead anymore to a decrease of the solution error, as one would expect. This behavior is assumed to be related to the dependency of the solution error e_ϕ containing both the numerical dissipation and dispersion error on the acoustic CFL number. For this matter, let us consider the convergence test in time. The acoustic CFL number of the smallest time step - being $1 \cdot 10^{-4}\,\text{s}$ - equals 1. For the second simulation, the time step size has been increased from $1 \cdot 10^{-4}\,\text{s}$ to $1.\overline{1} \cdot 10^{-4}\,\text{s}$, which corresponds to an acoustic CFL number of $1.\overline{1}$. The time step size of the third simulation has been set to a value of $1.25 \cdot 10^{-4}\,\text{s}$, which causes the acoustic CFL number to increase to raise to a value of 1.25, and so forth. In addition to the fact that the error variable e_ϕ includes both the amount of numerical dissipation and dispersion produced, the latter ones are strongly dependent on the acoustic CFL applied, as analyzed further below within section 5.3.1.1. Aside from this, a reduction of the acoustic CFL number does not necessarily end up in a smaller amount of numerical dispersion for the present test case considered, cf. section 5.3.1.1. As a result of this, it exits an "optimum" acoustic CFL number, with which the amount of numerical dissipation and dispersion is minimized. The convergence test conducted for the spatial discretization shows an analogous behavior to the the one performed for the temporal discretization.

α_{pr} [−]	order of accuracy [−]	
	in space	in time
0.5	0.25	0.125
1	1	0.5
1.5	1.75	1
2	2	2
2.5	1.75	1

Table 5.1.: Spatial and temporal order of accuracy as a function of α_{pr}

Aside from this, one observes that choosing the projection weighting factor to the value of 2 results in a second-order accurate numerical scheme in space and time. Setting α_{pr} to 1 represents the unperturbed incremental projection scheme for compressible flows and yields in a spatial order of $\mathcal{O}(1)$ and a temporal order of $\mathcal{O}(0.5)$. Choosing $\alpha_{\text{pr}} = 2$ proves again to be the most accurate setup for the CPM method, as seen earlier on and postulated by Shen [224] for the incremental projection method in conjunction with incompressible

constant density flows. Table 5.1 shows a summary of the order of accuracy in space and time as a function of the projection weighting factor.

The numerical dissipation and dispersion errors produced with a projection weighting factor of 2 are determined next. As a result of the analysis summarized within figure 5.3.1 and table 5.1, the following interpretation of the projection weighting factor α_{pr} is given: α_{pr}

- clearly influences the accuracy and stability of the numerical simulation performed (see figure 5.3.1 and table 5.1),
- has an impact on the amount of numerical dissipation and dispersion produced (see figure 5.3.1) and
- mathematically acts as a multiplier of the pressure correction Laplacian within the pressure correction equation (3.4.16).

The last reflection point can be illustrated by taking a closer look at the generic form of the compressible pressure correction equation (3.4.17):

$$\Delta_{\mathrm{L}}\delta p + d \cdot \delta p = b \Leftrightarrow \frac{1}{\alpha_{\mathrm{pr}}}\Delta_{\mathrm{L}}\delta p + d^* \cdot \delta p = b^* \quad \text{with} \begin{bmatrix} b^* \\ d^* \end{bmatrix} \equiv \frac{1}{\alpha_{\mathrm{pr}}} \begin{bmatrix} b \\ d \end{bmatrix} . \tag{5.3.18}$$

As a result of the transformed generic pressure correction equation (5.3.18), it can be seen that α_{pr} acts as a multiplier of the pressure correction Laplacian. As a consequence of the results obtained above, α_{pr} is set to the value of 2 for the calculations to follow. The results obtained from the CPM calculations are compared to those obtained by Föller [58] and Gunasekaran [79]. The dissipation and dispersion errors are evaluated after ten wavelengths entered the computational domain. The dissipation error is determined by calculating the error of the first maximum of the velocity reached after ten periods at the position of $37/4 \cdot \Lambda_{\mathrm{ref}}$ relative to the maximum of the analytical velocity:

$$e_{\mathrm{diss}} \equiv 100 \cdot \frac{|u - u_{\mathrm{an}}|}{u_{\mathrm{an}}} \, [\%] \, . \tag{5.3.19}$$

The maximum of the velocity of the analytical solution can be determined by seeking the maximum value reached within equation (5.3.4). The numerical velocity values u are evaluated by means of functional analysis. The numerical solution is characterized by a set of discrete points which can be fitted to a function. In order to find the best-fitting function to a given set of discrete points, the least square fitting approach [14, 198] is applied. Inserting the least square fitting approach into the sine solution functions (5.3.12)-(5.3.14) would lead to a non-linear system of equations to be solved for. As a remedy to this, trigonometric

functions - such as sine or cosine functions - can be generally transformed into power series, which represent polynomial functions [110]: $\phi_{\text{ls}} \equiv \sum_{i=0}^{N_d} \xi_i x^i$. Thus, a polynomial least square fitting approach is proposed in this work in order to determine the amount of numerical dissipation and dispersion. The application of this approach onto the present test case leads to a linear system of equations, which can be solved more easily. The polynomial least square fitting approach will be described in the following: A sine wave can be transformed into a cosine wave by moving it by the amount of $\pi/2$:

$$\sin(\alpha) = \cos\left(\alpha - \frac{\pi}{2}\right) = \cos(\beta) \quad \text{with} \quad \beta \equiv \alpha - \frac{\pi}{2}\,. \tag{5.3.20}$$

A cosine curve can be described by means of a power series built around the characteristic point β_0 [110]:

$$\cos(\beta - \beta_0) = \sum_{i=0}^{\infty} (-1)^i \frac{1}{(2i)!} (\beta - \beta_0)^{2i}\,, \tag{5.3.21}$$

wherein the symbol i denotes the imaginary unit. The dissipation error is evaluated by means of the maximum of the sine perturbation function occurring at $37/4 \cdot \Lambda_{\text{ref}}$. Transforming this metric position into an angle results in the following value:

$$\alpha_0 = 2\pi \left(\frac{x}{\Lambda_{\text{ref}}} - 9\right) = 2\pi \left(\frac{37}{4} - 9\right) = \frac{\pi}{2}\,. \tag{5.3.22}$$

As a result of equation (5.3.22), $\beta_0 = \alpha_0 - \pi/2$ equals zero. Moreover, the cosine function becomes very small for $\beta \ll 1$, see equation (5.3.21). Together with $\alpha_0 = 0$, this allows the following approximation based on equation (5.3.21):

$$\cos(\beta) \approx 1 - \frac{1}{2}\beta^2 \quad \text{for} \quad \beta_0 = 0 \;\text{ and }\; \beta \ll 1\,. \tag{5.3.23}$$

Thus, a cosine curve can be approximated by a quadratic function in the vicinity of $\beta_0 = 0$. Let ϕ_{ls} be the quadratic least-square fit of function (5.3.23), defined by the following equation:

$$\phi_{\text{ls}} = \sum_{i=0}^{2} \xi_i x^i = \xi_2 x^2 + \xi_1 x + \xi_0\,. \tag{5.3.24}$$

Denote e_ϕ

$$e_\phi \equiv \sqrt{\sum_{i=1}^{N_p} \left(\phi_i - \phi_{\text{ls}_i}\right)^2} = \sqrt{\sum_{i=1}^{N_p} \left[\phi_i - (\xi_2 x_i^2 + \xi_1 x_i + \xi_0)\right]^2}\,. \tag{5.3.25}$$

the error in the ℓ^2-norm of a set of functions ϕ_i, $i = \{1, \ldots, N_p\}$ relative to the parabolic

approach given by equation (5.3.24). The local minimum of the parabolic approximation is found by taking the derivatives of the error e_ϕ relative to ξ_i and setting them to zero. Following this, a system of equations is obtained which can then be solved for the unknowns ξ_i, $\{i = 1, \ldots, N_d\}$. In conjunction with the quadratic approach (5.3.24), this results in the following system of equations:

$$\begin{bmatrix} \xi_2 \\ \xi_1 \\ \xi_0 \end{bmatrix} = \begin{bmatrix} \sum_{i=1}^{N_p} x_i^4 & \sum_{i=1}^{N_p} x_i^3 & \sum_{i=1}^{N_p} x_i^2 \\ \sum_{i=1}^{N_p} x_i^3 & \sum_{i=1}^{N_p} x_i^2 & \sum_{i=1}^{N_p} x_i \\ \sum_{i=1}^{N_p} x_i^2 & \sum_{i=1}^{N_p} x_i & N_p \end{bmatrix}^{-1} \cdot \begin{bmatrix} \sum_{i=1}^{N_p} x_i^2 \phi_i \\ \sum_{i=1}^{N_p} x_i \phi_i \\ \sum_{i=1}^{N_p} \phi_i \end{bmatrix} . \tag{5.3.26}$$

Solving the linear system of equations (5.3.26) for ξ_0, ξ_1 and ξ_2, the continuous parabolic function (5.3.24) can be assembled. The maximum of this quadratic curve - which equals the maximum value of the numerical velocity u - is obtained by first taking its derivative and setting the result to zero. Knowing the location x of $u_{\max}$, its value can be constructed by inserting x and the calculated coefficients ξ_0, ξ_1 and ξ_2 into equation (5.3.24). Applying equation (5.3.19), the dissipation error is finally obtained. Determining the dissipation error with the aid of the least square method, only the discrete points in the vicinity of the spatial point $x = 37/4 \cdot \Lambda_{\text{ref}}$ obeying the condition (5.3.27) are considered:

$$\forall i \in \{1, \ldots, N_p\}\,, \forall \left(\frac{x_i}{\Lambda_{\text{ref}}}\right) \in [9; 10] \,|\, \max_{i=0,1,\ldots,N_p} \left[u\left(x_i\right)\right] - u\left(x_i\right) \leqslant 0.03\,\text{m/s}\,. \tag{5.3.27}$$

Figure 5.3.4 illustrates the good quality realized by making use of the quadratic least square fitting method for a fixed resolution of 80, 90 and 100 PPW. The dispersion error is set to the

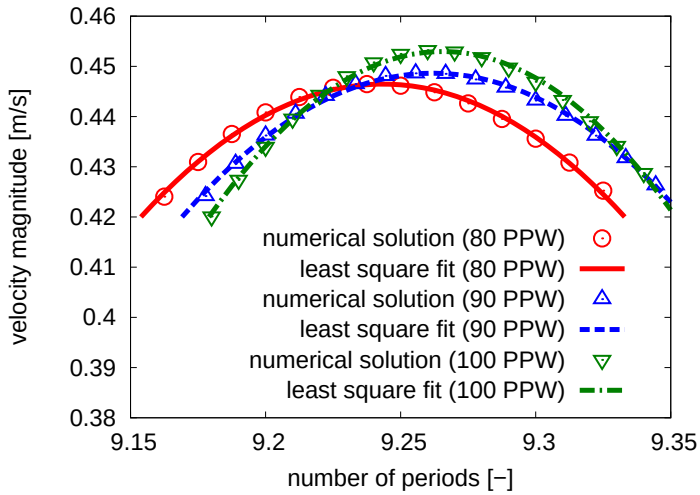

Figure 5.3.4.: Quality of the quadratic least square fitting approach for a fixed resolution of 80, 90 and 100 PPW.

error of the numerical wavelength relative to the reference value, thus giving the following expression for the dispersion error e_{disp}:

$$e_{\text{disp}} \equiv 100 \cdot \frac{|\Lambda - \Lambda_{\text{ref}}|}{\Lambda_{\text{ref}}} \, [\%] \; . \tag{5.3.28}$$

The wavelength obtained from the numerical simulation is determined by taking the difference of the propagating wave at the zero-crossings $x = 19/2 \cdot \Lambda_{\text{ref}}$ and $x = 17/2 \cdot \Lambda_{\text{ref}}$. The linear least square fitting approach is chosen for the calculation of the numerical wavelength. The justification for using the linear approach is given by the fact that a sinusoidal function can be approximated by its argument α for small values of α [110]:

$$\sin(\alpha) = \sum_{i=0}^{\infty} (-1)^i \frac{1}{(2i+1)!} \alpha^{2i+1} \approx \alpha \quad \text{for} \quad \alpha \ll 1 \, . \tag{5.3.29}$$

Minimizing the error e_ϕ defined in the ℓ^2-norm of a set of functions ϕ_i, $i = \{1, \ldots, N_p\}$ relative to the affine function $\phi_{\text{ls}} = \xi_1 x + \xi_0$

$$e_\phi \equiv \sqrt{\sum_{i=1}^{N_p} \left(\phi_i - \phi_{\text{ls}_i}\right)^2} = \sqrt{\sum_{i=1}^{N_p} \left[\phi_i - (\xi_1 x_i + \xi_0)\right]^2} \tag{5.3.30}$$

leads to the linear least squares fitting method by which the best-fitting affine function ϕ_{ls} is found to a given set of discrete points ϕ_i. This yields in the following system of equations to be solved for the unknowns ξ_0 and ξ_1:

$$\begin{bmatrix} \xi_1 \\ \xi_0 \end{bmatrix} = \begin{bmatrix} \sum_{i=1}^{N_p} x_i^2 & \sum_{i=1}^{N_p} x_i \\ \sum_{i=1}^{N_p} x_i & N_p \end{bmatrix}^{-1} \cdot \begin{bmatrix} \sum_{i=1}^{N_p} x_i \phi_i \\ \sum_{i=1}^{N_p} \phi_i \end{bmatrix} \; . \tag{5.3.31}$$

The linear system of equations (5.3.31) is solved for the unknowns ξ_0 and ξ_1, which form the affine function $\phi_{\text{ls}} = \xi_1 x + \xi_0$ to be determined. In order to evaluate the numerical wavelength, the actual positions of the propagating sonic wave at $x_2 = 19/2 \cdot \Lambda_{\text{ref}}$ and $x_1 = 17/2 \cdot \Lambda_{\text{ref}}$ have to be calculated. At these two positions, the value of ϕ_{ls} has to be equal to $u = u_{\text{ref}} = 0.25\,\text{m/s}$. The x_i values can thus be obtained by solving $\phi_{\text{ls}} = u_{\text{ref}} = \xi_1 x_i + \xi_0$ for $i = \{1, 2\}$. The numerical wavelength can eventually be calculated by taking the difference of both x_i values:

$$\Lambda = x_2 - x_1 \, . \tag{5.3.32}$$

The dispersion error is then evaluated by means of equation (5.3.28). The linear least square fitting method used above takes into account the numerical points in the vicinity of the

spatial points $x = 17/2 \cdot \Lambda_{\text{ref}}$, respectively $x = 19/2 \cdot \Lambda_{\text{ref}}$, obeying the following condition:

$$\forall \left(\frac{x_i}{\Lambda_{\text{ref}}} \right) \in \left\{ \left[\frac{17}{2} - \epsilon; \frac{17}{2} + \epsilon \right] \cup \left[\frac{19}{2} - \epsilon; \frac{19}{2} + \epsilon \right] \right\} \Big| \, u\left(x_i\right) - u_{\text{ref}} \leqslant 0.03\,\text{m/s}\,, \qquad (5.3.33)$$

$\forall i \in \{1, \ldots, N_p\}$ and $\forall \epsilon \ll 1$. Following the above condition, the target window describing the difference of the discrete values of the velocity to the value of the respective zero-crossing amounts to 0.03 m/s. Making use of the linear approximation (5.3.29), this target window equals an angle of approximately 2° and yields in a truncation error respective to the wavelength of 0.03%. This error can be interpreted as the value of ϵ introduced in condition (5.3.33). Due to the small value of the truncation error, equation (5.3.29) respresents a good approximation of the sinusoidal wave form. Hence, no significant influences on the evaluation of the numerical wavelengths are expected.

Tables 5.2 and 5.3 show the numerical dissipation and dispersion errors of the CPM method and compares them to the errors obtained from the computational methods applied by Föller and Gunasekaran, denoted by their respective references: [58] and [79]. $\mathcal{O}$ denotes the Landau symbol and gives the spatial order of accuracy of the discretized equations. For all methods shown, a second-order accurate temporal discretization scheme has been applied [58, 79, 202]. The results shown in tables 5.2 and 5.3 reveal an overall decreasing dissipation and dispersion error with an increasing number of points per wavelength. An anomaly here to can be observed in the calculation of the dissipation error, which is described by a strong fall of the amount of numerical dissipation at 40 PPW, followed by an increase of dissipation error at 50 PPW. However, the small dissipation errors calculated with 40 and 50 PPW are mapped to an increased dispersion error, see table 5.3. Increasing the resolution further on from 50 to 90 PPW leads to an reduction of the dissipation error. Setting the number of sampling points per wavelength to 60 PPW reduces the amount of numerical dissipation to 1 %, which represents a good target value. Increasing the resolution from 90 to 100 PPW, the amount of numerical dissipation increases slightly. As can be seen from figure 5.3.4, the velocity amplitude is overpredicted in the latter case.

The dispersion error is overall reduced by the augmentation of the number of points per wavelength. However, an anomaly here to can be seen in table 5.3 between the simulations 20, 30 and 40 PPW. The numerical dispersion error seems to decrease in a significant amount using 30 PPW. However, the evaluation based on the wavelength presented through equation (5.3.28) does not account for the error of the wave propagation speed giving the discrepancy between the actual and theoretical position of the wave. Resolving the sonic waves with fewer sampling points per wavelength results in a greater error of the wave propagation speed towards smaller values. This correlation is visualized in figure 5.3.5, wherein the amplitude of

PPW [−]	e_{diss} [%]			
	CPM $\in \mathcal{O}(2)$	[58] $\in \mathcal{O}(2)$	[79] $\in \mathcal{O}(2)$	[79] $\in \mathcal{O}(5)$
10	37.5	34.7	23.2	14.7
20	22.3	2.77	5.4	1.7
30	7.49	1.15	1.5	0.6
40	0.33	0.40	0.6	0.2
50	2.24	0.23		
60	1.00	0.18		
70	0.81	0.14		
80	0.78	0.08		
90	0.30	0.06		
100	0.66	0.02		

Table 5.2.: Amount of numerical dissipation after 10 periods

PPW [−]	e_{disp} [%]			
	CPM $\in \mathcal{O}(2)$	[58] $\in \mathcal{O}(2)$	[79] $\in \mathcal{O}(2)$	[79] $\in \mathcal{O}(5)$
10	43.7	2.89	0.02	0.04
20	7.51	0.08	0.02	0.03
30	1.89	0.05	0.02	0.02
40	2.35	0.05	0.02	0.02
50	2.25	0.04		
60	1.25	0.04		
70	0.53	0.02		
80	0.13	0.03		
90	0.51	0.02		
100	0.55	0.03		

Table 5.3.: Amount of numerical dispersion after 10 periods

the propagating waves is shown as a function of the normalized axial coordinate - represented through the number of periods - for the resolutions 20, 30 and 40 PPW. Choosing a resolution of 60 points per wavelength decreases the dispersion error to a value of the order of 1 %. Computing the propagation of sonic waves by means of the commercial CFD software ANSYS CFX using a spatially and temporally second-order accurate SIMPLE-based method, a spatial resolution of 60 PPW has also been found to achieve reliable results, as empirically shown by Lourier et al. [135] and Widenhorn [257].

Based on the obtained results, a resolution of 60 PPW decreases the amount of numerical dissipation and dispersion to a value of approximately 1 %. In conjunction with the CPM method, a resolution greater than 60 PPW is thus recommended in order to predict acoustic phenomena reliably. The reference methods of second-order accuracy - denoted by the results

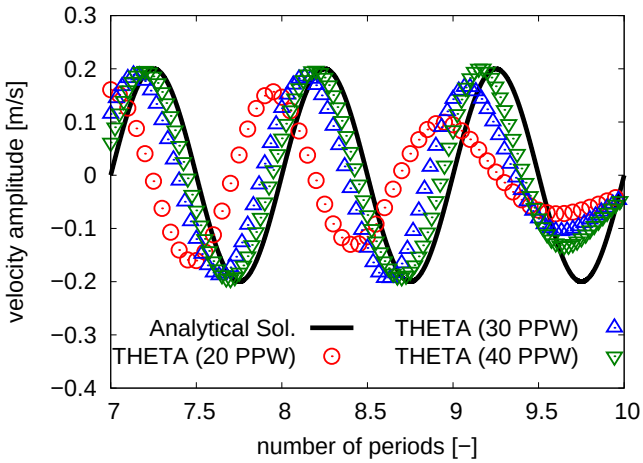

Figure 5.3.5.: Wave amplitude plotted for different resolutions

[58] $\in \mathcal{O}(2)$ and [79] $\in \mathcal{O}(2)$ - produce smaller numerical dissipation and dispersion errors when comparing the results obtained from the CPM method. The increased accuracy of the reference schemes could be associated with a higher discretization accuracy of the convective terms, which produces a smaller amount of numerical dispersion and diffusion. The higher accuracy achieved through the use of the fifth order WENO scheme given by the work of Gunasekaran [79] is supposed to be related to an increased computational effort and is as of now limited to the application of structured grids, so that the results of [79] $\in \mathcal{O}(5)$ do not seem to be applicable to more complex test cases.

5.3.1.1. Influence of the Acoustic CFL number on the Amount of Numerical Dissipation and Dispersion

The influence of the acoustic CFL number on the amount of numerical dissipation considering one-dimensional acoustics is analyzed within this section. Herefore, the one-dimensional test case introduced within the previous section with a spatial acoustic resolution of 80 PPW is used. The following values of the acoustic CFL number based on equation (5.3.15) are set: $\mathrm{CFL}_{\mathrm{ac}} = \left\{0.\overline{3}, 0.5, 1, 2, 3\right\}$. The results are extracted directly from the NetCDF result files, analogously to the analysis concerning the projection weighting factor conducted further earlier on. Following this, the numerical results can directly be compared to the analytical solution of the sonic wave propagation. Figure 5.3.6(a) displays the profiles of the wave amplitude based on the velocity amplitude for the values of the acoustic CFL number noted above. A closer look into the region surrounding $x = 39/4 \cdot \Lambda_{\mathrm{ref}}$ is given by figure 5.3.6(b). The dissipation error increases significantly for a CFL number above unity. A decrease of the CFL number below one does however only lead to a small decrease of the numerical dissipation error, see figure 5.3.6(b). Aside from this, one assumes from figure 5.3.6(b) that

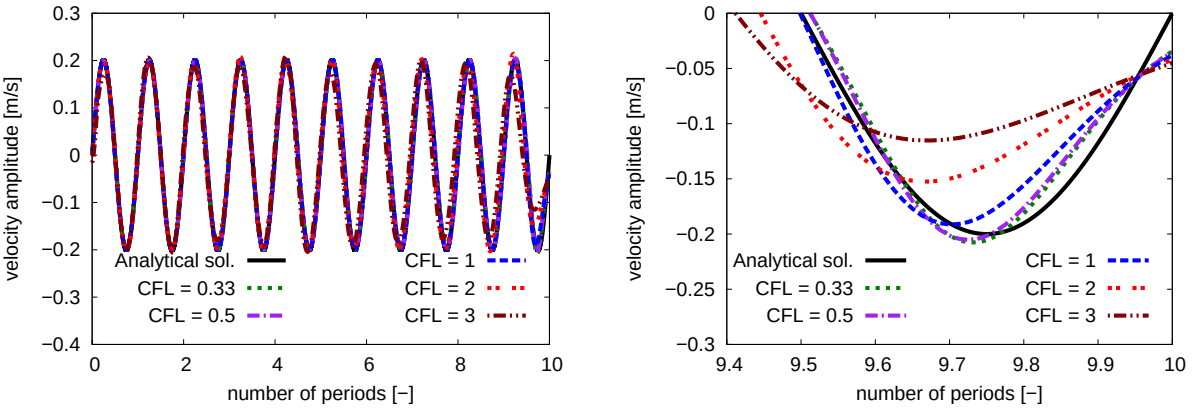

(a) Whole domain (b) Zoom into the region surrounding $x = 39/4 \cdot \Lambda_{\mathrm{ref}}$

Figure 5.3.6.: Wave amplitude plotted for different values of the acoustic CFL number for a fixed resolution of 80 PPW

the dispersion error increases with rising CFL number. However, this is not the case. In order to demonstrate this, a closer look into this analysis is taken: In the following, the amount of numerical dissipation and dispersion is determined based on the methodology described within the previous section.

$\mathrm{CFL}_{\mathrm{ac}}$ [–]	e_{diss} [%]	e_{disp} [%]
$0.\overline{3}$	0.35	0.56
0.5	0.87	0.66
1	0.78	0.13
2	1.29	1.47
3	6.98	1.60

Table 5.4.: Amount of numerical dissipation and dispersion after 10 periods for a fixed spatial resolution of 80 PPW

Table 5.4 shows the amount of numerical dissipation and dispersion after 10 periods as a function of the discrete acoustic CFL number field $\left\{0.\overline{3}; 0.5; 1; 2; 3\right\}$ for a fixed spatial resolution of 80 PPW. As can be seen from table 5.4, the application of an acoustic CFL number greater than unity leads to a monotonic increase of the numerical dissipation and dispersion errors. Additionally, it can be seen that the application of an acoustic CFL number of unity produces the lowest amount of numerical dispersion. This interesting result has also been obtained by Roller [208], who applied a compressible pressure-based in-house solver to a similar test case. The results obtained by Roller thus verifies the observations made within this work.

By lowering $\mathrm{CFL}_{\mathrm{ac}}$ to the value of $0.\overline{3}$, a reduction of the amount of numerical dissipation relative to an acoustic CFL number of one can be achieved. The dissipation error of the cases

$\mathrm{CFL}_{\mathrm{ac}} = \left\{0.\overline{3}, 0.5, 1\right\}$ is however of the same order of magnitude, which reflects an interesting result. A decrease of the acoustic CFL number is related to an augmentation of the numerical dispersion error as well as the time step size, which increases the computational effort. As an acoustic CFL number of unity produces very low dissipation and dispersion errors in conjunction with a reasonable amount of computational time required, a $\mathrm{CFL}_{\mathrm{ac}}$ value of one constitutes the best setup with respect to the decisive criteria (time step size and amount of numerical dissipation and dispersion) and is thus recommended for the determination of the time step size.

5.3.2. Validation of the Acoustic Boundary Conditions

The previously described NSCBC approach has been implemented into the THETA code to work with the CPM solution strategy. Within this section, the NSCBC method is validated by means of a reflective and partially non-reflective behavior of the acoustic waves at the in- and outflow boundaries of a one-dimensional channel. As the definition of a "perfectly non-reflective" boundary condition leads to an ill-posed problem [103, 212, 213], the term partially non-reflective is used to express an approximately non-reflective behavior at a specific boundary.

The one-dimensional test case is addressed to a channel built up by an orthonormal computational grid consisting of hexahedral cells. Symmetric boundary conditions are applied to the lateral walls, thus neglecting the influence of viscous forces on the flow field. The mean flow field is initialized with a sinusoidal perturbation of the velocity and pressure at the center of the channel, see figure 5.3.7. This perturbation generates a plane acoustic wave,

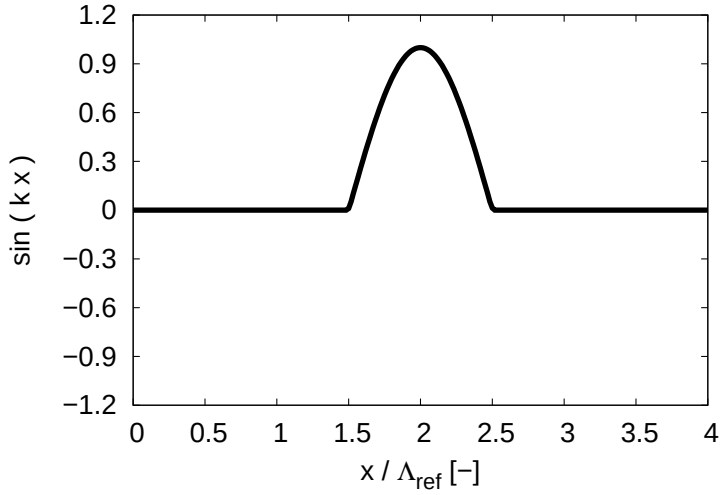

Figure 5.3.7.: Sinusoidal perturbation set at the center of the channel

which then propagates along the channel. At the in- and outflow boundaries, two cases are addressed: The first case is described by a complete reflection of the induced sonic wave. The second case involves a partially non-reflective boundary condition, whereby an approximately non-reflective behavior of the outflow boundary is considered. The length of the channel is chosen to measure four times the wavelength of the perturbation function.

As seen within section 5.3.1.1, the application of an acoustic CFL number of unity produces very low dissipation and dispersion errors. Thus, an acoustic CFL number of unity is used to verify the implementation of the acoustic boundary conditions. Equation (5.2.21) is used

along with an acoustic CFL number of unity to determine the time step size:

$$\Delta t = \frac{\Delta x}{(u+c)_{\text{ref}}}\,. \tag{5.3.34}$$

An accurate prediction of the propagating waves can be accomplished by resolving the defined sine wave with 60 PPW. This value holds for the application of the CPM solution strategy on orthonormal grids and has been derived earlier on within section 5.3.1. The grid resolution of 60 PPW has been found to achieve a reliable prediction of acoustic phenomena, at which the dissipation and dispersion errors approximately amount to a value of 1 %.

Resolving the propagating sonic wave with 60 PPW and inserting equation (5.3.16) into formula (5.3.34), the time step size Δt is determined by the following equation:

$$\Delta t = \frac{1}{\text{PPW}}\,\frac{\Lambda}{u+c}\bigg|_{\text{ref}} = \frac{1}{60}\,\frac{\Lambda}{u+c}\bigg|_{\text{ref}}\,. \tag{5.3.35}$$

The initial velocity and pressure fields are excited using the function $\tilde{f}$ defined within equation (5.3.3). Moreover, the wavelength is set in the following to its reference value. Setting the perturbation at the center of the channel results in the following equations for the initial velocity and pressure fields:

$$u^0 = u_{\text{ref}} + u' \sin\left(\pi\,\frac{x-\frac{\Lambda_{\text{ref}}}{2}}{\Lambda_{\text{ref}}}\right) \quad \text{with} \quad u' = \frac{p'}{(\rho c)_{\text{ref}}}\,, \text{ and} \tag{5.3.36}$$

$$p^0 = p' \sin\left(\pi\,\frac{x-\frac{\Lambda_{\text{ref}}}{2}}{\Lambda_{\text{ref}}}\right) \quad \text{for} \quad \left[2\Lambda_{\text{ref}} - \frac{\Lambda_{\text{ref}}}{2}\right] \leq x \leq \left[2\Lambda_{\text{ref}} + \frac{\Lambda_{\text{ref}}}{2}\right]\,. \tag{5.3.37}$$

The perturbation function is shown in figure 5.3.7. The amplitude of the pressure amplitude is set to 10 Pa. This corresponds to a velocity excitation of $u' = 0.025\,\text{m/s}$. The mean flow velocity is set to $u_{\text{ref}} = 1\,\text{m/s}$. Air consisting of nitrogen and oxygen with the respective mass fractions 0.768 and 0.232 is taken as a gas mixture. Regarding the chosen gas mixture composition, the ratio of specific heats is $\gamma_{\text{ref}} = 1.4$. The reference values of the density, pressure and temperature amount to $1.172\,\text{kg/m}^3$, 101325 Pa and 300 K, respectively. Knowing this, the reference value of the speed of sound thus amounts to $c_{\text{ref}} = 348\,\text{m/s}$. The frequency of the half period of the sine wave is chosen to equal 1 kHz. The wavelength is evaluated by dividing the speed of sound through the excitation frequency resulting in a value of $\Lambda_{\text{ref}} = 0.348\,\text{m}$.

The heat and diffusion fluxes within the enthalpy and species mass fractions equations are modeled using the formulas from the previous chapter, cf. formulas (5.3.6) and (5.3.7). As the flow field of the present test case is laminar, the turbulent parts vanish in the above

equations. The laminar part of the diffusion tensor $\underline{D_l}$ is computed by means of the equations (2.2.14) and (2.2.15).

case number	method	boundary condition applied	
		inflow	outflow
1	Dirichlet	-	fixed
2	NSCBC	-	partially non-reflective
3	Dirichlet	fixed	-
4	NSCBC	partially non-reflective	-

Table 5.5.: Computed cases for the one-dimensional test case

The temporal discretization is performed using the three points backward scheme, which is of second-order accuracy. The convective part of the momentum equations is discretized using the second-order accurate CDS scheme. THETA uses standardly a three-dimensional formulation of the conservation equations (2.2.1)-(2.2.4), so that the physically one-dimensional, but computationally three-dimensional channel is meshed in the radial and tangential directions with four nodes, giving three equi-sized cells in each direction. The projection weighting factor is set to a value of 2. Initializing the flow field with the constant mean velocity u_{ref} and exciting the velocity and pressure fields with the sinusoidal profiles given by the equations (5.3.36) and (5.3.37), the cases listed within table 5.5 are computed.

In table 5.5, "-" means that the boundary condition is not relevant for the case considered. The numerical simulation performed in order to predict the reflective behavior of the outflow boundary is started from $t = 0$ up to a time of $t = 4 \cdot \Lambda_{\mathrm{ref}} \,/\, (u + c)_{\mathrm{ref}}$. Since case one features a fully reflective behavior of the outflow, the results of test case one are used as starting solution for the calculation of the reflective behavior of the inflow boundary. The results of the four cases defined within the table above are shown in the figures 5.3.8(a)-5.3.9(b).

For the cases 2 and 4, the constant σ is set to the optimal value of 0.27, see reference [212] and section 4.4 for details. Figure 5.3.8(a) displays the initial state of the excited flow field. Regarding the fully reflective outlet, the initially induced sonic wave is fully reflected at the outflow boundary and thus fed back into the domain in case of imposing a fixed pressure at the outflow, see figure 5.3.8(b). The reflection coefficient has a value of $R = -1$. This is consistent to the theory of acoustics [190]. The small oscillations occurring behind the reflected sonic waves are a typical effect of second order accurate discretizations, see e.g. [79, 257]. In case of applying the partially non-reflective boundary condition at the outflow, the maximum magnitude of the reflected part of the initially induced acoustic wave amounts to 1 Pa, see figure 5.3.8(b). This constitutes for most cases an acceptable amount of reflection at the outflow boundary.

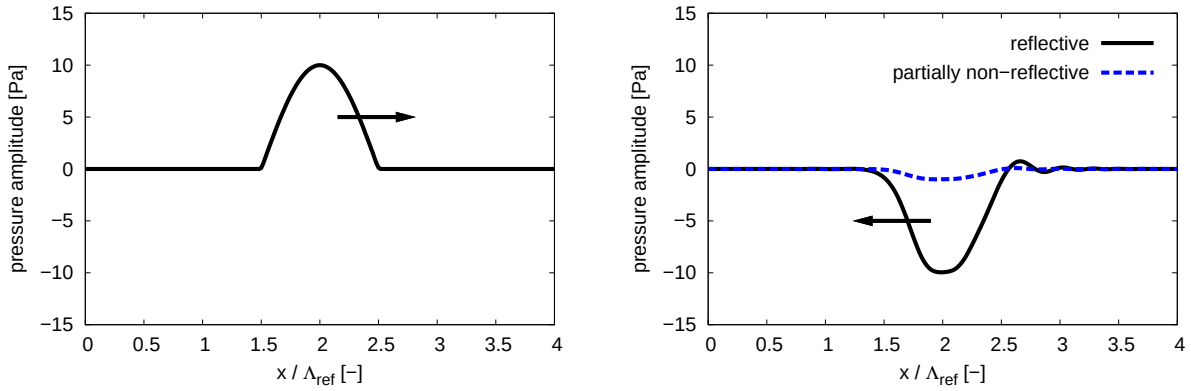

(a) $t = 0$ (b) $t = 4 \left.\frac{\Lambda}{u+c}\right|_{\text{ref}}$

Figure 5.3.8.: Behavior of the acoustic wave propagation at the outlet (cases 1 & 2)

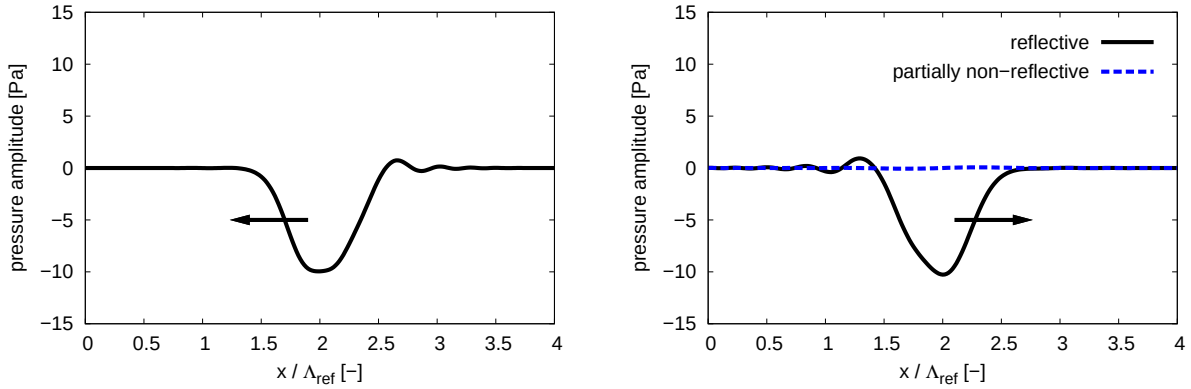

(a) $t = 4 \left.\frac{\Lambda}{u+c}\right|_{\text{ref}}$ (b) $t = 8 \left.\frac{\Lambda}{u+c}\right|_{\text{ref}}$

Figure 5.3.9.: Behavior of the acoustic wave propagation at the inlet (cases 3 & 4)

The initial state for the calculation of the fully reflective and partially non-reflective inflow boundary conditions is visualized in figure 5.3.9(a). Figure 5.3.9(b) shows the responses of the fully reflective and partially non-reflective boundary conditions applied to the inlet boundary of the computational domain. The backwards traveling acoustic wave is fully reflected a the inflow boundary in case of applying a fixed boundary condition, i.e. a Dirichlet boundary condition for the inlet velocity. The reflection coefficient amounts to $R = 1$, which is in accordance with the theory of acoustics [190]. In the case of the partially non-reflective boundary condition applied, the maximum magnitude of the reflected part of the acoustic wave is below 0.1 Pa, which represents a negligible amount of reflection.

5.3.3. Two-Dimensional Subsonic Flow in a Convergent Nozzle

In order to demonstrate the ability of the compressible projection method to calculate subsonic compressible flows, a two-dimensional test case originally proposed by Colella [28] is considered in the present work. The test case features a two-dimensional inviscid flow within a plane convergent nozzle. As the walls of the nozzle are considered adiabatic, the inviscid flow field can be characterized as being homentropic. Colella drew the upper wall of the nozzle as a hyperbolic tangent function of the axial coordinate and used non-dimensional quantities in order to describe the flow field and its boundary conditions. The essential test case parameters along with the boundary conditions are given within this work as variables with dimensions.

The dimensions of the present test case read: $x_1 \in [0; 40]$ mm, $x_2 \in [0; 10]$ mm, $x_3 \in [-0.125; 0.125]$ mm. Following Collela's definition, the upper wall can be described by the hyperbolic tangent function noted below:

$$x_2\left(x_1\right) \equiv 2.5 \cdot 10^{-3} \left\{3\,\text{mm} - \tanh\left[400 \cdot \left(x_1 - 20\,\text{mm}\right)\right]\right\} . \tag{5.3.38}$$

Figure 5.3.10 shows the the two-dimensional geometry of the nozzle. The hyperbolic tangent function (5.3.38) is applied to the upper wall of the nozzle. A second test case based on

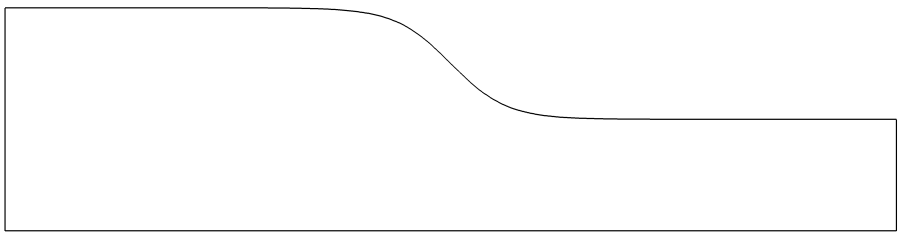

Figure 5.3.10.: Two-dimensional geometry of the nozzle

the homentropic flow configuration is added in this work, wherein a linear profile of the inlet velocity is prescribed. In order to determine the dependency of the flow field on the inlet Mach number imposed, the Mach number at the inlet boundary surface is stepwise increased for the homentropic test case.

All numerical calculations presented within this section are performed using the same approach for the computation of the coefficients concerning the diffusive term of the enthalpy and species equations. The heat and diffusion fluxes within the enthalpy and species mass fractions equations are expressed through the following equations:

$$\underline{q} = -\frac{\mu_l}{\text{Pr}_l} \nabla h \,, \tag{5.3.39}$$

$$\underline{\underline{j}} = -\frac{\mu_l}{\mathrm{Sc}_l} \nabla \underline{Y} \,. \tag{5.3.40}$$

The laminar Prandtl and Schmidt numbers are set to a value of 0.7. In the following, the setup and numerical results of the said test cases are addressed to.

5.3.3.1. Homentropic Case

The computational grid of the nozzle is shown in figure 5.3.11. The two-dimensional geometry is meshed using hexahedral cells with a uniform distribution of the grid nodes. The length of a grid cell along one direction amounts to approximately 0.25 mm. In the direction of the third coordinate x_3, the grid is meshed with one cell. As a consequence of this, a grid cell can roughly be described through the following dimensions: $[0.25 \times 0.25 \times 0.25]$ mm. A slip

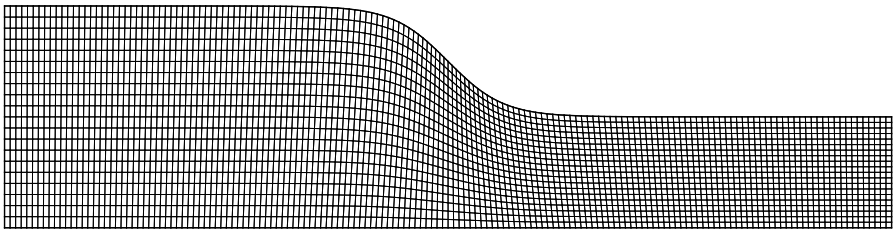

Figure 5.3.11.: Computational mesh of the nozzle for the homentropic case

boundary condition is applied to the upper and lower boundaries. The lateral boundaries are modeled as symmetry walls. In order to model an homentropic flow, the viscosity is set to zero. As a result of this, the viscous terms included in the governing equations vanish. The governing equations are thus reduced from the Navier-Stokes equations to the so-called Euler equations. The reference values of the pressure p and density ρ are set to 101325 Pa and 1.172 kg/m^3, respectively. Within the present test case, the inlet Mach number represents a characteristic quantity to describe the state of the flow field at the inlet. In a first case, the inlet Mach number is set to a value of 0.01. Further on, the inlet Mach number is increased step by step to the values of 0.1, 0.2 and 0.3, respectively. The inlet temperature T_{in} is set to a fixed value of 300 K. The flow field is modeled as air composed of oxygen O_2 and nitrogen N_2, with the respective mass fractions of 0.768 and 0.232. The inlet boundary conditions for the Mach number and velocity magnitude are noted within table 5.6. As the inlet boundary surface is located perpendicular to the first coordinate x_1, the velocity magnitude $\|\underline{u}_{\mathrm{in}}\|_2$ is equal to the first velocity component u_1. At the outlet, the relative pressure is set to a fixed value of zero.

The acoustic CFL number is defined through the previously noted formula (5.2.16). Rewriting equation (5.2.16) along with an acoustic CFL number equal to one leads to the determi-

Case number	$\mathrm{Ma}_{\mathrm{in}}$ [−]	$\|\underline{u}_{\mathrm{in}}\|_2$ [−]
1	0.01	3.48
2	0.1	34.8
3	0.2	69.6
4	0.3	104.4

Table 5.6.: Inlet boundary conditions for the Mach number and velocity magnitude applied at the two-dimensional nozzle

nation of the time step size:

$$\Delta t = \frac{\Delta x}{u_{\mathrm{ref}} + c_{\mathrm{ref}}} \quad \text{with} \quad u_{\mathrm{ref}} = u_{\mathrm{in}}\,. \tag{5.3.41}$$

The figures 5.3.12(a)-5.3.12(d) illustrate the convergence behavior of the numerical simulations performed. In the simulation case 1, the residuals of the momentum, pressure correction and enthalpy equations decrease seven orders of magnitude. For the cases 2-4, a reduction of the residuals of about four orders of magnitude can be observed. The residuals eventually stagnate, which results in a convergence stall of the numerical simulations. As the Mach number is increased, a deterioration of the convergence behavior can thus be observed. The deteriorating convergence behavior hints at a loss in accuracy of the CPM method towards higher Mach numbers. This conjecture proves to be true as the projection weighting factor α_{pr} has to be increased step by step towards higher Mach numbers in order to avoid the numerical computations from diverging. The gain in stability achieved by a decreased projection weighting factor is related to a loss in accuracy of the results. As proved for the one-dimensional acoustic test case seen in section 5.3.1 and seen further below based on an increasing error of the two-dimensional numerical simulations performed within this section (cf. tables 5.8 and 5.11). The highest possible projection weighting factor is given as a function of the inlet Mach number within table 5.7. Moreover, table 5.7 lists the maximum Mach number occurring within the flow field for each case.

Case number	$\mathrm{Ma}_{\mathrm{in}}$ [−]	$\mathrm{Ma}_{\mathrm{max}}$ [m/s]	α_{pr} [−]
1	0.01	0.02	2
2	0.1	0.23	1
3	0.2	0.49	0.75
4	0.3	0.92	0.25

Table 5.7.: Maximum Mach number $\mathrm{Ma}_{\mathrm{max}}$ and projection weighting factor α_{pr} as a function of the inlet Mach number $\mathrm{Ma}_{\mathrm{in}}$

The QUDS scheme is used to discretize the convective parts of the partial differential

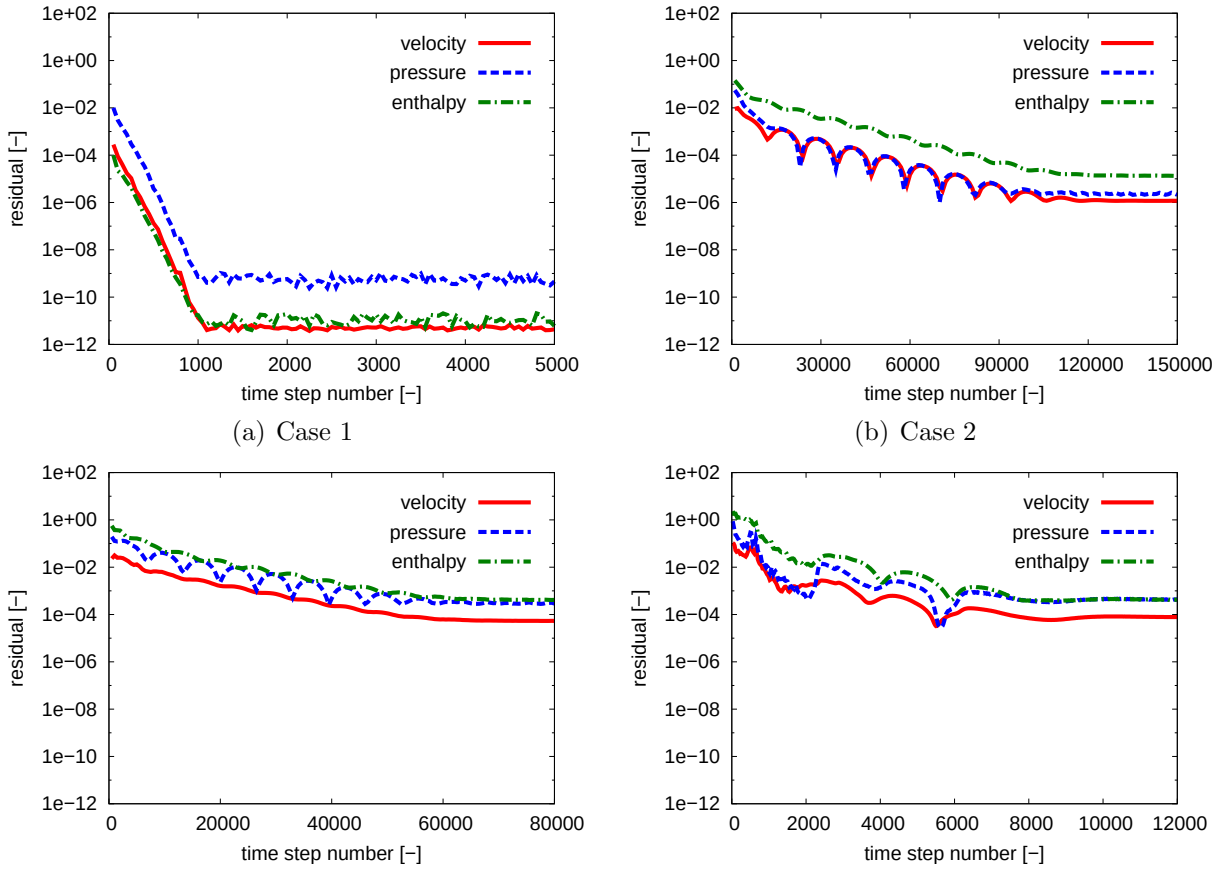

(a) Case 1 (b) Case 2

(c) Case 3 (d) Case 4

Figure 5.3.12.: Residuals of the momentum, pressure correction and enthalpy equations dependent on the time step number

equations in space. The diffusive terms are discretized by applying the CDS scheme. For the discretization in time the TPB discretization formula is used. In order to compare the numerical results of the present test case with analytical data, the polytropic relationship between the pressure and the density is evaluated at the in- and outlet of the nozzle. The polytropic relationship relates the pressure to the density via the following equation [7, 88]:

$$\frac{p_{\mathrm{ref}} + p}{\rho^a} = \text{const.} \Rightarrow \left.\frac{p_{\mathrm{ref}} + p}{\rho^a}\right|_{\mathrm{in}} = \left.\frac{p_{\mathrm{ref}} + p}{\rho^a}\right|_{\mathrm{out}}, \tag{5.3.42}$$

where $a \in \mathbb{R}_+ = \{\mathbb{R} \,|\, n \geq 0\}$ denotes an arbitrary positive exponent. In the case where a equals the heat capacity ratio γ, the above formula may also be referred to as the homentropic relation. This relation can be applied to the flow field within the present test case as the latter one is characterized as being homentropic. Equation (5.3.42) requires the knowledge of the pressure p, the density ρ and the ratio of specific heats γ at the inlet or outlet boundary face. The in- and outlet boundaries are composed of 40 grid cells, so that the values of p, ρ and γ

Case number	p [Pa]		ρ [kg /m^3]		γ [−]	
	Inlet	Outlet	Inlet	Outlet	Inlet	Outlet
1	21.3	0	1.1720	1.1718	1.3995	1.3995
2	2250	0	1.1978	1.1791	1.3995	1.3996
3	11028	0	1.2993	1.2068	1.3995	1.4001
4	52985	0	1.7845	1.3213	1.3995	1.4019

Table 5.8.: Area-weighted averages of the pressure p, the density ρ and the ratio of specific heats γ at the in- and outlet boundary faces

at the in- and outlet are determined as area-weighted averages of the boundary surfaces. The values obtained for the different cases are listed in table 5.8. The homentropic relationship

Case number	$(p_{\text{ref}} + p) / \rho^{\gamma}$ $\left[10^3 \cdot \text{Pa} / (\text{kg} / \text{m}^3)^{\gamma}\right]$		e_{rel} [%]
	Inlet	Outlet	
1	81.16	81.16	$1.80 \cdot 10^{-5}$
2	80.46	80.46	$2.30 \cdot 10^{-3}$
3	77.89	77.88	$1.22 \cdot 10^{-2}$
4	68.61	68.56	$7.20 \cdot 10^{-2}$

Table 5.9.: Evaluation of the homentropic relation between the pressure p and the density ρ at the in- and outlet

according to equation (5.3.42) is evaluated next. The result at the in- and outlet boundary surface is listed for each case in table 5.9. Let e_{rel} be the relative error of the homentropic relation between the in- and outlet surfaces, defined by the following equation:

$$e_{\text{rel}} \equiv \cdot \frac{\left| \frac{p_{\text{in}}}{\rho_{\text{in}}^{\gamma_{\text{in}}}} - \frac{p_{\text{out}}}{\rho_{\text{out}}^{\gamma_{\text{out}}}} \right|}{\frac{p_{\text{in}}}{\rho_{\text{in}}^{\gamma_{\text{in}}}}} [\%] = 100 \cdot \left| 1 - \frac{p_{\text{out}}}{\rho_{\text{out}}^{\gamma_{\text{out}}}} \cdot \frac{\rho_{\text{in}}^{\gamma_{\text{in}}}}{p_{\text{in}}} \right| [\%] \ . \tag{5.3.43}$$

The results of the homentropic relationship analysis are given in table 5.9. The relative errors between the in- and outlet surfaces e_{rel} are in the range of $[1.80 \cdot 10^{-5}; 7.20 \cdot 10^{-2}]$ [%], which respresents a negligible amount. The homentropic relationship analysis thus gives an analytical verification to the numerical results.

In the following, the area-weighted averages of the temperature issuing from the numerical simulations are compared to outlet values obtained from a steady-state homentropic analysis of the flow field. For this analytical analysis, the mixture composition is regarded as a homogeneous calorically perfect gas mixture.

As the analytical consideration regards a calorically perfect gas mixture, the specific gas constant R and the specific heat at constant pressure c_p do not vary with the temperature

and can hence be considered as constants. In the following, they are set to their respective reference value. As the ratio of specific heats γ is calculated from R and c_p, γ can also be specified as a constant value:

$$\underline{w} \neq \underline{w}\,(T) \Rightarrow \underline{w}_{\text{in}} = \underline{w}_{\text{out}} = \underline{w}_{\text{ref}} \quad \text{for} \quad \underline{w} \equiv \Big[R\ c_p\ \gamma\Big]^T\ . \tag{5.3.44}$$

The reference values of R, c_p and γ amount to $288\,\text{J}/\,(\text{kg}\cdot\text{K})$, $1.01\cdot10^3\,\text{J}/\,(\text{kg}\cdot\text{K})$ and 1.4 respectively. By taking into account the one-dimensional steady-state and inviscid mass, momentum and energy conservation equations, a relationship between the Mach number Ma and cross section area A

$$\frac{\text{Ma}\cdot A}{\left[1+\frac{1}{2}\left(\gamma_{\text{ref}}-1\right)\text{Ma}^2\right]^{\frac{1}{2}\frac{\gamma_{\text{ref}}+1}{\gamma_{\text{ref}}-1}}} = \text{const.} \tag{5.3.45}$$

$$\Rightarrow \quad \frac{\text{Ma}_{\text{in}}\cdot A_{\text{in}}}{\left[1+\frac{1}{2}\left(\gamma_{\text{ref}}-1\right)\text{Ma}_{\text{in}}^2\right]^{\frac{1}{2}\frac{\gamma_{\text{ref}}+1}{\gamma_{\text{ref}}-1}}} = \frac{\text{Ma}_{\text{out}}\cdot A_{\text{out}}}{\left[1+\frac{1}{2}\left(\gamma_{\text{ref}}-1\right)\text{Ma}_{\text{out}}^2\right]^{\frac{1}{2}\frac{\gamma_{\text{ref}}+1}{\gamma_{\text{ref}}-1}}} \tag{5.3.46}$$

can be defined [219]. The Mach number at the outlet Ma_{out} can be calculated by applying an iterative solution procedure to the equation (5.3.45). It is important to emphasize at this point that by assuming a constant the ratio of specific heats in relation (5.3.45), the Mach number only depends on the cross section area. The result of the outlet Mach number as well as the known values of the cross section area and inlet Mach number are summarized in table 5.10. The reference value of γ amounts to 1.4. The coss section area of the in- and outlet are $2.5\,\text{mm}^2$ and $1.25\,\text{mm}^2$, respectively. The residual of Ma_{out} describes the absolute

Case number	Ma [−]		residual of Ma_{out} [−]
	inlet	outlet	
1	0.01	0.02	$5.00\cdot10^{-12}$
2	0.1	0.2038	$4.88\cdot10^{-13}$
3	0.2	0.43704	$1.43\cdot10^{-12}$
4	0.3	0.86126	$1.19\cdot10^{-12}$

Table 5.10.: Analytical determination of the outlet Mach number for the cases 1-4

error of the iterative solution procedure. By taking the square of the outlet Mach number definition, the square of the velocity u_{out}^2 can be specified by the following expression:

$$\text{Ma}_{\text{out}}^2 = \frac{u_{\text{out}}^2}{c_{\text{out}}^2} = \frac{u_{\text{out}}^2}{\gamma_{\text{ref}}\cdot\frac{p_{\text{ref}}}{\rho_{\text{out}}}} = \frac{u_{\text{out}}^2}{\gamma_{\text{ref}}\,R_{\text{ref}}\,T_{\text{out}}} \Leftrightarrow u_{\text{out}}^2 = \gamma_{\text{ref}}\cdot R_{\text{ref}}\,\text{Ma}_{\text{out}}^2\,T_{\text{out}}\,. \tag{5.3.47}$$

Formulating the energy conservation law in its integral form between the in and outlet of

the nozzle geometry for a one-dimensional steady-state inviscid flow without heat conduction and species diffusion results in the following equation:

$$h + \frac{1}{2}u^2 = \text{const.} \Rightarrow h_{\text{out}} - h_{\text{in}} + \frac{1}{2}\left(u_{\text{out}}^2 - u_{\text{in}}^2\right) = 0\,, \tag{5.3.48}$$

whereby the enthalpy is calculated by considering a homogeneous calorically and gas mixture consisting of the pure substances O_2 and N_2:

$$h = c_{p_{\text{ref}}}\, T \tag{5.3.49}$$

with

$$c_{p_{\text{ref}}} = Y_{O_2} c_{p_{O_2}}\big|_{\text{ref}} + Y_{N_2} c_{p_{N_2}}\big|_{\text{ref}} = \text{const.}\,. \tag{5.3.50}$$

A calorically and thermally perfect gas mixture restricts c_p and c_v to constant values [66]. For details concerning the derivation of equation (5.3.8), the reader is referred to the equations (4.4.31)-(4.4.34) described within section 4.4. Introducing the equations (5.3.47) and (5.3.49) along with equation (5.3.50) into the energy conservation law (5.3.48) leads to the following formula for the determination of the outlet temperature T_{out}:

$$T_{\text{out}} = \frac{2\, c_{p_{\text{ref}}} T_{\text{in}} + u_{\text{in}}^2}{2\, c_{p_{\text{ref}}} + \gamma_{\text{ref}} R_{\text{ref}} \text{Ma}_{\text{out}}^2}\,. \tag{5.3.51}$$

The results of the analytical and numerical outlet temperatures are displayed in table 5.11. Moreover, the relative error between the numerical and analytical values

$$e_T \equiv 100 \cdot \frac{|T_{\text{out}}^{\text{an}} - T_{\text{out}}^{\text{num}}|}{T_{\text{out}}^{\text{an}}}\,[\%] \tag{5.3.52}$$

is evaluated and shown in table 5.11.

Case number	T_{out} [K]		e_T [%]
	analytical	numerical	
1	299.982	299.982	$1.47 \cdot 10^{-5}$
2	298.128	298.125	$9.06 \cdot 10^{-4}$
3	291.293	291.280	$4.15 \cdot 10^{-3}$
4	266.010	266.055	$1.69 \cdot 10^{-2}$

Table 5.11.: Analytical determination of the outlet temperature values for the cases 1-4

Table 5.11 unveils that the relative error between the numerical and analytical outlet temperatures are in the range of of $[1.47 \cdot 10^{-5}; 1.69 \cdot 10^{-2}]$ [%]. This error represents a negligible amount. In addition to the results obtained, the gain in stability achieved by a

decreased projection weighting factor for an increased Mach number is related to a loss in accuracy of the results. The reduction of the accuracy can directly be seen based on increased errors towards higher Mach numbers, see tables 5.8 and 5.11.

Moreover, it can be observed that the value of e_T increases as the Mach number augments. The maximum value of the relative error amounts to $1.69 \cdot 10^{-2}\,\%$ for a maximum occurring Mach number of $\mathrm{Ma}_{\mathrm{max}} = 0.92$, which is still very low. As a result, the outlet temperature is predicted very accurately using the CPM approach.

In addition to the homentropic relationship analysis performed above, contour plots of the two-dimensional distribution of the Mach number, axial and radial velocity components are visualized. These plots can be compared to the results produced by COLELLA, see figures 5.3.13 to 5.3.15. However, COLELLA makes use of a dimensionless consideration. The pattern of the plotted variables remain however qualitatively mainly unchanged (see [28]), so that the comparison of the results may be conducted qualitatively.

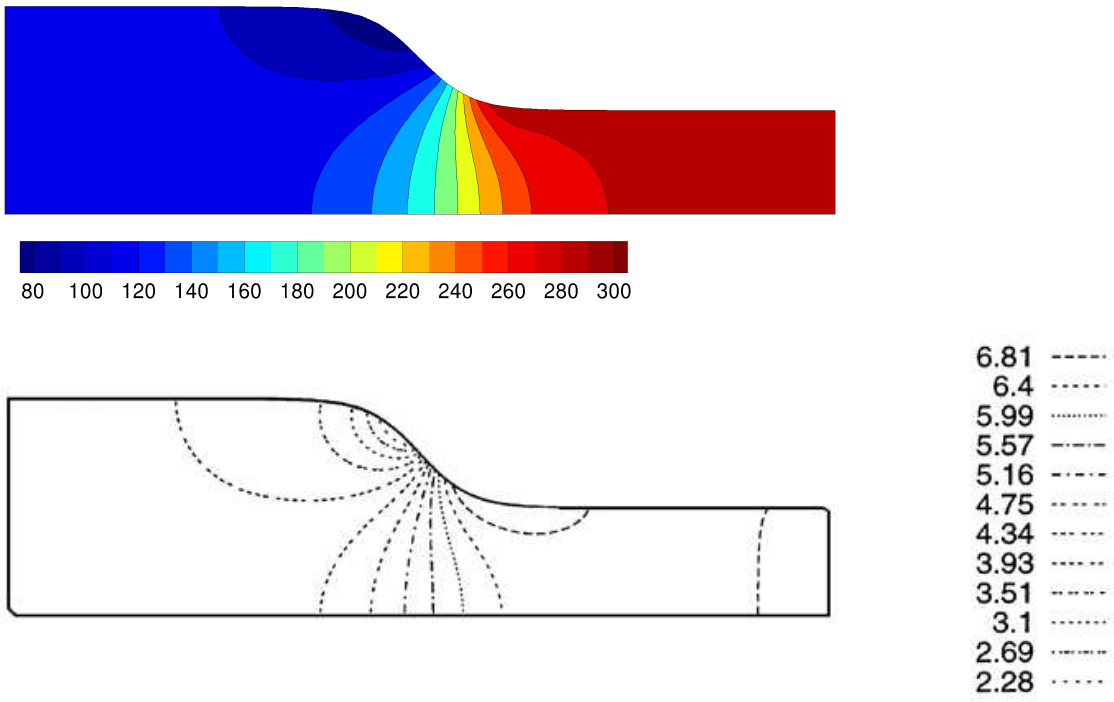

Figure 5.3.13.: Distribution of the axial velocity field u_1 [m/s] at $\mathrm{Ma}_{\mathrm{in}} = 0.3$ (homentropic case, lower figure from [28])

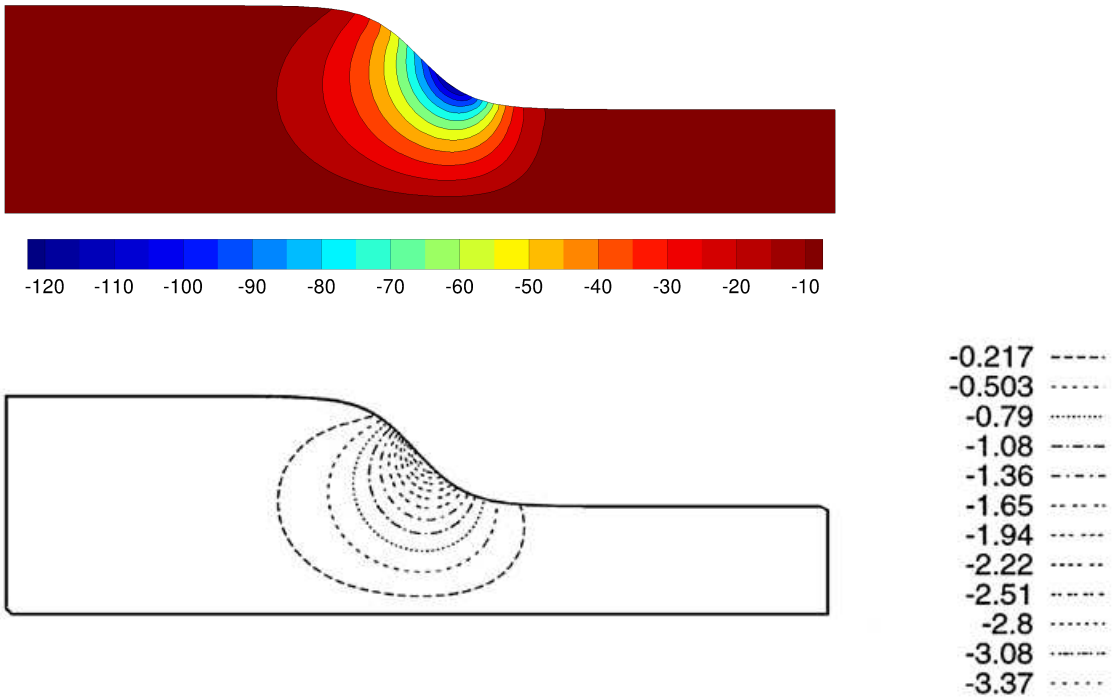

Figure 5.3.14.: Distribution of the radial velocity field u_2 [m/s] at $\mathrm{Ma}_{\mathrm{in}} = 0.3$ (homentropic case, lower figure from [28])

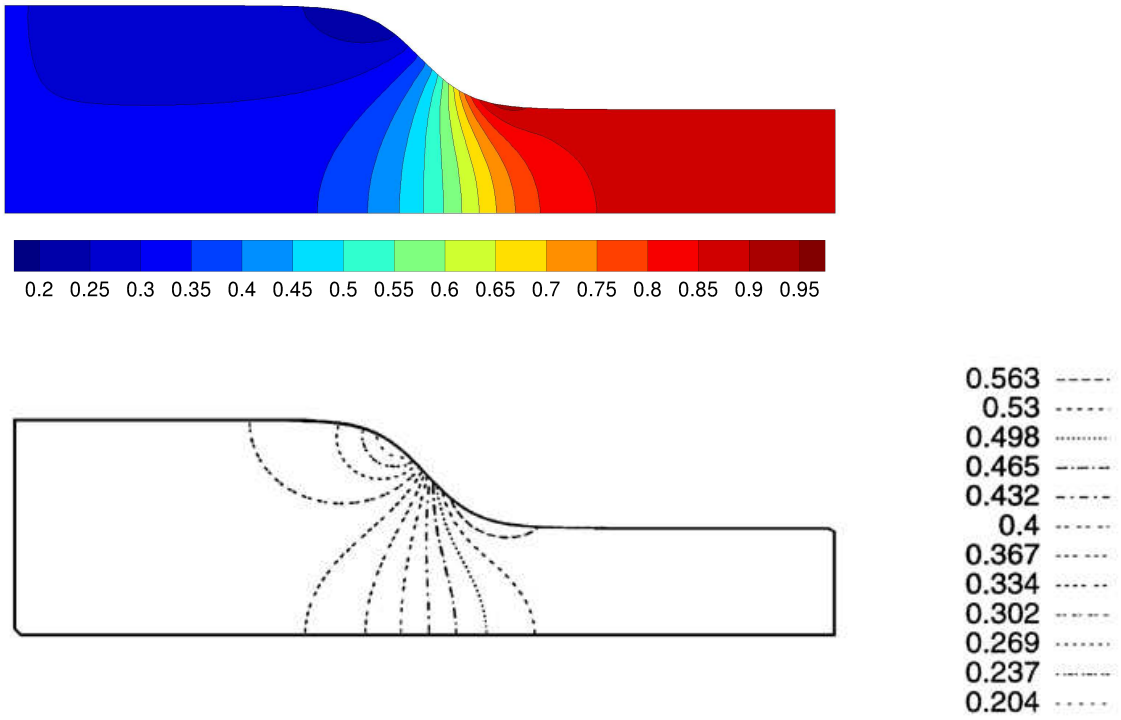

Figure 5.3.15.: Distribution of the Mach number field Ma [−] at $\mathrm{Ma}_{\mathrm{in}} = 0.3$ (homentropic case, lower figure from [28])

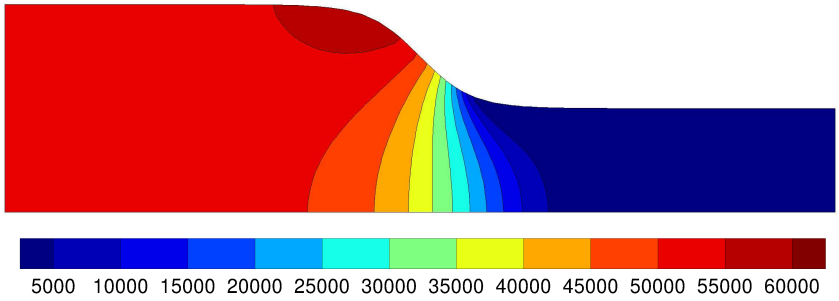

Figure 5.3.16.: Distribution of the pressure field p [Pa] at $\mathrm{Ma}_{\mathrm{in}} = 0.3$ (homentropic case)

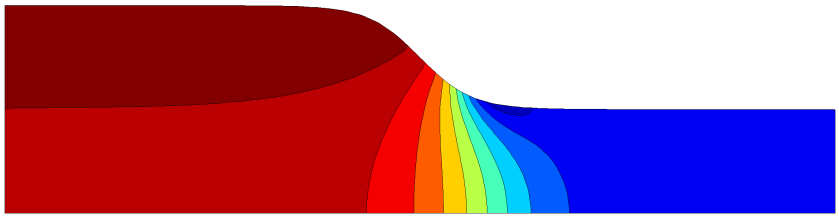

Figure 5.3.17.: Distribution of the temperature field T [K] at $\mathrm{Ma}_{\mathrm{in}} = 0.3$ (homentropic case)

In addition to this, contour plots of the pressure and temperature are evaluated, see figures 5.3.16 to 5.3.17. The contour plots 5.3.13-5.3.17 are shown exemplarily for the fourth case with an inlet Mach number of 0.3. The cases 1-3 show qualitatively similar results. As the inlet Mach number and thus the mass flux is increased, the changes concerning the fluid- and thermodynamic variables gain in importance. The qualitative distribution of the variables however remains mainly unchanged.

The results correlate well with the results obtained by Colella [28]. The maximum Mach number is reached in the vicinity of the nozzle throat. The axial velocity is drastically increased as the flow passes through the contraction. This leads to a reduction of the static pressure. Due to this, the convective term of the pressure $\underline{u} \cdot \nabla p$ within the compressible energy equation becomes negative in the vicinity of the throat. This forces the static enthalpy h and therefore the static temperature T to decrease, see figures 5.3.13-5.3.16.

In the following, let us take a more detailed look into the vorticity of the homentropic flow considered. The vorticity of a flow $\underline{\omega}$ is defined as the vector product of the nabla operator ∇ and of the velocity vector $\underline{u}$, resulting in the rotation of $\underline{u}$:

$$\underline{\omega} \equiv \nabla \times \underline{u} = \begin{bmatrix} \frac{\partial u_3}{\partial x_2} - \frac{\partial u_2}{\partial x_3} \\ \frac{\partial u_1}{\partial x_3} - \frac{\partial u_3}{\partial x_1} \\ \frac{\partial u_1}{\partial x_2} - \frac{\partial u_2}{\partial x_1} \end{bmatrix} . \tag{5.3.53}$$

Considering a two-dimensional flow, the velocity parallel to the third coordinate as well as the derivatives of the velocity components with respect to the third coordinate vanish so that the vorticity vector (5.3.53) reduces to the following scalar equation:

$$\omega = \frac{\partial u_1}{\partial x_2} - \frac{\partial u_2}{\partial x_1} \,. \tag{5.3.54}$$

A potential flow is defined as being stationary, homentropic, irrotational and homoenergetic [83]. The test case considered within the current section is characterized as being stationary and homentropic. An irrotational flow is characterized by a zero value of the rotation of the velocity and thus by a zero value of the vorticity magnitude. Figure 5.3.18 displays the distribution of the vorticity of the homentropic flow within the two-dimensional convergent nozzle exemplarily for an inlet Mach number of 0.3.

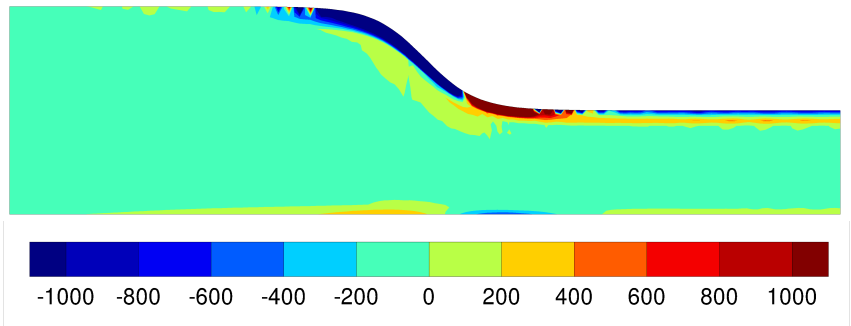

Figure 5.3.18.: Distribution of the vorticity ω [1/s] at $\mathrm{Ma}_{\mathrm{in}} = 0.3$ (homentropic case)

Figure 5.3.18 reveals that the vorticity is zero, apart from few areas in the vicinity of the nozzle contraction. Let us consider a homoenergetic flow. Aside from the time derivative of the total enthalpy $h_t \equiv h + \frac{1}{2}\|\underline{u}\|_2^2$, its gradient ∇h_t vanishes in a homoenergetic flow, so that the following equation holds:

$$\nabla h_t = 0 \Leftrightarrow \nabla \left(h + \frac{1}{2}\|\underline{u}\|_2^2 \right) = 0 \Rightarrow h + \frac{1}{2}\|\underline{u}\|_2^2 = \text{const.} \,. \tag{5.3.55}$$

If a flow is characterized as being homentropic and irrotational, Crocco's theorem [34, 217, 269]

$$\underline{u} \times (\nabla \times \underline{u}) = \nabla h_t - T \nabla s \tag{5.3.56}$$

implies the homoenergetic state of the flow:

$$\nabla s = 0 \quad \text{and} \quad \nabla \times \underline{u} = 0 \Rightarrow \nabla h_t = 0 \,. \tag{5.3.57}$$

As a result of this, the two-dimensional flow considered within this section can be seen as

a homoenergetic flow. With the fulfilled conditions of being stationary, homentropic and mostly irrotational, this flow can thus be described as being mostly potential. Under the assumption of having a stationary, homentropic and mostly irrotational flow, the appearance of vorticity in some thin fluid layers in an essentially vorticity-free flow is described as being *almost potential* by Chorin and Marsden [26].

The two-dimensional test case presented within this section demonstrates that the CPM method is capable of computing flows reaching a Mach number of approximately 0.9. Taking into account the results discussed within section 5.2, the CPM scheme shows the ability to compute flows with a Mach number close to the incompressible limit, as well as flows with a Mach number reaching the limit of $\mathrm{Ma} \rightarrow 1$.

5.3.3.2. Isentropic Case with a Linear Inlet Velocity Profile

The second case treated features a linear profile of the inlet velocity. For this purpose, the second case with a mean inlet Mach number of $\mathrm{Ma}_{\mathrm{in}} = 0.1$ is used. At the bottom of the inlet boundary, the unchanged velocity condition of $u_{\mathrm{in,\,bottom}} = \mathrm{Ma}_{\mathrm{in}} \cdot c_{\mathrm{ref}} = 34.8\,\mathrm{m/s}$ is prescribed. At the top of the inlet surface, a velocity of $u_{\mathrm{in,\,top}} = 1.1 \cdot u_{\mathrm{in,\,bottom}} = 38.3\,\mathrm{m/s}$ is imprinted. Between both values, a linear distribution of the velocity is set, see figure 5.3.19.

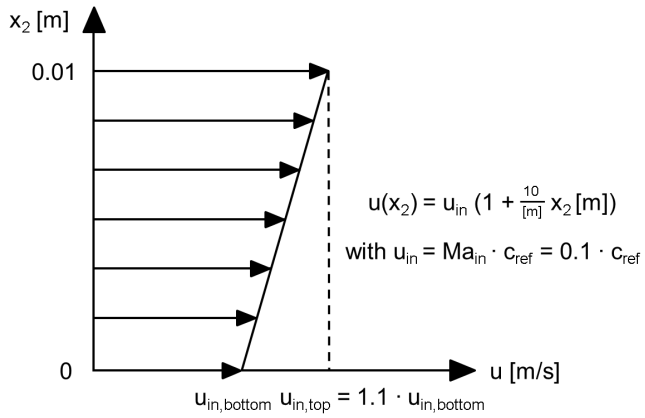

Figure 5.3.19.: Visualization of the linear inlet velocity profile

In order to conduct the numerical simulation, the grid of the homentropic test case is used. The numerical setup remains unchanged with the exception of the projection weighting factor, which is set to a value of 0.25 due to the higher amount of unsteadiness within the start-up phase of the flow field. The solution of the second case defined within the previous section (inlet Mach number of 0.1) constitutes the starting point for the numerical simulation featuring the linear profile of the inlet velocity. The outlet relative static pressure is set to zero, i.e. the outflow is modeled as fully reflective. Figure 5.3.20 depicts the residuals of the momentum, pressure correction and enthalpy equations as a function of the time step

number.

Figure 5.3.20 reveals that convergence of the numerical solution is reached. The residuals of the momentum decrease below the value of 10^{-5}. The residual of the pressure correction and enthalpy equations is reduced to a value below 10^{-4}.

Due to the prescription of a non-constant velocity profile at the inlet boundary, the flow field requires a certain time in order to adopt its steady state. In order to capture this unsteady movement, a sequence of states at different time stamps is shown within figure 5.3.21. Hereby, two-dimensional contour plots displaying the distribution of the axial velocity are plotted.

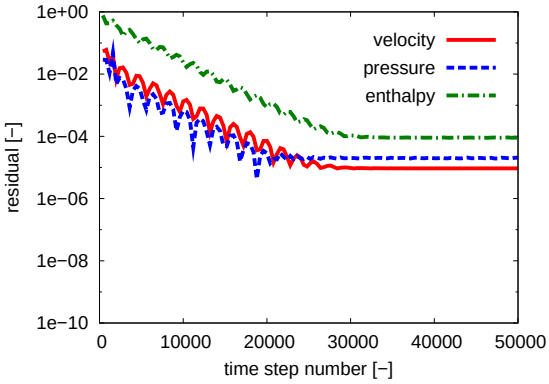

Figure 5.3.20.: Residuals of the momentum, pressure correction and enthalpy equations as a function of the time step number (fully reflective outlet)

Changing the inlet boundary condition to the linear velocity distribution, an unsteady perturbation of the flow field within the start-up phase can be observed (see figures 5.3.21(a)-5.3.21(f)). Following the high amount of initial unsteadiness, the flow field sways in a wave-like form. From the figures 5.3.21(g) and 5.3.21(h), a downwards directed motion of the flow can be detected. This is followed by an upwards directed motion, see the transition from figure 5.3.21(i) to figure 5.3.21(j). The movement sequence observed is repeated as the simulation time increases (see figures 5.3.21(k) - figure 5.3.21(m)) and is damped due to the presence of numerical dissipation until a steady state is reached. The final state acquired can be seen in figure 5.3.21(n).

The density is decreased based on the reduction of the static pressure in streamwise direction. This mechanism is due to the compression of the flow at the nozzle contraction and is of compressible, i.e. “acoustic“, nature. The introduction of a linear excitation profile of the inlet velocity introduces additional perturbation of the pressure field. The induced pressure perturbations are then convected through the flow field by means of the convective term $\underline{u} \cdot \nabla p$. Taking into account the compressibility relation, the pressure perturbations are transferred to the density field. The unsteady movement detected can hence be explained through a combined convective/acoustic mechanism of the flow field.

Moreover, figure 5.3.21(n) reveals an increased maximum value of the axial velocity compared to the homentropic case with a constant inlet velocity distribution. This gives a hint on the maximum Mach number occurring within the flow field. Regarding the homentropic case with a constant inlet velocity distribution, a maximum Mach number of 0.23 is observed. Compared here to, a maximum Mach number of 0.40 is obtained for the linear inlet velocity profile prescribed. Thus, an increase of 10 % in the velocity at the top of the inlet boundary plane causes an augmentation of 75 % regarding the maximum occurring Mach number.

Figure 5.3.22 displays the time sequence visualizing the transient movement of the density distribution. Analogously to the sequence of the axial velocity field, an initial start-up phase featuring a high amount of unsteadiness can be detected (see figures 5.3.22(a)-5.3.22(f)). Following this, a swaying movement of the density field can be observed, see figures 5.3.22(g)-5.3.22(m). This transient movement is repeated and stepwise damped, so that a steady state of the solution is finally obtained, see figure 5.3.22(o).

Besides applying a fully reflective outlet boundary condition, a partially non-reflective outflow boundary condition is used to conduct further investigations concerning the pulsating behavior of the acoustic flow field. The reflection factor is set to a value of $\sigma = 0.27$, see section 4.4 for details. Figure 5.3.23 displays the time sequence regarding the movement of the density field under the prescription of a partially non-reflective outflow condition.

Figures 5.3.23(a)-5.3.23(m) reveal that the amplitude of the density pulsations is far smaller than the one generated by the application of the fully reflective boundary condition. Through the prescription of a partially non-reflective outlet, only a small amount of the generated acoustic waves is thrown back into the computational domain so that the convective-acoustic flow movement decays a lot faster. This enables the flow to reach its steady state faster than it does when setting a fully reflective boundary condition at the outflow. So in conclusion, it can be said that aside from the combined convective/acoustic transport of the unsteady movement, the reflection of acoustic waves at the outlet additionally influences the exhibit of an up- and downwards movement of the flow field. Figure 5.3.23(n) shows the steady state of the flow field with a partially non-reflective outlet at a time of $t = 59.1\,\mathrm{ms}$.

The residuals of the simulation run with the partially reflective outlet are shown in figure 5.3.24. The ultimate residuals remain widely unchanged compared to the residual history of the fully reflective case, cf. figure 5.3.20. It can however be observed that by setting a partially reflective outlet condition, convergence is achieved much faster. The faster convergence in case of setting a partially reflective outlet confirms the results obtained from the contour plots 5.3.23, wherein the steady state of the numerical simulation is reached much earlier than for the fully reflective outlet condition, see contour plots 5.3.22.

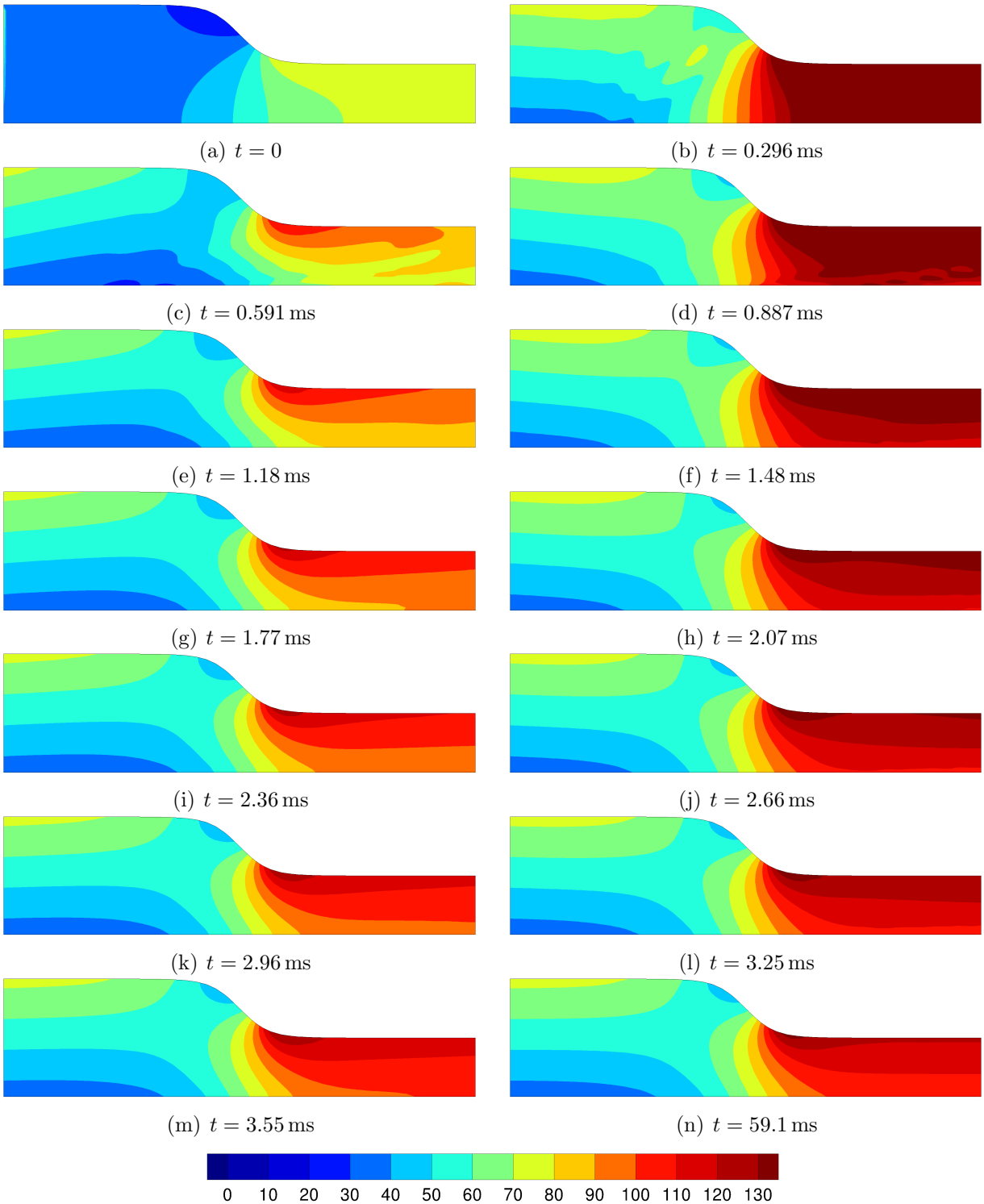

(a) $t = 0$ (b) $t = 0.296\,\text{ms}$

(c) $t = 0.591\,\text{ms}$ (d) $t = 0.887\,\text{ms}$

(e) $t = 1.18\,\text{ms}$ (f) $t = 1.48\,\text{ms}$

(g) $t = 1.77\,\text{ms}$ (h) $t = 2.07\,\text{ms}$

(i) $t = 2.36\,\text{ms}$ (j) $t = 2.66\,\text{ms}$

(k) $t = 2.96\,\text{ms}$ (l) $t = 3.25\,\text{ms}$

(m) $t = 3.55\,\text{ms}$ (n) $t = 59.1\,\text{ms}$

(o) axial velocity u_1 [m/s]

Figure 5.3.21.: Time sequence of different states displaying the movement of the axial velocity field (fully reflective outlet)

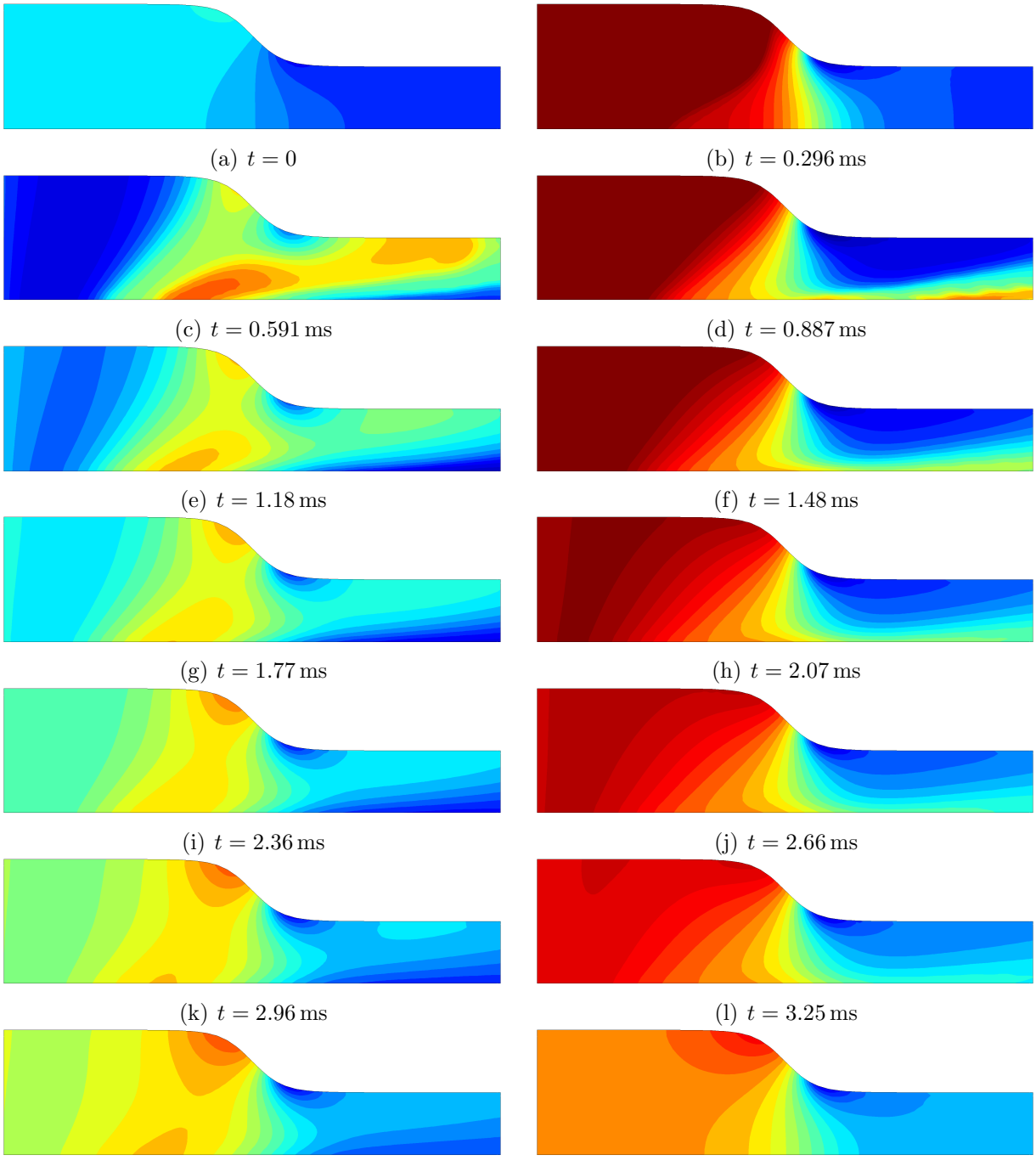

(a) $t = 0$ (b) $t = 0.296\,\text{ms}$

(c) $t = 0.591\,\text{ms}$ (d) $t = 0.887\,\text{ms}$

(e) $t = 1.18\,\text{ms}$ (f) $t = 1.48\,\text{ms}$

(g) $t = 1.77\,\text{ms}$ (h) $t = 2.07\,\text{ms}$

(i) $t = 2.36\,\text{ms}$ (j) $t = 2.66\,\text{ms}$

(k) $t = 2.96\,\text{ms}$ (l) $t = 3.25\,\text{ms}$

(m) $t = 3.55\,\text{ms}$ (n) $t = 59.1\,\text{ms}$

(o) density ρ $[\text{kg/m}^3]$

Figure 5.3.22.: Time sequence of different states displaying the movement of the density field (fully reflective outlet)

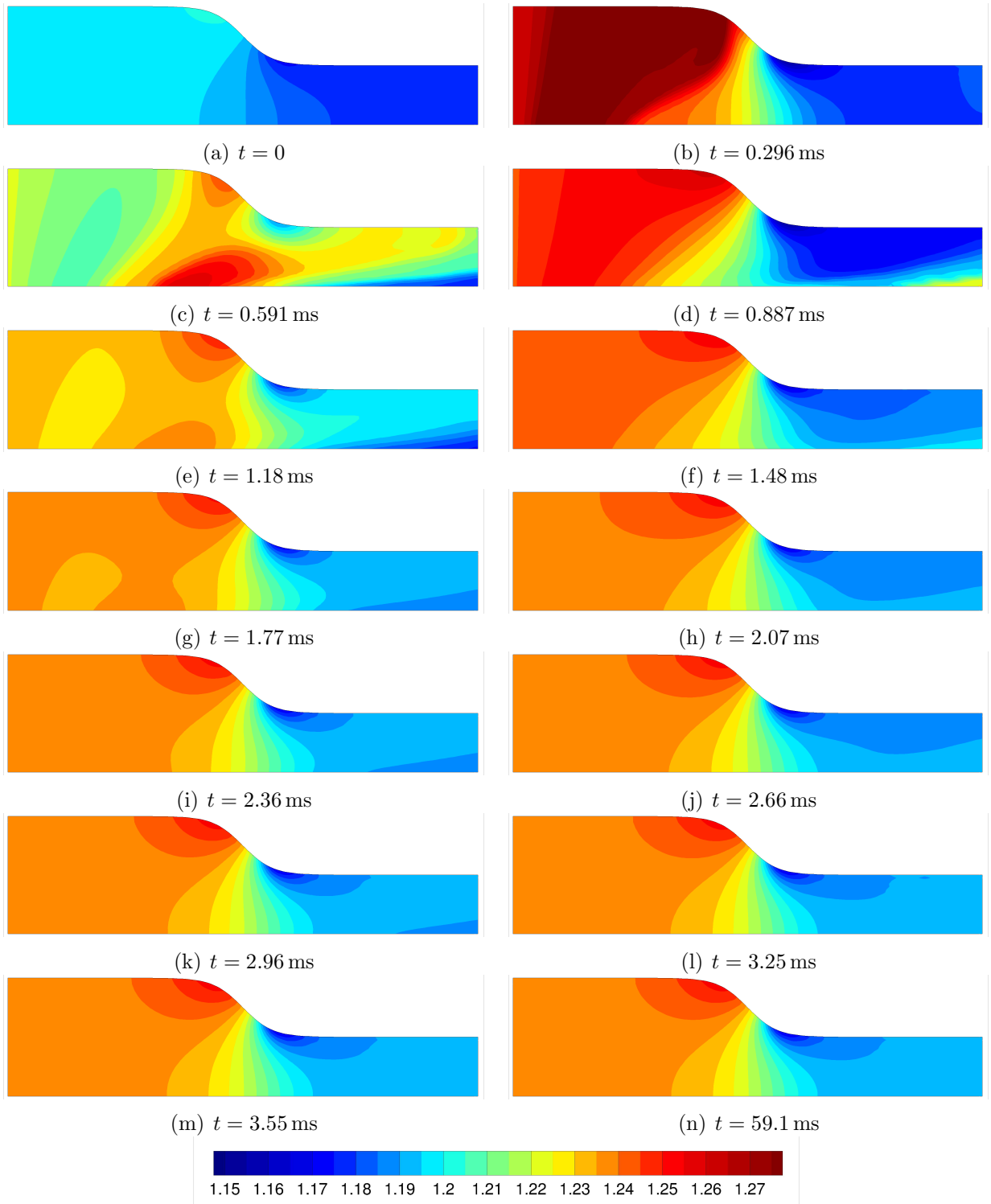

(a) $t = 0$ (b) $t = 0.296\,\text{ms}$

(c) $t = 0.591\,\text{ms}$ (d) $t = 0.887\,\text{ms}$

(e) $t = 1.18\,\text{ms}$ (f) $t = 1.48\,\text{ms}$

(g) $t = 1.77\,\text{ms}$ (h) $t = 2.07\,\text{ms}$

(i) $t = 2.36\,\text{ms}$ (j) $t = 2.66\,\text{ms}$

(k) $t = 2.96\,\text{ms}$ (l) $t = 3.25\,\text{ms}$

(m) $t = 3.55\,\text{ms}$ (n) $t = 59.1\,\text{ms}$

(o) density ρ $[\text{kg/m}^3]$

Figure 5.3.23.: Time sequence of different states displaying the movement of the density field (partially non-reflective outlet)

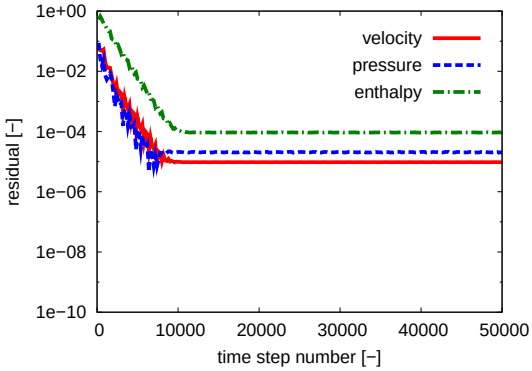

Figure 5.3.24.: Residuals of the momentum, pressure correction and enthalpy equations as a function of the time step number (partially reflective outlet)

Figure 5.3.25(a) compares the density magnitude profile of the numerical solutions featuring the partially non-reflective and fully reflective outlet along the lower wall of the two-dimensional nozzle. In order to better visualize the differences between both profiles, the relative error

$$e_\rho \equiv 100 \cdot \frac{|\rho_{\text{pnrefl}} - \rho_{\text{frefl}}|}{\rho_{\text{frefl}}} \, [\%] \tag{5.3.58}$$

between both density magnitude curves is evaluated, see figure 5.3.25(b). The subscripts pnrefl and frefl denote the states at partially non-reflective and fully reflective conditions, respectively. The values of e_ρ revealed by figure 5.3.25(b) are below $3.5 \cdot 10^{-4}\,\%$, which represents a negligible amount.

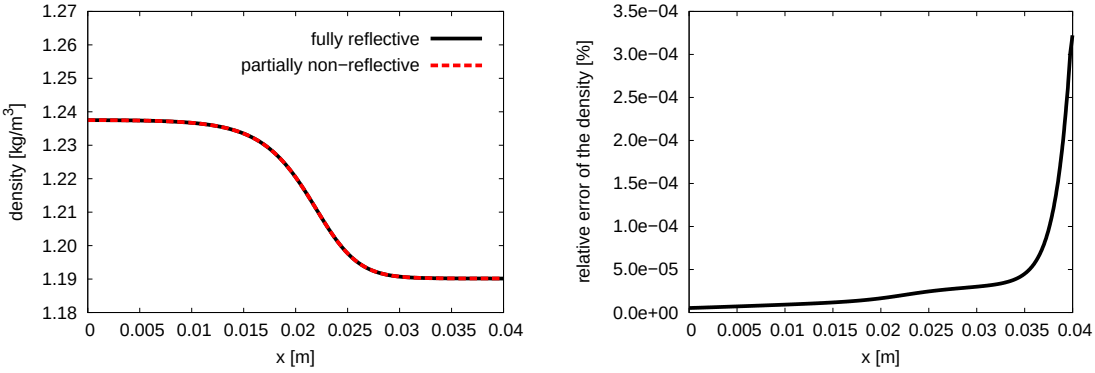

(a) Absolute density profiles (b) Relative error between both density profiles

Figure 5.3.25.: Absolute and relative density profiles along the lower wall

The two-dimensional test case presented within this section demonstrates that the CPM method is capable of computing flows reaching a Mach number of approximately 0.9. Taking into account the results discussed within section 5.2, the CPM scheme shows the ability to compute flows with a Mach number close to the incompressible limit, as well as flows with a Mach number reaching the limit of $\text{Ma} \to 1$.

5.3.4. Three-Dimensional Flow in a Double-Swirled Gas Turbine Combustor

5.3.4.1. Background to Flows in Swirled Gas Turbine Combustors

Regarding the design of modern gas turbine combustor systems, it has become common use to inject the air stream in the form of a swirling jet [67, 99, 126, 130, 131, 146, 233, 253]. Due to the swirled flow injection, an outer and inner recirculation zone are developed [67, 126, 130, 131, 146, 233]. This allows a high energy conversion of chemical in thermal and kinetic energy within a compact volume [99, 130]. Figure 5.3.26 displays schematically the topology of the mean flow field within a partially premixed swirled gas turbine combustion chamber. The abbreviations IRZ and ORZ stand for the inner and outer recirculation zone, respectively.

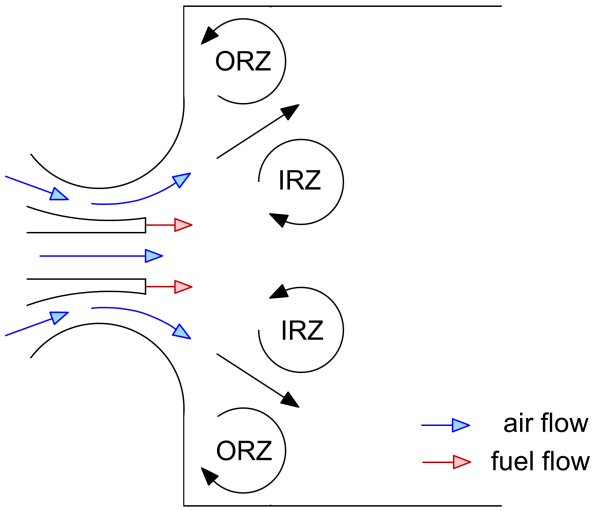

Figure 5.3.26.: Schematic overview of the mean flow topology within a partially premixed swirled gas turbine combustion chamber

Calculating non-reactive and reactive flows, these recirculation regions contribute significantly to the stabilization of the highly turbulent flow and flame structures [126, 130, 131, 67, 146, 233, 253]. Due to the recirculating flow, burned gas is convected backwards thus helping the fresh mixture to ignite. This mechanism improves the stability mechanism of the flame structure, thus helping the flame to be operated under the desired lean conditions [126, 72, 233]. The detailed physical phenomena improving the stability of lean-burning turbulent swirling flames are of high complexity and subject to current research [126, 130, 146, 233].

Depending on the operating conditions, swirling flows may exhibit different flow topologies [21, 53, 126, 127, 156, 234]. Besides the appearance of turbulent velocity fluctuations, coher-

ent flow structures may occur [233]. Helical structures, often referred to as PVC (Precessing Vortex Core) unsteadiness, are the most common coherent flow structures concerning swirled combustion systems [233, 238]. Precessing vortex cores are often encountered in typical swirled gas turbine combustor designs [67, 146, 233]. Further unsteady phenomena concerning swirling flows can arise during the operation of the gas turbine combustors, e.g. due to unsteady vortex breakdowns or thermo-acoustic phenomena caused by interaction mechanisms between the flow field, heat release of the flame and combustor acoustics [104, 180]. The occurring unsteady mechanisms may lead to a significant impact on the development of the flow field and combustion dynamics [258, 259]. Thus, the ability of the numerics to capture the interaction mechanisms of flow structures with combustion processes is of great importance.

Within this section, compressible numerical simulations of the non-reactive and reactive flow in a swirled combustor are carried out. These computations serve to validate the CPM method. Besides conducting numerical simulations using the CPM solution strategy, incompressible computations using the IPM method are performed. The incompressible calculations serve as verification computations for the compressible simulations and are carried out using the solution algorithm for variable density flows. Moreover, URANS (Unsteady Reynolds-Averaged Navier-Stokes), as well as hybrid URANS/LES (Large Eddy Simulation) computations are conducted and compared to one another within this work. For the URANS calculations, the k-ω-SST turbulence model of Menter [149] is applied. The k-ω-SST-SAS (Shear Stress Transport - Scale Adaptive Simulation) turbulence model of Menter et al. [150, 151, 152, 153, 155] is used as a hybrid URANS/LES approach. The ability of the CPM method to calculate the turbulent flow in a swirled gas turbine combustor with occurring Mach numbers approaching the incompressible limit, as well as Mach numbers around 0.3 is demonstrated. Moreover, measurements of the combustor have previously been conducted, which allow a validation of the numerical results.

5.3.4.2. Numerical Setup, Results and Discussion

Within this section the semi-technical gas turbine model combustor test case is presented. In a first step, the numerical setup is described. The numerical results of the incompressible and compressible, as well as of the URANS and SAS calculations are shown next. The gas turbine combustor model used for numerical validation purposes within the present section has been experimentally investigated and characterized within the frame of previous works, cf. references [145, 233, 252]. These experimental data are used in a final step to validate the results of the numerical simulations carried out within the present work.

Numerical Setup The setup of the numerical computations is presented in the following. The air flow is injected at the air inlet and is at first conducted through a plenum, see figures 5.3.27 and 5.3.28(a). After this, the main air flow is separated into two streams, each of which is conducted through a swirler and concentric nozzle into the combustion chamber. The diameter of the inner air nozzle amounts to 15 mm. The outer air nozzle is designed as an annular nozzle and is bounded by an inner and outer diameter of 16 mm and 25 mm, respectively.

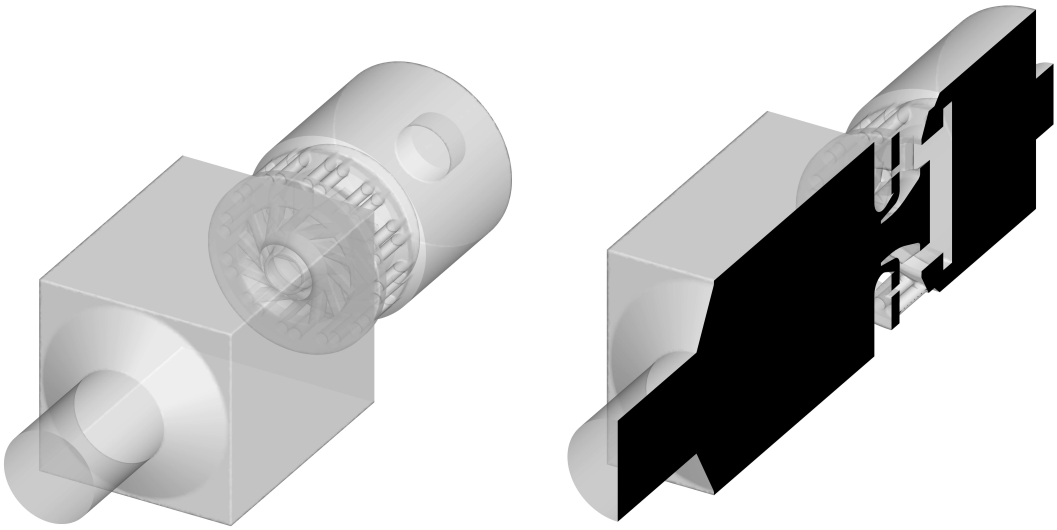

(a) Computational domain (b) x_1-x_3 plane at $x_2 = 0$

Figure 5.3.27.: Computational domain and x_1-x_3 plane at $x_2 = 0$ of the swirled model combustor

The combustion chamber has the dimensions of $[114 \times 85 \times 85]$ mm. The diameter of the outlet nozzle is 40 mm. The fuel is inserted through an annular nozzle into the swirled air streams thus resulting in a partially premixed injection. The inner and outer swirler are composed of eight, respective twelve ducts. The outer and inner swirler are displayed in the figures 5.3.28(b) and 5.3.28(c), respectively.

The computational domain of the model combustor is meshed applying an unstructured grid. The inner field is modeled using tetrahedral volume cells. At the boundaries of the concentric nozzles and combustion chamber, prism cells are used in order to resolve the boundary layer with an appropriate number of grid nodes perpendicular to the respective boundary surface. The parallel arrangement of the prism cells improves the spatial accuracy of the numerical computations near the boundaries. Due to the high complexity of the flow structures at the entrance of the combustion chamber, the accurate resolution of the domain boundaries - especially of the inner and outer nozzles ahead of the combustion chamber - plays an important role within the meshing process of the model. The near-wall regions of

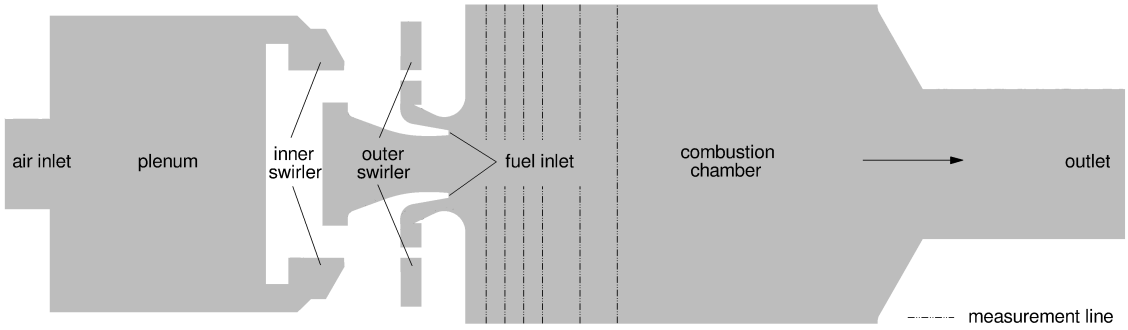

(a) Model description (x_1-x_2 plane)

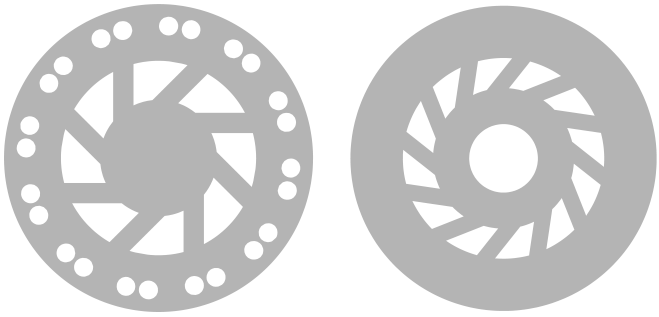

(b) Outer swirler (c) Inner swirler

Figure 5.3.28.: Visualization of the model, outer and inner swirler

the nozzles and combustion chamber are meshed such that the condition $y^+ \approx 1$ is satisfied for the k-ω based turbulence models applied. 12 prism layers are applied in order to mesh the near-wall region. This yields a total number of 14 near-wall grid points, including the shifted boundary node generated by the preprocessor of the DLR THETA code, see section 4.4 for details. The mesh of the x_1-x_2 plane at $x_3 = 0$ is displayed in figure 5.3.29(a). A closer look onto the mesh at the outlet of the outer nozzle is given in figure 5.3.29(b).

The surface of the model combustor is discretized by means of triangular- and quadrilateral-shaped faces. The prism layers are connected to the tetrahedral cells via pyramids. In total, the computational model is composed of 11.3 million volume cells and 2.38 million grid nodes. A detailed specification of the number of grid cells is given in table 5.12.

Within this work, several numerical simulations of the turbulent unsteady flow within the swirled model combustor are carried out. In doing so, the incompressible and compressible

Number of surface cells [10^6]		Number of volume cells [10^6]		
Triangles	Quads	Prisms	Tetrahedra	Pyramids
0.219	0.00160	1.36	9.91	0.00459

Table 5.12.: Number of grid cells of the discretized combustor model

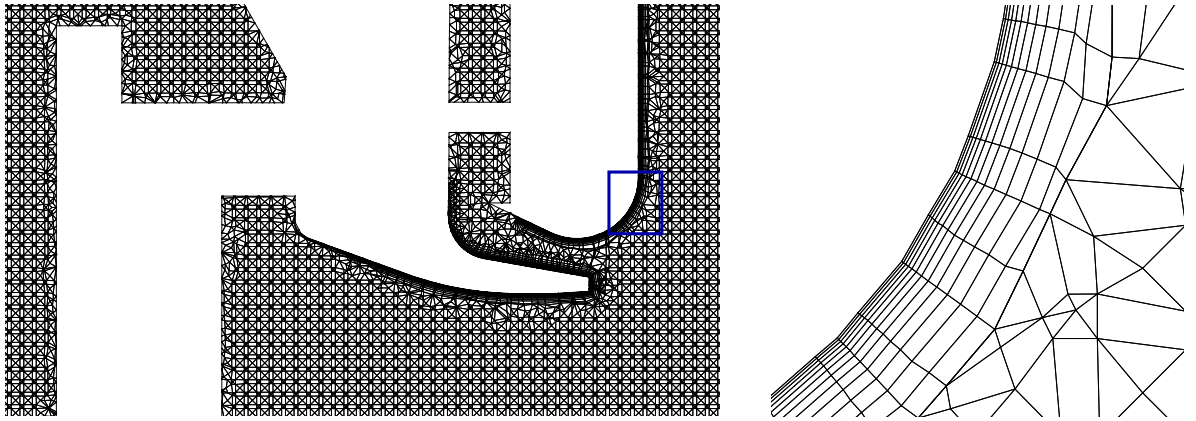

(a) x_1-x_2 plane at $x_3 = 0$ (b) Zoom into the outer nozzle outlet

Figure 5.3.29.: Mesh of the swirled model combustor

projection methods (IPM/CPM) are applied. Calculations with and without combustion (reactive/non-reactive flow) are conducted. Moreover, the influence of the turbulence modeling is analyzed. Table 5.13 summarizes the numerical simulations conducted in this work.

The Reynolds number has been evaluated based upon the experimental test rig to $52.5 \cdot 10^3$ [233]. The swirl number, being defined as the ratio of the tangential to the axial momentum has been determined within the framework of previously conducted experimental studies to a value of 0.9 [252]. In the case of the reactive flow, the model combustor is operated at a global equivalence ratio of 0.65. The thermal power of the combustor amounts to 35 kW. For the reactive simulations, the combined EDM/FRC combustion approach is applied. The URANS and SAS calculations are conducted using the k-ω-SST and k-ω-SST-SAS turbulence model, respectively. Assuming that the URANS based computation of the compressible reactive case does not provide any additional information compared to the URANS based incompressible reactive simulation, it is not carried out within the frame of this work.

At the air inlet, a mass flux of $\dot{m}_{\text{air, in}} = 18.25\,\text{g/s}$ is prescribed. The air inlet introduces a gas mixture into the plenum consisting of oxygen and nitrogen, with the respective mass

Case number	Solution strategy	Combustion modeling	Turbulence modeling
1	IPM	non-reactive	URANS
2	IPM	non-reactive	SAS
3	CPM	non-reactive	URANS
4	CPM	non-reactive	SAS
5	IPM	reactive	URANS
6	IPM	reactive	SAS
7	CPM	reactive	SAS

Table 5.13.: Computed cases of the model combustor

fractions of 0.767 and 0.232. The fuel inlet mass flux amounts to $\dot{m}_{\text{fuel, in}} = 0.697\,\text{g/s}$. Gaseous methane is used as fuel species. As methane is the only species prescribed at the fuel inlet, its mass fraction is set to 1. The temperature at the air and fuel inlet boundaries is set to 330 K. The reference density values of air and methane at $T_{\text{ref}} = 330\,\text{K}$ amount to $\rho_{\text{air, ref}} = 1.065\,\text{kg/m}^3$ and $\rho_{\text{fuel, ref}} = 0.592\,\text{kg/m}^3$, respectively. At both inlets, the turbulence degree and the turbulent length scale are set to the values of 5 % and $5 \cdot 10^{-4}$, respectively. The reference value of the absolute pressure is set to 101325 Pa. The relative pressure is set to zero at the outlet of the combustion chamber. The heat and diffusion fluxes within the enthalpy and species mass fractions equations are set to the following expressions:

$$\underline{q} = -\left(\frac{\mu_l}{\text{Pr}_l} + \frac{\mu_t}{\text{Pr}_t}\right)\nabla h\,, \tag{5.3.59}$$

$$\underline{\underline{j}} = -\left(\frac{\kappa}{c_p} + \frac{\mu_t}{\text{Sc}_t}\right)\nabla \underline{Y}\,. \tag{5.3.60}$$

In the non-reactive cases 1-4, all wall boundaries are set to adiabatic walls. Concerning the reactive cases 5-7, a temperature of 600 K is used as isothermal boundary condition at the combustion chamber bottom. The temperature at the combustion chamber walls is set to a fixed value of 1050 K. These temperature values have been determined based on an estimation obtained from the experimental setup. It has to be emphasized at this point that the assumption of a constant wall temperature at the combustion chamber bottom and combustion chamber walls introduces a certain error into the numerical simulation concerning the near-wall modeling of the heat transfer. Concerning the kinematic boundary conditions, a no-slip boundary condition is applied to all walls.

The time step size is set to the value of $\Delta t = 10^{-6}\,\text{s}$. In case of the compressible reactive SAS simulation, the time step size is reduced by one quarter to a value of $2.5 \cdot 10^{-7}\,\text{s}$ due to stability reasons. The residence time of the flow approximately amounts to 0.035 s. This value has been calculated analytically by separating the combustor geometry into simple geometrical segments and assuming mean flow velocities for each segment. The numerical simulations are performed in the following way: A steady-state computation is conducted at first and serves as initial solution state for the unsteady calculations. In a next step, two residence times of the flow field are run through in order to avoid numerical influences of the initial solution. Following this, the flow field of the numerical simulations is averaged over the time period of four residence times resulting in an averaging time window of 0.14 s.

The temporal discretization is performed using the TPB scheme. The convective part of the momentum, enthalpy and species equations is discretized using the QUDS scheme. For the compressible reactive computation (case 7), the LUDS scheme has been applied to

discretize the convective terms of the conservation equations. The CDS discretization formula is applied to the diffusive terms of the governing equations. The PBCGS algorithm is used in order to solve the momentum, enthalpy, species mass fractions and turbulence equations. The error after which the linear solver exits the inner iteration loop is set to 10^{-4}. The projection weighting factor is set to a value of 0.5 in case of the URANS calculations. Dealing with the SAS computations, a value of 0.25 is chosen for the projection weighting factor. For the compressible reactive simulation (case 7), the projection weighting factor is set to a value of 0.125 due to stability reasons.

Concerning the reactive cases, the reaction mechanism of Nicol et al. [171] is applied to model the chemical kinetics of the air/methane mixture. Since the analysis of NO_x formation is not of primary interest to the present test case, the reactions concerning nitric oxide are dropped. As a consequence, the reaction mechanism applied includes three steps:

$$CH_4 + \frac{3}{2}O_2 \rightarrow CO + 2H_2O \tag{5.3.61}$$

$$CO + \frac{1}{2}O_2 \rightarrow CO_2 \tag{5.3.62}$$

$$CO_2 \rightarrow CO + \frac{1}{2}O_2 \tag{5.3.63}$$

The velocities of the forward and backward reactions, as well as the Arrhenius parameters are set to the values given by Nicol et al. [171].

In the following, the results of the numerical simulations 1-7 are presented. In a first step, the instantaneous flow field is analyzed. Following this, the time-averaged results obtained from the numerical simulations are presented and validated against experimental data.

Instantaneous Flow Field The visualization of the instantaneous flow field can provide information on highly unsteady flow characteristics, which may not be visible anymore within the time-averaged data. Figure 5.3.30 displays the instantaneous flow field of the cases 5 and 6 (see table 5.13) at the time $t = 0.15\,\mathrm{s}$. The streamlines are colored with the instantaneous velocity magnitude $\|\underline{u}\|_2$.

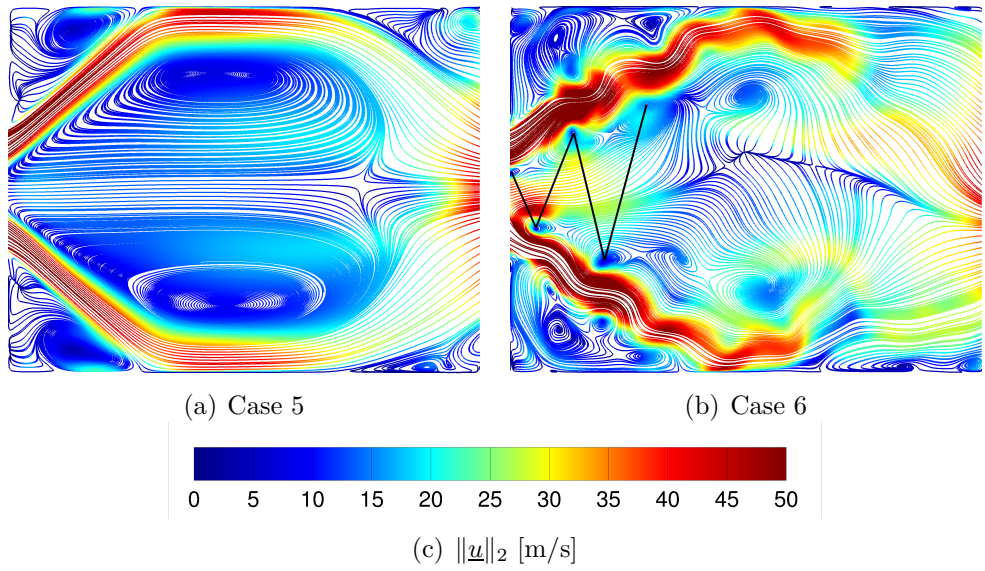

(a) Case 5 (b) Case 6

(c) $\|\underline{u}\|_2$ [m/s]

Figure 5.3.30.: Visualization of the instantaneous flow field at $t = 0.15\,\mathrm{s}$

Figure 5.3.30(a) shows the URANS solution, whereas figure 5.3.30(b) depicts the SAS result. The URANS calculation shows a time-averaged like instantaneous flow field. The URANS calculation in this particular case is not able to resolve the unsteadiness of the flow field. The SAS computation shows however the ability of resolving the fine structures within the turbulent flow field, see 5.3.30(b). As a result of this, the high spatial resolution of the turbulent structures achieved through the LES-like mode of the SAS computation is of essential importance to resolve the unsteady phenomena of the flow field.

The instantaneous flow field of the SAS computation is capable of resolving a high amount of the flow unsteadiness. As it can be seen from figure 5.3.30(b), the instantaneous solution gives information on the occurrence of a helical flow structure. This hydrodynamic structure can be observed by a zig-zag arrangement of the occurring vortices and indicates the presence of a PVC (Precessing Vortex Core), which represents a typical unsteady phenomenon for swirled flows within combustion systems. The PVC structure is a complex hydrodynamic mechanism, which is influenced in a large part by the swirl number, the geometry of the

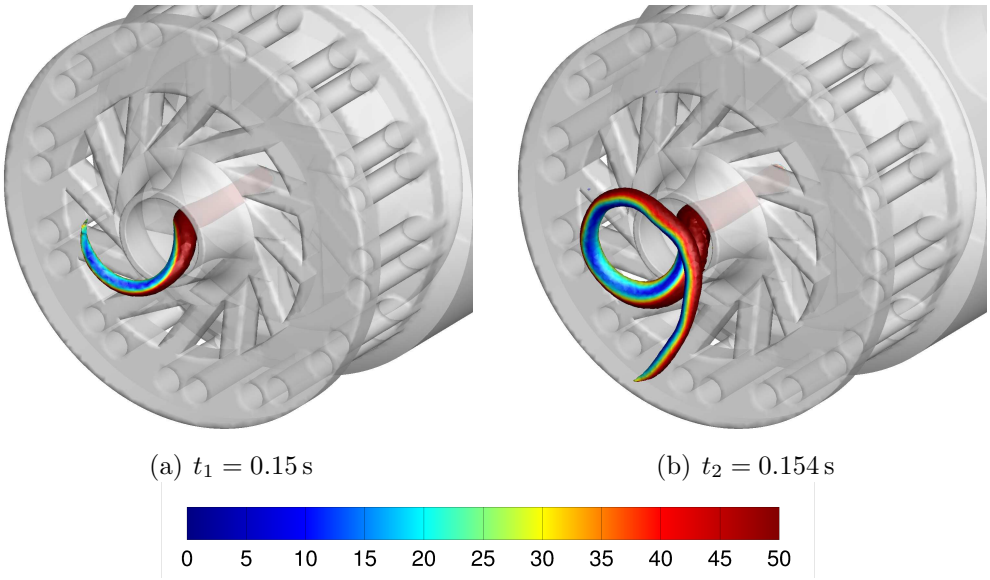

(a) $t_1 = 0.15\,\mathrm{s}$ (b) $t_2 = 0.154\,\mathrm{s}$

(c) $\|\underline{u}\|_2$ [m/s]

Figure 5.3.31.: Visualization of the three-dimensional structure of the PVC at two different times (case 6)

swirler and nozzles within the combustion system as well as by the equivalence ratio of the gas mixture, as noted by Syred [238] and Widenhorn et al. [258, 259].

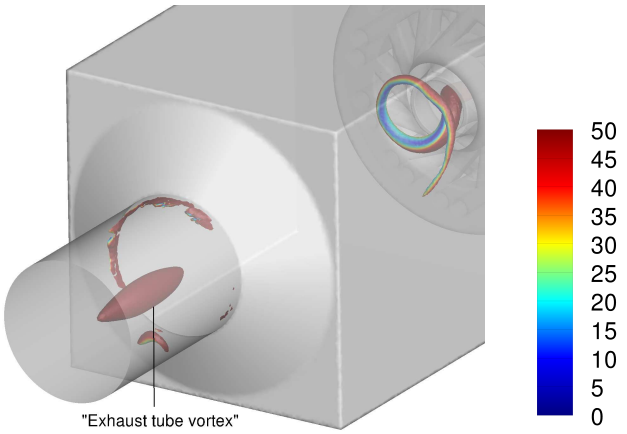

(a) Exhaust tube vortex (b) $\|\underline{u}\|_2$ [m/s]

Figure 5.3.32.: Exhaust tube vortex appearing at the combustion chamber top (case 6 at $t = 0.154\,\mathrm{s}$)

In order to visualize the three-dimensional structure of the PVC, iso surfaces of the pressure are evaluated at two different times. The analysis is conducted based on the SAS simulation (case 6). Concerning the iso surfaces, the relative pressure is set to a value of $p = 150\,\mathrm{Pa}$. Moreover, the iso surfaces are colored with the instantaneous velocity magnitude.

Based on figure 5.3.31, it can be seen that the PVC rotates around the axial axis of the

combustor. The rotation direction is equal to the rotation of the air swirler. The helical structure of the PVC results in the generation of highly turbulent and unsteady vortices which improve the mixing mechanism of the air and fuel streams.

In addition to the precessing vortex core, a vortex appears at the contraction of the combustion chamber close to the outlet. This "exhaust tube vortex" is created at the top of the combustor and spreads along the center line upstream into the combustion chamber. The exhaust tube vortex can also be detected as "tornado-like" curve in axial direction along the combustor centerline within flow field topology of the instantaneous SAS results, see figure 5.3.30(b). The vortex occurring at the top of the combustion chamber has been extracted from the results of the sixth case (incompressible reactive computation using the k-ω-SAS-SST turbulence model) after an elapsed physical time of $t = 0.154\,\mathrm{s}$ and has also been observed in numerical simulations using the commercial CFD software ANSYS CFX [259, 260], as well as in the experimental results [233] conducted within the frame of previous works. The exhaust tube vortex is detected by applying iso surfaces of the pressure at $p = -250\,\mathrm{Pa}$ and shown within figure 5.3.31. The iso surfaces of the pressure are colored with the instantaneous velocity magnitude $\|\underline{u}\|_2$.

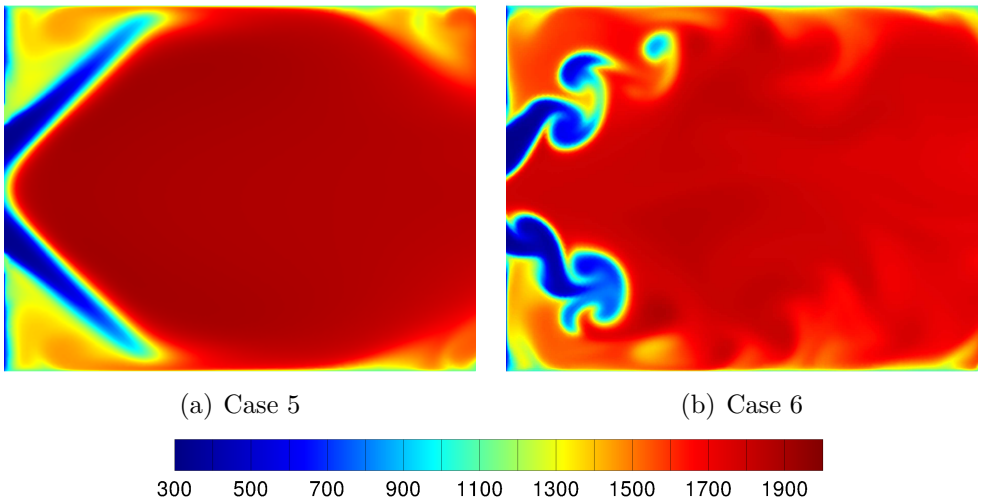

(a) Case 5 (b) Case 6

(c) T [K]

Figure 5.3.33.: Visualization of the instantaneous temperature field at $t = 0.15\,\mathrm{s}$

The figures 5.3.33(a) and 5.3.33(b) show the instantaneous distribution of the temperature field at the time of $t = 0.15\,\mathrm{s}$ for the simulation cases 5 and 6, respectively. The URANS-based computation (case 5) is not able to picture the unsteadiness of the heat release generated by the flame, see figure 5.3.33(a). Contrary here to, the SAS-based calculation (case 6) resolves a high amount of unsteadiness concerning the heat release of the flame, see figure 5.3.33(b). The SAS computation reveals a highly turbulent wrinkled-like shape of the flame

front. Opposed here to, the URANS calculation unveils a connected, cone-like shape of the flame front. Both cases reveal a V-shaped form of the flame structure.

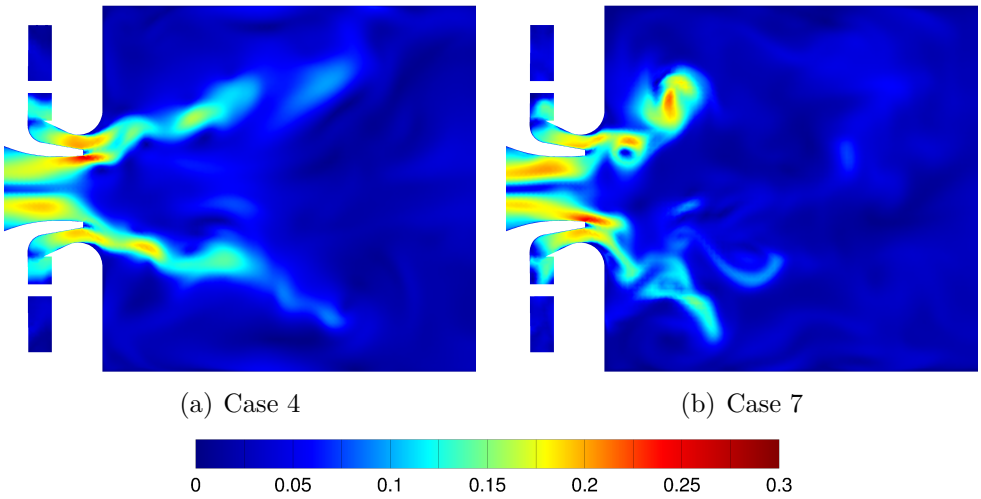

(a) Case 4 (b) Case 7

(c) Ma [–]

Figure 5.3.34.: Distribution of the instantaneous Mach number field (cases 4 and 7)

Figure 5.3.34 displays the distribution of the instantaneous Mach number field on the x_1-x_2-plane at $x_3 = 0$ of the compressible non-reactive (figure 5.3.34(a)) and reactive (figure 5.3.34(b)) SAS computations. The highest Mach numbers appear at the outflow of the inner as well as at the outer air nozzle, where the flow is accelerated. The maximum Mach number amounts to Ma = 0.26 for the non-reactive case and to Ma = 0.25 for the reactive case. It can be noticed that both maxima are quite close to each other. This is due to the fact that in the reactive flow, the zones of highest Mach numbers occur before the ignition of the gas, as shown in the distribution of the temperature field (cf. figures 5.3.33 and 5.3.50. The ignition of the gas mixture downstream of the combustion chamber entrance leads to an increase of the temperature and speed of sound. As a consequence, the Mach number is decreased to small values up to the order of $10^{-6} \div 10^{-4}$ in downstream direction, see figures 5.3.34(a) and 5.3.34(b).

Due to the strong swirl of the flow, a separation of the flow at the outlet of the outer air nozzle is observed. This flow separation is of unsteady nature. Figure 5.3.35 shows a sequence of contour plots, which reveal the distribution of the instantaneous axial velocity field of the incompressible reactive SAS computation (case 6). The black lines found within the countour plots denote isolines of zero axial velocity. They indicate the location of recirculation zones. The first contour plot depicts the axial velocity field at $t = 0.156\,\mathrm{s}$. The difference in time between each instantaneous plot amounts to 2 ms.

Figures 5.3.35(a)-5.3.35(f) reveal a high amount of unsteadiness, which influences the struc-

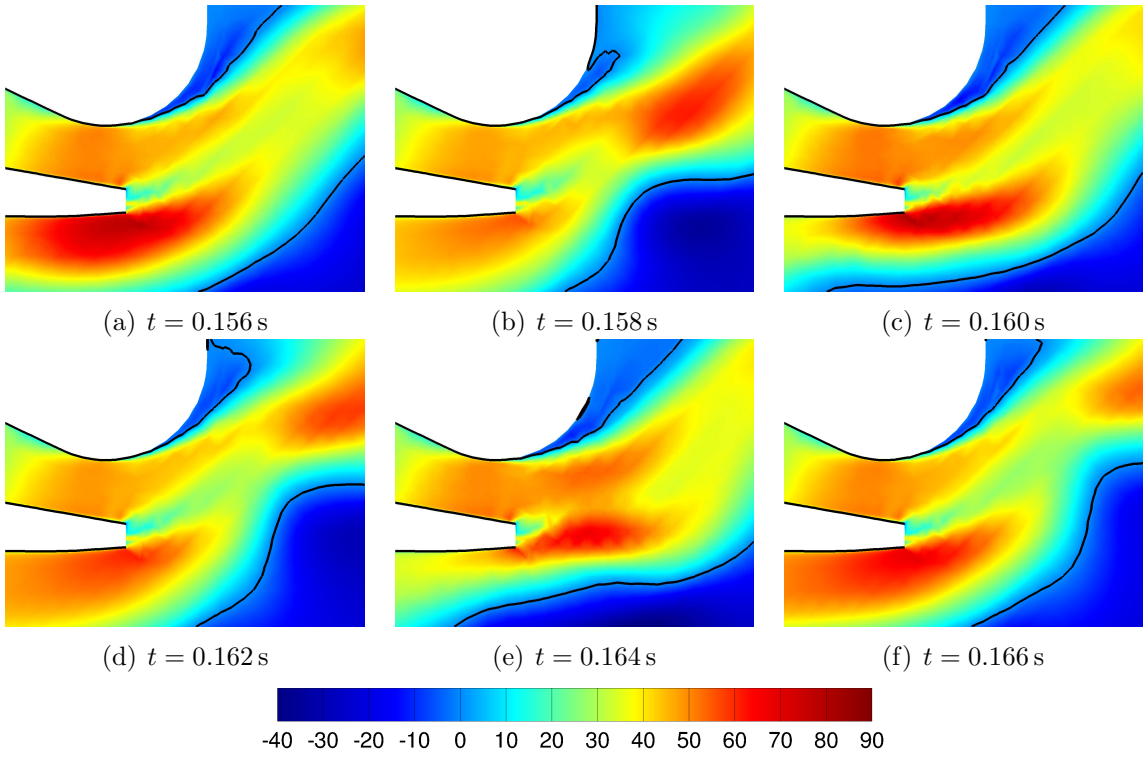

(a) $t = 0.156\,\mathrm{s}$ (b) $t = 0.158\,\mathrm{s}$ (c) $t = 0.160\,\mathrm{s}$

(d) $t = 0.162\,\mathrm{s}$ (e) $t = 0.164\,\mathrm{s}$ (f) $t = 0.166\,\mathrm{s}$

(g) u_1 [m/s]

Figure 5.3.35.: Sequence of instantaneous axial velocity contour plots with zero axial velocity isolines (SAS computation, incompressible reactive case)

ture and size of the recirculation zone occurring at the outer air nozzle exit. The lower recirculation area seen within figures 5.3.35(a)-5.3.35(f) is identified as the inner recirculation zone of the combustor. The sequence of contour plots additionally reveals an oscillating behavior of the recirculation zones. It can be seen that the high axial velocity region coming from the outer part of the inner nozzle merges with the high velocity area from the outer nozzle and is convected in upwards direction into the combustion chamber. This process is repeated so that it can be described as being oscillating. As this mechanism is observed in the incompressible solution, it is not related to thermo-acoustic interaction mechanisms, but of hydrodynamic nature. Figure 5.3.36 displays the instantaneous flow topology colored with the axial velocity and pressure in addition to zero axial velocity isolines of the incompressible reactive SAS computation at 0.160 s, 0.162 s and 0.164 s.

The streamlines seen in figure 5.3.36 depict the helical structure of the precessing vortex core. Furthermore, it can be seen that the zero axial velocity isolines of the inner recirculation zone match with the vortex centers. The first PVC vortex appearing at lower left corner adds momentum to the flow on the upper side of it, so that the flow accelerates, see figure 5.3.36(a). The increased velocity leads to a reduction of the local pressure, see figure 5.3.36(e). A suction

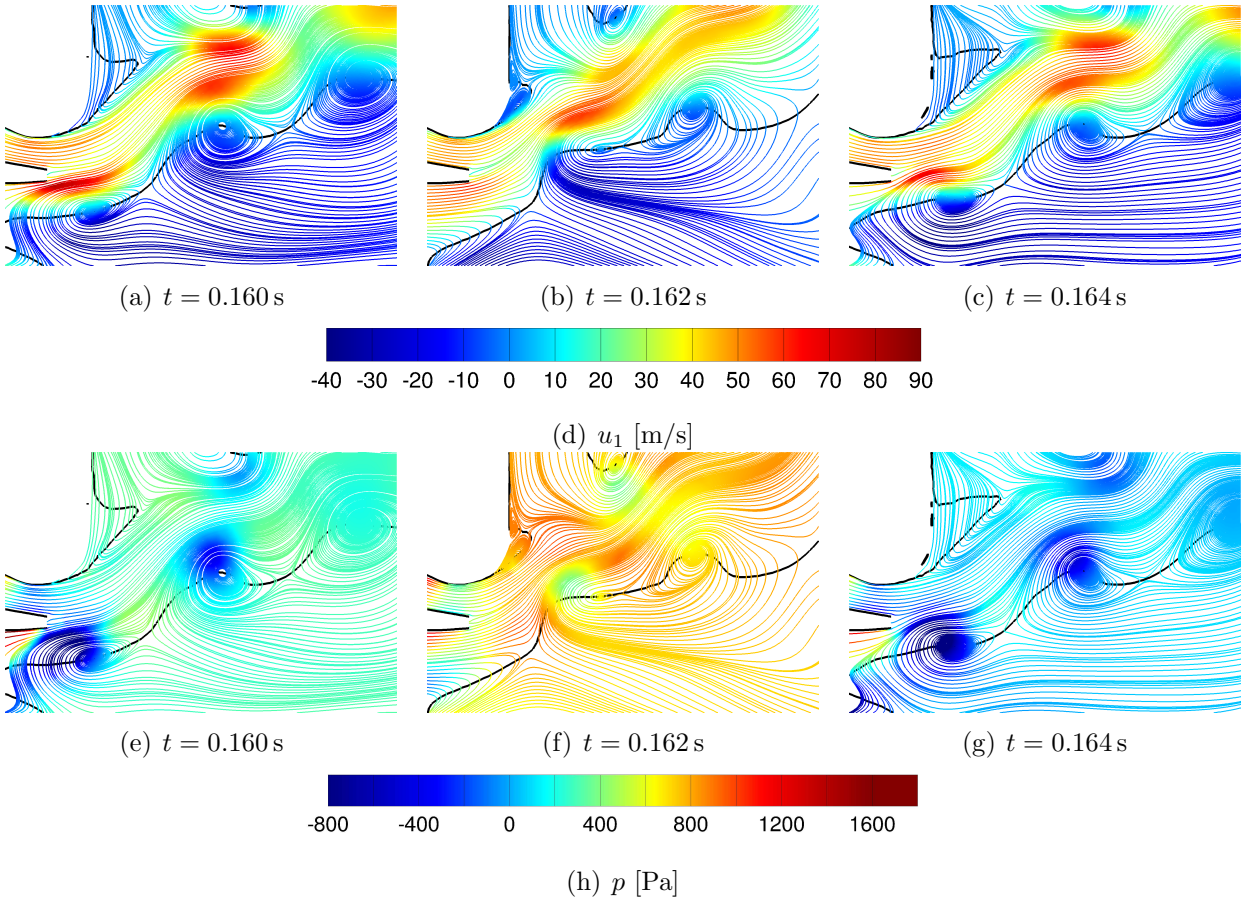

(a) $t = 0.160\,\mathrm{s}$ (b) $t = 0.162\,\mathrm{s}$ (c) $t = 0.164\,\mathrm{s}$

(d) u_1 [m/s]

(e) $t = 0.160\,\mathrm{s}$ (f) $t = 0.162\,\mathrm{s}$ (g) $t = 0.164\,\mathrm{s}$

(h) p [Pa]

Figure 5.3.36.: Instantaneous flow topology colored with the axial velocity and pressure in addition to zero axial velocity isolines (SAS computation, incompressible reactive case)

is thus created, which pulls the recirculation zone from the outer nozzle wall towards it. This enlarges the recirculation area, see figures 5.3.36(e). The movement of the local PVC vortex in downstream direction results in an augmentation of the pressure and thus a reduction of the recirculation zone, see figure 5.3.36(f). This periodic process repeats itself, see figures 5.3.36(c) and 5.3.36(g).

Time Averaged Flow Field In order to validate the averaged data obtained from the numerical results, experimental data issued from previous works [145, 233, 252] is utilized. In the case of the non-reactive and reactive flow configurations, stereoscopic PIV (Particle Image Velocimetry) measurements are available [233]. The distribution of the temperature field has been previously measured using Raman spectroscopy [145, 252]. According to [233], the measurement error of the instantaneous velocity values determined from the PIV experiments due to the inertia of the inserted particles amounts to $e_{\mathrm{PIV}} = 2\ \%$. Further uncertainty errors include the inaccuracy of the air and fuel mass flux controllers during operation of the test rig

(quantified to approximately $e_{\dot{m}} \approx \pm 2\ \%$) [233] and the evaluation of in-plane (quantified to $e_{u_{1,2}} = \pm 1.4\,\mathrm{m/s} \approx \pm 0.014 \cdot u_{1_{\max}}$) [234] and out-of-plane (quantified to approximately $e_{u_3} \approx 3 \cdot e_{u_{1,2}} = \pm 4.2\,\mathrm{m/s} \approx \pm 0.05 \cdot u_{3_{\max}}$) [234] velocity components from particle images. Aside from these error sources, there are areas where greater inaccuracies occur due to the reflection of particles at walls and the interpolation over missing data e.g. due to low particle densities in vortex centers (part of missing data smaller than 2 %) [234]. The overall measurement error of the velocity fluctuations is estimated to $e_{u_i'} \approx \pm 10\ \%$ [234].

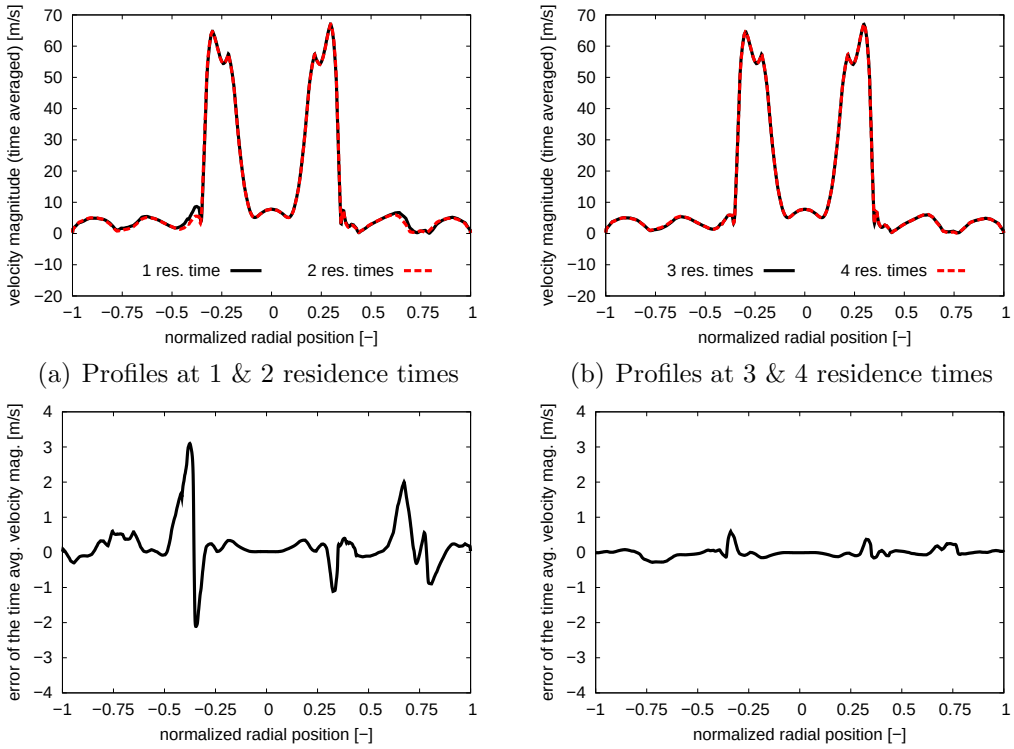

(a) Profiles at 1 & 2 residence times

(b) Profiles at 3 & 4 residence times

(c) Error between the profiles at 2 & 1 residence times

(d) Error between the profiles at 4 & 3 residence times

Figure 5.3.37.: Analysis of the averaging time period at $x_1 = 0\,\mathrm{m}$ (case 1)

Concerning the experimental determination of the temperature field by means of the Raman measurement technique, the error approximately amounts to $e_T \approx \pm(3 \div 4)\ \%$ [145, 252, 253]. This error is mainly due to errors occurring during the calibration of the Raman signals by means of the CARS (Coherent Anti-Stokes Raman Spectroscopy) measurement method, e.g. due to errors within the output of the mass flux controllers [5, 253]. In addition to this, uncertainties through drifts appearing in the detection of the laser energy or through the displacement of signal wavelengths introduce a certain error into the experimentally determined temperature field [5, 253]. The measurement error for the temperature has been determined based on a reference value of 1900 K. In regions with significantly lower temperatures, such as fresh gas areas, the density is higher. This increases the intensity of

the Raman signal, which eventually results in smaller measurement uncertainties [5, 253]. Having said that, the uncertainties noted above have to be accounted for when the numerical results are compared to the experimental data.

Before considering the results, the assumption of choosing an averaging window of four residence times is verified. In doing so, the time-averaged velocity magnitude is determined after one, two, three and four residence times of the flow field at the combustion chamber bottom, equivalent to the position $x_1 = 0$. The results are presented in figure 5.3.37 and refer to the second case (see table 5.13).

Figures 5.3.37(a) and 5.3.37(c) show small changes in the velocity magnitude remain between the solutions after one and two residence times. The maximum occurring difference equals 3.1 m/s. Considering the profiles after three and four residence times, the remaining differences between both solutions are of one magnitude smaller. The maximum discrepancy between both profiles is 0.6 m/s, which represents a negligible amount. The assumption of using an averaging window of four residence times equivalent to a physical time of 0.14 s is thus eligible to conduct a reasonable analysis of the time-averaged numerical results.

In the following, one-dimensional profiles of the time-averaged (first moments) and root-mean squared (second moments) velocity components obtained from the numerical simulations are compared to the measurement results along selected measurement lines. The measurement lines are illustrated within figure 5.3.28(a). Let ϕ be an arbitrary scalar variable. Moreover, denote t^0 and δt the initial time and the recording time window, respectively. The time-averaged value of ϕ is then defined by the following formula:

$$\phi^{\mathrm{avg}} \equiv \lim_{\delta t \to \infty} \frac{1}{\delta t} \int_{t^0}^{t^0+\delta t} \phi\,(t)\, dt \approx \sum_{i=1}^{N_{\mathrm{ts}}} \left(\frac{t_i}{t_i + \Delta t} \phi_{i-1}^{\mathrm{avg}} + \frac{\Delta t}{t_i + \Delta t} \phi_i \right) . \tag{5.3.64}$$

The root-mean-squared value of ϕ is described by the following equation:

$$\begin{aligned} \phi^{\mathrm{rms}} &\equiv \lim_{\delta t \to \infty} \sqrt{\frac{1}{\delta t} \int_{t^0}^{t^0+\delta t} \left[\phi\,(t) - \phi^{\mathrm{avg}}\,(t)\right]^2 dt} \\ &\approx \sum_{i=1}^{N_{\mathrm{ts}}} \left[\frac{t_i}{t_i + \Delta t} \phi_{i-1}^{\mathrm{rms}} + \frac{\Delta t}{t_i + \Delta t} \left(\phi_i - \phi_{i-1}^{\mathrm{avg}}\right) \cdot \left(\phi_i - \phi_i^{\mathrm{avg}}\right) \right] \end{aligned} \tag{5.3.65}$$

with the initial values

$$\phi_{i=0}^{\mathrm{avg}} = 0 \quad \text{and} \quad \phi_{i=0}^{\mathrm{rms}} = 0\,.$$

According to the k-ω-SST and k-ω-SST-SAS turbulence models applied, two third of the modeled turbulent kinetic energy $2/3\, k_{\mathrm{mod}}^{\mathrm{avg}}$ has to be added to the root-mean-squared values of the axial, radial and tangential velocities (cf. Boussinesq's approximation, references

[96, 262]):

$$u_{i_{\mathrm{cor}}}^{\mathrm{rms}} \equiv \sqrt{\left(u_i^{\mathrm{rms}}\right)^2 + \frac{2}{3} k_{\mathrm{mod}}^{\mathrm{avg}}} \ , \ \forall i \in \{1, \ldots, 3\} \ . \tag{5.3.66}$$

The variable $k_{\mathrm{mod}}^{\mathrm{avg}}$ denotes the time-averaged value of the modeled turbulent kinetic energy. $u_{i_{\mathrm{cor}}}^{\mathrm{rms}}$ describes the corrected root-mean-squared value of the velocity component i due to the addition of the modeled turbulent kinetic energy.

In the following, radial profiles of the time-averaged and root-mean-squared velocity components for the measurement lines specified in figure 5.3.28(a) are shown for the non-reactive and reactive flow. In addition to the velocity components, time-averaged temperature profiles along the selected measurement lines are displayed for the reactive flow field. Errorbars depicting the uncertainty of the experimental results are shown for the velocity and temperature profiles. The lengths of the respective errorbars are obtained through the sum of the individual measurement uncertainties quantified further above. As a result, the following measurement uncertainties are obtained for the velocity components:

$$e_{u_{1,2}}^{\mathrm{avg}} = (-5.5 \div +7.5) \ \% \, , \tag{5.3.67}$$

$$e_{u_3}^{\mathrm{avg}} = (-9 \div +11) \ \% \, , \tag{5.3.68}$$

$$e_{u_{1,2,3}}^{\mathrm{rms}} = (-10 \div +10) \ \% \, . \tag{5.3.69}$$

The measurement uncertainty for the temperature is determined based on an arithmetic average of the uncertainty range provided further above and is quantified to:

$$e_T^{\mathrm{avg}} = (-3.5 \div +3.5) \ \% \, . \tag{5.3.70}$$

It should be noted that these summed up uncertainties represent global errors and can thus be understood as reference values for the experimental error. It has to be borne in mind though that the local errors contained in the experimental results may be smaller or higher than the global errors provided by equations (5.3.67)-(5.3.70).

Figures 5.3.38-5.3.40 display the time-averaged values of the axial, radial and tangential velocities along the previously defined measurement lines (see figure 5.3.28(a)). As it can be seen from the time-averaged axial velocity profiles of the URANS calculations, the peaks of the incompressible and compressible curves are shifted towards the radial boundaries of the combustion chamber walls. Moreover, it can be observed that the time-averaged radial velocities obtained from the URANS computations are overpredicted by the factor of 2. The shift of the axial velocities and the overprediction of the radial velocities is due to a higher velocity magnitude detected at the outlet of the air nozzles. This causes an opening angle of the flow entering the combustion chamber which is greater than the one predicted by the

experiments. The time-averaged velocity profiles obtained from the SAS computations are in very good agreement with the experimental data. An overprediction of the maxima within the axial velocity profiles at $x_1 = 30\,\text{mm}$ and $x_1 = 40\,\text{mm}$ is observed. However, the velocity profiles issued from the PIV measurements do possess a certain uncertainty error displayed by errorbars. This uncertainty accounted for, it can be concluded that the one-dimensional time-averaged velocities obtained from the incompressible and compressible SAS calculations are in good agreement with the experimental values.

Concerning the root-mean-squared profiles (figures 5.3.41-5.3.43), the velocity components are underpredicted in case of the URANS-based computations. This underprediction is associated with the issue that the URANS-based computations do only resolve a small amount of the turbulent flow structures, as shown within the analysis of the instantaneous flow field and further below in figures 5.3.53 and 5.3.55. The small amount of resolved turbulent flow structures within the URANS computations results in deceased values of the velocity fluctuations. Analogously to the time-averaged values, the profile peaks of the velocity fluctuations are shifted towards the radial bounds of the combustion chamber. Compared to the results obtained from the PIV experiments, the numerical root-mean-squared values of the radial velocity obtained from the SAS calculations are underpredicted in the vicinity of the combustion chamber bottom ($x_1 = 5\,\text{mm}$, $x_1 = 10\,\text{mm}$ and $x_1 = 15\,\text{mm}$) and overpredicted further downstream ($x_1 = 30\,\text{mm}$ and $x_1 = 40\,\text{mm}$. The measurement uncertainty of the root-mean-squared velocity values is approximately quantified to 10 % [233]. The discrepancies between the peak rms-values of the radial velocity of the numerical and experimental data exceeds the estimated measurement uncertainty at the measurement lines $x_1 = \{5, 10, 30, 40\}$ mm. Opposed here to, the differences between the rms curves of the radial velocity obtained from the numerical and experimental results at the lines $x_1 = \{15, 20\}$ mm are located under the given uncertainty threshold of 10 %. The fluctuating values of the axial and tangential velocity values predicted by the SAS simulations agree well with the measurement data.

Concerning the SAS-based computations, it can be noticed that the ratio of the root-mean-squared to the time-averaged velocity values approximately amounts to one half, which represents a high level of fluctuation, cf. figures 5.3.41-5.3.43. The high level of fluctuation found within the velocity components of the SAS-based calculations points out the strong turbulent character of the flow field in the gas turbine model combustor.

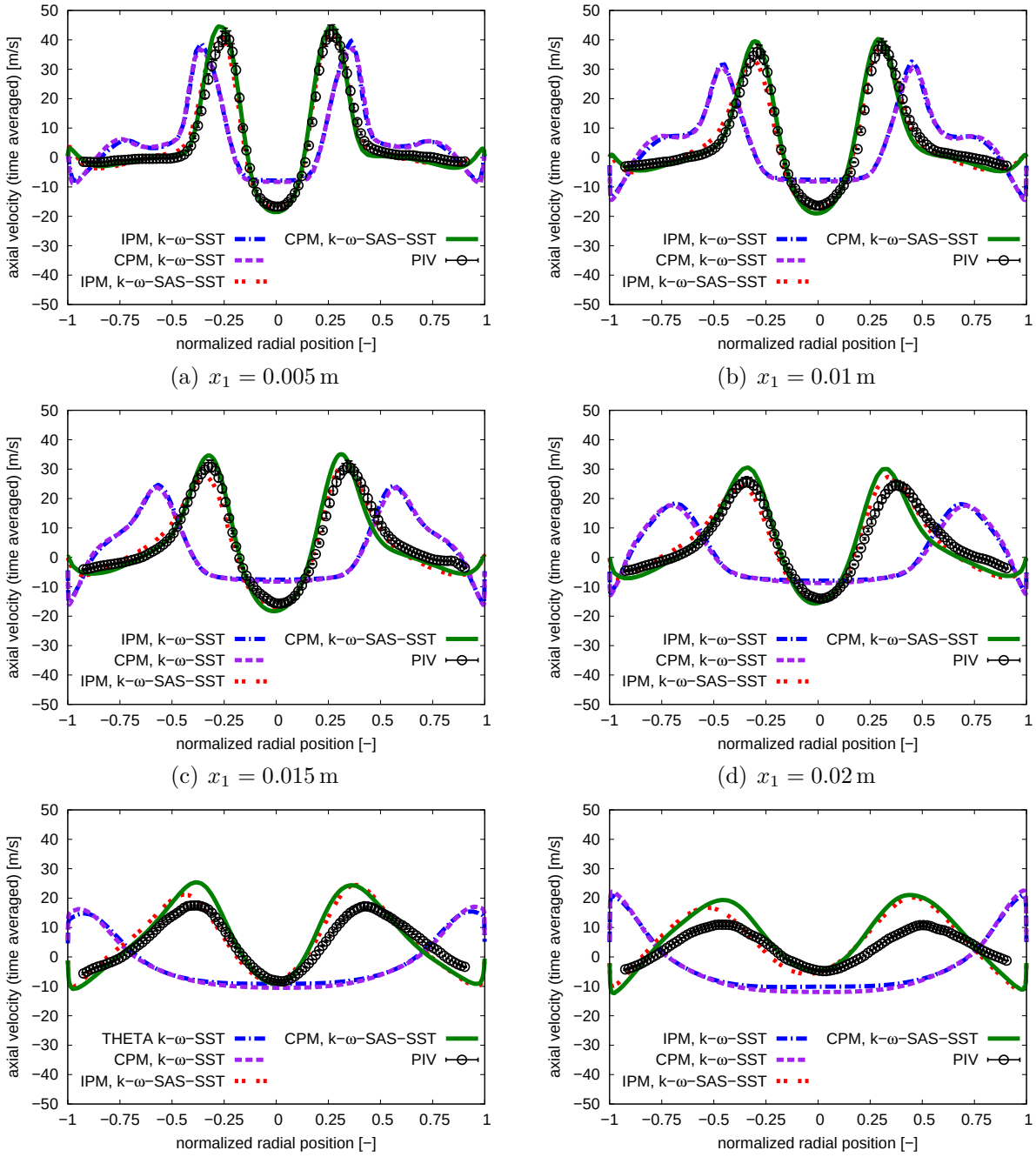

(a) $x_1 = 0.005\,\mathrm{m}$ (b) $x_1 = 0.01\,\mathrm{m}$

(c) $x_1 = 0.015\,\mathrm{m}$ (d) $x_1 = 0.02\,\mathrm{m}$

(e) $x_1 = 0.03\,\mathrm{m}$ (f) $x_1 = 0.04\,\mathrm{m}$

Figure 5.3.38.: Radial profiles of the time-averaged axial velocity (non-reactive cases)

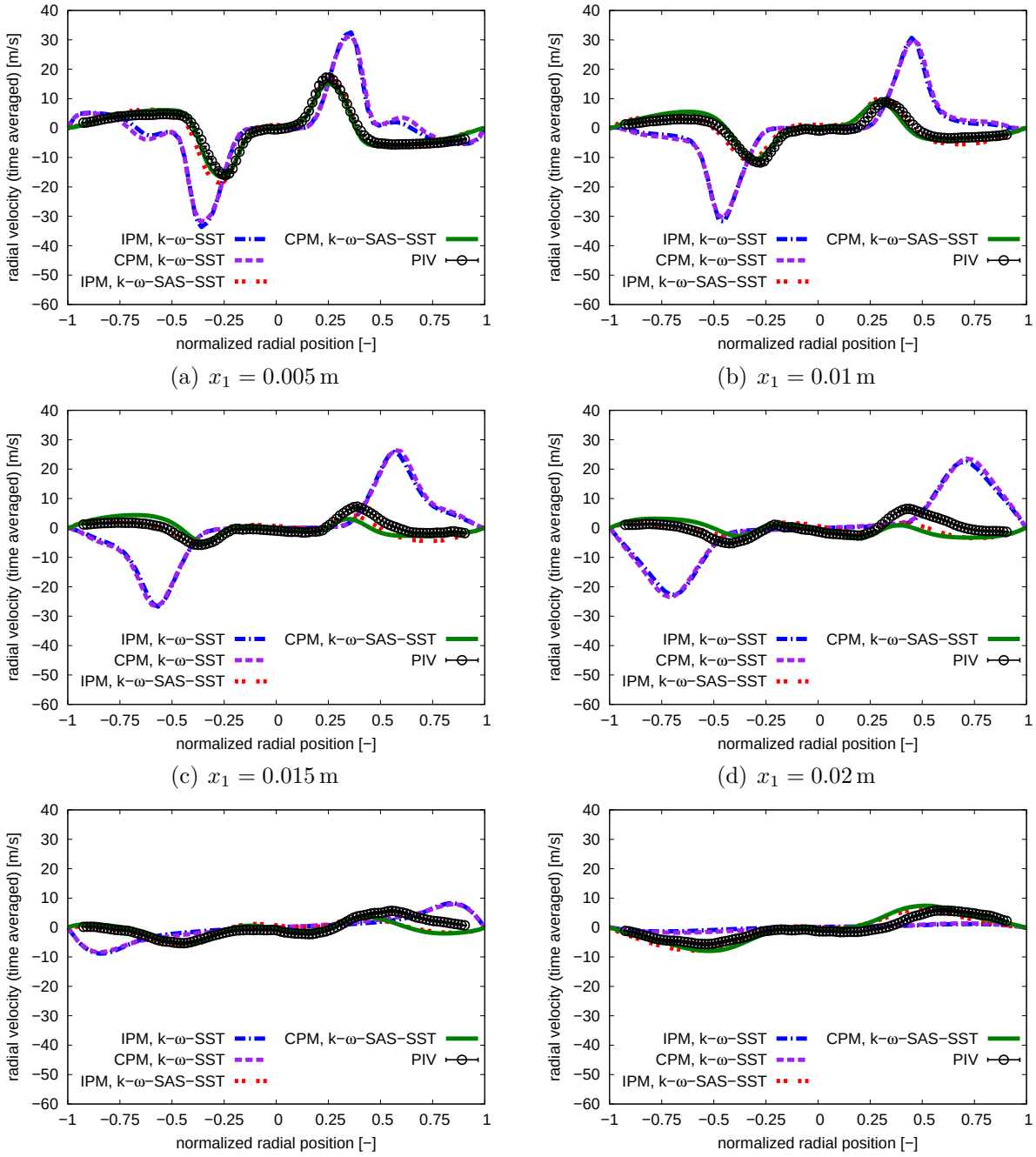

(a) $x_1 = 0.005\,\mathrm{m}$ (b) $x_1 = 0.01\,\mathrm{m}$

(c) $x_1 = 0.015\,\mathrm{m}$ (d) $x_1 = 0.02\,\mathrm{m}$

(e) $x_1 = 0.03\,\mathrm{m}$ (f) $x_1 = 0.04\,\mathrm{m}$

Figure 5.3.39.: Radial profiles of the time-averaged radial velocity (non-reactive cases)

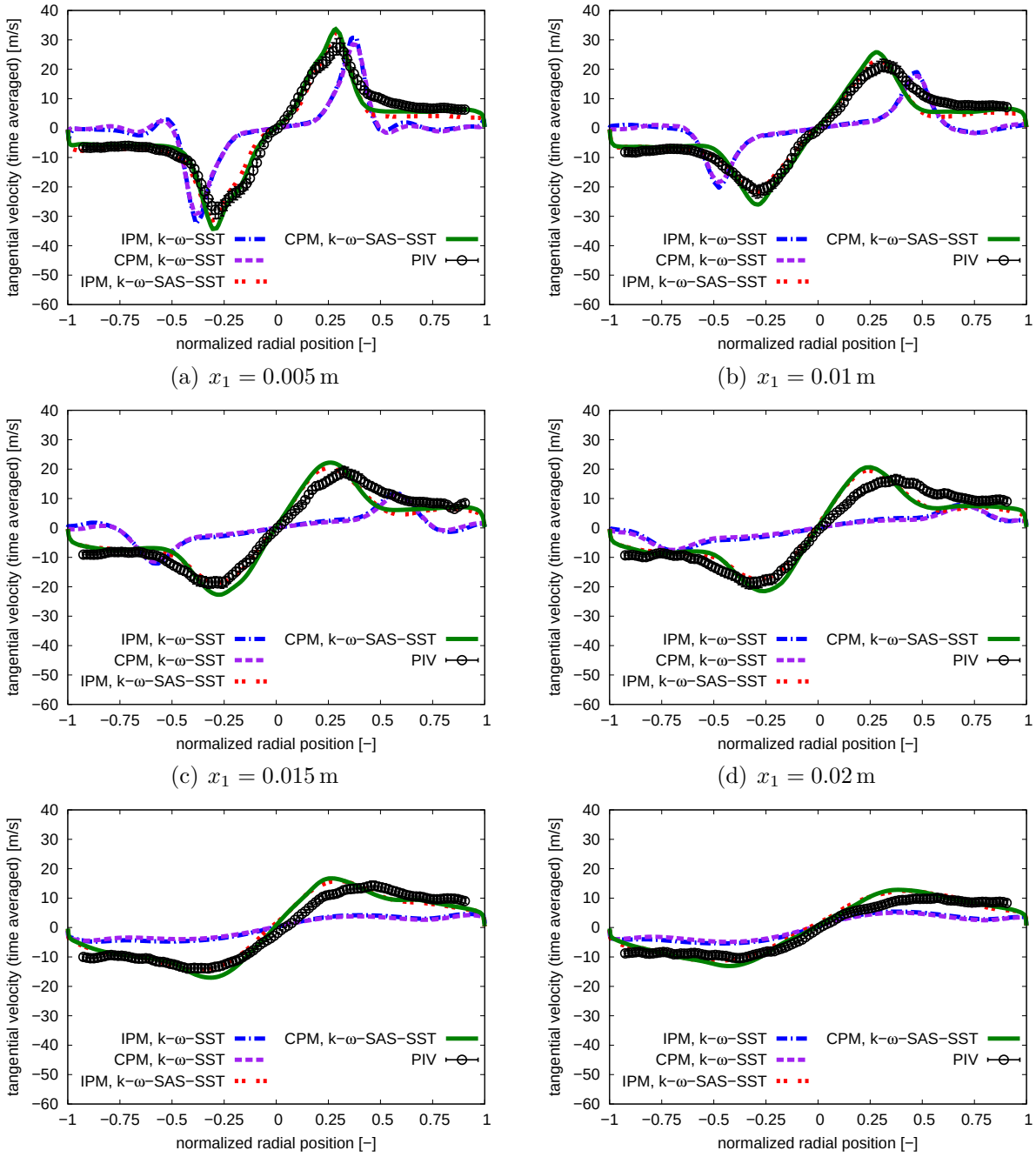

(a) $x_1 = 0.005\,\mathrm{m}$ (b) $x_1 = 0.01\,\mathrm{m}$

(c) $x_1 = 0.015\,\mathrm{m}$ (d) $x_1 = 0.02\,\mathrm{m}$

(e) $x_1 = 0.03\,\mathrm{m}$ (f) $x_1 = 0.04\,\mathrm{m}$

Figure 5.3.40.: Radial profiles of the time-averaged tangential velocity (non-reactive cases)

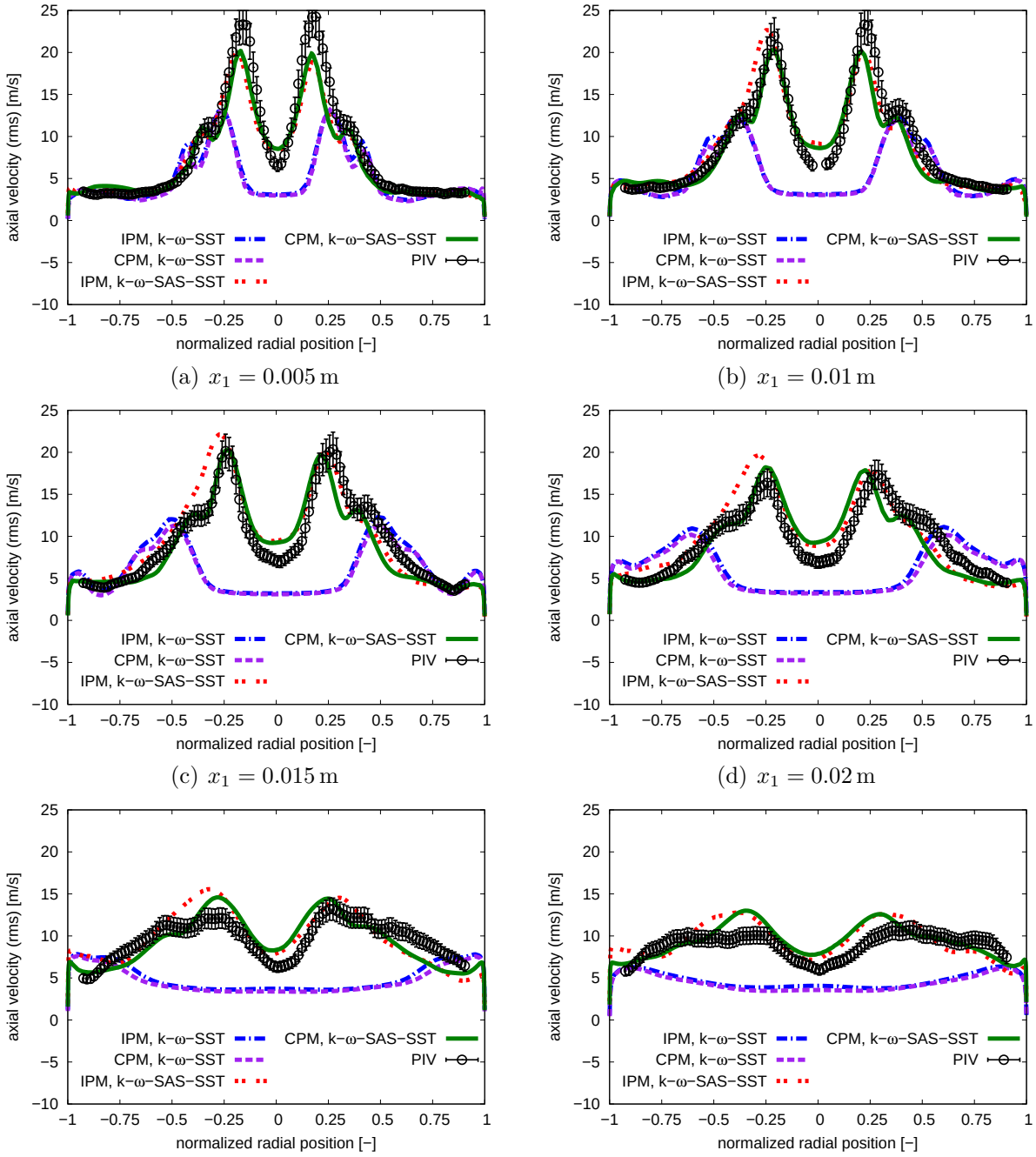

(a) $x_1 = 0.005\,\mathrm{m}$ (b) $x_1 = 0.01\,\mathrm{m}$

(c) $x_1 = 0.015\,\mathrm{m}$ (d) $x_1 = 0.02\,\mathrm{m}$

(e) $x_1 = 0.03\,\mathrm{m}$ (f) $x_1 = 0.04\,\mathrm{m}$

Figure 5.3.41.: Radial profiles of the root-mean-squared axial velocity (non-reactive cases)

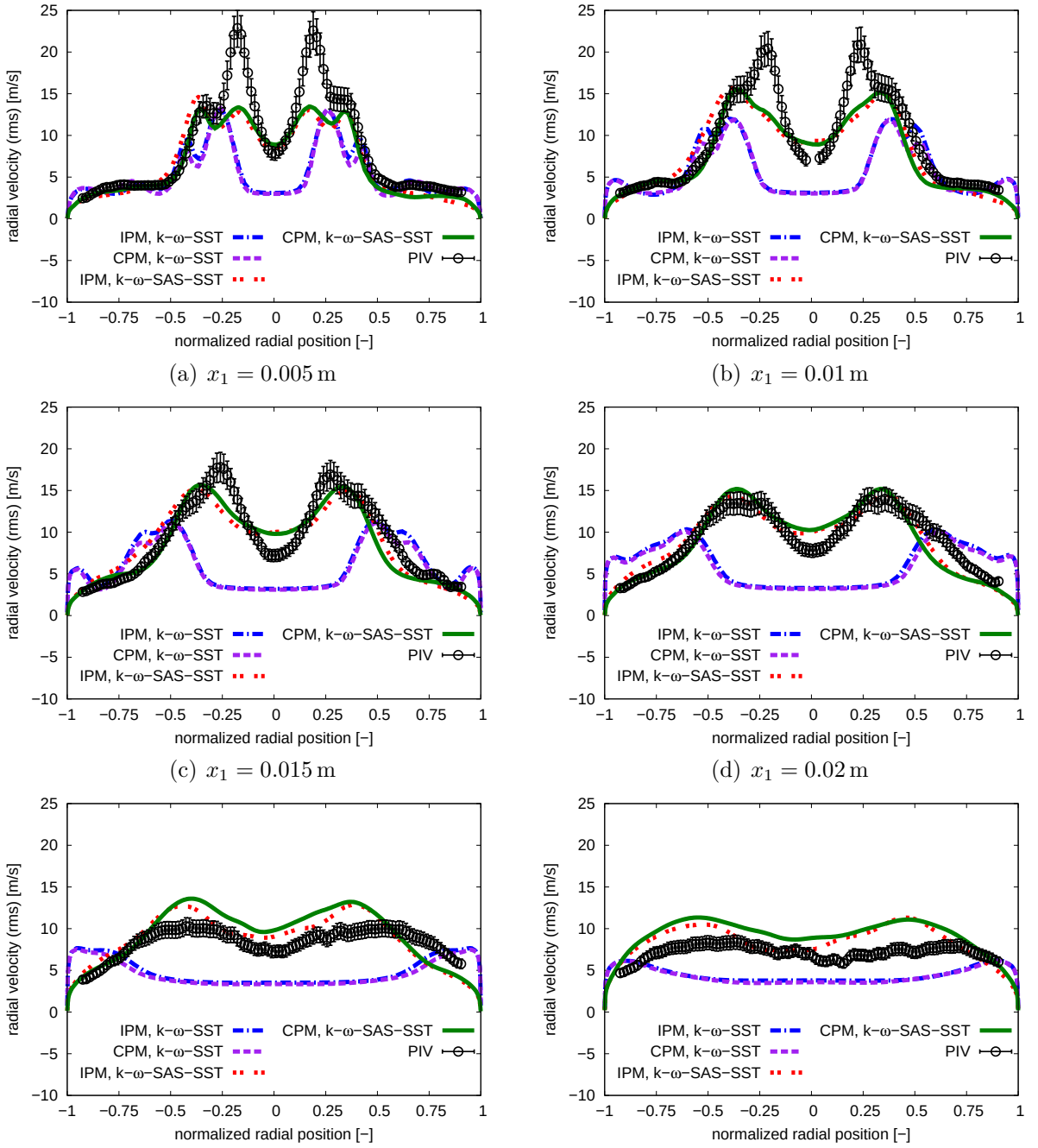

(a) $x_1 = 0.005\,\mathrm{m}$ (b) $x_1 = 0.01\,\mathrm{m}$

(c) $x_1 = 0.015\,\mathrm{m}$ (d) $x_1 = 0.02\,\mathrm{m}$

(e) $x_1 = 0.03\,\mathrm{m}$ (f) $x_1 = 0.04\,\mathrm{m}$

Figure 5.3.42.: Radial profiles of the root-mean-squared radial velocity (non-reactive cases)

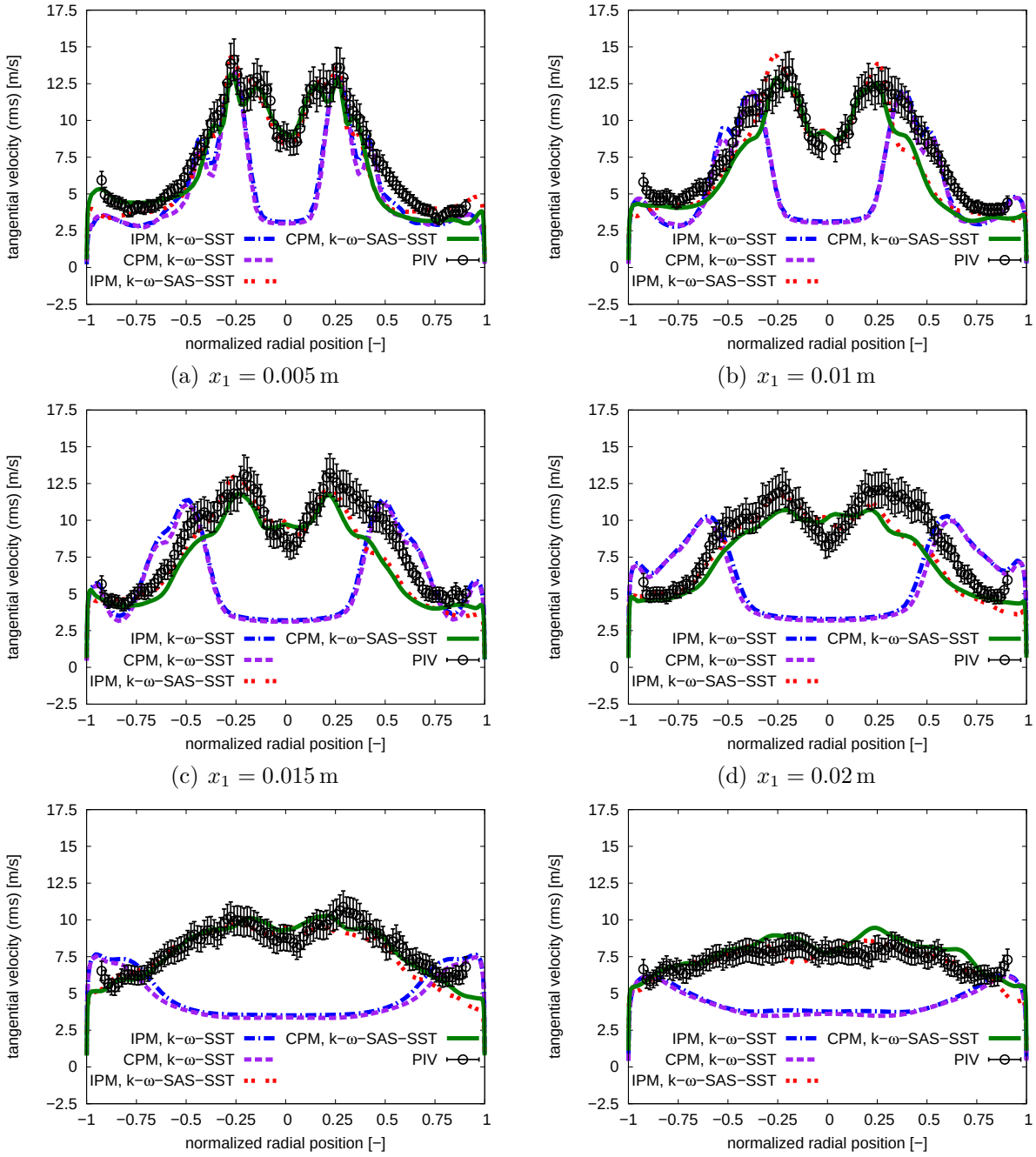

(a) $x_1 = 0.005\,\mathrm{m}$ (b) $x_1 = 0.01\,\mathrm{m}$

(c) $x_1 = 0.015\,\mathrm{m}$ (d) $x_1 = 0.02\,\mathrm{m}$

(e) $x_1 = 0.03\,\mathrm{m}$ (f) $x_1 = 0.04\,\mathrm{m}$

Figure 5.3.43.: Radial profiles of the root-mean-squared tangential velocity (non-reactive cases)

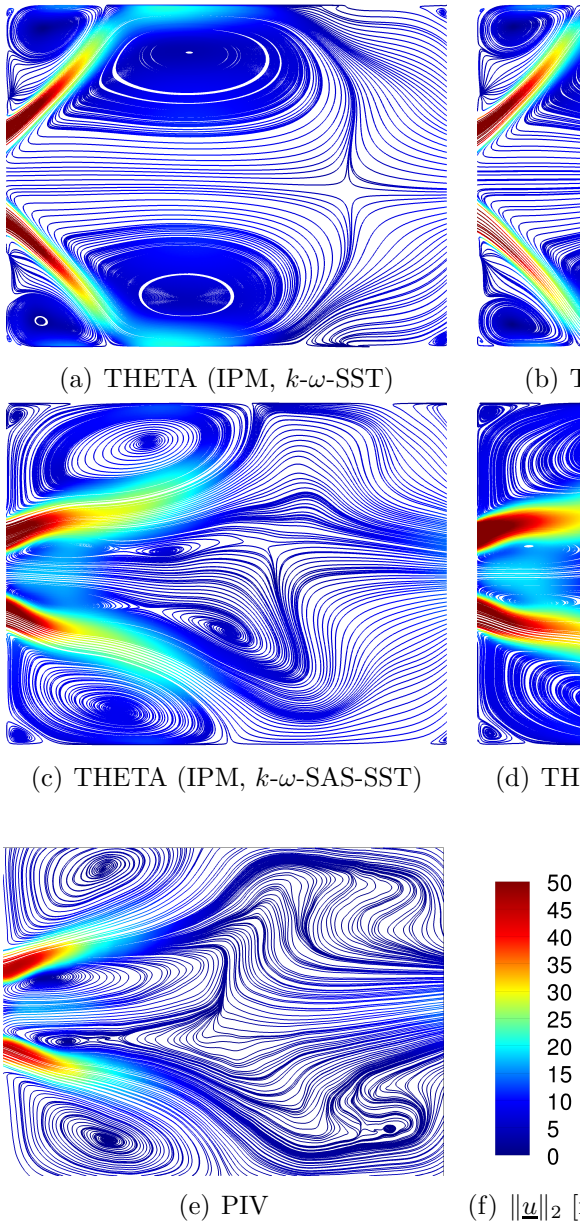

(a) THETA (IPM, k-ω-SST) (b) THETA (CPM, k-ω-SST)

(c) THETA (IPM, k-ω-SAS-SST) (d) THETA (CPM, k-ω-SAS-SST)

(e) PIV (f) $\|\underline{u}\|_2$ [m/s]

Figure 5.3.44.: Visualization of the streamlines colored with the velocity magnitude (non-reactive cases)

Between the incompressible and compressible profiles of the numerical simulations, only small differences can be observed. A slight asymmetry concerning the numerical and experimental results can be observed within the one-dimensional profiles. This effect is weakened for smaller thermal powers, as experienced for the operating points 7.4 kW and 10 kW and is enforced as the thermal power is increased up to a value of 35 kW [234], which corresponds to the thermal power of the operating point presented within this work.

Besides regarding one-dimensional profiles of the time-averaged and root-mean-squared velocity components, the time-averaged flow field structures of the non-reactive cases 1-4

within the combustion chamber are visualized in figures 5.3.44(a)-5.3.44(e). The streamlines of the flow field are colored with the velocity magnitude. The time-averaged flow structures reveal that the swirl of the inner and outer air streams causes the flow to adopt a V-shaped structure. Moreover, an inner recirculation zone along the centerline is created, which plays an important part in the stabilization mechanism of the flow field. At the combustion chamber bottom, an outer recirculation zone is developed, see figure 5.3.44. As observed within the visualization of the one-dimensional radial profiles (see figures 5.3.38 - 5.3.40), the time-averaged results of the URANS-based numerical simulations show a greater opening angle compared to the experimental data. This can also be seen in the streamline plots of the incompressible solutions 5.3.44(a) and 5.3.44(b) and is due to an increased velocity of the flow at the entrance of the combustion chamber. Opposed to this, the time-averaged flow field of the SAS-based computations agrees well with the one obtained from the measurements. Only small differences within the time-averaged flow field structures can be observed when comparing the results of the incompressible and compressible URANS-, respective SAS-based computations. Differences between the incompressible and compressible solutions can be detected within the vortex structures of the inner recirculation zone.

After showing the results of the non-reactive flow (cases 1-4), the results obtained from the reactive flow (cases 5-7) are presented. The swirl of the inner and outer air streams causes the flow to adopt a V-shaped flow and thus a V-shaped flame front. An inner and outer recirculation zone are developed, as seen within the inert flow computations. The occurrence of the recirculation zones causes the burned gas to move back upstream. Through this mechanism, hot gas is convected back into the stream of unburned gas. This helps igniting the unburned gas mixture and contributes significantly to the stabilization of the flame. By taking a closer look at the instantaneous SAS-based flow field (figure 5.3.30(b)), it can be seen that the actual recirculation process does not occur on the large scales of the inner and outer recirculation zones depicted in the time-averaged solution, but on the far smaller scales of the turbulent structures displayed in the instantaneous flow field structures, compare the conclusions drawn from the experimental results [233].

The figures 5.3.45-5.3.47 reveal a very good agreement of the time-averaged velocity components predicted by the incompressible and compressible SAS computations compared to the experimental data. Opposed to this, the maxima of the axial velocity profiles obtained from the URANS simulations seem to drift away from the center line of the combustion chamber as the flow moves in streamwise direction. This is caused by an overpredicted opening angle of the V-shaped flame. This relation can also be seen within the visualization of the flow field, see figure 5.3.49. An overprediction of the time-averaged radial and tangential velocities can also be observed when comparing the URANS-based computations to the

measurements, see figures 5.3.46 and 5.3.47. Considering the tangential velocity component of the time-averaged results, a discrepancy of the occurring maxima can be observed when validating the predicted values of the URANS calculations to the values obtained from the experiments, see figure 5.3.47.

As can be observed from the time-averaged profiles of the temperature 5.3.50(a)-5.3.50(e), the values issued from the SAS simulations agree well with the experimental results obtained from the Raman measurements. The differences between the numerical and experimental profiles are greater in the case of the incompressible URANS calculation. It can be noticed that the URANS simulation underpredicts the temperature in the near-wall region of the combustion chamber bottom. This issue is related to the higher opening angle of the flame seen within the URANS computation, see figure 5.3.49(a). Due to the overprediction of the opening angle, the flame spreads wider which prevents the outer recirculation zone from reaching the burned gas zone. This hinders the outer recirculation zone from transporting hot gas from the combustion region upstream towards the combustor bottom. As a result, the overall temperature level is decreased in the outer recirculation zone. Approaching the combustion chamber walls further downstream, the incompressible computations overpredict the temperature values. It seems that within the results obtained from the compressible SAS calculation, the temperature rise and thus ignition and combustion of the air fuel mixture is delayed in streamwise direction. Whereas the temperature level is much lower in the vicinity of the combustor bottom, the temperature profile issued from compressible SAS computation matches much better with the results obtained from the Raman measurements at the measurement lines $x_1 = 30\,\text{mm}$ and $x_1 = 40\,\text{mm}$.

Within the numerical simulations, isothermal boundary conditions are applied to the combustion chamber bottom and to the combustion chamber walls. Comparing the numerical to the experimental temperature profiles, it can be seen from figures 5.3.48(a)-5.3.48(f) that the near-wall temperatures obtained from the isothermal boundary conditions specified match quite well with the measured near-wall temperature course. Nevertheless, it has to be emphasized at this point that the x_2-range of the temperature distribution evaluated from the Raman measurements is limited to the bounds of $x_2 \in [0, 30]$ mm, cf. figure 5.3.50(d). The compressible SAS computation underpredicts the temperature within the inner recirculation zone in the vicinity of the combustion chamber entrance. However, the course of the temperature fall and rise in the V-shaped flow stream between the inner and outer recirculation zones is far better predicted by the compressible SAS solution than by the incompressible SAS result, see figures 5.3.48(a)-5.3.48(e). In addition to this, figure 5.3.48(f) unveils that the radial temperature profiles "smooth out" further downstream towards the combustion chamber exit.

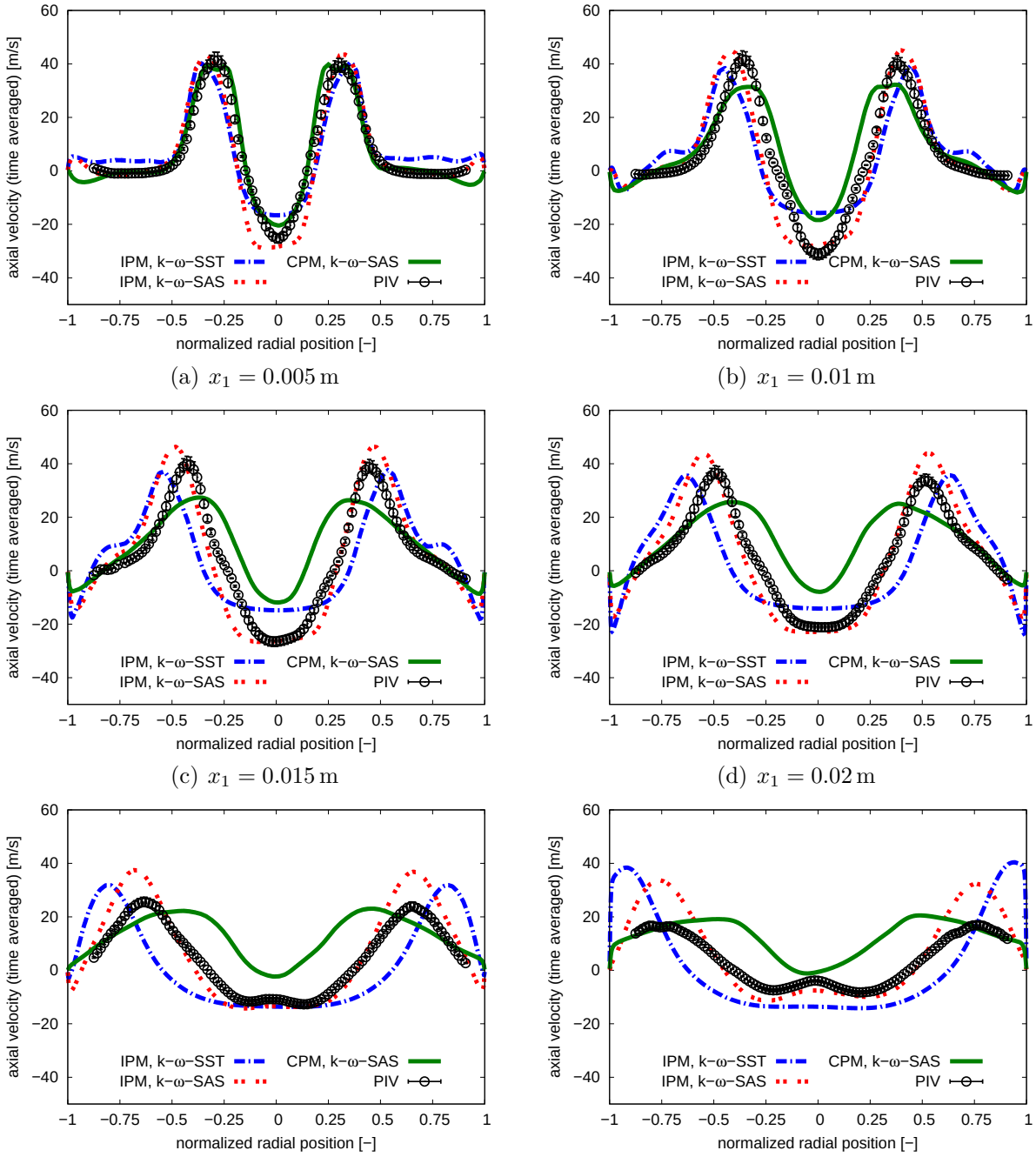

(a) $x_1 = 0.005\,\mathrm{m}$ (b) $x_1 = 0.01\,\mathrm{m}$

(c) $x_1 = 0.015\,\mathrm{m}$ (d) $x_1 = 0.02\,\mathrm{m}$

(e) $x_1 = 0.03\,\mathrm{m}$ (f) $x_1 = 0.04\,\mathrm{m}$

Figure 5.3.45.: Radial profiles of the time-averaged axial velocity (reactive cases)

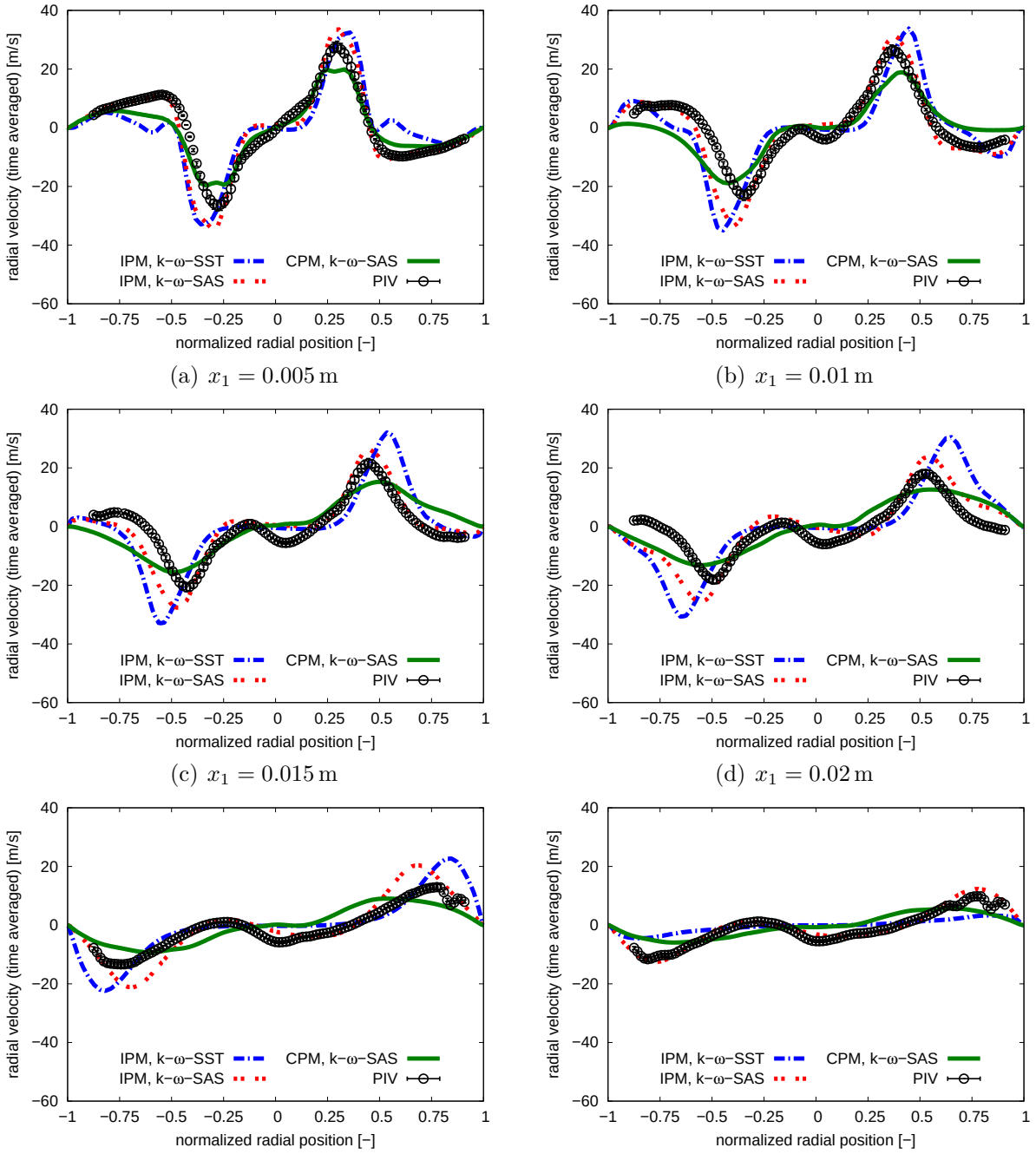

(a) $x_1 = 0.005\,\mathrm{m}$ (b) $x_1 = 0.01\,\mathrm{m}$

(c) $x_1 = 0.015\,\mathrm{m}$ (d) $x_1 = 0.02\,\mathrm{m}$

(e) $x_1 = 0.03\,\mathrm{m}$ (f) $x_1 = 0.04\,\mathrm{m}$

Figure 5.3.46.: Radial profiles of the time-averaged radial velocity (reactive cases)

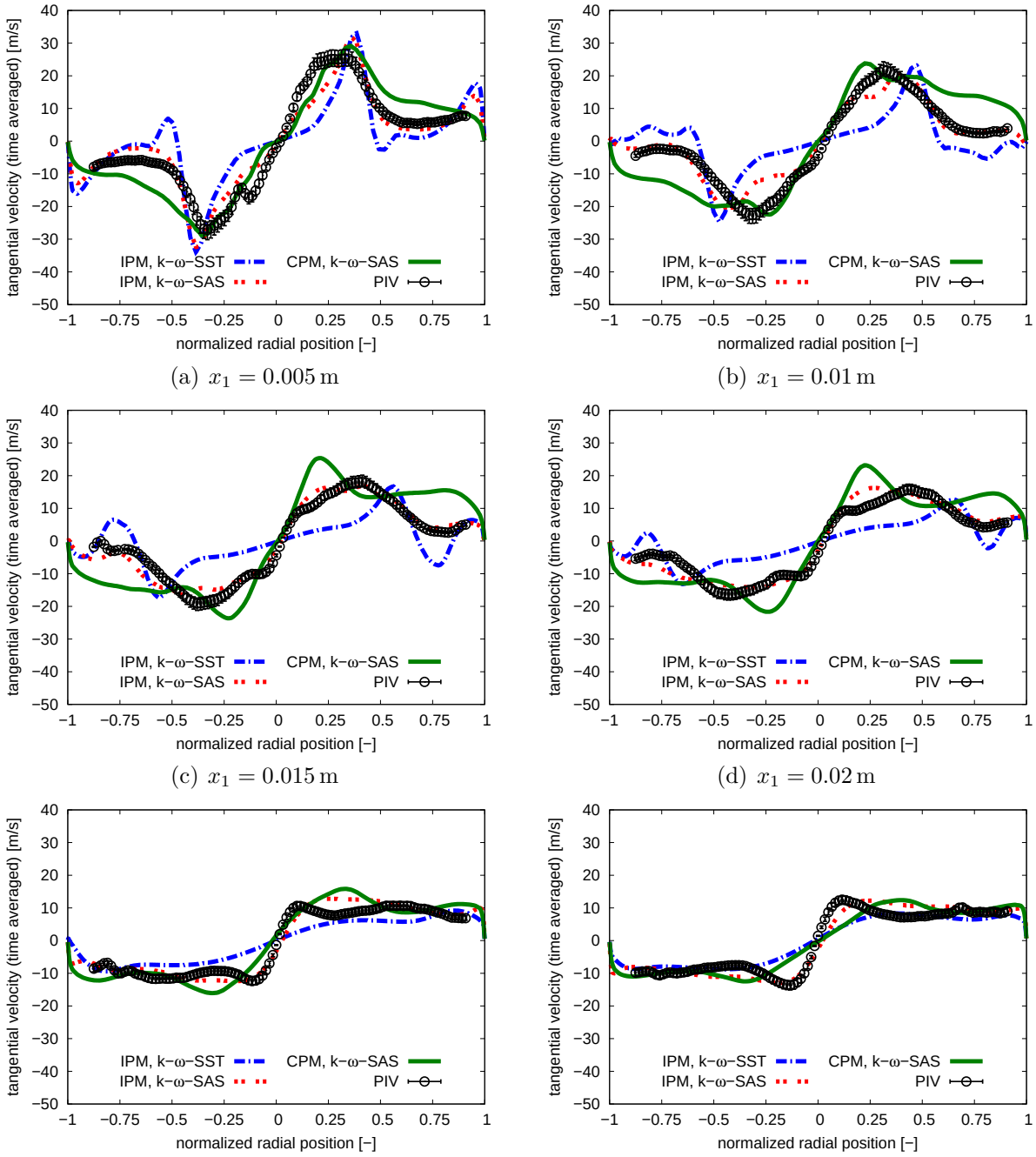

(a) $x_1 = 0.005\,\mathrm{m}$ (b) $x_1 = 0.01\,\mathrm{m}$

(c) $x_1 = 0.015\,\mathrm{m}$ (d) $x_1 = 0.02\,\mathrm{m}$

(e) $x_1 = 0.03\,\mathrm{m}$ (f) $x_1 = 0.04\,\mathrm{m}$

Figure 5.3.47.: Radial profiles of the time-averaged tangential velocity (reactive cases)

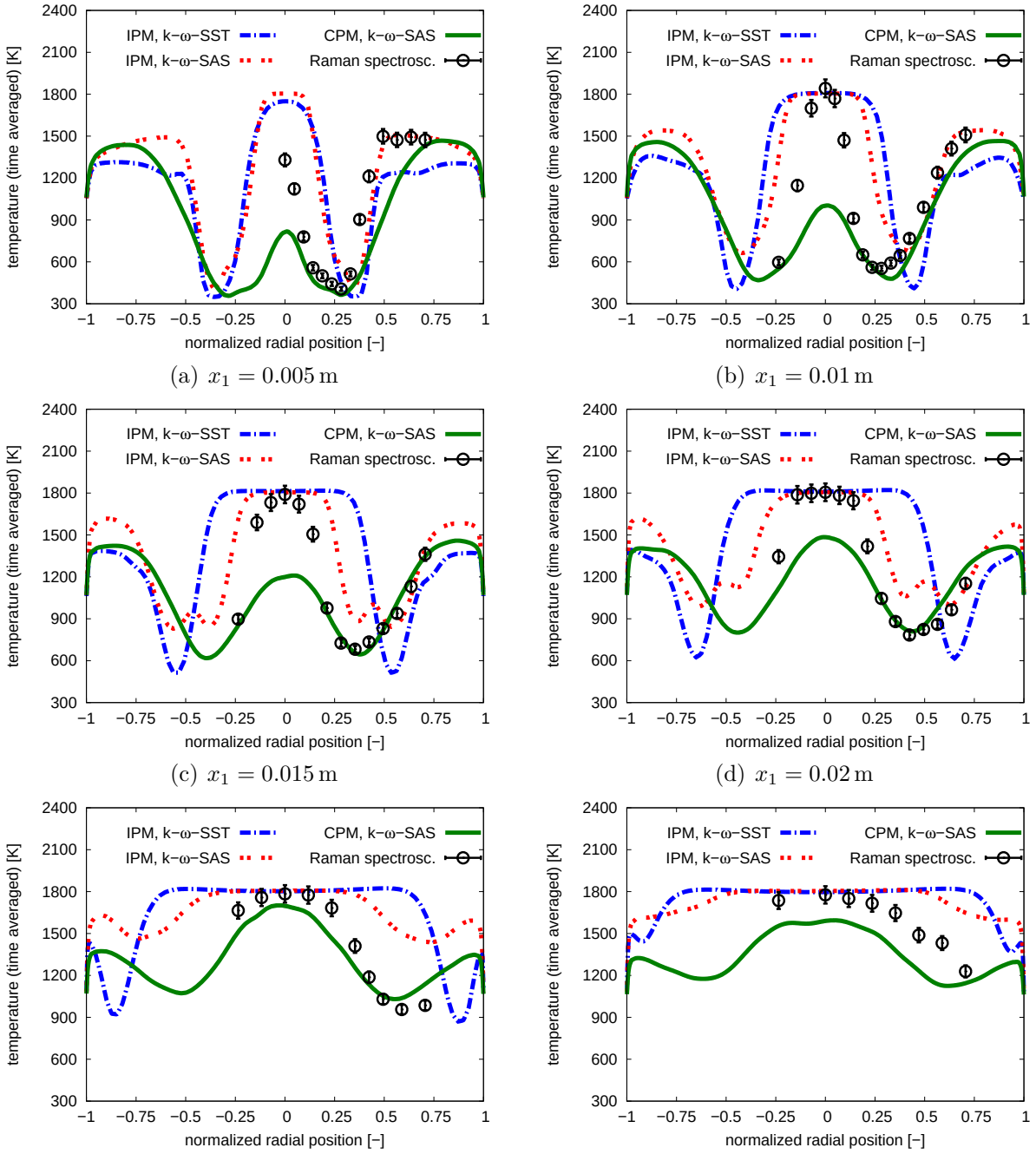

(a) $x_1 = 0.005\,\mathrm{m}$ (b) $x_1 = 0.01\,\mathrm{m}$

(c) $x_1 = 0.015\,\mathrm{m}$ (d) $x_1 = 0.02\,\mathrm{m}$

(e) $x_1 = 0.03\,\mathrm{m}$ (f) $x_1 = 0.04\,\mathrm{m}$

Figure 5.3.48.: Radial profiles of the time-averaged temperature (reactive cases)

The lower temperature level within the outer recirculation zone compared to the one within the inner recirculation region is due to a temperature decrease within the near-wall area due to heat losses from the warmer flow field to the colder combustor wall.

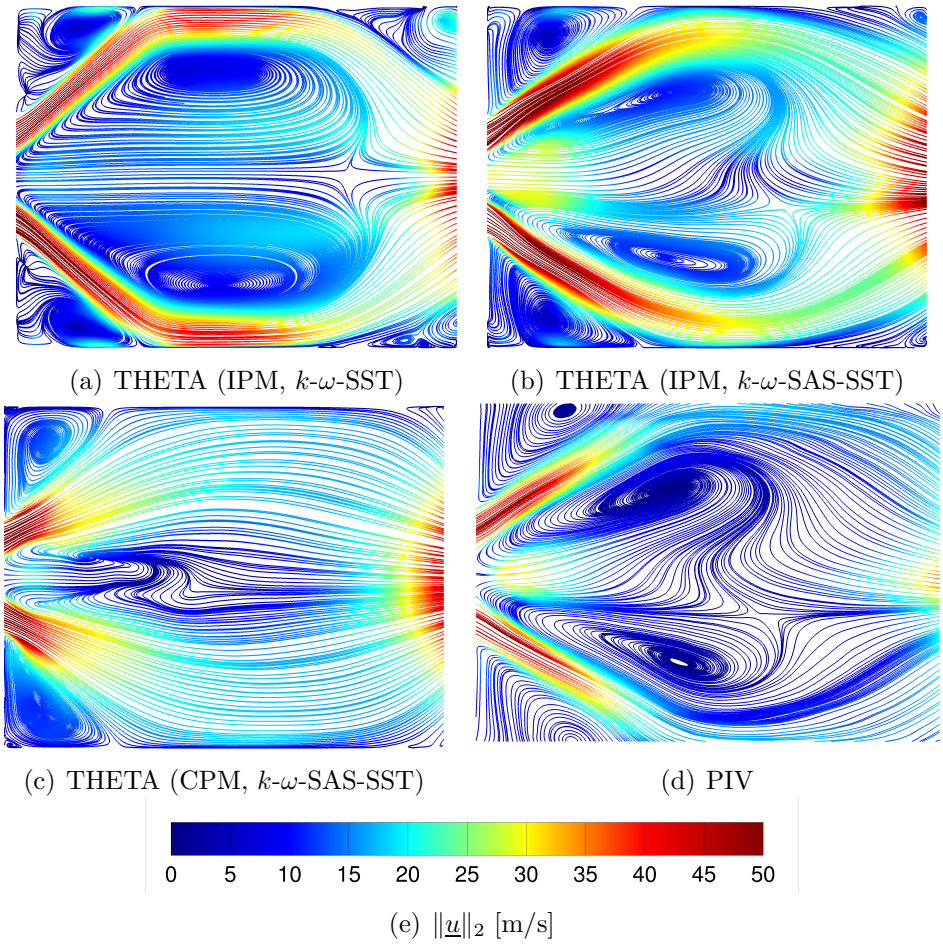

(a) THETA (IPM, k-ω-SST) (b) THETA (IPM, k-ω-SAS-SST)

(c) THETA (CPM, k-ω-SAS-SST) (d) PIV

(e) $\|\underline{u}\|_2$ [m/s]

Figure 5.3.49.: Visualization of the streamlines colored with the velocity magnitude (reactive cases)

The time-averaged flow field structure of the reactive cases 5-7 is displayed within figures 5.3.49(a)-5.3.49(c) and put against the flow field obtained from the PIV measurements, cf. figure 5.3.49(d). It can be observed that the URANS-based numerical simulations overpredict the velocity at the air nozzle outflow, which causes a higher opening angle of the V-shaped flow field. The mean flow topology displayed by the compressible SAS calculation agrees well with the experimental plot concerning the opening angle of the flow at the combustor bottom and the development of the outer recirculation zone. Moreover, figure 5.3.49(d) reveals that the annular jet is dissipated faster than in the results obtained from the measurements. Opposed to this, the incompressible SAS results reveal an annular jet that is less dissipated, thus maintaining higher velocities in streamwise direction, see figure 5.3.49(b).

It can be seen based on the visualization of the flow field that the solutions of the URANS computations unveil a more “symmetrical“ flow field structure than the results obtained from the SAS-based calculations, cf. figures 5.3.49(a)-5.3.49(c). However, a slight asymmetry can also be detected within the PIV measurements, see figure 5.3.49(d). Such small asymmetries can occur in swirled combustors due to the strong three-dimensional character of the flow field.

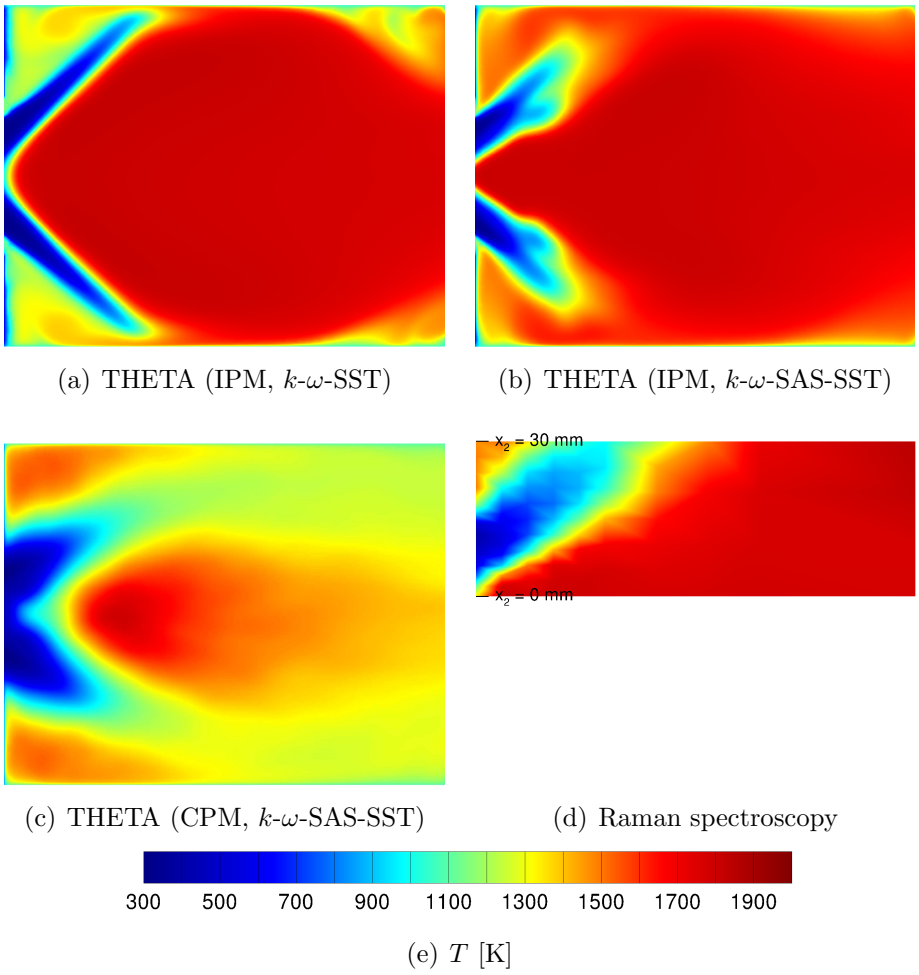

(a) THETA (IPM, k-ω-SST)

(b) THETA (IPM, k-ω-SAS-SST)

(c) THETA (CPM, k-ω-SAS-SST)

(d) Raman spectroscopy

(e) T [K]

Figure 5.3.50.: Distribution of the temperature field (reactive cases)

The contour plots of the temperature distribution obtained from the incompressible solutions reveal a V-shaped form of the flame front, see figures 5.3.50(a) and 5.3.50(b). By taking a closer look into the URANS-based results, it can be seen that the flame front spreads wider than observed within the SAS-based and experimental results. This is due to an overprediction of the velocity at the air nozzle outflow, as noticed earlier on. Despite the differences within the setup the the boundary conditions (cooling of the walls during the experiments and the specification of isothermal boundary conditions in case of the numerical simulations),

the SAS-based calculations are in good agreement with the results obtained from the Raman measurements.

The flow separation at the outlet of the outer air nozzle possesses a highly unsteady character, cf. the findings described within the presentation of the instantaneous results. Small variations of the air supply within the experimental setup, as well as the increasing roughness of the combustor walls due to a rising abrasion of the walls as a consequence of the the heat release of the flame may cause slight differences in the flow separation at the outlet of the outer air nozzle [234]. Aside from this, an interesting relation has been found concerning the flow structure at the exit of the outer air nozzle: Setting the time step too high, in the present work to a value of $\Delta t = 10^{-5}$ s, caused the mean flow structure at the outer nozzle exit to follow the geometry of the combustion chamber bottom. As a result of this, the flow did not separate at this point and caused the flow pattern to "open up". This led to a pot-like shape of the flame structure at the entrance of the combustion chamber in case of the reactive setup. Figure 5.3.51 displays this effect by revealing the flow field topology along with the distribution of the temperature field for the incompressible reactive SAS computation conducted with a time step size of $\Delta t = 10^{-5}$ s.

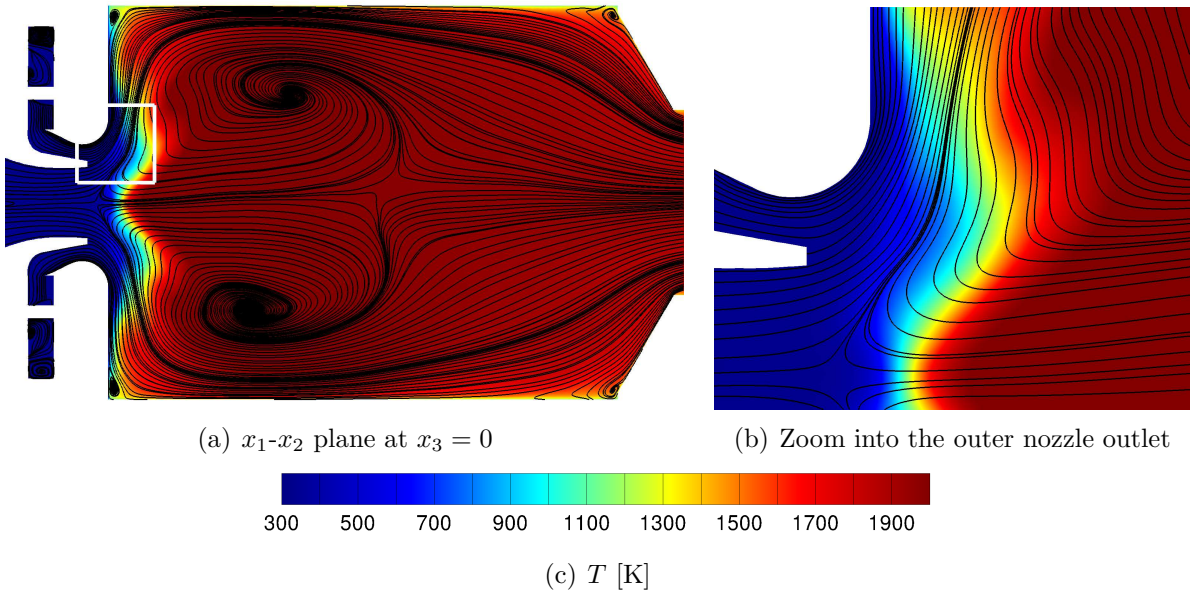

(a) x_1-x_2 plane at $x_3 = 0$ (b) Zoom into the outer nozzle outlet

(c) T [K]

Figure 5.3.51.: Distribution of the temperature field and visualization of the flow field topology (incompressible reactive SAS computation with $\Delta t = 10^{-5}$ s)

Choosing the time step size too high thus led to a completely different flow structure. This different flow topology might be explained through the following relation: Increasing the time step size leads to a loss concerning the temporal resolution of the flow phenomena. As a consequence, small turbulent structures like small vortices due to occurring velocity gradients within the flow field cannot be resolved accurately anymore by the numerical solver. As a

result, small turbulent structures are damped out of the solution causing an insufficient resolution of the flow turbulence. This matter can be visualized by plotting the turbulent time scale. By reminding us of the fact that the turbulent time scale τ_t is equal to the inverse of the turbulent dissipation frequency ω

$$\tau_t = \omega^{-1}\,, \tag{5.3.71}$$

the turbulent time scale can directly be extracted as a postprocessed variable from the result file. For the purpose of evaluation, the time-averaged value of the turbulent dissipation frequency ω^{avg} is used for the determination of the time-averaged turbulent time scale τ_t. The distribution of τ_t within the combustion chamber along with the visualization of the flow topology is visualized in figure 5.3.52.

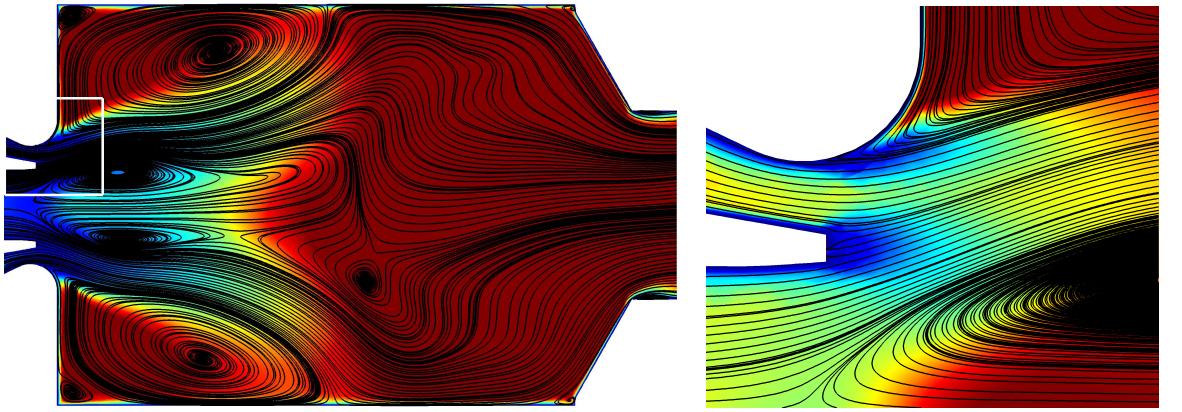

(a) x_1-x_2 plane at $x_3 = 0$ (b) Zoom into the outer nozzle outlet

(c) τ_t [s] (d) τ_t [s]

Figure 5.3.52.: Distribution of the time-averaged turbulent time scale along with the visualization of the flow topology (SAS computation, compressible non-reactive case)

As can be seen from figure 5.3.52, the turbulent time scale is of the order of $\mathcal{O}\left[(10^{-6} \div 10^{-5})\ \text{s}\right]$ in the vicinity of the outer nozzle exit. Thus, a time step size of $\Delta t = 10^{-5}\,\text{s}$ is not sufficient in order to resolve the occurring turbulent structures within the said region. As a consequence, the time step size should at least be set to a value of the order of $\mathcal{O}\left(10^{-6}\,\text{s}\right)$. The flow separation mechanism of the flow at the outer air nozzle exit is influenced by many factors, such as the pressure level inside the combustion chamber, the temporal and spatial order of accuracy of the computational method achieved and the time step size [203]. Beyond this, the flow separation at the outlet of the outer air nozzle has been found to show a highly unsteady behavior, see figure 5.3.35.

In order to provide additional insight into the prediction quality of the URANS and SAS simulations, the resolved amount of the turbulent kinetic energy can be compared to the overall amount of turbulent kinetic energy consisting of the resolved and modeled parts. For this purpose, an additional postprocessing variable figuring as the ratio of the resolved to the total turbulent kinetic energy is defined:

$$r_k \equiv \frac{k_{\mathrm{res}}}{k_{\mathrm{tot}}} = \frac{k_{\mathrm{res}}}{k_{\mathrm{res}} + k_{\mathrm{mod}}} \,. \tag{5.3.72}$$

The total amount of turbulent kinetic energy k_{tot} is equal to the sum of the resolved and modeled part turbulent kinetic energy. k_{mod} denotes the time-averaged value of the modeled turbulent kinetic energy and is thus equal to the value of $k_{\mathrm{mod}}^{\mathrm{avg}}$. This value is obtained from the turbulence model applied and represents the outcome of the k-equation. Opposed to this, the resolved amount of the turbulent kinetic energy is denoted by the variable k_{res} and represents the amount of turbulent kinetic energy which originates from the turbulent fluctuations of the velocity components. k_{res} can thus be expressed through the following equation:

$$k_{\mathrm{res}} \equiv \frac{1}{2} \sum_{i=1}^{3} \overline{u_i' u_i'} = \frac{1}{2} \left(\overline{u_1' u_1'} + \overline{u_2' u_2'} + \overline{u_3' u_3'} \right) \tag{5.3.73}$$

with

$$\overline{\phi' \phi'} \;\equiv\; \phi^{\mathrm{rms}} \phi^{\mathrm{rms}} = \lim_{\delta t \to \infty} \frac{1}{\delta t} \int_{t^0}^{t^0 + \delta t} \left[\phi\left(t\right) - \phi^{\mathrm{avg}}\left(t\right) \right]^2 dt \quad \text{for} \quad \phi = \begin{bmatrix} u_1 \\ u_2 \\ u_3 \end{bmatrix} \,. \tag{5.3.74}$$

By means of the definitions made above, the ratio of the resolved to the overall turbulent kinetic energy r_k can be determined as a postprocessing variable from the results of the numerical simulations.

Based on the results obtained from the compressible computations, figure 5.3.53 displays r_k as a scalar field over the x_1-x_2 plane at $x_3 = 0$ of the inner combustion chamber field for the URANS and SAS calculations. The evaluation of the ratio of the resolved to the overall turbulent kinetic energy is performed exemplarily using the results obtained from the non-reactive cases. It is assumed that the reactive cases provide similar results.

The ratio of the resolved to the overall turbulent kinetic energy r_k can be used to determine the quality of the results issued from a pure LES or LES-like computation. In detail, r_k serves as measure in order to describe the amount of the resolved turbulence. In addition to being a measuring quantity which characterizes the amount of the resolved turbulence, r_k can be thought of as a quantity indicating the "LES zones" within the results of the SAS based

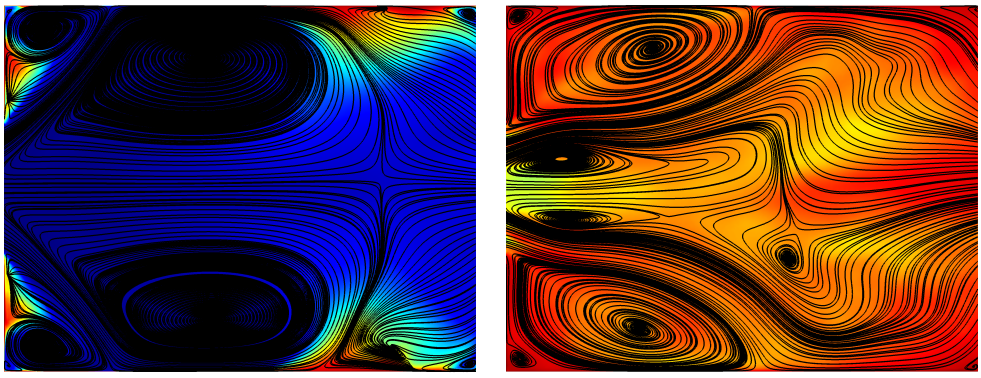

(a) THETA (CPM, k-ω-SST) (b) THETA (CPM, k-ω-SAS-SST)

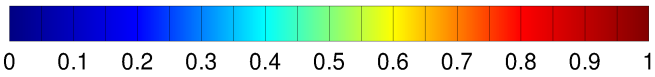

(c) r_k [–]

Figure 5.3.53.: Distribution of the ratio of the resolved to the overall turbulent kinetic energy along with the visualization of the flow topology (non-reactive case)

computations. According to Pope [192], at least 80 % of the turbulent kinetic energy should be resolved in order to obatin a "good" LES simulation. However, this criterion has not been mathematically derived and is of empiric nature. It does thus be handled with care.

Figure 5.3.53 unveils the distribution of the ratio of the resolved to the overall turbulent kinetic energy along with the visualization of the flow topology for the URANS and SAS computations of the compressible non-reactive flow. Opposed to the URANS computation,

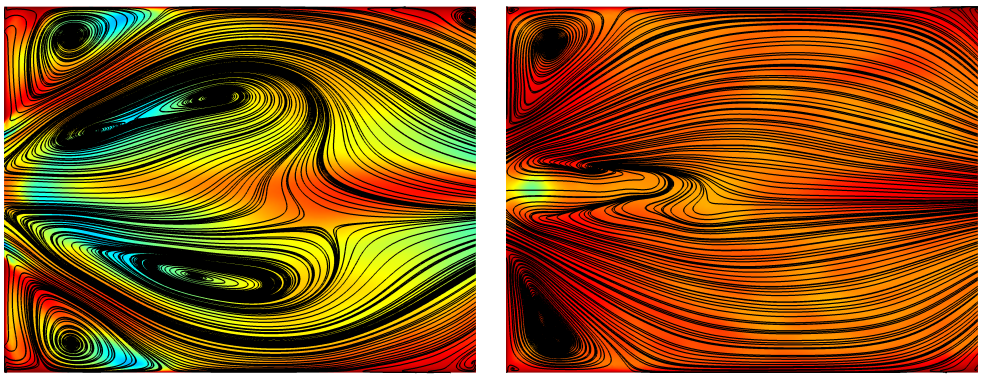

(a) THETA (IPM, k-ω-SAS-SST) (b) THETA (CPM, k-ω-SAS-SST)

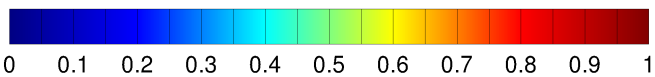

(c) r_k [–]

Figure 5.3.54.: Distribution of the ratio of the resolved to the overall turbulent kinetic energy along with the visualization of the flow topology (reactive case)

the SAS calculation is capable of resolving a higher amount of the turbulent kinetic energy. A resolution beyond the value of 80 % is reached within most areas of the plane.

Figure 5.3.54 displays the distribution of the ratio of the resolved to the overall turbulent kinetic energy along with the visualization of the flow topology for the incompressible and compressible SAS-based computations of the reactive flow. Concerning the incompressible solution, figure 5.3.54(a) reveals that the turbulent kinetic energy is well resolved in the vicinity of the combustor bottom, in the annular jet and at the centerline of the combustion chamber downstream of the inner recirculation zone. Opposed to the, large part of the turbulent kinetic energy is modeled in the inner and outer recirculation zones. Averaging the cell surface weighted values of r_k over the area displayed in figure 5.3.54, an amount of 62 % is obtained. The solution of the compressible reactive SAS calculation reveals that the turbulent kinetic energy is well resolved apart from a circular area located at the centerline of the combustion chamber entrance. Values above 75 % are achieved within most regions of the combustion chamber. In the circular area at the centerline of the combustion chamber entrance, a minimum value of 54 % is detected. The cell surface weighted average issuing from the compressible SAS-based reactive computation amounts to 76 %, which represents a good value regarding the amount of resolved turbulence.

Besides displaying the ratio of the resolved to the overall turbulent kinetic energy, the ratio of the time-avergaged turbulent to laminar viscosity

$$r_\nu \equiv \frac{\nu_t}{\nu_l} \tag{5.3.75}$$

can also be used to identify the "LES zones" within the SAS computation [45]. The smaller the value of r_ν, the larger the range of turbulence resolved. As a consequence, one can say that the ratio of the time-avergaged turbulent to laminar viscosity figures as indicator for the amount of turbulence resolved.

According to equation (5.3.75), r_ν stands for the amount of turbulent viscosity relative to the value of the molecular viscosity. The molecular part of the viscosity ν_l describes a property of the flow, whereas the turbulent - or eddy - viscosity ν_t characterizes the modeled part of the flow turbulence. The turbulent viscosity is obtained from the turbulence model applied and thus denotes a model variable. Figure 5.3.55 displays the two-dimensional plot of r_ν along with the visualization of the flow topology issuing from the non-reactive URANS and SAS simulations. In URANS solutions, the turbulent viscosity should be far larger than the one obtained from the SAS simulations. This is due to the fact that the degree of turbulence modeling does directly affect the amount of turbulent viscosity generated. In URANS based calculations, most of the flow turbulence is modeled. Opposed here to, the modeling of the

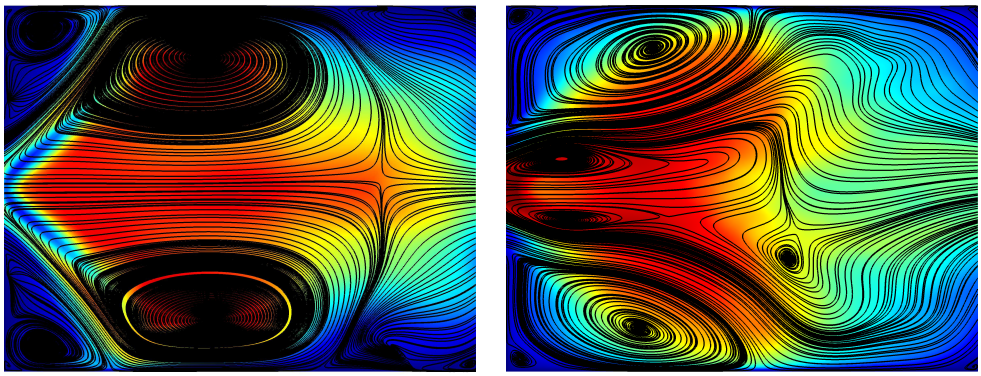

(a) THETA (CPM, k-ω-SST)

(b) THETA (CPM, k-ω-SAS-SST)

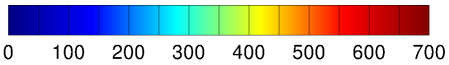

(c) r_ν [–]

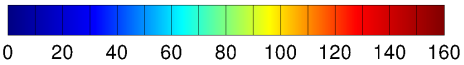

(d) r_ν [–]

Figure 5.3.55.: Distribution of the ratio of the time-avergaged turbulent to laminar viscosity along with the visualization of the flow topology (non-reactive case)

turbulent structures within the "LES zones" of the SAS computations is limited to the small scales. Large vortices as they occur within turbulent flows are resolved directly by means of the filtered equations.

Comparing figures 5.3.55(a) and 5.3.55(b), it can be seen that within the inner recirculation zone $r_{\nu_{\mathrm{URANS}}}$ is roughly of the factor 5 to 6 higher than $r_{\nu_{\mathrm{SAS}}}$. Further downstream of the inner recirculation zone, the ratio of $r_{\nu_{\mathrm{URANS}}}$ to $r_{\nu_{\mathrm{SAS}}}$ reaches a value of 7 to 8. Menter et al. [155] conducted SAS based computations which reveal a modeled turbulent viscosity level of approximately one magnitude smaller than the level obtained through the application of the URANS based k-ω-SST turbulence model. The high amount of turbulent viscosity within the results obtained with the k-ω-SST model leads to the conclusion that the performed URANS simulation is not able to resolve the flow unsteadiness. Opposed to this, the SAS simulation is capable of resolving the unsteady structures within the turbulent flow field. The higher amount of resolved turbulent structures through the occurrence of "LES zones" within the solution of the SAS simulation decreases the generation of turbulent viscosity and thus the amount of r_ν. Figure 5.3.56 depicts the distribution of r_ν along with the visualization of the flow topology for the incompressible and compressible reactive SAS-based solutions. As the field of r_ν is plotted using an exponential distribution, caution has to be taken during the analysis of the results depicted in figure 5.3.56. Compared to the non-reactive SAS results, the annular jet is much more focused and opens wider into the combustion chamber. It can be seen that the highest viscosity ratios occur within the jet flow. The increase of the viscosity ratio in the core of the annular jet due to the fact that the jet core brings

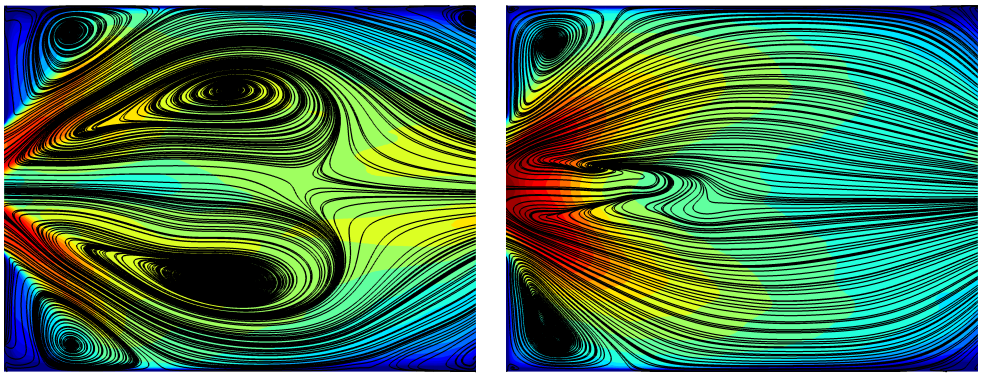

(a) THETA (IPM, k-ω-SST) (b) THETA (CPM, k-ω-SAS-SST)

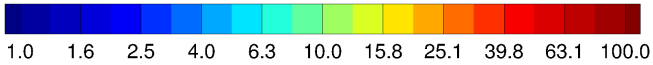

(c) r_ν [−]

Figure 5.3.56.: Distribution of the ratio of the time-avergaged turbulent to laminar viscosity along with the visualization of the flow topology (reactive case)

fresh gas into the combustion chamber and therefore possesses the initial, much smaller, temperature of the unburned gas. Due to the smaller temperature of the jet core, the laminar viscosity is decreased (see figure 5.3.57 further below). Opposed to the non-reactive case, the laminar viscosity depends on the temperature and mixture composition under reactive flow conditions. It increases with the square root of the temperature, see [36, 225] for details. The decreased values of the laminar viscosity end up in higher values of the viscosity ratio r_ν. Moreover, the high temperature of the burned gas found within the combustion chamber leads to a reduction of the overall r_ν-level compared to the non-reactive SAS-based solution. In the incompressible as well as in the compressible solution, r_ν decreases to a value of $7 \div 10$ downstream of the combustion chamber entrance. Apart from this, r_ν rises to a value of 65 in the jet flow obtained from the incompressible solution, see figure 5.3.56(a). The compressible solution reveals an increase of the ratio of the time-avergaged turbulent to laminar viscosity to a value of 100 within the inner shear layer and recirculation zone close to the combustion chamber entrance, see figure 5.3.56(b). The small r_ν-values reached in a broad area of the combustion chamber by the reactive numerical simulations indicates a good quality of the SAS-based computations regarding the amount of resolved turbulence. The reduction of r_ν is mainly due to the change in laminar viscosity due to the higher temperature level in case of the reactive flow field. The laminar viscosity is mainly constant in the non-reactive flow and possesses a mean value of $1.75 \cdot 10^{-5}\,\mathrm{m^2/s}$ based on a cell-surface averaged calculation. Figure 5.3.57 unveils the contour plot of the time-avergaged laminar viscosity along with the visualization of the flow topology for the incompressible and compressible

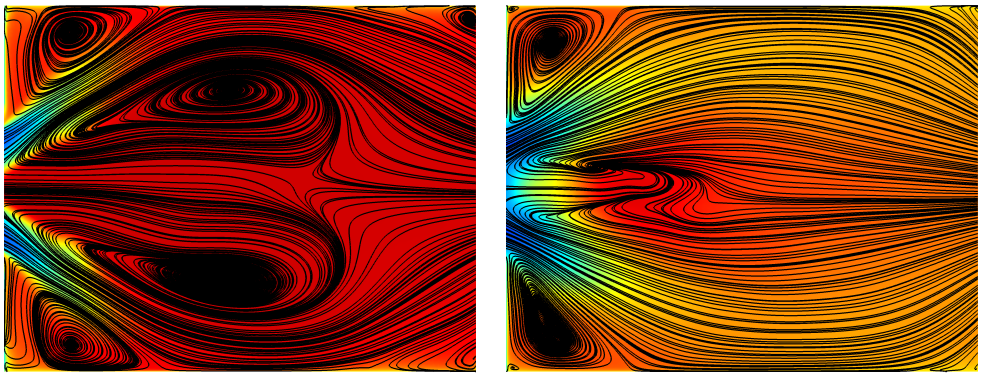

(a) THETA (IPM, k-ω-SST) (b) THETA (CPM, k-ω-SAS-SST)

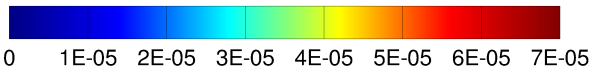

(c) ν_l $[\mathrm{m}^2/\mathrm{s}]$

Figure 5.3.57.: Distribution of the time-avergaged laminar viscosity along with the visualization of the flow topology (reactive case)

reactive computations. The laminar kinematic viscosity is proportional to the square root of the temperature [36, 225]. As a consequence, ν_l augments with increasing temperature. This relationship is reflected when comparing the distributions of both variables, see figures 5.3.50 and 5.3.57. For the burned gas domain, ν_l is approximately three times higher than the one determined under non-reactive conditions. The increased laminar viscosity under reactive conditions thus causes the ratio of the time-avergaged turbulent to laminar viscosity to decrease by a factor of approximately 3.

In case of the compressible reactive SAS computation, the rise of r_ν and fall of r_k at the combustion chamber entrance cause the resolution of the turbulent scales to deteriorate. This hints at an increased modeling of the turbulent flow structures in this region and might be the cause for the discrepancies found in the structure of the inner recirculation zone and the temperature distribution when compared to the incompressible and experimental results. As shown based on the r_k and r_ν plots, the SAS based calculation adopts an LES-like mode within a broad area of the inner combustion chamber field. Together with the observations made within the discussion of the instantaneous results, it can be concluded that the flow field given as solution of the compressible SAS simulation provides a detailed insight into the detailed mechanisms concerning the turbulent structures of the flow field.

5.3.4.3. Analysis of the Pressure Spectra

Within this section, the pressure spectrum of the non-reactive and reactive flow within the swirled gas turbine model combustor is analyzed. For this purpose, the pressure spectra of the

numerical simulations are compared to the ones obtained from the acoustic measurements. A microphone measuring the acoustic pressure has been mounted the corner of the combustion chamber walls within the experimental setup. The microphone is located at the position $\{x_1,\ x_2,\ x_3\} = \{16,\ 42,\ 42\}$ mm, see figure 5.3.58.

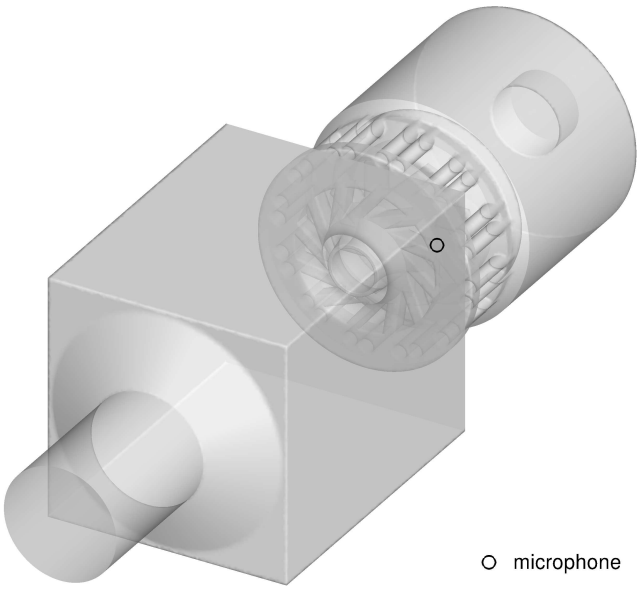

Figure 5.3.58.: Graphical visualization of the microphone position

The time signals of the pressure obtained from the numerical simulations, as well as from the acoustic measurement are firstly transformed into the frequency domain. This is done by conducting a (Fast Fourier Transform) [18, 176] of the pressure signals. Let f be a sequence of the length N. The DFT (Discrete Fourier Transform) [18, 264] of f is then defined by the following sequence of the length n [18, 176]:

$$\forall k \in \{1, \ldots, n\}\,,\ F_k \equiv \sum_{j=0}^{N-1} f_j \cdot \exp\left(-\frac{2\pi k j}{N} i\right)\,, \tag{5.3.76}$$

where F is the DFT transform of f and i denotes the imaginary unit. The DFT decomposes the sequence f into components of different frequencies. Applying a DFT analysis to a large sequence of numbers is computational expensive. Evaluating the definition given above by a direct approach requires $\mathcal{O}\left(n^2\right)$ operations. The FFT analysis permits to transform a time signal to a frequency spectrum much faster. This is realized by enlarging the sequence length n so that n is equal to a number, which is a power of 2. The computational complexity can thus be reduced to the order of $\mathcal{O}\left(n \log n\right)$. The Hanning window function [176] is used within the process of the FFT analysis. The sound pressure level L_p is obtained from the

following definition [176]:

$$L_p \equiv 10 \cdot \log\left(\frac{p^2}{p_{\text{ref}}^2}\right) , \tag{5.3.77}$$

where $p_{\text{ref}} = 2 \cdot 10^{-5}\,\text{Pa}$ describes the threshold of the human hearing and figures as reference value within equation (5.3.77). Once the sound pressure level profile is determined, its spectrum is smoothed by means of an FFT filter smoothing approach, which removes Fourier components with frequencies higher than a cutoff frequency.

Within the conduct of experimental work issued from previous works, as well as within the analysis of the instantaneous results obtained from the SAS based computations, the so-called precessing vortex core could be identified as a hydrodynamic unsteadiness of the flow field. How far this hydrodynamic phenomenon can be seen within the evaluation of the pressure spectra will be discussed within the following subsections.

Non-Reactive Case Figures 5.3.59(a) and 5.3.59(b) show the sound pressure levels of the URANS and SAS based computations as a comparison to the sound pressure levels obtained from the acoustic measurement as a function of the frequency for the non-reactive case.

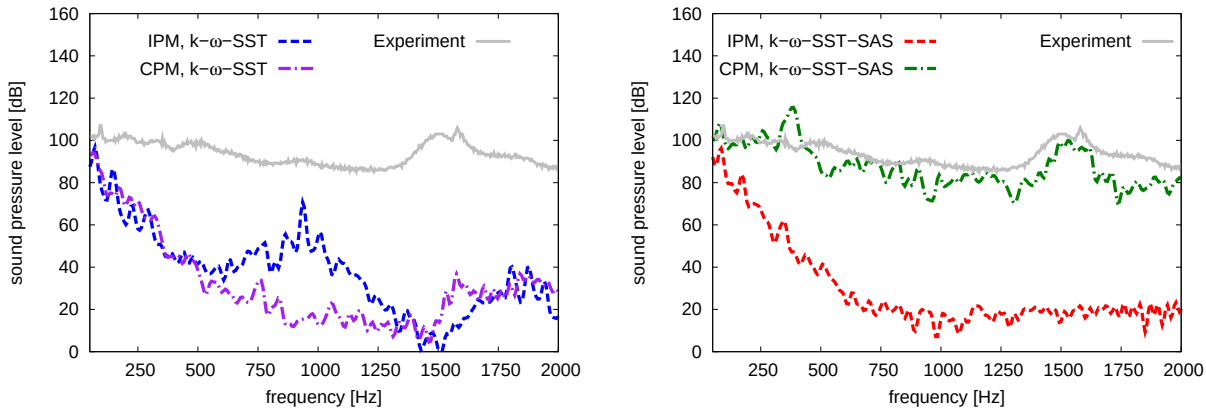

(a) URANS based computation (b) SAS based computation

Figure 5.3.59.: Sound pressure level as a function of the frequency (non-reactive case)

Figure 5.3.59(a) reveals that the URANS based computation provides a rather poor agreement to the experimental data concerning the pressure spectra at the microphone locations. Opposed to the CPM solution algorithm, the incompressible projection method is not able to capture any acoustic phenomena. It should thus be borne in mind that the profiles obtained from the incompressible calculations do not properly represent the acoustic part of the pressure spectra. They solely include the pressure fluctuations from the hydrodynamic flow field.

The precessing vortex core represents a hydrodynamic phenomenon. This mechanism is detected within the experimental results, as can be seen from figures 5.3.59(a)-5.3.59(b).

Within the conduct of the experiment, the acoustic microphone records the PVC unsteadiness at a frequency of roughly 1500 Hz. However, neither the incompressible, nor the compressible URANS computations seem to capture the experimentally determined PVC location.

Opposed to the URANS computations, the pressure spectra obtained from the results of the SAS based calculation agree very well with the profiles issued from the experiment. Moreover, it can be seen from figure 5.3.59(b) that the occurrence of the PVC is well depicted within the numerical results. The SAS based computation predicts the occurrence of the precessing vortex core at approximately 1525 Hz. Compared to this, the frequency obtained from the experiments amounts to 1582 Hz. This results in a discrepancy of 3.6 %. The pressure sound level magnitude amounts to 100dB in the case of the SAS calculation and 90dB in the case of the experimental results, which corresponds to a relative error of 10 %. It should however be noted at this point that a rise of 6 dB represents a pressure magnitude augmentation of 100 %. The error of 10 dB found in the sound pressure level thus corresponds to a pressure magnitude increase of 320 %. As a matter of fact, computational methods available up to now are able to predict pressure magnitudes occurring within technical combustors with an accuracy of several orders of magnitude [131, 117, 118, 201, 243]. Taking this into account, the determined error of 320 % in the pressure magnitude represents a very good value. Aside from the location and pressure sound level magnitude of the precessing vortex core, it is important to note that the profile of the pressure amplitude predicted by SAS computation agrees very well with the profile obtained from the experiment, see figure 5.3.59(b). This verifies that the conduct of an acoustic analysis requires the ability of a compressible solver in order to correctly depict the acoustics of the flow field.

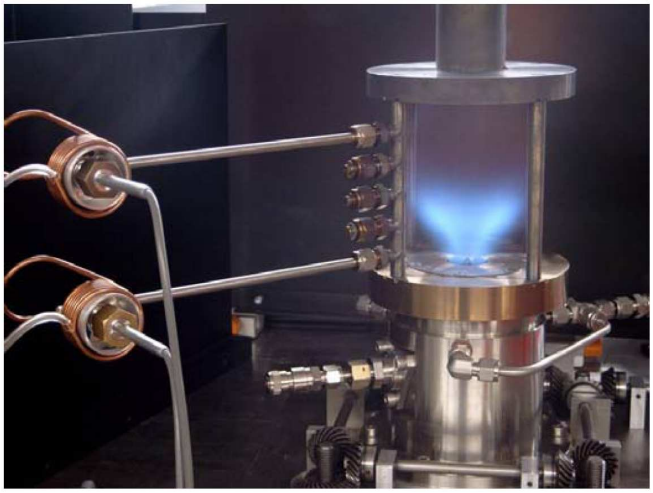

Figure 5.3.60.: Experimental setup of the model combustor

Apart from the observations made above, a peak within the pressure spectrum of the SAS based computation can be observed at 380 Hz. This peak is probably associated with the

so-called Helmholtz mode, which is of acoustic nature and occurs as zero-th mode within a Helmholtz resonator. To verify this assumption, it is possible to determine the resonance frequency f_{res} of a Helmholtz resonator. Modeling the gas turbine combustion chamber used within this section as a simple rectangular can, an analytical relationship between the resonance frequency and the geometrical dimensions of the resonator is given through the following formula [111]:

$$f_{\text{res}} \equiv \frac{c}{2\pi}\sqrt{\frac{\pi r_0^2}{V L_0}}\,, \tag{5.3.78}$$

where f_{res} denotes the resonance frequency of the Helmholtz resonator. r_0 and L_0 are the radius and length of the resonator neck. V characterizes the volume of the gas contained within the resonator. The variable c describes the speed of sound. Regarding the non-reactive case, assuming a homogeneous temperature field with a value of 330 K and a ratio of specific heats equivalent to 1.4, the isentropic speed of sound amounts to 365 m/s. The radius and length of the resonator neck equal 0.01 m and 0.012 m, respectively. The volume of the gas contained within the resonator amounts to $V = 875 \cdot 10^{-6}\,\text{m}^3$. Knowing the values of r_0, L_0, V and c, the resonance frequency equals

$$f_{\text{res}} \equiv \frac{c}{2\pi}\sqrt{\frac{\pi r_0^2}{V L_0}} = \frac{365\,\text{m/s}}{2\pi}\sqrt{\frac{\pi\, 0.01^2\,\text{m}^2}{791 \cdot 10^{-6}\,\text{m}^3\, 0.012\,\text{m}}} = 318\,\text{Hz} \tag{5.3.79}$$

With a value of 318 Hz, the analytically determined resonance frequency is close to the frequency obtained from the numerical simulation. This rather rough estimation verifies the assumption that the first peak detected within the numerical results at a frequency of 380 Hz is related to the Helmholtz mode. In addition to the analytical resonance frequency determined in the present work, the acoustics of the swirled model combustor have been numerically investigated by Stöhr et al. [235] using the commercial software COMSOL. Stöhr et al. determined the eigenmodes of the model combustor by solving the Helmholtz equation for the acoustic pressure. They found that the Helmholtz mode of the combustor lies at 295 Hz [235].

It is however not possible to clearly depict the 380 Hz-peak within the experimental results. Previous studies reveal that the damping properties of the combustion chamber and plenum are of crucial importance regarding the prediction of the acoustic amplitudes [234]. The glass and steel walls of the experimental model combustor setup possess a certain damping. This property is not taken into account within the present numerical simulations. Additionally, the numerical configuration represents a simplified geometrical model of the combustor without modeling the ducts for air and fuel supply, see figure 5.3.60. Aside from this, acoustic

modes may introduce vibrations into the mechanic parts of the model combustor through the excitation of the flow. The neglection of these issues within the numerical simulation thus introduces additional uncertainties when comparing the numerical to the experimental pressure spectra.

Reactive Case As expected, the URANS-based solutions show larger discrepancies than the SAS-based results within the pressure spectra of the non-reactive flow. This behavior is assumed not to change under reactive conditions, so that only the spectra obtained from the SAS are presented. Figure 5.3.61 unveils the sound pressure level of the SAS-based incompressible and compressible computations and compares them to the results obtained from the acoustic measurements for the reactive case.

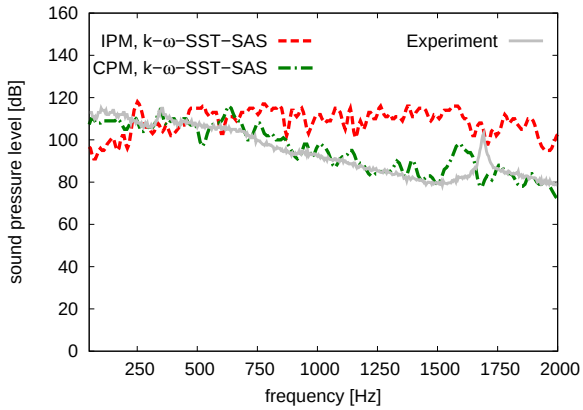

Figure 5.3.61.: Sound pressure level as a function of the frequency (reactive case)

Figure 5.3.61 reveals a very good agreement of the sound pressure levels obtained from the compressible SAS computation with the acoustic measurements. The sound pressure level decreases with rising frequency and indicates a higher noise level of the combustor operated under reactive conditions in the low frequency range. The CPM-based computation predicts the PVC unsteadiness at a frequency of 1596 Hz. By means of the results issued from the acoustic measurements, the PVC structure is detected at a frequency of 1692 Hz. The pressure sound level peaks of the compressible numerical and experimental results are 97.5 dB and 103.5 dB, respectively. Yet again, it has to be said that an absolute difference of 6 dB found between the sound pressure level magnitudes of the compressible numerical and experimental results corresponds to an increase of 100 % in the pressure magnitude for the PVC-related peak. Taking into account that computational methods available up to now are able to predict pressure magnitudes occurring within technical combustors with an accuracy of several orders of magnitude [131, 117, 118, 201, 243], the determined error of 100 % in the pressure magnitude represents an good value. The fluctuating pressure level predicted by the incompressible SAS computation does not show a decreasing progress, but is rather

preserved towards higher frequencies.

In the non-reactive numerical SAS-based solution, a peak associated with the Helmholtz mode is detected at 380 Hz. Under reactive conditions, this Helmholtz mode is found for the compressible numerical solution and the experimental results solutions at 300 Hz. The peak associated with the Helmholtz mode is much more dominant under non-reactive than under reactive flow conditions. The overall pressure sound level issued from the reactive case are higher than the one obtained from the non-reactive flow. This hints at a higher noise level in the case where combustion occurs. Moreover, the sound pressure level and frequency of the precessing vortex core is shifted towards higher values in the reactive case compared to non-reactive flow conditions, see figures 5.3.59 and 5.3.61.

5.3.4.4. Computational Resources and Efficiency

Most of the numerical simulations have been performed on an DLR in-house computing cluster. The compressible computation of the reactive flow has been conducted on the high performance NEC Nehalem computing cluster of the High Performance Computing Center Stuttgart (HLRS). Concerning the numerical simulations on the in-house cluster, 4 nodes have been used each of which features 2 Quad-Core Intel Xeon E5540 "Nehalem" processors. This results in a total number of 32 cores used. Regarding the compressible reactive calculation performed on the NEC Nehalem computing cluster, 16 Intel Xeon E5-2670 "Sandy Bridge" nodes have been utilized. Each of these nodes is composed of 2 Eight-Core processors, giving in a total amount of 16 cores. Thus, a total number of 256 cores has been applied to conduct the numerical simulations on the NEC Nehalem computing cluster.

For the total unsteady simulation period of 6 residence times, the SAS-based computation of the incompressible reactive flow field conducted on the in-house cluster required a simulation time of 19 228 Coreh, which corresponds to a physical time of 25.6 days. Concerning the compressible reactive SAS-based case computed on the NEC Nehalem computing cluster, the computational time of 6 residence times has been achieved within a total amount of 81 783 Coreh. This is equivalent to a required physical time of 13.3 days. It has to be said at this point that the compressible reactive computation needed a four times smaller time step size than the incompressible reactive calculation. By taking the ratio of the simulation times required by the compressible and incompressible solvers, a factor of 4.25 is obtained. This value is obtained by a number of effects: First, the SAS-based compressible reactive computation needs a higher number of inner iterations in order to guarantee a stable run of the calculations. The increased number of inner iterations multiplies the overall computation time by a factor of approximately 2.5. Second, the Sandybridge nodes used on the NEC Nehalem cluster proved to be more efficient than the Nehalem nodes available on the DLR

in-house computing cluster. Computing the same setup of the compressible reactive test case of the present work on both architectures, a reduction factor of 2.8 has been observed when switching from Nehalem to Sandybridge nodes. Third, the loss in computational efficiency of the THETA code in the case where 256 cores are used to compute the solution of the compressible flow induces a certain performance loss. Fourth, compared to the IPM solution algorithm, the computation time required to conduct one time step increases by 10 % in the case of using the CPM solution strategy. This amount is determined further below based on the non-reactive case and is assumed not to differ noticeably for the computation of reactive flows, cf. table 5.14. Taking into account the time step size, the difference in inner iterations, the node architecture and the difference in computational efficiency between the CPM and IPM method, a factor of 3.9 between the incompressible and compressible solutions is obtained. As a result of this, a remaining factor of approximately 1.08 can be related to the performance loss issues when increasing the number of cores from 32 to 256.

The THETA code incorporates an unsteady incompressible constant density formulation of Patankar's SIMPLE [181, 182] solution strategy. The unsteady SIMPLE algorithm is implemented by adding external loops based on the time resolution to the iterative procedure of the steady-state scheme. In order to assess the computational efficiency of the CPM solution approach, the computational time needed by the CPM scheme to accomplish one time step is compared to the ones needed by the IPM and unsteady SIMPLE methods. The determination of the computational efficiency is conducted based on the non-reactive SAS calculation on the DLR in-house computing cluster. The PBCGS algorithm is applied to solve all linear equations. As the unsteady SIMPLE implementation within the THETA code can only cope with constant density flows, the mass flux of the fuel inlet is modified according to the ratio of the fuel and air density values:

$$\dot{m}_{\text{fuel, in}} \equiv \rho_{\text{fuel, ref}}\,\dot{V}_{\text{in}} = \frac{\rho_{\text{fuel, ref}}}{\rho_{\text{ref}}}\,\rho_{\text{ref}}\,\dot{V}_{\text{in}} = \frac{\rho_{\text{fuel, ref}}}{\rho_{\text{air, ref}}}\,\dot{m}_{\text{in}} \tag{5.3.80}$$

with

$$\dot{V}_{\text{in}} \equiv \|\underline{u}_{\text{in}}\|_2\, A_{\text{in}}\ ,\quad \rho_{\text{ref}} = \rho_{\text{air, ref}} = \text{const.}\,. \tag{5.3.81}$$

The parameters of the linear solvers concerning the unsteady SIMPLE computations are set to the ones chosen for the calculations performed with the incompressible and compressible projection methods. Let $t_{\text{ts}}^{\text{avg}}$ be the averaged time required to accomplish one time step. Concerning the IPM and CPM approach, $t_{\text{ts}}^{\text{avg}}$ is averaged over at least 10000 time steps. As the unsteady SIMPLE scheme requires more time to calculate one time step, the time per time step is averaged over 200 time steps. The results of the average time per time step of the IPM, CPM and unsteady SIMPLE solution schemes are shown in table 5.14. As it can be

	IPM	CPM	Unsteady SIMPLE
$t_{\mathrm{ts}}^{\mathrm{avg}}$ [s]	7.11	7.90	379
$t_{\mathrm{ts}_{\mathrm{SIMPLE}}}^{\mathrm{avg}}/t_{\mathrm{ts}}^{\mathrm{avg}}$ [−]	53.4	48.0	1

Table 5.14.: Average time per time step of the IPM, CPM and unsteady SIMPLE solution schemes

seen from table 5.14, the difference in the computed averaged time per time step between the IPM and CPM solution schemes amounts to 10 %. This represents a relatively small amount. Neglecting the differences between an incompressible and compressible algorithm, it can be concluded that for the presented semi-technical test case the CPM solution strategy is 48 times faster than an unsteady SIMPLE based solution scheme. This large difference relative to the iterative procedure of the unsteady SIMPLE algorithm is due to the non-iterative nature of projection methods, which makes them very fast in case of computing unsteady flow fields.

6. Summary and Conclusions

A novel projection-based numerical method able to compute compressible reactive flows referred to as the CPM (Compressible Projection Method) method has been developed within this work. It is based on a generic form of the Helmholtz decomposition derived within the frame of this work, leading to a fractional step scheme which solves a predictor and a corrector step. The Poisson equation solved for the pressure within the IPM (Incompressible Projection Method) solution strategy is extended to a Helmholtz equation for the computation of compressible flows. Thus, the CPM method can be seen as an extension of the IPM method towards the regime of compressible flows. Applying the predictor and corrector steps to the conservation equations of the enthalpy and species including DALTON's law, mixing and combustion phenomena can be included into the computation process, thus enabling the calculation of reactive flows. Since no iterations of the solution process need to be performed, the CPM method describes a highly efficient numerical scheme for the numerical computation of compressible reactive flows.

The accurate prediction of compressible unsteady flows using computational methods requires an appropriate modeling of the processes at the domain boundaries. In order to satisfy this need, accurate boundary conditions have been adopted based on a characteristic analysis of the governing flow equations. The application of characteristic boundary conditions enables an accurate resolution and control of the incoming and outgoing acoustic waves at the boundaries of the computational domain. Aside from applying fully reflective boundary conditions, the application of partially reflective boundary conditions can be realized using this ability. The characteristic boundary conditions have been implemented into the THETA code in order to be used in conjunction with the CPM solution method. They have successfully been verified by means of an analytical approach verifying the response of the acoustic waves at the in- and outflow boundaries of a one-dimensional rectangular duct.

The ability of the created numerical scheme to compute flows in the incompressible limit has been demonstrated by means of an analytical analysis and a numerical test case. The CPM algorithm has successfully been verified against a one-dimensional acoustic test case. Based on the obtained results, an acoustic CFL number of unity should be used to determine the time step size. In conjunction with an acoustic CFL number of unity, a spatial resolution

of 60 points per wavelength decreases the amount of numerical dissipation and dispersion to an acceptable amount of 1 %. As a result of this, a spatial resolution of at least 60 pints per wavelength along with an acoustic CFL number of unity is recommended in order to predict the movement of acoustic phenomena accurately in space and time.

The spatial and temporal order of accuracy of incompressible projection schemes have been investigated. Following this, the influence of the projection weighting factor on the order of accuracy has been addressed to. For this purpose, convergence tests in space and time have been conducted for different values of the projection weighting factor in order to determine the accuracy of the CPM method. As a result of this, it could be shown that choosing the projection weighting factor of the CPM method equal to the value of 2 leads to a second-order accurate numerical scheme in space and time.

The computation of the homentropic flow in a two-dimensional convergent nozzle has been addressed to. Numerical calculations increasing the highest occurring Mach number up to 0.92 have been conducted and validated by means of analytically derived data and numerical results issued from previous works. The successful validation by means of this test case demonstates the ability of the CPM method of accurately computing flows with a maximum occurring Mach number of 0.92. Furthermore, homentropic calculations prescribing a linear distribution of the inlet velocity have been conducted. The prescription of a linear velocity profile at the inlet boundary surface causes an unsteady perturbation of the flow field within the start-up phase of the calculation which is followed by an up- and downwards directed flow movement. This wave-like movement can be explained through a combined convective/acoustic mechanism of the flow field. By setting a partially non-reflective boundary condition at the outflow and comparing it to the results of a fully reflective outlet, it could be seen that the reflection of the occurring acoustic waves at the outlet additionally influences the oscillating movement of the flow field. Together with the results obtained from the analysis in the incompressible limit, the CPM scheme thus shows the ability to compute flows close to the zero Mach number limit, as well as flows with a Mach number reaching the limit of $\mathrm{Ma} \rightarrow 1$.

As an application-related and validation test case, the three-dimensional turbulent flow in a double-swirled gas turbine combustor has been computed. The influences of the incompressible and compressible projection schemes on the numerical results have been analyzed. Moreover, the differences between applying the k-ω-SST and k-ω-SST-SAS turbulence models concerning the prediction of the numerical results have been identified. Based on the instantaneous results of the SAS-based computations, the existence of a helical vortex structure and thus of a hydrodynamic precessing vortex core and exhaust tube vortex could be seen. This is in accordance with the experimental observations issued from previous works.

Contrary to the SAS computations, the URANS calculations are not able to resolve the unsteadiness of the instantaneous flow field within the combustion chamber. As a result of this, the high spatial resolution achieved though the LES mode of the SAS computations is of essential importance for the resolution of the unsteady phenomena of the flow field. Compared to the experimental data of the non-reactive and reactive flow field, the incompressible and compressible URANS-based computations overpredict the velocity at the outflow of the air nozzles, which leads to a greater opening angle of the v-shaped flow field. Regarding the numerical results of the three-dimensional flow, the SAS-based compressible computations reveal a good agreement to the experimental data. The CPM method additionally provides the possibility to resolve acoustic phenomena, which can be detected in contour plots of the solution or in a spectral analysis of the pressure time signal. The computation of this test case demonstrates the ability of the CPM approach of calculating the highly unsteady and turbulent flow field in a double-swirled gas turbine combustor where Mach numbers approaching the incompressible limit, as well as Mach numbers of the order of 0.25 occur. Moreover, it could be shown for this test case that the CPM solution strategy is roughly 50 times faster than a comparable unsteady SIMPLE based solution scheme. This demonstrates the computational efficiency of the CPM method. Only small differences concerning the computational efficiency between the IPM and CPM solution methods have been detected.

A. Mathematical Notation

The equations given within this work are written using the so-called tensor notation, cf. [109, 110, 188]. Partial differential equations used to describe physical phenomena are usually of complex nature. They often require much space to be written down. The tensor notation allows to write complex equations using very little space. The meaning of the mathematical operators used within the tensor notation is however not intuitive so that they require additional explanation. This is done in the following.

Within this work, vectors are underlined once, matrices twice. The operator $\cdot$ denotes the scalar product of two vectors. Let $\underline{\Psi}$ and $\underline{\Phi}$ be arbitrary N-dimensional vector fields. The scalar product of $\underline{\Psi}$ and $\underline{\Phi}$ then reads:

$$\begin{aligned} \underline{\Psi} \cdot \underline{\Phi} &\equiv \sum_{i=1}^{N} \Psi_i \Phi_i \\ &= \Psi_1 \Phi_1 + \Psi_2 \Phi_2 + \ldots + \Psi_N \Phi_N \,. \end{aligned} \tag{A.0.1}$$

In the case where $\underline{\Psi} = \underline{\Phi}$, the above equation equals the L^2-norm of $\underline{\Phi}$:

$$\underline{\Phi} \cdot \underline{\Phi} \equiv \|\underline{\Phi}\|_2 = \sum_{i=1}^{N} \Phi_i \Phi_i \,. \tag{A.0.2}$$

The scalar product of two matrices is performed analogously to the calculation given above. The structure of matrices is however more complex, so that the scalar product of two matrices requires the multiplication of each row of the first matrix with each column of the second matrix. Suppose that $\underline{\underline{A}}$ and $\underline{\underline{B}}$ constitute two matrices of the dimensions $N \times M$ and $M \times P$, respectively. The scalar product of $\underline{\underline{A}}$ and $\underline{\underline{B}}$ then yields the following formula:

$$\underline{\underline{A}} \cdot \underline{\underline{B}} \equiv \begin{bmatrix} \sum_{i=1}^{M} A_{1i} B_{i1} & \sum_{i=1}^{M} A_{1i} B_{i2} & \cdots & \sum_{i=1}^{M} A_{1i} B_{iP} \\ \sum_{i=1}^{M} A_{2i} B_{i1} & \sum_{i=1}^{M} A_{2i} B_{i2} & \cdots & \sum_{i=1}^{M} A_{2i} B_{iP} \\ \vdots & \vdots & \ddots & \vdots \\ \sum_{i=1}^{M} A_{Ni} B_{i1} & \sum_{i=1}^{M} A_{Ni} B_{i2} & \cdots & \sum_{i=1}^{M} A_{Ni} B_{iP} \end{bmatrix} , \tag{A.0.3}$$

where A_{ij} and B_{ij} are the elements of the matrices $\underline{\underline{A}}$ and $\underline{\underline{B}}$, respectively. Let $\underline{\Psi}$ and $\underline{\Phi}$ two vectors of the dimensions M and N, respectively. The operator $\otimes$ then denotes the dyadic product of $\underline{\Psi}$ and $\underline{\Phi}$:

$$\underline{\Psi} \otimes \underline{\Phi} \equiv \underline{\Psi} \cdot \underline{\Phi}^T = \begin{bmatrix} \Psi_1\Phi_1 & \Psi_1\Phi_2 & \cdots & \Psi_1\Phi_N \\ \Psi_2\Phi_1 & \Psi_2\Phi_2 & \cdots & \Psi_2\Phi_N \\ \vdots & \vdots & \ddots & \vdots \\ \Psi_M\Phi_1 & \Psi_M\Phi_2 & \cdots & \Psi_M\Phi_N \end{bmatrix} . \tag{A.0.4}$$

Note that the result of $\underline{\Psi} \otimes \underline{\Phi}$ is a matrix of the dimension $M \times N$. ∇ is defined as the vector containing the spatial derivatives with respect to the coordinates $x_i, i \in \{1, \ldots, N\}$ and is referred to as the spatial gradient:

$$\nabla \equiv \begin{bmatrix} \frac{\partial}{\partial x_1} \\ \frac{\partial}{\partial x_2} \\ \vdots \\ \frac{\partial}{\partial x_N} \end{bmatrix} . \tag{A.0.5}$$

In a N-dimensional domain, the dimension of ∇ equals N. It is remembered that $\underline{\Psi}$ is an arbitrary N-dimensional vector field. The spatial gradient of $\underline{\Psi}$ then reads:

$$\nabla\underline{\Psi} \equiv \begin{bmatrix} \frac{\partial\Psi_1}{\partial x_1} & \frac{\partial\Psi_1}{\partial x_2} & \cdots & \frac{\partial\Psi_1}{\partial x_N} \\ \frac{\partial\Psi_2}{\partial x_1} & \frac{\partial\Psi_2}{\partial x_2} & \cdots & \frac{\partial\Psi_2}{\partial x_N} \\ \vdots & \vdots & \ddots & \vdots \\ \frac{\partial\Psi_N}{\partial x_1} & \frac{\partial\Psi_N}{\partial x_2} & \cdots & \frac{\partial\Psi_N}{\partial x_N} \end{bmatrix} . \tag{A.0.6}$$

Applying the N-dimensional spatial gradient ∇ onto the N-dimensional vector field $\underline{\Psi}$ results in a matrix of the dimension $N \times N$. If the dimension of $\underline{\Psi}$ equals one, then $\underline{\Psi} = \Psi$ constitutes a scalar field. In this case, the spatial gradient of Ψ reduces to the following vector:

$$\nabla\Psi \equiv \begin{bmatrix} \frac{\partial\Psi}{\partial x_1} \\ \frac{\partial\Psi}{\partial x_2} \\ \vdots \\ \frac{\partial\Psi}{\partial x_N} \end{bmatrix} . \tag{A.0.7}$$

The scalar product of the spatial gradient ∇ and the N-dimensional vector field $\underline{\Psi}$ is referred

to as the divergence of $\underline{\Psi}$:

$$\nabla \cdot \underline{\Psi} \equiv \sum_{i=1}^{N} \frac{\partial \Psi_i}{\partial x_i} = \frac{\partial \Psi_1}{\partial x_1} + \frac{\partial \Psi_2}{\partial x_2} + \ldots + \frac{\partial \Psi_N}{\partial x_N} \,. \tag{A.0.8}$$

Suppose that matrix $\underline{\underline{A}}$ of the dimension $N \times N$ is given. The divergence of $\underline{\underline{A}}$ then yields the following result:

$$\nabla \cdot \underline{\underline{A}} \equiv \begin{bmatrix} \sum_{i=1}^{N} \frac{\partial A_{1i}}{\partial x_i} \\ \sum_{i=1}^{N} \frac{\partial A_{2i}}{\partial x_i} \\ \vdots \\ \sum_{i=1}^{N} \frac{\partial A_{Ni}}{\partial x_i} \end{bmatrix} = \begin{bmatrix} \frac{\partial A_{11}}{\partial x_1} + \frac{\partial A_{12}}{\partial x_2} + \ldots + \frac{\partial A_{1N}}{\partial x_N} \\ \frac{\partial A_{21}}{\partial x_1} + \frac{\partial A_{22}}{\partial x_2} + \ldots + \frac{\partial A_{2N}}{\partial x_N} \\ \vdots \quad\quad \vdots \quad\quad \ddots \quad\quad \vdots \\ \frac{\partial A_{N1}}{\partial x_1} + \frac{\partial A_{N2}}{\partial x_2} + \ldots + \frac{\partial A_{NN}}{\partial x_N} \end{bmatrix} . \tag{A.0.9}$$

$\Delta_{\mathrm{L}} \underline{\Psi}$ denotes the Laplacian of a twice continuously differentiable vector field $\underline{\Psi}$ of the dimension N and is defined by the following expression:

$$\Delta_{\mathrm{L}} \underline{\Psi} \equiv \nabla^T \cdot (\nabla \underline{\Psi}) = \begin{bmatrix} \sum_{i=1}^{N} \frac{\partial^2 \Psi_1}{\partial x_i^2} \\ \sum_{i=1}^{N} \frac{\partial^2 \Psi_2}{\partial x_i^2} \\ \vdots \\ \sum_{i=1}^{N} \frac{\partial^2 \Psi_N}{\partial x_i^2} \end{bmatrix} . \tag{A.0.10}$$

The L^2-norm of $\Delta_{\mathrm{L}} \underline{\Psi}$ describes its magnitude and is given by the following equation:

$$\| \Delta_{\mathrm{L}} \underline{\Psi} \|_2 \equiv \sqrt{\sum_{i=1}^{N} \left(\sum_{j=1}^{N} \frac{\partial^2 \Psi_i}{\partial x_j^2} \right)^2} \,. \tag{A.0.11}$$

For $\dim(\underline{\Psi}) = 1$, equations (A.0.10) and (A.0.11) reduce to the following respective forms:

$$\Delta_{\mathrm{L}} \Psi \equiv \nabla \cdot (\nabla \Psi) = \sum_{i=1}^{N} \frac{\partial^2 \Psi_1}{\partial x_i^2} \,, \tag{A.0.12}$$

$$\| \Delta_{\mathrm{L}} \Psi \|_2 \equiv \sqrt{\sum_{j=1}^{N} \left(\frac{\partial^2 \Psi}{\partial x_j^2} \right)^2} \,. \tag{A.0.13}$$

The material derivative of an arbitrary vector field $\underline{\Psi}$ is defined by the following equation:

$$\frac{D \underline{\Psi}}{Dt} \equiv \frac{\partial \underline{\Psi}}{\partial t} + \underline{u} \otimes \nabla \underline{\Psi} \,, \tag{A.0.14}$$

where $\underline{u}$ denotes the velocity vector. For $\dim(\underline{\Psi}) = 1$, equation reduces to the following

formula:

$$\frac{D\Psi}{Dt} \equiv \frac{\partial \Psi}{\partial t} + \underline{u} \cdot \nabla \Psi \,. \tag{A.0.15}$$

The notation : describes the Frobenius inner product of two tensors. Let $\underline{\underline{A}}$ and $\underline{\underline{B}}$ be two quadratic matrices of the dimension $N \times N$. The Frobenius inner product of $\underline{\underline{A}}$ and $\underline{\underline{B}}$ then reads:

$$\underline{\underline{A}} : \underline{\underline{B}} \equiv \mathrm{tr}\left(A^T B\right) = \sum_{i=1}^{N} \sum_{j=1}^{N} A_{ij} B_{ij} \,, \tag{A.0.16}$$

where the operator tr denotes the trace of a matrix. Let $\underline{\underline{A}}$ be a matrix of the dimension $N \times N$. Its trace is then defined through the following formula:

$$\mathrm{tr}\left(\underline{\underline{A}}\right) \equiv \sum_{i=1}^{N} A_{ii} \,. \tag{A.0.17}$$

The Frobenius norm of a matrix $\underline{\underline{A}} \in \mathbb{R}^{N \times N}$ corresponds to the square root of the Frobenius inner product of $\underline{\underline{A}}$ with itself. It is thus defined by the following expression:

$$\|\underline{\underline{A}}\|_F \equiv \sqrt{\underline{\underline{A}} : \underline{\underline{A}}} = \sqrt{\mathrm{tr}\left(\underline{\underline{A}}^T \cdot \underline{\underline{A}}\right)} = \sqrt{\sum_{i=1}^{N} \sum_{j=1}^{N} A_{ij}^2} \,. \tag{A.0.18}$$

The matrix $\underline{\underline{I}}$ and the vector $\underline{I}$ describe the identity matrix and vector, respectively:

$$\underline{\underline{I}} \equiv \begin{bmatrix} 1 & 1 & \cdots & 1 \\ 1 & 1 & \cdots & 1 \\ \vdots & \vdots & \ddots & \vdots \\ 1 & 1 & \cdots & 1 \end{bmatrix} \quad \text{and} \quad \underline{I} \equiv \begin{bmatrix} 1 \\ 1 \\ \vdots \\ 1 \end{bmatrix} \,. \tag{A.0.19}$$

$\underline{\underline{I}}$ is of the dimension $N \times N$, whereas $\underline{I}$ possesses the dimension $N \times 1$.

B. Analytical Derivations

B.1. Derivation of the Pressure Equation

The derivation of the pressure equation (primitive energy equation formulated for the pressure) is performed in this appendix. Consider a fully unsteady, compressible, viscous, chemically reactive. The gas mixture is assumed to be ideal and chemically reactive, consisting of N_s components. By additionally neglecting specific body forces (see section 2.2), the enthalpy equation (conservative energy equation formulated for the enthalpy) reads:

$$\frac{\partial\left(\rho h\right)}{\partial t}+\nabla\cdot\left(\rho\underline{u}h\right)-\frac{\partial p}{\partial t}-\underline{u}\cdot\nabla p=-\nabla\cdot\underline{q}+\underline{\underline{\tau}}:\nabla\underline{u}\,. \tag{B.1.1}$$

By applying the product rule and making use of the continuity equation

$$\frac{\partial\rho}{\partial t}+\nabla\cdot\left(\rho\underline{u}\right)=0\,, \tag{B.1.2}$$

the enthalpy equation can be recast into the primitive form:

$$\begin{aligned}\rho\left(\frac{\partial h}{\partial t}+\underline{u}\nabla\cdot h\right)+h\underbrace{\left[\frac{\partial\rho}{\partial t}+\nabla\cdot\left(\rho\underline{u}\right)\right]}_{=0}-\frac{\partial p}{\partial t}-\underline{u}\cdot\nabla p &= -\nabla\cdot\underline{q}+\underline{\underline{\tau}}:\nabla\underline{u}\\ \rho\left(\frac{\partial h}{\partial t}+\underline{u}\nabla\cdot h\right)-\frac{\partial p}{\partial t}-\underline{u}\cdot\nabla p &= -\nabla\cdot\underline{q}+\underline{\underline{\tau}}:\nabla\underline{u}\,.\end{aligned} \tag{B.1.3}$$

By using the material derivative of the enthalpy and pressure

$$\frac{Dh}{Dt}\equiv\frac{\partial h}{\partial t}+\underline{u}\cdot\nabla h\;,\quad\frac{Dp}{Dt}\equiv\frac{\partial p}{\partial t}+\underline{u}\cdot\nabla p\,, \tag{B.1.4}$$

the enthalpy equation can be written using a more compact notation:

$$\rho\frac{Dh}{Dt}-\frac{Dp}{Dt}=-\nabla\cdot\underline{q}+\underline{\underline{\tau}}:\nabla\underline{u}\,. \tag{B.1.5}$$

The enthalpy is defined as the so-called sensible chemical enthalpy:

$$h = \sum_{i=1}^{N_s} Y_i h_i \equiv \sum_{i=1}^{N_s} Y_i \left[h_{f_i}^0 + \int_{T_0}^{T} c_{p_i} \left(\tilde{T} \right) d\tilde{T} \right] . \tag{B.1.6}$$

The total derivative of the material derivative of $h = h\left(T, Y_i\right)$, $i = \{1, 2, \ldots, N_s\}$ can thus be formulated as:

$$\frac{Dh}{Dt} = \left.\frac{\partial h}{\partial T}\right|_{p,Y_i} \frac{DT}{Dt} + \sum_{i=1}^{N_s} \left.\frac{\partial h}{\partial Y_i}\right|_{T,p,Y_{j,j\neq i}} \frac{DY_i}{Dt} . \tag{B.1.7}$$

With

$$\left.\frac{\partial h}{\partial T}\right|_{p,Y_i} = c_p \ , \quad \left.\frac{\partial h}{\partial Y_i}\right|_{T,p,Y_{j,j\neq i}} = h_i \, , \tag{B.1.8}$$

equation (B.1.7) can be rewritten to the following formula:

$$\frac{Dh}{Dt} = c_p \frac{DT}{Dt} + \sum_{i=1}^{N_s} h_i \frac{DY_i}{Dt} . \tag{B.1.9}$$

The equation of state formulated for the temperature $T = T\left(p, \rho, Y_i\right)$, $i = \{1, 2, \ldots, N_s\}$ reads:

$$T = \frac{p_{\text{ref}} + p}{\rho R} = \frac{p_{\text{ref}} + p}{\rho \mathcal{R} \sum_{i=1}^{N_s} \frac{Y_i}{M_i}} . \tag{B.1.10}$$

Writing the total derivative of the temperature material derivative then leads to the following formula:

$$\frac{DT}{Dt} = \left.\frac{\partial T}{\partial p}\right|_{\rho,Y_i} \frac{Dp}{Dt} + \left.\frac{\partial T}{\partial \rho}\right|_{p,Y_i} \frac{D\rho}{Dt} + \sum_{i=1}^{N_s} \left.\frac{\partial T}{\partial Y_i}\right|_{p,\rho,Y_{j,j\neq i}} \frac{DY_i}{Dt} . \tag{B.1.11}$$

Inserting the derivatives

$$\left.\frac{\partial T}{\partial p}\right|_{\rho,Y_i} = \frac{T}{p_{\text{ref}} + p} \ , \quad \left.\frac{\partial T}{\partial \rho}\right|_{p,Y_i} = -\frac{T}{\rho} \quad \text{and} \quad \left.\frac{\partial T}{\partial Y_i}\right|_{p,\rho,Y_{j,j\neq i}} = -\frac{T}{Y_i} \tag{B.1.12}$$

into (B.1.12) leads to the following equation:

$$\frac{DT}{Dt} = \frac{T}{p_{\text{ref}} + p} \frac{Dp}{Dt} - \frac{T}{\rho} \frac{D\rho}{Dt} - \sum_{i=1}^{N_s} \frac{T}{Y_i} \frac{DY_i}{Dt} . \tag{B.1.13}$$

Introducing equation (B.1.13) into the total enthalpy material derivative (B.1.9) yields:

$$\frac{Dh}{Dt} = \left(\frac{1}{p_{\text{ref}} + p} \frac{Dp}{Dt} - \frac{1}{\rho} \frac{D\rho}{Dt} \right) c_p T + \sum_{i=1}^{N_s} \left(h_i - \frac{1}{Y_i} c_p T \right) \frac{DY_i}{Dt} . \tag{B.1.14}$$

Making use of the relationship $c_p/R = \gamma\,/\,(\gamma-1)$, recasting and multiplying equation (B.1.14) with ρ leads to:

$$\rho\frac{Dh}{Dt} = \frac{\gamma}{\gamma-1}\frac{Dp}{Dt} - \frac{\gamma}{\gamma-1}\frac{p_{\text{ref}}+p}{\rho}\frac{D\rho}{Dt} + \sum_{i=1}^{N_s}\left(\rho h_i - \frac{\gamma}{\gamma-1}\frac{p_{\text{ref}}+p}{Y_i}\right)\frac{DY_i}{Dt}\,. \tag{B.1.15}$$

Rewriting the species mass fractions conservation equations (2.2.4) into the primitive form leads to:

$$\forall i \in \{1,2,\ldots,N_s\}\,,\ \rho\left(\frac{\partial Y_i}{\partial t} + \underline{u}\cdot\nabla Y_i\right) = -\nabla\cdot\underline{j}_i + S_{Y_i}\,. \tag{B.1.16}$$

By using the material derivative of Y_i, (B.1.16) can be reformulated to the following equation:

$$\forall i \in \{1,2,\ldots,N_s\}\,,\ \rho\frac{DY_i}{Dt} = -\nabla\cdot\underline{j}_i + S_{Y_i}\,. \tag{B.1.17}$$

Replacing the material derivative of the species mass fractions Y_i, $i \in \{1,2,\ldots,N_s\}$ appearing on the right hand side of equation (B.1.15) with the equation (B.1.17) deduced above, one obtains the following result:

$$\rho\frac{Dh}{Dt} = \frac{\gamma}{\gamma-1}\frac{Dp}{Dt} - \frac{\gamma}{\gamma-1}\frac{p_{\text{ref}}+p}{\rho}\frac{D\rho}{Dt} + \sum_{i=1}^{N_s}\left(h_i - \frac{\gamma}{\gamma-1}\frac{p_{\text{ref}}+p}{Y_i\rho}\right)\left(S_{Y_i} - \nabla\cdot\underline{j}_i\right)\,. \tag{B.1.18}$$

Introducing the result (B.1.15) and the continuity equation (B.1.2) into the equation (B.1.5) and recasting the terms results in the following equation:

$$\begin{aligned}\frac{Dp}{Dt} - \gamma\frac{p_{\text{ref}}+p}{\rho}\frac{D\rho}{Dt} = (\gamma-1)\Bigg[&\sum_{i=1}^{N_s}\left(\frac{\gamma}{\gamma-1}\frac{p_{\text{ref}}+p}{Y_i\rho} - h_i\right)\left(S_{Y_i} - \nabla\cdot\underline{j}_i\right)\\ &-\nabla\cdot\underline{q} + \underline{\underline{\tau}} : \nabla\underline{u}\Bigg]\,.\end{aligned} \tag{B.1.19}$$

Reformulating the pressure derivative and introducing the mixing and combustion source term $S_{\text{m\&c}}$

$$S_{\text{m\&c}} \equiv \sum_{i=1}^{N_s}\left(\frac{\gamma}{\gamma-1}\frac{p_{\text{ref}}+p}{\rho Y_i} - h_i\right)\left(S_{Y_i} - \nabla\cdot\underline{j}_i\right) \tag{B.1.20}$$

finally leads to the pressure equation:

$$\frac{\partial p}{\partial t} + \underline{u}\cdot\nabla p + \gamma p\nabla\cdot\underline{u} = (\gamma-1)\left(S_{\text{m\&c}} - \nabla\cdot\underline{q} + \underline{\underline{\tau}} : \nabla\underline{u}\right)\,. \tag{B.1.21}$$

Note that the chemical reactions source term elements S_{Y_i}, $i \in \{1, 2, \ldots, N_s\}$ disappear if an inert, i.e. chemically non-reactive, gas mixture is computed. If a homogeneous gas mixture is considered, $S_{\mathrm{m\&c}}$ vanishes. In the latter case, the pressure equation reduces to the following formula:

$$\frac{\partial p}{\partial t} + \underline{u} \cdot \nabla p + \gamma \nabla \cdot \underline{u} = (\gamma - 1) \left(-\nabla \cdot \underline{q} + \underline{\underline{\tau}} : \nabla \underline{u} \right) . \tag{B.1.22}$$

B.2. Recast of the Velocity Divergence Constraint

Based on the pressure equation formulation, the velocity divergence is recast in order to obtain a formula involving the material derivative of the density, i.e. a formula that can be directly linked to the mass conservation equation. Consider a fully unsteady, compressible, viscous, chemically reactive. The gas mixture is assumed to be ideal and chemically reactive, consisting of N_s components. The equation of state formulated for the pressure $p = p(\rho, T, Y_i)$, $i = \{1, 2, \ldots, N_s\}$ reads:

$$p = \rho R T - p_{\mathrm{ref}} = \rho \mathcal{R} T \sum_{i=1}^{N_s} \frac{Y_i}{M_i} - p_{\mathrm{ref}} . \tag{B.2.1}$$

The total derivative of the pressure material derivative then reads:

$$\frac{Dp}{Dt} = \left.\frac{\partial p}{\partial \rho}\right|_{T,Y_i} \frac{D\rho}{Dt} + \left.\frac{\partial p}{\partial T}\right|_{\rho,Y_i} \frac{DT}{Dt} + \sum_{i=1}^{N_s} \left.\frac{\partial p}{\partial Y_i}\right|_{\rho,T,Y_{j,j\neq i}} \frac{DY_i}{Dt} . \tag{B.2.2}$$

Inserting the derivatives

$$\left.\frac{\partial p}{\partial \rho}\right|_{T,Y_i} = \frac{p_{\mathrm{ref}} + p}{\rho} , \quad \left.\frac{\partial p}{\partial T}\right|_{\rho,Y_i} = \frac{p_{\mathrm{ref}} + p}{T} \quad \text{and} \quad \left.\frac{\partial p}{\partial Y_i}\right|_{\rho,T,Y_{j,j\neq i}} = \frac{p_{\mathrm{ref}} + p}{Y_i} \tag{B.2.3}$$

into (B.2.2) leads to the following result:

$$\frac{Dp}{Dt} = (p_{\mathrm{ref}} + p) \left(\frac{1}{\rho} \frac{D\rho}{Dt} + \frac{1}{T} \frac{DT}{Dt} - \sum_{i=1}^{N_s} \frac{1}{Y_i} \frac{DY_i}{Dt} \right) . \tag{B.2.4}$$

The temperature equation (primitive energy equation formulated for the temperature) can be derived based on the enthalpy conservation equation (2.2.3) and is described by the following equation [193]:

$$\frac{DT}{Dt} = \frac{1}{\rho c_p} \left[\frac{Dp}{Dt} - \sum_{i=1}^{N_s} h_i \left(S_{Y_i} - \nabla \cdot \underline{j}_i \right) - \nabla \cdot \underline{q} + \underline{\underline{\tau}} : \nabla \underline{u} \right] . \tag{B.2.5}$$

For details concerning the derivation of the temperature equation (B.2.5), the reader is referred to the publication of POWERS [193]. Multiplying equation (B.2.5) with $1/T$ and inserting $1\,/\,(\rho c_p T) = (\gamma - 1)\,/\,[\gamma\,(p_{\mathrm{ref}} + p)]$ the following result is obtained:

$$\frac{1}{T}\frac{DT}{Dt} = \frac{\gamma - 1}{\gamma\,(p_{\mathrm{ref}} + p)}\left[\frac{Dp}{Dt} - \sum_{i=1}^{N_s} h_i \left(S_{Y_i} - \nabla \cdot \underline{j}_i\right) - \nabla \cdot \underline{q} + \underline{\underline{\tau}} : \nabla \underline{u}\right] . \tag{B.2.6}$$

Inserting the result (B.2.6) as well as the primitive form of the species mass fractions conservation equation (B.1.16) into equation (B.2.4) yields:

$$\begin{aligned}\frac{Dp}{Dt} = \gamma\,(p_{\mathrm{ref}} + p)\,\frac{1}{\rho}\frac{D\rho}{Dt} + (\gamma - 1)\Bigg[&-\nabla \cdot \underline{q} + \underline{\underline{\tau}} : \nabla \underline{u} \\ &- \sum_{i=1}^{N_s}\left[h_i + \frac{\gamma}{\gamma - 1}\frac{p_{\mathrm{ref}} + p}{\rho Y_i}\right]\left(S_{Y_i} - \nabla \cdot \underline{j}_i\right)\Bigg] .\end{aligned} \tag{B.2.7}$$

Reformulating equation (B.2.7) results in:

$$\begin{aligned}\frac{\partial p}{\partial t} + \underline{u} \cdot \nabla p = \gamma\,(p_{\mathrm{ref}} + p)\,\frac{1}{\rho}\left(\frac{\partial \rho}{\partial t} + \underline{u} \cdot \nabla \rho\right) \\ + (\gamma - 1)\left[-\nabla \cdot \underline{q} + \underline{\underline{\tau}} : \nabla \underline{u} - \sum_{i=1}^{N_s}\left[h_i + \frac{\gamma}{\gamma - 1}\frac{p_{\mathrm{ref}} + p}{\rho Y_i}\right]\left(S_{Y_i} - \nabla \cdot \underline{j}_i\right)\right] .\end{aligned} \tag{B.2.8}$$

By introducing the pressure equation (B.1.21) into the equation (B.2.8) derived above, one observes that most of the terms cancel out and that an alternative formulation of the velocity divergence is obtained:

$$\nabla \cdot \underline{u} = -\frac{1}{\rho}\left(\frac{\partial \rho}{\partial t} + \underline{u} \cdot \nabla \rho\right) . \tag{B.2.9}$$

In the form (B.2.9), the velocity divergence is described by the spatial and temporal derivative of the density.

It is important to emphasize at this point that relation (B.2.9) can be directly derived from the continuity equation (2.2.1)

$$\frac{\partial \rho}{\partial t} + \nabla \cdot (\rho \underline{u}) = 0 \Leftrightarrow \nabla \cdot \underline{u} = -\frac{1}{\rho}\left(\frac{\partial \rho}{\partial t} + \underline{u} \cdot \nabla \rho\right) . \tag{B.2.10}$$

Equations (B.2.9) and (B.2.10) are identical. This demonstration proves that the derivation of the velocity divergence from the pressure equation is consistent to the continuity equation. The implementation of equation ensures the fulfillment of mass conservation.

C. Description and Evaluation of the Residuals Issuing from the Linear Solver

Let $\underline{\underline{A}} \cdot \underline{\phi} = \underline{b}$ be a system of linear equations for solving the variable $\underline{\phi}$. $\underline{\underline{A}}$ and $\underline{b}$ denote the the coefficient matrix and source vector, respectively. The element ϕ_i, $i = \{1, 2, \ldots, N_p\}$ of the solution variable $\underline{\phi}$ corresponds to the value of ϕ at the grid node i. For this set of equations, a sequence of residual vectors

$$\forall m \in \{1, 2, \ldots, N_{\mathrm{ii}}\}\,,\ \underline{\mathrm{res}}^m = \left[\mathrm{res}_1^m\ \mathrm{res}_2^m\ \ldots\ \mathrm{res}_{N_p}^m\right]^T \equiv \underline{b}^m - \underline{\underline{A}}^m \cdot \underline{\phi}^m \tag{C.0.1}$$

is defined as the left-over of the linear equations being solved for. The variable N_{ii} describes the number of inner iterations conducted by the linear solver. The overall residual RES after m, $1 \leqslant m \leqslant N_{\mathrm{ii}}$ inner iterations at the time step $n \in \{1, 2, \ldots, N_{\mathrm{ts}}\}$ is finally obtained through the L^2-norm of the individual residuals $\mathrm{res}_i^{m,n}$:

$$\mathrm{RES}^{m,n} \equiv \sqrt{\sum_{i=1}^{N_p} \left(\mathrm{res}_i^{m,n}\right)^2}\,. \tag{C.0.2}$$

Within this work, all residual plots depict the initial residuals $\mathrm{RES}^{0,n}$, $\forall n \in \{1, 2, \ldots, N_{\mathrm{ts}}\}$ of the linear equations. The initial residuals denote the residuals computed with the initial solution, being the solution from the previous time step.

Bibliography

[1] Adams, R. A., Fournier, J. J. F., "Sobolev Spaces", *Academic Press*, second edition, 2003.

[2] Alt, H.-W., "Lineare Funktionalanalysis" (Linear Functional Analysis), *Springer*, fifth edition, 2006. In German.

[3] AIAA, "Guide for the verification and validation of computational fluid dynamics simulations", *American Institute of Aeronautics and Astronautics*, No. AIAA-G-077-1998, Reston, Virginia, USA, 1998.

[4] Arfken, G., "Gauss's Theorem", *Mathematical Methods for Physicists, Academic Press*, third edition, 1985.

[5] Ax, H., *Personal communication*, 2013.

[6] Babik, F., Gallouët, T., Latché, J.-C., Suardy, S., Vola, D., "On two fractional step finite volume and finite element schemes for reactive low Mach number flows", *The International Symposium on Finite Volumes for Complex Applications IV - Problems and Perspectives, July 4-8, Marrakech*, 2005.

[7] Baehr, H. D., "Thermodynamik: Grundlagen und technische Anwendungen" (Thermodynamics: Fundamentals and Technical Applications), *Springer*, fourteenth edition, 2009.

[8] Barnes, H. A., Hutton, J. F., Walters, K., "An Introduction to Rheology", *Elsevier*, 1989.

[9] Barone, M. F., Lele, S. K., "A numerical technique for trailing edge acoustic scattering problems", *Proceedings of the 40th AIAA Aerospace Sciences Meeting including the New Horizons Forum and Aerospace Exposition, January 14-17, Reno, Nevada, USA*, No. AIAA-2002-0226, 2002.

[10] Batchelor, G. K., "An Introduction to Fluid Dynamics", *Cambridge University Press*, 1967.

[11] Blandamer, M. J., "Newton-Laplace Equation", *University of Leicester*, downloaded from `http://www.le.ac.uk/chemistry/thermodynamics/pdfs/3000/Topic2540.pdf` on October 21st, 2013.

[12] Bell, J. B., Markus, D. L., "A Second-Order Projection Method for Variable-Density Flows", *Journal of Computational Physics*, Vol. 101, pp. 334-348, 1992.

[13] Bijl, H., Wesseling, P., "A unified method for computing incompressible and compressible flows in boundary-fitted coordinates", *Journal of Computational Physics*, Vol. 141, No. 2, pp. 153-173, 1998.

[14] Björk, Å., "Numerical Methods for Least Squares Problems", *Society for Industrial and Applied Mathematics (SIAM)*, 1996.

[15] Blacha, T., "Effiziente Rußmodellierung in laminaren und turbulenten Flammen unterschiedlicher Brennstoffe" (Efficient soot modeling in laminar and turbulent flames of different fuels), *Institute of Combustion Technology of Aerospace Engineering, University of Stuttgart*, Ph.D. thesis, 2012. In German.

[16] Bogey, C., Bailly, C., Juve, D., "Computation of flow noise using source terms in linearized Euler's equation", *AIAA Journal*, Vol. 40, pp. 235-243, 2002.

[17] Boussinesq, J., "Essai sur la théorie des eaux courantes" (Essay on the theory of water flows), *Mémoires présentés par divers savants à l'Académie des Sciences*, Vol. 23, Series 3, No. 1, pp. 1-680, 1877. In French.

[18] Brigham, E. O., "Fast Fourier Transform and Its Applications", *Prentice Hall*, first edition, 1988.

[19] Burcat, A., "Thermochemical Data for Combustion Calculations", *Combustion Chemistry, ed. W. C. Gardiner*, Springer, 1984.

[20] Burcat, A., McBride, B. J., "1994 ideal gas thermodynamic data for combustion and air-pollution use", *Faculty of Aerospace Engineering, Israel Institute of Technology,* TAE report, 1993.

[21] Cala, C. E., Fernandez, E. C., Heitor, M. V., Shtork, S. I., "Coherent Structures in Unsteady Swirling Jet Flows", *Experiments in Fluids*, Vol. 40, No. 2, pp. 267-276, 2006.

[22] Campa, G., Camporeale, S. M., "A Novel FEM Method for Predicting Thermoacoustic Combustion Instability", *Proceedings of the COMSOL Conference, Milan, Italy*, 2009.

[23] Candel, S., "Combustion dynamics and control: Progress and challenges", *Proceedings of the Combustion Institute*, Vol. 29, Issue 1, pp. 1-28, 2002.

[24] Chorin, A. J., "A Numerical Method for Solving Incompressible Viscous Flow Problems", *Journal of Computational Physics*, Vol. 2, pp. 12-26, 1967.

[25] Chorin, A. J., "Numerical Solution of the Navier-Stokes Equations", *Mathematics of Computation*, Vol. 22, pp. 745-762, 1968.

[26] Chorin, A. J., Marsden, J. E., "A Mathematical Introduction to Fluid Mechanics", *Springer*, third edition, 1993.

[27] Clausius, R., "Über die bewegende Kraft der Wärme" (On the Moving Force of Heat, and the Laws regarding the Nature of Heat itself which are deducible therefrom), *Annalen der Physik*, Vol. 79, pp. 368-397 and 500-524, 1850.

[28] Colella, P., "A Projection Method for Low Speed Flows", *Journal of Computational Physics*, Vol. 149, pp. 245-269, 1999.

[29] Colonius T., Lele, S. K., Moin, P., "Sound generation in a mixing layer", *Journal of Fluid Mechanics*, Vol. 330, pp. 375-409, 1997.

[30] Colonius, T., Lele, S. K., "Computational aeroacoustics: progress on nonlinear problems of sound generation", *Progress in Aerospace Sciences*, Vol. 40, pp. 345-416, 2004.

[31] Coré, X., Angot, P., Latché, J.-C., "A multilevel local mesh refinement projection method for low Mach number flows ", *Mathematics and Computers in Simulation*, Vol. 61, Issues 3-6, pp. 477-488, 2003.

[32] Courant, R., Friedrichs, K., Lewy, H., "Über die partiellen Differenzengleichungen der mathematischen Physik" (On the partial difference equations of mathematical physics), *Mathematische Annalen*, Vol. 100, No. 1, pp. 32-74, 1928. In German.

[33] Crighton, D. G., Dowling, A. P., Ffowcs Williams, J. E., Heckl, M., Leppington, F. G., "Thermoacoustics and Instabilities", *Modern methods in analytical acoustics, Springer*, Lecture Notes, pp. 378-405, 1992.

[34] Crocco, L., "Eine neue Stromfunktion für die Erforschung der Bewegung der Gase mit Rotation" (A novel stream function for the research of gas motion with rotation), *Zeitschrift für Angewandte Mathematik und Mechanik (ZAMM)*, Vol. 17, No. 1, pp. 1-7, 1937. In German.

[35] Demirdžić, I., Lilek, Ž., Perić, Ž., "A collocated finite volume method for predicting flows at all speeds", *International Journal for Numerical Methods in Fluids*, Vol. 16, pp. 1029-1050, 1993.

[36] Di Domenico, M., "Numerical Simulation of Soot Formation in Turbulent Flows", *Institute of Combustion Technology for Aerospace Engineering, University of Stuttgart*, Ph.D. thesis, 2008.

[37] Di Domenico, M., Gerlinger, P., Noll, B., "Numerical Simulations of Confined, Turbulent, Lean, Premixed Flames using a Detailed Chemistry Combustion Model", *Proceedings of the ASME Turbo Expo, June 6-10, Vancouver, British Columbia, Canada*, No. GT2011-45520, 2011.

[38] Dowling, A. P., "Acoustics of unstable flows", *Theoretical and Applied Mechanics, edited by T. Tatsumi, E. Watanabe and T. Kambe, Elsevier*, pp. 171-186, 1996.

[39] Durbin, P. A., Petterson-Reif, B. A., "Statistical theory and modeling for turbulent flows", *John Wiley and Sons*, 2001.

[40] Durst, F., "Grundlagen der Strömungsmechanik (Fundamentals of Fluid Mechanics)", *Springer*, 2006. In German.

[41] Dutt, P., "Stable boundary conditions and difference schemes for Navier Stokes equations", *Journal on Numerical Analysis*, Vol. 25, pp. 245-267, 1988.

[42] E, W., Liu, J. G., "Gauge method for viscous incompressible flows", *Communications in Mathematical Sciences*, Vol. 1, No. 2, pp. 317-332, 2003.

[43] Ebin, D. G., "The motion of slightly compressible fluids viewed as a motion with strong constraining force", *Annals of Mathematics*, Second Series, Vol. 105, No. 1, pp. 141-200, 1977.

[44] Ebin, D. G., "Motion of slightly compressible fluids in a bounded domain", *Communications on Pure and Applied Mathematics*, Vol. 35, Issue 4, pp. 451-485, 1982.

[45] Egorov, Y., Menter, F. R., "Development and application of SST-SAS turbulence model in the DESIDER project", *Advances in hybrid RANS-LES modelling. Notes on numerical fluid mechanics and multidisciplinary design, Springer*, Vol. 97, pp. 261-270, 2008.

[46] Ehrenfried, K., "Skript zur Vorlesung Strömungsakustik I" (Lecture notes on aeroacoustics), *Berlin University of Technology*, 2003. In German.

[47] Eidelman, S., Colella, P., Shreeve, R. P., "Application of the Godunov method and its second-order extension to cascade flow modelling", *AIAA Journal*, Vol. 22, No. 11, pp. 1609-1615, 1984.

[48] Engquist, B., Majda, A., "Absorbing Boundary Conditions for the Numerical Simulation of Waves", *Mathematics of Computation*, Vol. 31, No. 139, pp. 629-651, 1977.

[49] ERCOFTAC, "Special Interest Group on Quality and Trust in Industrial CFD: Best Practice Guidelines", *ed.: Michael Casey, Torsten Wintergerste*, 2000.

[50] Esch, T., Menter, F. R., "Heat Transfer Prediction Based on Two-Equation Turbulence Models with Advanced Wall Treatment", *Proceedings of the Turbulence Heat and Mass Transfer, ed. Hanjalic, Nagano and Tummers, Antalya, Turkey*, 2003.

[51] Ewert, R., Meinke, M., Schröder, W., "Comparison of source term formulations for a hybrid CFD/CAA method", *Proceedings of the 7th AIAA/CEAS Aeroacoustics Conference and Exhibit, May 28-30, Maastricht, Netherlands*, No. AIAA-2001-2200, 2001.

[52] Eymard, R., Gallouët, T., Herbin, R., Latché, J.-C., "A convergent Finite Element-Finite Volume scheme for the compressible Stokes problem, Part II - the isentropic case", *Mathematics of Computation*, Vol. 79, pp. 649-675, 2009.

[53] Fernandez, E. C., Heitor, M. V., Shtork, S. I., "An Analysis of Unsteady Highly Turbulent Swirling Flow in a Model Vortex Combustor", *Experiments in Fluids*, Vol. 40, pp. 177-187, 2006.

[54] Ferziger, J., Perić, Ž., "Computational Methods for Fluid Dynamics, third revised version", *Springer*, 2002.

[55] Ffowcs Williams, J. E., Hawkings, D. L., "Sound generation by turbulence and surfaces in arbitrary motion", *Proceedings of the Royal Society London A*, Vol. 264, pp. 321-342, 1969.

[56] Fick, A., "Über Diffusion (On Diffusion)", *Annalen der Physik und Chemie von J. C. Pogendorff*, Vol. 94, pp. 59-86, 1855. In German.

[57] Flemming, F., Sadiki, A., Janicka, J., "Investigation of combustion noise using a LES/CAA hybrid approach", *Proceedings of the Combustion Institute*, Vol. 31, Issue 2, pp. 3189-3196, 2007.

[58] Föller, S., Polifke W., "Determination of Acoustic Transfer Matrices via Large Eddy Simulation and System Identification", *Proceedings of the 16th AIAA/CEAS Aeroacoustic Conference, June 7-9, Stockholm, Sweden*, No. AIAA 2010-3998, 2010.

[59] Fortenbach, R., "Mehrskalenmodellierung von aeroakustischen Quellen in schwach kompressibler Strömungen" (Multiscale modeling of aeroacoustic sources in low Mach number flows), *Institute of Aerodynamics and Gasdynamics, University of Stuttgart*, Ph.D. thesis, 2006. In German.

[60] Fourier, J. B. J., "Théorie analytique de la chaleur" (Analytic theory of heat), *Firmin Didot*, 1822. In French.

[61] Freund, J. B., Lele, S. K., Moin, P., "Direct numerical simulation of a Mach 1.92 turbulent jet and its soundfield", *AIAA Journal*, Vol. 38, Issue 11, pp. 2023-2031, 2000.

[62] Freund, J. B., "Noise sources in a low-Reynolds-number turbulent jet at Mach 0.9.", *Journal of Fluid Mechanics*, Vol. 438, pp. 277-305, 2001.

[63] Gallouët, T., Gastaldo, L., Latché, J.-C., Herbin, R., "An unconditionnally stable pressure correction scheme for compressible barotropic Navier-Stokes equations", *ESAIM: Mathematical Modelling and Numerical Analysis*, Vol. 42, pp. 303-331, 2008.

[64] Gallouët, T., Herbin, R., Latché, J.-C., "A convergent Finite Element-Finite Volume scheme for the compressible Stokes problem Part I - the isothermal case", *Mathematics of Computation*, Vol. 78, pp. 1333-1352, 2009.

[65] Geratz, K. J., Klein, R., Munz, C.-D., Roller, S., "Multiple Pressure Variable (MPV) Approach for Low Mach Number Flows Based on Asymptotic Analysis", *Flow Simulations with High-Performance Computers II, ed. E. H. Hirschel, Vieweg,* pp. 340-354, 1996.

[66] Gerlinger, P., "Numerische Verbrennungssimulation, Effiziente numerische Simulation turbulenter Verbrennung" (Numerical combustion simulation, efficient numerical simulation of turbulent combustion), *Springer*, 2005. In German.

[67] Giezendanner-Thoben, R., "Untersuchung von Verbrennungsinstabilitäten mit phasenkorrelierten Lasermesstechniken" (Investigation of combustion instabilities with phase-correlated laser measurement techniques), *Institute of Combustion Technology for Aerospace Engineering, University of Stuttgart*, Ph.D. thesis, 2006. In German.

[68] Goda, K., "A multistep technique with implicit difference schemes for calculating two- or three-dimensional cavity flows", *Journal of Computational Physics*, Vol. 30, pp. 76-95, 1979.

[69] Gordon, S., McBride, J., "A Fortran Computer Program for Calculation of Complex Chemical Equilibrium Compositions, Rocket Performance, Incident and Reflected Shocks and Chapman-Jouget Detonations", *NASA SP-273*, 1971.

[70] Gran, I. R., Magnussen, B. F., "A Numerical Study of a Bluff-Body Stabilized Diffusion Flame. Part 2. Influence of Combustion Modeling and Finite-Rate Chemistry. *Combustion Science and Technology*, Vol.119, pp. 191-217, 1996.

[71] Groth, C. P. T., Zingg, D. W., "Computational Fluid Dynamics", *Proceedings of the Third International Conference on Computational Fluid Dynamics, ICCFD3, July 12-16, 2004, Toronto, Canada*, 2006.

[72] Grupta, A., Lewis, M., Qi, S., "Effect of swirl on combustion characteristics in premixed flames", *Journal of Engineering for Gas Turbines and Power*, Vol. 120, Issue 3, pp 488-494, 1998.

[73] Guermond, J.-L., "Un résultat de convergence d'ordre deux en temps pour l'approximation des équations de Navier–Stokes par une technique de projection incrémentale" (A result of second order convergence in time for the approximation of the Navier-Stokes equations with an incremental projection technique), *ESAIM: Mathematical Modelling and Numerical Analysis January*, Vol. 33, pp. 169-189, 1999. In French.

[74] Guermond, J.-L., Minev, P., "Error analysis of pressure-correction schemes for the Navier-Stokes equations with open boundary conditions", *SIAM Journal on Numerical Analysis*", Vol. 43, pp. 239-258, 2005.

[75] Guermond, J.-L., Minev, P., Shen, J., "An overview of projection methods for incompressible flows", *Computer Methods in Applied Mechanics Engineering*, Vol. 196, pp. 6011-6045, 2006.

[76] Guermond, J.-L., Salgado, A., "A fractional step method based on a pressure Poisson equation for incompressible flows with variable density", *Comptes Rendus de l'Académie des Sciences, Série I - Mathématique*, Vol. 346, pp. 913-918, 2008.

[77] Guermond, J.-L., "Fast techniques for the incompressible variable density Navier-Stokes equations", *Winter school "New trends in scientific computing", February 9-13, Marseille, France*, 2009.

[78] Gui, Y. F., Dou, W. B., "A rigorous and completed statement on Helmholtz theorem", *Progress In Electromagnetics Research*, Vol. 69, pp. 287-304, 2007.

[79] Gunasekaran, B., McGuirk, J. J., "Mildly-Compressible Pressure-Based CFD-Methodology for Acoustic Propagation and Absorption Prediction", *Proceedings of the ASME Turbo Expo, June 6-10, Vancouver, British Columbia, Canada*, No. GT2011-45311, 2011.

[80] Gunasekaran, B., "Development and validation of a pressure based CFD methodology for acoustic wave propagation and damping", *Loughborough University*, Ph.D. Thesis, 2011.

[81] Hackbusch, W., "Multigrid Methods and Applications", *Springer*, 1985.

[82] Hähl, H., "Höhere Mathematik III" (Higher Mathematics III), *University of Stuttgart*, lecture notes, 2007. In German.

[83] Hänel, D., "Mathematische Strömungslehre I + II" (Lecture notes on mathematical fluid mechanics I + II), *RWTH Aachen University*, 2012. In German.

[84] Hardin, J., Pope, D., "A new technique for aerodynamic noise calculation", *Proceedings of the 14th DGLR/AIAA Aeroacoustics Conference, May 11-14, Aachen, Germany*, Vol. 1, pp. 448-456, 1992.

[85] Hardin, J., Pope, D., "An acoustic/viscous splitting technique for computational aeroacoustics", *Theoretical and Computational Fluid Dynamics*, Vol. 6, pp 323-340, 1994.

[86] Harlow, F. H., Welch, J. E., "Numerical calculation of time-dependent viscous incompressible flow of fluid with a free surface", *The Pysics of Fluids*, Vol. 8, Number 12, pp. 2182-2189, 1965.

[87] Harlow, F. H., Amsden, A. A., "Numerical calculation of almost incompressible flow", *Journal of Computational Physics*, Vol. 3, Issue 1, pp. 80-93, 1968.

[88] Hasse, H., "Technische Thermodynamik I + II" (Technical Thermodynamics I + II), *University of Stuttgart*, lecture notes, 2007. In German.

[89] Helmholtz, H., "Über Integrale der hydrodynamischen Gleichungen, welcher der Wirbelbewegungen entsprechen" (On integrals of the hydrodynamic equations which correspond to vortex motions), *Journal für die reine und angewandte Mathematik, 55: 25-55*, Vol. 55, pp. 25-55, 1858. In German.

[90] Hirsch, C., "Numerical computation of internal and external flows: The fundamentals of computational fluid dynamics", *Butterworth-Heinemann*, second edition, 2007.

[91] Huber, A., "Impact of fuel supply impedance and fuel staging on gas turbine combustion stability", *Institute of Thermodynamics, Technical University of Munich*, Ph.D. thesis, 2009.

[92] Iserles, A., "A First Course in the Numerical Analysis of Differential Equations", *Cambridge Texts in Applied Mathematics*, second edition, 1996.

[93] Issa, R. I., Gosman, A. D., Watkins, A. P., "The computation of compressible and incompressible recirculating flows by a non-iterative implicit scheme", *Journal of Computational Physics*, Vol. 62, pp. 66-82, 1985.

[94] Issa, R. I., "Solution of the Implicitly Discretized Fluid Flow Equation by Operator Splitting", *Journal of Computational Physics*, Vol. 62, pp. 40-65, 1986.

[95] Ivanova, E., Noll, B., Griebel, P., Aigner, M., Syed, K., "Numerical simulations of turbulent mixing and autoignition of hydrogen fuel at reheat combustor operating conditions" *Journal of Engineering for Gas Turbines and Power*, Vol. 134, No. 4, 2012.

[96] Ivanova, E., "Numerical Simulations of Turbulent Mixing in Complex Flows" *Institute of Combustion Technology for Aerospace Engineering, University of Stuttgart*, Ph.D. thesis, 2012.

[97] Jain, P. K., Khalil, A., "Functional analysis", *New Age International*, second edition, 1995.

[98] Jones, W. P., Launder, B. E., "The prediction of laminarization with a two-equation model of turbulence", *International Journal of Heat and Mass Transfer*, Vol. 15, Issue 2, pp. 301-314, 1972.

[99] Joos, F., "Technische Verbrennung" (Combustion technology), *Springer*, 2006. In German.

[100] Juvé, D., Bailly, C., Bogey, C., Gloerfelt, X., Pérot, F., "Two Topics in Computational Aeroacoustics: some comments on hybrid methods and CAA as a tool to understand the mechanisms of sound generation" *Presentation held at the DFG-CNRS Seminar, September 6-7, Orléans*, 2004.

[101] Katz, V., "The history of Stokes's theorem", *Mathematics Magazine, Mathematical Association of America*, Vol. 52, pp. 146-156, 1979.

[102] Kee, R. J., Rupley, F. M., Miller, J. A., "The Chemkin Thermodynamic Data Base", *SAND87-8215*, 1987.

[103] Keller, J. O., Givoli, D., "Exact non-reflecting boundary conditions", *Journal of Computational Physics*, Vol. 82, pp. 172-192, 1989.

[104] Keller, J., "Thermoacoustic oscillations in combustion chambers of gas turbines". *AIAA Journal*, Vol. 13, Issue 12, pp. 2280-2287, 1995.

[105] Khalighi, Y., Mani, A., Ham, F., Moin, P., "Prediction of Sound Generated by Complex Flows at Low Mach Numbers", *AIAA Journal*, Vol. 48, pp. 306-316, 2010.

[106] Khalil, M., Wesseling, P., "Vertex-centered and cell-centered multigrid for interface problems", *Journal of Computational Physics*, Vol. 98, No. 1, pp. 1-10, 1992.

[107] Khosla, P. K., Rubin, S. G., "A diagonally dominant second-order accurate implicit scheme", *Computers and Fluids*, Vol. 2, No. 2, pp. 207-209, 1974.

[108] Kim, J., Moin, P., "Application of a fractional-step method to incompressible Navier–Stokes equations", *Journal of Computational Physics*, Vol. 59, Issue 2, pp. 308-323, 1985.

[109] Kimmerle, W., Stroppel, M., "Lineare Algebra" (Linear Algebra), *University of Stuttgart*, lecture notes, 2006. In German.

[110] Kimmerle, W., Stroppel, M., "Analysis" (Analysis), *University of Stuttgart*, lecture notes, 2006. In German.

[111] Kinsler, L. E., Frey, A., "Fundamentals of Acoustics", *John Wiley & Sons, Inc., New York, London, Sydney*, Second Edition, p. 193, 1964.

[112] Klainerman, S., Majda, A., "Singular limits of quasilinear hyperbolic systems with large parameters and the incompressible Limit of Compressible Fluids", *Communications on Pure and Applied Mathematics*, Vol. 34, pp. 481-524, 1981.

[113] Klainerman, S., Majda, A., "Compressible and incompressible fuids", *Communications on Pure and Applied Mathematics*, Vol. 35, pp. 629-653, 1982.

[114] Klein, R., Munz, C.-D., "The Multiple Pressure Variable (MPV) Approach for the Numerical Approximation of Weakly Compressible Fluid Flow", *Proceedings of Numerical Modelling in Continuum Mechanics, ed. M. Feistauer, R. Rannacher and K. Kozel*, pp. 123-133, 1994.

[115] Klein, R., Lange, K., Willems, W., Munz, C.-D., "Semi-Implicit High Resolution Schemes for Low Mach Number Flows", *Proceedings of the Fifth International Conference on Hyperbolic Problems, Theory, Numerics and Applications*, 1994.

[116] Klein, R., "Semi-implicit extension of a Godunov-type scheme based on low Mach number asymptotics I: One dimensional flow", *Journal of Computational Physics*, Vol. 121, pp. 213-237, 1995.

[117] Klewer, C., "Numerische Berechnung von Verbrennungslärm und thermoakustischen Instabilitäten" (Numerical simulation of combustion noise and thermo-acoustic instabilites), *Institute of Combustion Technology for Aerospace Engineering, Technical University of Darmstadt*, Ph.D. thesis, 2011. In German.

[118] Kostrzewa, K., "Advanced computational methods in identification of thermo-acoustic systems", *Institute of Combustion Technology for Aerospace Engineering, University of Stuttgart*, Ph.D. thesis, 2011.

[119] Krämer, E., "Theoretische Untersuchungen der stationären Rotorblattumströmung mit Hilfe eines Euler-Verfahrens" (Theoretical Investigations of the Stationary Flow of a Rotor Blade using an Euler Method), *Institute of Aerodynamics and Gasdynamics, University of Stuttgart*, Ph.D. thesis, 1991. In German.

[120] Krediet, H. J., "Prediction of limit cycle pressure oscillations in gas turbine combustion systems using the flame describing function", *University of Twente*, Ph.D. thesis, 2012.

[121] Kreiss, H.-O., "Initial boundary value problems for hyperbolic systems", *Communications on Pure and Applied Mathematics*, Vol. 23, pp. 277-298, 1970.

[122] Lambert, M., "THETA-Code Developer's Guide", *Institute of Aerodynamics and Flow Technology, German Aerospace Center (DLR)*, Release 8.2, 2011.

[123] Landau, L. D., Lifschitz, E. M., "Lehrbuch der theoretischen Physik VI - Hydrodynamik" (Textbook of theoretical physics VI - hydrodynamics), *Akademie-Verlag*, fifth edition, 1991.

[124] Laplace, P.-S., "Sur la vitesse du son dans l'air et dans l'eau" (On the speed of sound in air and water), *Annales de chimie et de physique*, Vol. 3, pp. 238-241, 1816. In French.

[125] Launder, B. E., Sharma, B. I., "Application of the energy-dissipation model of turbulence to the calculation of flow near a spinning disc", *Letters in Heat and Mass Transfer*, Vol. 1, pp. 131-138, 1974.

[126] Lefebvre, A., H., Ballal, D. R., "Gas Turbine Combustion: Alternative Fuels and Emissions", *Tailor and Francis*, third edition, 2010.

[127] Liang, H., Maxworthy, T., "An Experimental Investigation of Swirling Jets", *Journal of Fluid Mechanics*, Vol. 525, pp. 115-159, 2005.

[128] Lieuwen, T., C., Torres, H., Johnson, C., Zinn, B. T., "A Mechanism of Combustion Instability in Lean Premixed Gas Turbine Combustors", *Journal of Engineering for Gas Turbines and Power*, 2012. Vol. 123, No. 1, pp. 182-189, 2001.

[129] Lieuwen, T., C., Yang, V., "Combustion Instabilities in Gas Turbine Engines: Operational Experience, Fundamental Mechanisms, and Modeling", *Progress in astronautics and aeronautics, ed. Frank K. Lu, American Institute of Aeronautics and Astronautics, Inc.*, Vol. 210, 2005.

[130] Lieuwen, T., C., "Unsteady Combustor Physics", *Cambridge University Press*, 2012.

[131] Lieuwen, T., C., Yang, V., "Gas Turbine Emissions", *Cambridge University Press*, 2013.

[132] Lighthill, M. J., "On sound generated aerodynamically: I. General theory". *Proceedings of the Royal Society London A*, Vol. 211, No. 1107, pp. 564-587, 1952.

[133] Lighthill, M. J., "On sound generated aerodynamically: II. Turbulence as a source of sound". *Proceedings of the Royal Society London A*, Vol. 222, No. 1148, pp. 1-32, 1954.

[134] Lincke, A., "Verification and Validation of von Karman Length Scale for Identification of Turbulent Structures", *Institute for Numerical and Applied Mathematics, University of Göttingen*, Diploma Thesis, 2010.

[135] Lourier, J.-M., Reichling, G., Stöhr, M., Di Domenico, M., Noll, B., Aigner, M., "Numerical Analysis of Probe Microphones Used for Thermoacoustic Measurements", *Proceedings of the 50th AIAA Aerospace Sciences Meeting including the New Horizons Forum and Aerospace Exposition, January 9-12, Nashville, Tennessee, USA*, No. AIAA 2012-0545, 2012.

[136] Lourier, J.-M., Di Domenico, M., Noll, B., Aigner, M., "Implementation of an Efficient Pressure-Based CFD Solver for Accurate Thermoacoustic Computations", *Proceedings of the 18th AIAA/CEAS Aeroacoustics Conference, June 4-6, Colorado Springs, Colorado, USA*, No. AIAA 2012-2089, 2012.

[137] Ludwig, C., "Diffusion zwischen ungleich erwärmten Orten gleich zusammengesetzter Lösungen" (Diffusion between two different locations of a solution with the same composition), *Kaiserliche Akademie der Wissenschaften in Wien, Wilhelm Braumüller*, Vol. 65, pp. 539, 1856. In German.

[138] Lui C., Lele, S. K., "A numerical study of broadband shock noise", *Proceedings of the 8th AIAA/CEAS Aeroacoustics Conference and Exhibit, June 17-19, Breckenridge, Colorado, USA*, No. AIAA-2002-2530, 2002.

[139] Lui C., Lele, S. K., "Sound generation mechanism of shock associated noise", *Proceedings of the 9th AIAA/CEAS Aeroacoustics Conference and Exhibit, May 12-14, Hilton Head Island, South California, USA*, No. AIAA-2003-3315, 2003.

[140] Lunev, W. W., "Real Gas Flows with High Velocities", *CRC Press*, first edition, 2009.

[141] Magnussen, B. F., Hjertager, B. H., "On Mathematical Modelling of Turbulent Combustion with Special Emphasis on Soot Formation and combustion", *16th Symposium (International) on Combustion*, Vol. 16, Issue 1, Pages 719-729 1977.

[142] Manning, T. A., "A Numerical investigation of sound generation in supersonic jet screech", *Stanford University*, Ph.D. thesis, 2000.

[143] Marble, F. E., Candel, S. M., "Acoustic disturbance from gas non-uniformities convected through a nozzle", *Journal of Sound and Vibration*, Vol. 55, No. 2, pp. 225-243, 1977.

[144] McBride, B. J., Gordon, S., Reno, M. A., "Coefficients for Calculating Thermodynamic and Transport Properties of Individual Species", *Faculty of Aerospace Engineering, Israel Institute of Technology,* NASA Report TM-4513, 1993.

[145] Meier, W., Keck, O., "Laser-Raman-Messungen an verdrallten Erdgas/Luft-Flammen" (Laser-Raman-Measurements on swirled mathane/oxygen flames), *Gaswärme International (GWI)*, Vol. 51, pp. 232-237, 2002. In German.

[146] Meier, W., Boxx, I., Stöhr, M., Carter, C. D., "Laser-based investigations in gas turbine model combustors", *Experiments of Fluids*, Vol. 49, pp. 865-882, 2010.

[147] Meister, A., "Numerik linearer Gleichungssysteme: Eine Einführung in moderne Verfahren" (Numerics of systems of linear equations: An introduction into modern methods), *Vieweg und Teubner*, fourth edition, 2011. In German.

[148] Meister, A., "Workshop on numerics of systems of linear equations", *High Performance Computing Center Stuttgart, March 12-16, Stuttgart, Germany.*

[149] Menter, F. R., "Two-Equation Eddy-Viscosity Turbulence Models for Engineering Applications", *AIAA Journal*, Vol. 32, No. 8, pp. 1598-1605, 1994.

[150] Menter, F. R., Kuntz, M., Langtry, R., "Ten Years of Industrial Experience with the SST Turbulence Model", *Turbulence, Heat and Mass Transfer 4, ed: K. Hanjalic, Y. Nagano, and M. Tummers, Begell House, Inc.*, pp. 625-632, 2003.

[151] Menter, F. R., Egorov, Y., "Re-visiting the turbulent scale equation. *IUTAM symposium on one hundred years of boundary layer research. Solid mechanics and its applications*, Vol. 129, pp. 279-290, 2006.

[152] Menter, F. R., Egorov, Y., "A scale-adaptive simulation model using two-equation models", *Proceedings of the 43rd AIAA Aerospace Sciences Meeting and Exhibit, January 10-13, 2006, Reno, Nevada, USA*, Vol. 13, 2006.

[153] Menter, F. R., Egorov, Y., "SAS Turbulence Modelling of Technical Flows", *Direct and Large-Eddy Simulation V*, Part XV, pp. 687-694, 2006.

[154] Menter, F. R., "Review of the shear-stress transport turbulence model experience from an industrial perspective", *International Journal of Computational Fluid Dynamic*, Vol. 23, Issue 4, pp. 305-316, 2009.

[155] Menter, F. R., Egorov, Y., "The Scale-Adaptive Simulation Method for Unsteady Turbulent Flow Predictions. Part 1: Theory and Model Description", *Flow Turbulence and Combustion*, Vol. 85, No. 1, pp. 113-138, 2010.

[156] Midgley, K., Spencer, A., McGuirk, J. J., "Unsteady Flow Structures in Radial Swirler Fed Fuel Injectors", *Journal of Engineering for Gas Turbines and Power*, Vol. 127, Issue 4, pp. 755-764, 2005.

[157] Mitchell, B. E., Lele, S. K., Moin, P., "Direct computation of the sound from a compressible co-rotating vortex pair", *Journal of Fluid Mechanics*, Vol. 285, pp. 181-202, 1995.

[158] Moretti, G., "A physical approach to the numerical treatment of boundaries in gas dynamics" *NASA Conference Publication 2201, October 19-24, Ames Research Center, NASA, Moffet Field, California, USA*, No. N81-33861, pp. 73-95, 1981.

[159] Morfey, C. L., "Amplification of aerodynamic noise by convected flow inhomogeneities", *Journal of Sound and Vibration*, Vol. 31, No. 4, pp. 391-397, 1973.

[160] Moukalled, F., Darwish M., "A High-Resolution Pressure-Based Algorithm for Fluid Flow at All Speeds", *Journal of Computational Physics*, Vol. 168, pp. 101-133, 2001.

[161] Moureau, V., Bérat, C., Pitsch, H., "An efficient semi-implicit compressible solver for large-eddy simulations", *Journal of Computational Physics*, Vol. 226, pp. 1256-1270, 2007.

[162] Mühlbauer, B., "Numerische Simulation von Verbrennungslärm" (Numerical simulation of combustion noise), *Institute of Combustion Technology for Aerospace Engineering, University of Stuttgart*, Ph.D. thesis, 2012. In German.

[163] Munz, C.-D., Roller, S., Sonnendrücker, E., "A Numerical Approach to Multiple Scale Problems Based on Asymptotic Analysis", *Proceedings of the 13th GAMM-Seminar, January 24-26, Kiel, Germany*, 1997.

[164] Munz, C.-D., Roller, S., Klein, R., Geratz, K. J., "The extension of incompressible flow solvers to the weakly compressible regime", *Computers & Fluids*, Vol. 32, Issue 2, pp. 173-196, 2003.

[165] Muzaferija, S., "Adaptive finite volume method for flow prediction using unstructured meshes and multigrid approach", *Imperial College*, Ph.D. thesis, 1994.

[166] Nerinckx, K., Vierendeels, J., Dick, E., "Mach-uniformity through the coupled pressure and temperature correction algorithm", *Journal of Computational Physics*, Vol. 206, pp. 597-623, 2005.

[167] Nerinckx, K., Vierendeels, J., Dick, E., "A Mach-uniform algorithm: Coupled versus segregated approach", *Journal of Computational Physics*, Vol. 224, pp. 314-331, 2007.

[168] Newton, I., "Philosophiae Naturalis Principia Mathematica" (Mathematical Principles of Natural Philosophy), Vol. II, Section VII, 1687. In Latin.

[169] Newton, I., "Methodus fluxionum et serierum infinitorum" (The method of fluxions and infinite series), written within 1664-1671, published in 1736. In Latin.

[170] Ni, M.-J., Komori, S., "General Second-Order Projection Formulas for Unsteady Flows", *AIAA Journal*, Vol. 40, Issue 7, pp. 1464-1467, 2002.

[171] Nicol, D. G., Malte, P. C., Hamer, A. J., Roby, R. J., Steele, R. C., "Development of a Five-Step Global Methane Oxidation-NO Formation Mechanism for Lean-Premixed Gas Turbine Combustion", *Journal of Engineering for Gas Turbines and Power*, Vol. 121, Issue 2, pp. 272-280, 1999.

[172] Noll, B., "Numerische Strömungsmechanik" (Numerical fluid mechanics), *Springer*, 1993. In German.

[173] Oberkampf, W. L., Trucano, T. G., "Verification and validation in computational fluid dynamics", *Progress in Aerospace Sciences*, Vol. 38, pp. 209-272, 2002.

[174] Oberkampf, W. L., "Verification and Validation in Computational Simulation", *Transport Task Force Meeting, April 29th, Salt Lake City, Utah, USA*, 2004.

[175] Oliger, J., Sundström, A., "Theoretical and practical aspects of some initial boundary value problems in fluid dynamics", *SIAM Journal on Applied Mathematics*, Vol. 35, pp. 419-446, 1978.

[176] Oppenheim, A. V., Schafer, R. W., "Zeitdiskrete Signalverarbeitung" (Time-Discrete Signal Processing), *Oldenbourg Wissenschaftsverlag*, third edition, 1999.

[177] Park, J.-H., "Ein konservatives MPV-Verfahren zur Simulation der Strömungen in allen Machzahlbereichen" (A conservative MPV-scheme for the simulation of all Mach number flows), *Institute of Aerodynamics and Gasdynamics, University of Stuttgart*, Ph.D. thesis, 2003. In German.

[178] Park, J.-H., Munz, C.-D., "Multiple pressure variables methods for fluid flow at all Mach numbers", *International Journal for Numerical Methoths in Fluids*, Vol. 49, pp. 905-931, 2005.

[179] Paschereit, C. O., Polifke, W., "Investigation of the Thermo-Acoustic Characteristics of a Lean Premixed Gas Turbine Burner", *International Gas Turbine and Aeroengine Congress & Exposition, Stockholm, Sweden*, No. ASME 98-GT-582, 1998.

[180] Paschereit, C. O., Gutmark, E., Weisenstein, W., "Coherent structures in swirling flows and their role in acoustic combustion control", *Physics of Fluids*, Vol. 11, Issue 9, pp. 2667-2678, 1999.

[181] Patankar, S. V., Spalding, D. B., " A calculation procedure for heat, mass, and momentum transfer in three-dimensional parabolic flow", *International Journal of Heat and Mass Transfer*, Vol. 15, Issue 1, pp. 787-806, 1972. Patankar SV, Spalding DB..

[182] Patankar, S. V., "Numerical heat transfer and fluid flow", *Hemisphere Publishing Corporation*, 1980.

[183] Patankar, S. V., "A Calculation Procedure for Two-Dimensional Elliptic Situations", *Numerical Heat Transfer*, Vol. 4, pp. 409-425, 1981.

[184] Patankar, S. V., Karki, K. C., "Pressure Based Calculation Procedure for Viscous Flows at All Speeds in Arbitrary Configurations", *AIAA Journal*, Vol. 27, pp. 1167-1174, 1989.

[185] Pember, R. B., Howell, L. H., Bell, J. B., Colella, P., Crutchfield, W. Y., Fiveland, W. A., Jessee, J. P., "An Adaptive Projection Method for Unsteady, Low-Mach Number Combustion", *Combustion Science and Technology*, Vol. 140, pp. 123-168, 1998.

[186] Peracchio, A. A., Proscia, W. M., "Nonlinear Heat-Release/Acoustic Model for Thermoacoustic Instability in Lean Premixed Combustors", *Journal of Engineering for Gas Turbines and Power*, Vol. 121, Issue 3, pp. 415-421, 1999.

[187] Pierce, C. D., Moin, P., "Progress-Variable Approach for Large-Eddy Simulation of Turbulent Combustion", *Stanford University*, Ph.D. thesis, 2001.

[188] Phan-Thien, N., "Understanding Viscoelasticity, an Introduction to Rheology", *Springer*, 2013.

[189] Poinsot, T., Lele, S., "Boundary Conditions for Direct Simulations of Compressible Viscous Flows", *Journal of Computational Physics*, Vol. 101, pp. 104-129, 1992.

[190] Poinsot, T., Veynante, D., "Theoretical and Numerical Combustion", *RT Edwards, Inc.*, 2005.

[191] Pope, S. B., "PDF Methods for Turbulent Reactive Flows", *Progress in Energy and Combustion Science*, Vol. 11, pp. 119-192, 1985.

[192] Pope, S. B., "Ten questions concerning the large-eddy simulation of turbulent flows", *New Journal of Physics*, Vol. 6, No. 35, 2004.

[193] Powers, J. M., "Lecture Notes on Fundamentals of Combustion", *Department of Aerospace and Mechanical Engineering, University of Notre Dame, Indiana, USA*, 2012.

[194] Powers, J. M., "Lecture Notes on Thermodynamics", *Department of Aerospace and Mechanical Engineering, University of Notre Dame, Indiana, USA*, 2012.

[195] Pozarlik, A., "Vibro-acoustical instabilities induced by combustion dynamics in gas turbine combustors", *University of Twente*, Ph.D. thesis, 2010.

[196] Ran H., Colonius T., "Numerical simulation of the sound radiated from a turbulent vortex ring", *International Journal of Aeroacoustics*, Vol. 8, Number 4, pp. 317-336, 2009.

[197] Rannacher, R., "On Chorin's projection method for the incompressible navier-stokes equations", *Lecture Notes in Mathematics*, Vol. 1530, pp. 167-183, 1690.

[198] Rao, C. R., Toutenburg, H., Fieger, A., Heumann, C., Nittner, T., Scheid, S., "Linear Models: Least Squares and Alternatives", *Springer Series in Statistics*, 1999.

[199] Raphson, J., "Analysis aequationum universalis" (Universal analysis of equations), 1690. In Latin.

[200] Rauwoens, P., Vierendeels J., Dick E., Merci B., "A conservative discrete compatibility-constraint low-Mach pressure-correction algorithm for time-accurate simulations of variable density flows", *Journal of Computational Physics*, Vol. 228, pp. 4714-4744, 2009.

[201] Rebosio, F., Widenhorn, A., Noll, B., Aigner, M., "Numerical simulation of a gas turbine model combustor operated near the lean extinction limit", *Proceedings of the ASME Turbo Expo, June 14-18, Glasgow, Scotland, UK*, No. GT2010-22751, 2010.

[202] Reichling, G., Noll, B., Aigner, M., "Development of a Projection-Based Method for the Numerical Calculation of Compressible Reactive Flows", *Proceedings of the 51st AIAA Aerospace Sciences Meeting including the New Horizons Forum and Aerospace Exposition, January 7-10, Grapevine, Texas, USA*, No. AIAA 2013-1003, 2013.

[203] Reichling, G., Noll, B., Aigner, M., "Numerical Simulation of the Non-Reactive and Reactive Flow in a Swirled Model Gas Turbine Combustor", *Proceedings of the 21st AIAA Computational Fluid Dynamics Conference, June 24-27, San Diego, California, USA*, No. AIAA 2013-2434, 2013.

[204] Rienstra, S. W., Hirschberg, A., "An Introduction to Acoustics", *Eindhoven University of Technology*, revised edition of IWDE 92-06, 2006.

[205] Rohde, A., "Eigenvalues and Eigenvectors of the Euler Equations in General Geometries", *Proceedings of the 15th AIAA Computational Fluid Dynamics Conference, June 11-14, Anaheim, California, USA*, No. AIAA-2001-2609, 2001.

[206] Roller, S., Munz, C.-D., "A low Mach number scheme based on multi-scale asymptotics", *Computational Visual Science*, Vol. 3, pp. 85-91, 2000.

[207] Roller, S., Munz, C.-D., "Calculation of low mach number acoustics: A comparison of MPV, EIF and Linearized Euler Equations", *ESAIM: Mathematical Modelling and Numerical Analysis* , Vol. 39, Issue 3, pp. 561-576, 2005.

[208] Roller, S., "Ein numerisches Verfahren zur Simulation schwach kompressibler Strömungen" (A numerical scheme for the simulation of low Mach number flows), *Institute of Aerodynamics and Gasdynamics, University of Stuttgart*, Ph.D. thesis, 2005. In German.

[209] Roller, S., Fortenbach, R., Schwartzkopff, T., Munz, C.-D., "The numerical modeling of acoustic wave propagation using the multiple pressure variables approach", *Computing and Visualization in Science*, Vol. 9, No. 4, pp. 229-237, 2006.

[210] Rotta, J. C., "Turbulente Strömungen: eine Einführung in die Theorie und ihre Anwendung" (Turbulent flows: An introduction into theory and application) *B. G. Teubner, Stuttgart*, 1972. In German.

[211] Rowley, C. W., Colonius, T., Basu, A. J., "On self-sustained oscillations in two-dimensional compressible flow over rectangular cavities", *Journal of Fluid Mechanics*, Vol. 455, pp. 315-46, 2002.

[212] Rudy, D. H., Strikwerda, J. C., "A non-reflecting outflow boundary condition for subsonic Navier Stokes calculations", *Journal of Computational Physics*, Vol. 36, pp. 55-70, 1980.

[213] Rudy, D. H., Strikwerda, J. C., "Boundary conditions for subsonic compressible Navier Stokes calculations", *Computers & Fluids*, Vol. 9, pp. 327-338, 1981.

[214] Ruprecht, A., "Computational Fluid Dynamics", *Institute of Fluid Mechanics and Hydraulic Machinery, University of Stuttgart*, lecture notes, 2008.

[215] Saad, Y., Schulz, M. H., "GMRES: A generalized minimal residual algorithm for solving nonsymmetric linear system", *SIAM Journal on Scientific and Statistical Computing*, Vol. 7, No. 3, pp. 856-869, 1986.

[216] Saad, Y., "Iterative Methods for Sparse Linear Systems", *Society for Industrial and Applied Mathematics*, second edition, 2003.

[217] Sanna, G. J., Tomassetti, G., "Introduction To Molecular Beams Gas Dynamics", *Imperial College Press*, pp. 106-108, 2005.

[218] Schmidt, D., "Grundlagen technischer Verbrennungsvorgänge III: Simulationstechnik" (Fundamentals on technical combustion processes III: simulation technique) , *University of Stuttgart*, 2008. In German.

[219] Schmidt, S., Adams, N. A., "Skriptum zur Vorlesung Gasdynamik" (Lecture notes on gas dynamics), *Technical University of Munich*, 2010. In German.

[220] Schönfeld, T., Rudgyard, M., "Steady and Unsteady Flow Simulations Using the Hybrid Flow Solver AVBP", *AIAA Journal*, Vol. 37, No. 11, pp. 1378-1385, 1999.

[221] Selle, L., Nicoud, F., Poinsot, T., "Actual impedance of non-reflecting boundary conditions: implications for computation of resonators", *AIAA journal*, Vol. 42, No. 5, pp. 958-964, 2004.

[222] Shen, J., "On error estimates of the projection methods for the Navier-Stokes equations: first-order schemes", *SIAM Journal on Numerical Analysis*, Vol. 29, pp. 57-77, 1992.

[223] Shen, J., "On error estimates of some higher order projection and penalty-projection methods for Navier-Stokes equations", *Journal of Numerical Mathematics*, Vol. 62, pp. 49-73, 1992.

[224] Shen, J., "On error estimates of projection methods for the Navier-Stokes equations: second-order schemes", *Mathematics of Computation*, Vol. 65, No. 215, pp. 1039-1065, 1996.

[225] Smits, A. J., Dussauge, J.-P., "Turbulent shear layers in supersonic flow", *Springer*, 2010.

[226] Schochet, S., "Asymptotics for symmetric hyperbolic systems with a large parameter", *Journal of Differential Equations*, Vol. 75, Issue 1, pp. 1-27, 1988.

[227] Soret, C., "Sur l'état d'équilibre que prend, du point de vue de sa concentration, une dissolution saline primitivement homogène, dont deux parties sont portées à des températures différentes" (On the equilibrium state that takes, from the point of view of its concentration, an initially homogeneous saline solution where two parts are conveyed to different temperatures), *Archives de Genève*, Vol. 2, pp. 48, 1879. In French.

[228] Spalart, P. R., Jou, W.-H., Stretlets, M., Allmaras, S. R., "Comments on the Feasibility of LES for Wings and on the Hybrid RANS/LES Approach", *Proceedings of the First AFOSR International Conference on DNS/LES*, 1997.

[229] Spalding, D. B., "Mathematical Modelling of Fluid Mechanics, Heat Transfer and Mass Transfer Processes", *Mechanical Engineering Department, Technical Report HTS-80-1, Imperial College of Science, Technology and Medicine, London*, 1980.

[230] Spalding, D. B., "Mixing and Chemical Reaction in Steady Confined Turbulent Flames", *13th Symposium (International) on Combustion*, pp. 649-657, 1971.

[231] Spalding, D. B., "Combustion and Mass Transfer", *Pergamon Press*, 1978.

[232] Strikwerda, J. C., "Initial boundary value problem for incompletely parabolic systems", *Communications on Pure and Applied Mathematics*, Vol. 30, Issue 6, pp. 797-822, 1977.

[233] Stöhr, M., Boxx, I., Carter, C. D., Meier, W., "Experimental study of vortex-flame interaction in a gas turbine model combustor", *Combustion and Flame*, Vol. 159, pp. 2636-2649, 2012.

[234] Stöhr, M., *Personal communication*, 2012.

[235] Stöhr, M., Meier, W., "Experimental study of vortex-flame interaction in a gas turbine model combustor", *Proceedings of the 6th European Combustion Meeting, June 25-28, Lund, Sweden*, 2013.

[236] Stull, D. R., Prophet, H., "JANAF Thermochemical Tables", 1971.

[237] Süli, E., Mayers, D., "An Introduction to Numerical Analysis", *Cambridge University Press*, 2003.

[238] Syred, N., "A review of oscillation mechanisms and the role of the precessing vortex core (PVC) in swirl combustion systems", *Progress in Energy and Combustion Science*, Vol. 32, pp. 93-161, 2006.

[239] Temam, R., "Sur l'approximation de la solution des équations de Navier-Stokes par la méthode des pas fractionnaires" (On the approximation of the solution of the Navier-Stokes eqations by means of the factional step method), *Archive for Rational Mechanics and Analysis*, Vol. 32, pp. 135-153, 1969. In French.

[240] Temam, R., "Remark on the pressure boundary condition for the projection method", *Theoretical and Computational Fluid Dynamics*, Vol. 3, No. 3, pp. 181-184, 1991.

[241] Thompson, K., "Time Dependent Boundary Conditions for Hyperbolic Systems", *Journal of Computational Physics*, Vol. 68, pp. 1-24, 1986.

[242] Traoré, P., Ahipo, Y. M., Louste, C., "A robust and efficient finite volume scheme for the discretization of diffusive flux on extremely skewed meshes in complex geometries", *Journal of Computational Physics*, Vol. 228, pp. 5148-5159, 2009.

[243] Tribuzi, S., "CFD Modelling of Combustion Instabilities in Gas Turbine Combustors by means of VRG Approach", *Italian Section of Combustion Institute, June 2006, Pisa, Italy*, 2006.

[244] van der Heul, D. R., Vuik, C., Wesseling, P., "A conservative pressure-correction method for flow at all speeds", *Computers & Fluids*, Vol. 32, pp. 1113-1132, 2003.

[245] van der Vorst, H. A., "BI-CGSTAB: A fast and smoothly converging variant of BI-CG for the solution of nonsymmetric linear systems", *SIAM Journal on Scientific and Statistical Computing*, Vol. 13, No. 2, pp. 631-644, 1992.

[246] van Doormal, J. P., Raithby, G. D., "Enhancements of the SIMPLE Method for Predicting Incompressible Fluid Flows", *Numerical Heat Transfer*, Vol. 7, Issue 2, pp. 147-163, 1984.

[247] van Doormal, J. P., Raithby, G. D., "An Evaluation of the Segregated Approach for Predicting Incompressible Fluid Flows", *ASME Paper 85-HT-9 presented at the National Heat Transfer Conference, Denver, Colorado, USA*, 1985.

[248] Vidovic, D., "Superlinearly convergent unstructured staggered schemes for compressible and incompressible flows", *Delft University of Technology*, Ph.D. thesis, 2005.

[249] Waldmann, A., *Personal communication*, 2013.

[250] Wall, C., Pierce, D. P., Moin, P., "A Semi-implicit Method for Resolution of Acoustic Waves in Low Mach Number Flows", *Journal of Computational Physics*, Vol. 181, pp. 545-563, 2002.

[251] Warnatz, J., Mass, U., Dibble, R. W., "Verbrennung: Physikalisch-Chemische Grundlagen, Modellierung und Simulation, Experimente, Schadstoffentstehung" (Combustion: Physical and Chemical Fundamentals, Modeling and Simulation, Experiments, Pollutant Formation), *Springer*, third edition, 2001. In German.

[252] Weigand, P., Meier, W., Duan, X. R., Stricker, W., Aigner, M., "Investigation of swirl flames in a gas turbine model combustor; I. Flow field, structures, temperatures and species distributions", *Combustion and Flame*, Vol. 144, pp. 205-224, 2006.

[253] Weigand, P., "Untersuchung periodischer Instabilitäten von eingeschlossenen turbulenten Drallflammen mit Lasermessverfahren" (Investigation of periodic instabilities of confined turbulent swirled flames using laser measurement techniques), *Institute of Combustion Technology for Aerospace Engineering, University of Stuttgart*, Ph.D. thesis, 2007. In German.

[254] Welch, J. E., Harlow, F. H., Shannon, J. P., Daly, B. J., "The MAC method", *Technical Report LA-3425, Los Alamos National Laboratory*, 1965.

[255] Werner, D., "Lineare Funktionalanalysis" (Linear Functional Analysis), *Springer*, fifth (advanced) edition, 2004. In German.

[256] Wesseling, P., "Principles of Computational Fluid Dynamics", *Springer*, 2001.

[257] Widenhorn, A., Noll, B., Aigner, M., "Accurate Boundary Conditions for the Numerical Simulation of Thermoacoustic Phenomena in Gas-Turbine Combustion Chambers", *Proceedings of the ASME Turbo Expo, May 8-11, Barcelona, Spain*, No. GT-2006-90441, 2006.

[258] Widenhorn, A., Noll, B., Aigner, M., "Numerical Characterization of the Non-Reacting Flow in a Swirled Gasturbine Model Combustor". *High Performance Computing in Science and Engineering '07, Transactions of the High Performance Computing Center Stuttgart (HLRS)*, pp. 431-444, 2008.

[259] Widenhorn, A., Noll, B., Stöhr, M., Aigner, M., "Numerical Characterization of the Reacting Flow in a Swirled Gasturbine Model Combustor". *High Performance Computing in Science and Engineering '08, Transactions of the High Performance Computing Center Stuttgart (HLRS)*, pp. 365-380, 2009.

[260] Widenhorn, A., Noll, B., Aigner, M., "Numerical Characterization of a Gas Turbine Model Combustor Applying Scale-Adaptive Simulation", *Proceedings of the ASME Turbo Expo, June 8-12, Orlando, Florida, USA*, No. GT-2009-59038, 2009.

[261] Wilcox, D. C., "Reassessement of the scale-determining equation for advanced turbulence models", *AIAA Journal*, Vol. 26, pp. 1299-1310, 1988.

[262] Wilcox, D. C., "Turbulence modeling for CFD", *DCW Industries*, third edition, 2006.

[263] Williams, F. A., "Combustion Theory", *Addison-Wesley Publishing Company*, 1985.

[264] Wong, M. W., "Discrete Fourier Analysis", *Birkhäuser*, 2011.

[265] Xiao, F., "Unified formulation for compressible and incompressible flows by using multi-integrated moments I: one-dimensional inviscid compressible flow", *Journal of Computational Physics*, Vol. 195, pp. 629-654, 2004.

[266] Xiao, F., "Unified formulation for compressible and incompressible flows by using multi-integrated moments II: Multi-dimensional version for compressible and incompressible flows", *Journal of Computational Physics*, Vol. 213, pp. 31-56, 2006.

[267] Zhang, X., "Identification of model and grid parameters for incompressible turbulent flows", *University of Göttingen*, Ph.D. thesis, 2007.

[268] Zhuang, M., Richter, C., "Computational AeroAcoustics and its Applications", *Berlin University of Technology*, lecture notes, 2010.

[269] Zukrow, M. J., Hoffman, J. D., "Gas dynamics", *J. Wiley & Sons*, p. 533, 1976.

Curriculum Vitae

Personal Data

Name	Gilles Reichling
Date of birth	June 11, 1986
Place of birth	Luxembourg
Nationality	Luxembourgish
Civil status	Married

School Education

09.1992 - 07.1994	École primaire Hagen
09.1994 - 07.1998	École primaire Kleinbettingen
09.1998 - 07.2005	Lycée Technique des Arts et Métiers, Luxembourg
07.2005	Diplôme de fin d'études secondaires techniques

Studies

10.2005 - 03.2010	Studies of Automotive Engineering, University of Stuttgart
03.2009 - 09.2009	Internship at Dr. Ing. h.c. F. Porsche AG, Weissach
10.2009 - 03.2010	Diploma Thesis at Dr. Ing. h.c. F. Porsche AG, Weissach in collaboration with the Institute of Fluid Mechanics and Hydraulic Machinery, University of Stuttgart
03.2010	Diplom-Ingenieur

Work Experience

04.2010 - 12.2013	Research Associate at the German Aerospace Center, Institute of Combustion Technology, Stuttgart
As of 01.2014	Staff Engineer at Goodyear Tire & Rubber Company, Goodyear Innovation Center * Luxembourg, Colmar-Berg